GENERATION, PROPAGATION AND DISSIPATION OF NEAR-INERTIAL WAVES IN THE TROPICAL OCEAN

A DISSERTATION SUBMITTED TO THE
GRADUATE DIVISION OF THE
UNIVERSITY OF HAWAI'I AT MĀNOA
IN PARTIAL FULFILLMENT OF THE
REQUIREMENTS FOR THE DEGREE OF

DOCTOR OF PHILOSOPHY

IN

OCEANOGRAPHY

MAY 2015

By

Saulo Müller Soares

Dissertation Committee:

Kelvin Richards, Chairperson
Eric Firing
Julian McCreary
Glenn Carter
Janet Becker

We certify that we have read this dissertation and that, in our opinion, it is satisfactory in scope and quality as a dissertation for the degree of Doctor of Philosophy in Oceanography.

DISSERTATION
COMMITTEE

Chairperson

Copyright 2015 by

Saulo Müller Soares

ACKNOWLEDGMENTS

First, I want to thank my advisor Dr. Kelvin Richards for accepting me into the program and mentoring me through the long, winding road of graduate studies.

I would also like to thank the support of my committee members: Dr. Eric Firing for the all he has patiently taught me over the years; Dr. Julian McCreary for teaching me his model and the complex fine-print of the theories of ocean waves; Dr. Glenn Carter for many invaluable field work lessons; Dr. Janet Becker for teaching me all the mathematics behind fluid flows. Their comments, critics and suggestions have greatly improved this research.

I would like to acknowledge the financial support from the Brazilian government through the CAPES/Fulbright scholarship, as well as support from the Department of Oceanography at the University of Hawai‘i and the National Oceanic and Atmospheric Administration.

Many thanks to Nancy Koike, Kristin Uyemura and Catalpa Kong for always making sure I was good with the system. Their kindness and service to the students of the department are invaluable.

A special thank you goes to Dr. Andrei Natarov for all the helpful discussions about my work, and in particular, help with setting up model experiments.

A shout-out to my colleagues whom I started this graduate program and the many friends I made during these amazing years in Hawai'i, which made this place feel like home in a heartbeat. Same to the good old friends back at home, for the encouragement.

Big mahalo goes to my brother André for taking charge and care of the family during this long absence, you are an example for me. And my appreciation for the unending support and understanding from the most inspirational person I've know, my dear mom Neusa and my dad Germano, to whom I dedicate this work, since after all, he drove me to this.

Finally, I have no words to describe how much the incredible Carolinita contributed to this work and myself as a person, your positiveness and sharpness kept me going when all I wanted was to throw the towel. Could not have done this without you, thanks for the support, motivation and inspiration, joinha!

ABSTRACT

Several aspects of the generation, propagation and dissipation of near-inertial waves were examined for tropical regions using a suite of numerical models and observational data. The primary goals were to investigate how the wind input of inertial kinetic energy partitions between loss by turbulent dissipation at the base of the mixed layer versus downward radiation of near-inertial waves, how deep the near-inertial energy penetrates into the interior, and how the background circulation and stratification impact the radiation of near-inertial waves. Results from a 1D model for upper ocean turbulence indicate that, in the eastern tropical Pacific, approximately 50% of the energy input by the wind is radiated downwards into the thermocline as near-inertial waves, despite displaying significant variability between forcing events. Estimates of the vertical energy flux for near-inertial wave packets observed in data collected in the tropical Indian Ocean are in general agreement with the 1D model results, such that 30% to 40% of the input of inertial energy per unit area by a single wind event is estimated to be radiated by a single packet seen in the 60 to 90 m depth range. The observations show that the near-inertial wave energy penetrates down to at least 200 m, where relatively high turbulent kinetic energy dissipation rates are estimated to have dissipated ≈20% of an energetic wave packet. A process study of the generation and propagation of these near-inertial waves using a linear continuously stratified model suggests that the inclusion of relative vorticity is a key mechanism that promotes localized regions of increased near-inertial energy, as well as increased depth penetration of energy in the vicinity of anticyclonic features. Furthermore, a combination of relative vorticity of order 10% of the local inertial frequency and increased thermocline stratification yields the highest near-inertial energy penetration into the thermocline.

TABLE OF CONTENTS

Acknowledgments . . . . . **iv**

Abstract . . . . . **v**

List of Tables . . . . . **ix**

List of Figures . . . . . **x**

1 Introduction **1**

1.1 Vertical mixing 1

1.2 Energy Sources for diapycnal mixing 2

1.3 Near-Inertial Energy in the Tropics 2

1.4 Objectives 4

1 References 4

2 Radiation of Inertial Kinetic Energy as Near Inertial Waves forced by Tropical Pacific Easterly Waves **8**

2.1 Introduction 8

2.2 Methods 9

2.2.1 Data 9

2.2.2 Finding easterly wave forcing events 10

2.2.3 Numerical modeling 11

2.3 Results and discussion 12

2.3.1 IKE decay timescales 12

2.3.2 Kinetic energy budget 13

2.4 Conclusions 15

Appendix 16

2.A Model energy budget 16

2 References 18

3 Near Inertial Waves during CINDY 2011: Energy fluxes and dissipation 26

3.1 Introduction 26

3.2 Data and Model output 28

3.3 Atmospheric Forcing 30

3.4 Background Upper Ocean Conditions 31

3.5 Mixed layer inertial oscillations 32

3.6 Near inertial Waves 34

3.6.1 Wave packet analysis methods 35

3.6.2 Results 41

3.6.3 Observed NIW patterns 46

3.6.4 Ray tracing 52

3.6.5 Wave Energy budget 56

3.7 Discussion and Concluding remarks 61

Appendix 62

3.A NIW polarization relations 62

3.B Complex demodulations 65

3.C 3D Ray tracing technique 66

3 References 67

4 Impacts of background stratification and circulation on Near-Inertial Wave dynamics 98

4.1 Introduction 98

4.1.1 Background and Motivation 98

4.1.2 Objectives 102

4.2 Model 103

4.2.1 Equations 103

4.2.2 Grid and Forcing 105

4.2.3 Experiments 107

4.3 Results 109

4.3.1 Quiescent Ocean Solutions 109

4.3.2 Eddying Ocean Solutions 118

4.4 Conclusions and Discussion 124

4 References 127

5 Concluding Remarks 180

5.1 Summary and Conclusions 180

5.2 Implications to parameterization of near-inertial mixing in OGCM 181

5.3 Future Work 184

5 References 185

LIST OF TABLES

2.1 Comparison between model and observed depth and time integrated IKE, wind IKE input in a 10m thick layer and model inertial velocity component skill for each EW forcing event. Skill estimated by Root Mean Square Differences between model and observations normalized by the observed range of velocities, with lower fractions indicating better skill. Integrated quantities shown as model to observed fractions. Observed IKE and wind input were estimated assuming a 10m thick layer with constant velocity. All fractions shown as mean and standard deviation of event simulations. 21

3.1 Summary table of wave properties. Most likely value, followed by range. 72

3.2 Energy budget terms. Units are mWm^{-2}. 73

4.1 Table of experiments, bold denotes the experiments discussed in this manuscript. . 130

4.2 Mode frequency as a function of wavelength. 131

LIST OF FIGURES

2.1 (a) Map of the study area with yellow stars marking the locations of the TAO/EPIC buoys at 12° and 8°N, 95°W used in this investigation and the composite structure of an EW at lag zero obtained by linear regression onto EW Outgoing Longwave Radiation (OLR) anomalies at 10°N, 95°W for June-November 2000-2003 periods (blue X). Arrows represent regressed Cross-Calibrated Multi-Platform (CCMP) ocean surface winds, while magenta dashed contours represent negative OLR anomalies and cyan contours represent positive OLR anomalies at 5 Wm^{-2} intervals from -30 to 30 Wm^{-2}. The OLR anomaly threshold that defines EW deep convection events is $18Wm^{-2}$. (b) Time series of lagged EW wind anomalies obtained from the 10°N, 95°W buoy in black arrows. The red curve shows the rotation rate of the wind anomalies scaled by the local inertial period and the grey filled area denotes the rate interval where winds are near resonant, while the blue line shows the EW OLR anomalies. 22

2.2 Time series of IKE at 10 m depth from moored current meters (grey filled) and wind rotation rate scaled by the local inertial period(blue line) overlain with EW deep convection events (red dashed line) used to define EW forcing events: (a) 8°N, 95°W buoy for June-November 2002 period; (b) 12°N, 95°W for June-November 2003 period. The dashed black lines indicate the rotation rate interval where resonant forcing is likely to occur and the green lines the model start/end dates. (c) Average value overlain with maximum and minimum of the decay timescale r^{-1} used to tune GOTM simulations of each EW forcing event (cyan bars). Average overlain with minima and maxima Park decay timescale for each EW event using ML depths and N^2 maxima below the ML from the GOTM simulations (magenta bars). 23

2.3 Average value overlain with maximum and minimum of the decay timescale r^{-1} used to tune GOTM simulations of each EW forcing event (cyan bars). Average overlain with minima and maxima Park decay timescale for each EW event using ML depths and N^2 maxima below the ML from the GOTM simulations (magenta bars) 24

2.4 (a) Median IKE for each term in equation 3.6.1 normalized by its wind input of IKE, over-bars denote the minima and maxima found across all simulations. (b) Scatter plot of GOTM simulation average NIW vertical energy flux ($\bar{\Pi}_r$) to the simulation averaged wind input of IKE ($\bar{\Pi}_w$). The black line is the linear fit with slope given by $d\Pi_{NIW}/d\Pi_w$. Symbols denote individual simulations as: $\lhd$ Jun/02; $\Diamond$ Jul/02; $\square$ Oct/02; $\bigcirc$ Nov/02; $\star$ Jun/03; $+$ Jul/03; $\rhd$ Sep/03; $*$ Oct/03. Colors denote the parameterization scheme. 25

3.1 Maps of the study area with black cross marking the location of the R/V *Mirai* station at 8°S, 80.5°E. Top maps show Outgoing long wave radiation (OLR) 3 days prior to the sampling period at the station (a) and 3 days after the start of the sampling period (b). The approximate OLR threshold that defines deep convection is 180 Wm^{-2}. Bottom maps show Cross-Calibrated Multi-Platform (CCMP) ocean 10-m surface winds 3 days prior to the sampling period (c) and 3 days after the start of the sampling period (d). Arrows represent wind vectors while the shading represent wind speed magnitude. 74

3.2 Top panels show *in situ* temperature collected during CINDY (a) and the MERCATOR model's potential temperature (b) at 8°S, 80.5°E. Middle panels show *in situ* salinity (c) and MERCATOR salinity (d). Bottom panels show the Brount-Vaisala frequency squared computed from (e) *in situ* density data and from (f) MERCATOR density output. 75

3.3 Top panels show LADCP u (a) and v (b) current components collected during CINDY at 8°S, 80.5°E. Middle panels show the SADCP u (c) and v (d) current components. Bottom panels show the u (e) and v (f) current components obtained from MERCATOR output at 8°S, 80.5°E. 76

3.4 (a) Turbulent Kinetic Energy (TKE) dissipation rate (ϵ) measured from Micro-Structure Profiler casts at 8°S, 80.5°E.(b) LADCP derived current shear magnitude ($|\frac{d\vec{u}}{dz}|$) at 8°S, 80.5°E. (c) 2-6 day band-passed upward phase propagating current shear magnitude ($|\frac{du_{\vec{NI}}}{dz}|$) derived from LADCP measurements at 8°S, 80.5°E. . . . 77

3.5 (a) Wind stress magnitude (shaded) with unit arrows indicating wind direction. (b) Inertial Kinetic Energy (IKE) in the ML (shaded) and SADCP demodulated inertial current components at 30m depth. (c) Wind work on ML inertial currents and the accumulated wind work. Time-series at 8°S, 80.5°E. 78

3.6 (a) Current vectors for surface down to 500m from LADCP (blue, 2 m inverval), SADCP (black, 16 m interval) and MERCATOR (red, 16 m interval) averaged for the station sampling period. (b) Near-surface current vectors averaged for the station sampling period at 8°S, 80.5°E. The LADCP and SADCP *in situ* currents (averaged over upper 45 m and at 30 m depth, respectively) are compared with MERCATOR (averaged over upper 45 m), AVISO and OSCAR products (at 15 m depth). 79

3.7 Time-series of (a) vorticity, (b) divergence, (c) normal component of the horizontal strain and (d) shear component of the horizontal strain at 8°S, 80.5°E. Dashed lines are for AVISO derived quantities, dashed dotted lines for OSCAR and solid lines represent MERCATOR at select depths (black: 15m, darker grey: 110m and light grey: 220m). Red vertical dahsed lines mark the beginning and end of the sampling period. 80

3.8 (a) Near-surface vorticity (shading) and circulation (lines) from AVISO 7 days averaged absolute geostrophic currents near the beginning of the fixed station sampling period and (b) near the end of the sampling period. (c) Same but for OSCAR 5 days averaged currents near the beginning of the fixed station sampling period and (d) at the end of the sampling period. (e) Vorticity (shading) and circulation (lines) from MERCATOR ≈90 m depth currents for the begining of the fixed station sampling period and (f) for the end of the sampling period. Crosses mark the location of the R/V *Mirai* station at 8°S, 80.5°E. Thickest lines denote flows in excess of 1 ms^{-1}. . 81

3.9 (a) Rotary spectrum for mixed layer currents from SADCP measurements. (b) Mixed layer current ellipse during the first 3 inertial periods (≈11 days) of the sampling period at 8°S, 80.5°E. Also shown are the inertial oscillation ellipses and its parameters obtained from the FFT (red) and HM94 (black, dashed line shows the major axis) methods. 82

3.10 Upper panels show depth-timeseries of upward phase (downward energy) propagating meridional velocity (v_{up}) components collected during CINDY at 8°S, 80.5°E for (a) LADCP and (b) SADCP. Lower panels show depth-timeseries of downward phase (upward energy) propagating meridional velocity (v_{dn}) components collected during CINDY at 8°S, 80.5°E for (c) LADCP and (d) SADCP. 83

3.11 Downward radiating near-inertial kinetic energy computed from 2-6 day bandpassed current anomalies for (a) SADCP, (b) LADCP and (c) LADCP but WKB scaled and plotted over WKB stretched depth. Wave packets of interest are labeled with white text as WPI, WPII and WPIII. The white dashed lines denote ray paths, one forward ray path extrapolating WPI using the wave packet method estimated c_{gz} and a backwards ray path extrapolating the WPII estimated c_{gz}. 84

3.12 (a) Rotary frequency spectra of LADCP currents. Directional energy density spectrum of NIW band at 70m (b), 113m (c) and 216m (d). Angles denote direction waves propagate towards, with 0° being North. Bins along the radius show the frequencies in the 2-6 day band from low at the center to high at the edges. Filled bin are color-coded based on the energy density and for every frequency it is shown the high, mean and low phase and energy estimates. Only values above the coherence significant value are shown. 85

3.13 (a) Variance in the 2-6 days band from the Wavelet Transform (WLT) of LADCP currents. (b) Peak frequency of the WLT spectrum of zonal currents (u). (c) Peak frequency of the WLT spectrum of meridional currents (v). Only values above the coherence significant value are shown. 86

3.14 Directional spectrum of the NIW band obtained from the WTL coherence phase between u and ρ for the wave packet I (60-90m) (a), wave packet II (110-140m) (b) and wave packet III (180-240m) (c). Angles denote direction waves propagate towards, with 0° being North. Bins along the radius show the frequencies in the 2-6 day band from low at the center to high at the edges. Filled bins are color-coded based on the u energy density. Only values above the coherence significant value are shown. 87

3.15 Wave properties estimated using the HM94 method. (a) Peak frequency $\omega_\circ$ (blue) and near-inertial ellipse tilt ϕ_2 (red). (b) Phase (red) and complex amplitude (blue) of demodulated rotary currents using $\omega_\circ = 0.92 f_\circ$ from WPI. (c) Same but using $\omega_\circ = 1.08 f_\circ$ from WPII. (d) Same but using $\omega_\circ = 1.0 f_\circ$ from WPIII. Also shown are linear fits to phase segments (defined by the blue dots) and it's corresponding vertical wavenumbers. 88

3.16 Near-Inertial ellipses computed from demodulated u_{up} and v_{up} at (a) 70 m using $\omega_\circ = 0.93 f_\circ$ (WPI), (b) at 113 m using $\omega_\circ = 1.12 f_\circ$ (WPII), (c) $\omega_\circ = 1.05 f_\circ$ at 216 m depth WPIII. Also shown are NIW ellipses obtained from FFT (red) and HM94 (black, dashed line shows the major axis) methods. Green dashed lines show ϕ_1 obtained from the coherence spectra. 89

3.17 (a) Profiles for r_1 and r_2 using different methods. Note that the FFT gives an average representation of the whole timeseries for a given frequency, at a given depth, whist the HM94 method describes this average behavior within a narrower interval in the timeseries, at a given depth. (b) r_1 at every time instance and depth using its primary WLT frequency. White contours denote the regions of elevated NIW variance. . . . 90

3.18 Estimates of NIW vertical wavenumber m. (a) WKB stretched m profiles using peak frequencies from the HM94 method (blue curve) and the FFT spectrum (red curve), note that these profiles follow the times where NIW energy is significant, e.g follow the ray path. (b) WKB stretched m based on demodulation with WLT peak frequencies. (c) Non stretched vertical wavenumber spectrum for wave packets I, II and III, note prominent peaks at wavelengths roughly consistent with non stretched HM94 analysis of (a) 0.27, 0.043 and 0.08-0.09. 91

3.19 (a) Ray depths for WPII and WPIII backtracked to the base of ML (solid lines) and forward traced for 15 days (dashed lines). Each line represents a different initial wavenumber and lighter shades of gray denote rays with a deeper starting depth. For reference, the color contours show the near-inertial kinetic energy from LADCP measurements. (b) Depth of forward traced WPI rays. Also shown are MERCATOR N (red curves) and f_{eff} (blue curves) profiles at the locations marked in Figure 3.23. 92

3.20 Properties for select WPII rays backwards and forwards traced from the CINDY station: (a) ω_i/f_{eff} (r), (b) vertical wavenumber $m_\circ$, (c) horizontal wavnumber $|k_H|$, (d) background f_{eff}/f. Approach to critical layer are indicated by $\omega_i/f_{\text{eff}} \to 1.0$ and $m_\circ \to \infty$. Circles denote the starting points. 93

3.21 Maps for WPII rays backward and forward traced from the CINDY station starting at 110m (top row), at 120m (middle row) and 130m (bottom row). Rays are color coded by depth in meters (first column), the ratio ω_i/f_{eff} (second column) and the ray tube volume relative to its initial volume (third column). Streamlines show the background circulation at the starting depth. Black circles mark the locations where profiles of background N and f_{eff} are extracted. 94

3.22 Maps for WPIII rays backward and forward traced starting at 185m (top row), at 200m (middle row) and 215m (bottom row). Rays are color coded as in Figure 3.23. Streamlines show the background circulation at the respective starting depth. . . . 95

3.23 Maps for WPI rays forward traced with starting depth at 55m (top row), at 75m (middle row) and 95m (bottom row). Rays are color coded as in Figure 3.23 and streamlines show the background circulation at the respective starting depth, while black circles mark the locations where background profiles of N and f_{eff} are extracted (note the Longitudes have changed). 96

3.24 Time series of energy balance terms for WPIII, depth integrated between 170-245m. The left axis is for fluxes (local rate of change of kinetic energy and turbulent kinetic energy dissipation ϵ, blue and red line respectively), while the right axis is for kinetic energy density. Quoted values denote quantities time integrated between 10/15 and 10/22. 97

4.1 Time averaged profiles of N^2 (a) and N (b) from CINDY measurements collected at 8°S, 80.5°E. The black dashed line denotes $\bar{N}$ calculated for the thermocline between 100 and 500 m. 132

4.2 Profiles of N^2 (a) used in LCS integrations and mode structure (ψ_n) for mode numbers 1 to 5, 10, 20 and 25 structure (b). 133

4.3 Modal decomposition parameters for the two N^2 profiles shown in Figure 4.2 (blue for Profile a and red for Profile b). (a) shows the mode phase speeds c_n. (b) shows the modal vertical wavelength (λ_z) calculated using $\bar{N}$, the black dashed lines indicate the $100--300$ m range. (c) shows the modal wind forcing amplitude, i.e. fraction of wind stress projected onto each mode, and the cumulative sum of these modal forcing amplitudes (solid lines). The lower 5 modes account for 98% and 76% of the total input for Profile a and Profile b, respectively. 134

4.4 Tropical Indian Ocean bathymetry with black cross marking the location of the R/V *Mirai* station at 8°S, 80.5°E. The LCS domain is shown in the magenta box. 135

4.5 Snapshots of the wind field over part of the domain, showing the time evolution of winds during the first two weeks of the model integration period. White contours show the Outgoing Longwave Radiation (OLR) anomalies, with positive anomalies in solid and negative anomalies in dashed. 136

4.6 Snapshots of the wind field over part of the domain, showing the time evolution of winds during the second two week period of model integration period. White contours show the Outgoing Longwave Radiation (OLR) anomalies, with positive anomalies in solid and negative anomalies in dashed. 137

4.7 MERCATOR time averaged vorticity (ζ) normalized by the local inertial frequency at 8°S, 80.5°E (Rossby number) for model domain. The Barotropic vorticity component used in experiments EDDY1_TL and EDDY1_WTL (a), and enhanced barotropic vorticity to mimic upper ocean values used in experiments EDDY2_TL and EDDY2_WTL (b). The black cross marks the location of the R/V *Mirai* station at 8°S, 80.5°E. . . 138

4.8 Modal damping timescale (c_n^2/A) for the profiles of N^2 used in LCS integrations. The black dashed line denotes the expected damping timescale derived from the observations. 139

4.9 Time series of near-inertial kinetic energy (NIKE) at the CINDY station 8°S 80.5°E for the ML, TL (60 m) and 120 m (thermocline), for (a) QUIET_TL, (b) QUIET_WTL, (c) VMIX_QUIET_TL, (d) VMIX_QUIET_WTL. 140

4.10 Frequency spectrum for mixed layer (ML) currents (a). Near-inertial current ellipse with parameters obtained from FFT rotary spectrum (b). 141

4.11 ML NIKE for Experiment QUIET_TL at (a) model day 11 ($t_\circ$, ML energy peak) (b) 1 IP after $t_\circ$ (c) 3 IP after $t_\circ$ and (d) 5 IP after $t_\circ$. The magenta box shows the region where spectrum, averages and integrations are carried out, while the dashed lines mark the extension used to calculate meridional spectra. 142

4.12 Same as Figure 4.11 but for the TL (60 m). 143

4.13 Same as Figure 4.11 but for the average thermocline near-inertial kinetic energy. . . 144

4.14 Experiment QUIET_TL depth-time series at 8°S 80.5°E of near-inertial (2-6 days band passed) zonal velocity anomalies u' (a), zonal upward phase propagating velocity anomalies u'_{up} (b), meridional velocity anomalies v' (c), meridional upward phase propagating velocity anomalies v'_{up} (d). 145

4.15 (a) For QUIET_TL; upper panel: Depth-time series of WKB scaled NIKE at 8°S 80.5°E. Lower panel: Maximum NIKE during first 8 inertial periods of integration along 80.5°E showing the extend of downward and equatorwad NIKE penetration. (b) Same but for QUIET_WTL. 146

4.16 Experiment QUIET_TL depth-latitude chart of near-inertial (2-6 days band passed) u' along 80.5°E at (a) $t_\circ$ (ML energy peak), (b) 1IP after $t_\circ$, (c) 3IP after $t_\circ$, and (d) 5IP after $t_\circ$. 147

4.17 NIKE (m^2s^{-2}) partition by mode number for the QUIET_TL experiment at (a) CINDY station (8°S 80.5°E) and (b) at the Equator. 148

4.18 Experiment QUIET_TL time-Latitude Hovmoller plots of NIKE for (a) mode 1, (b) mode 2, (c) mode 3, and (d) mode 4, along 80.5°E. 149

4.19 Energy density frequency spectra as a function of depth (a), NIW ellipse in the TL (60 m) with corresponding FFT parameters (b), NIW ellipse at 120 m (c), and NIW ellipse at 180 m, at the CINDY station, 8°S 80.5°E for experiment QUIET_TL. . . 150

4.20 Experiment QUIET_TL time and area integrated (magenta box in Figure 4.11) NIKE partitioned by mode number. Red curve shows the 1D projection of wind forcing, as in Figure 4.3c. It should be noted that, for all quiescent ocean solution, these integrated patterns represent quite well the partition into modes at any given location. 151

4.21 Experiment QUIET_TL variance preserving zonal spectra for (a) ML, (b) TL, (c) 120 m and (d) 180 m. Colors denote spectra calculated at times $t_\circ$ (ML energy peak) (blue), 1IP after $t_\circ$ (red), 3IP after $t_\circ$ (green) and 5IP after $t_\circ$ (black). 152

4.22 Experiment QUIET_TL variance preserving meridional spectra for (a) ML, (b) TL, (c) 120 m and (d) 180 m. Colors denote spectra calculated at times (ML energy peak ML) $t_\circ$ (blue), 1IP after $t_\circ$ (red), 3IP after $t_\circ$ (green) and 5IP after $t_\circ$ (black). 153

4.23 Same as Figure 4.14 but for experiment QUIET_WTL. 154

4.24 Same as Figure 4.23, but for experiment QUIET_WTL. 155

4.25 Experiment EDDY1_TL ML NIKE contours overlaying background flow ζ for (a) $t_\circ$ (b) 1 IP after $t_\circ$ (c) 3 IP after $t_\circ$ and (d) 5 IP after $t_\circ$. 156

4.26 Experiment EDDY1_TL TL NIKE contours overlaying background flow ζ for (a) $t_\circ$ (b) 1 IP after $t_\circ$ (c) 3 IP after $t_\circ$ and (d) 5 IP after $t_\circ$. 157

4.27 Experiment EDDY1_TL average thermocline NIKE contours overlaying background flow ζ for (a) $t_\circ$ (b) 1 IP after $t_\circ$ (c) 3 IP after $t_\circ$ and (d) 5 IP after $t_\circ$. 158

4.28 Same as Figure 4.25, but for experiment EDDY2_TL. 159

4.29 Same as Figure 4.26, but for experiment EDDY2_TL. 160

4.30 Same as Figure 4.27, but for experiment EDDY2_TL. 161

4.31 Experiment EDDY1_TL depth-time series at 8°S 80.5°E of near-inertial (2-6 days band passed) zonal velocity anomalies u' (a), zonal upward phase propagating velocity anomalies u'_{up} (b), meridional velocity anomalies v' (c), meridional upward phase propagating velocity anomalies v'_{up} (d). 162

4.32 Experiment EDDY1_TL depth-time series at 8.65°S 78°E of near-inertial (2-6 days band passed) zonal velocity anomalies u' (a), zonal upward phase propagating velocity anomalies u'_{up} (b), meridional velocity anomalies v' (c), meridional upward phase propagating velocity anomalies v'_{up} (d). 163

4.33 Same as Figure 4.31, but for experiment EDDY2_TL. 164

4.34 Same as Figure 4.32, but for experiment EDDY2_TL. 165

4.35 EDDY1_TL Energy density frequency spectra as a function of depth (a), NIW ellipse in the TL (60 m) (b), NIW ellipse at 120 m (c), and NIW ellipse at 180 m, for the CINDY station at 8°S 80.5°E. 166

4.36 EDDY1_TL Energy density frequency spectra as a function of depth (a), NIW ellipse in the TL (60 m) (b), NIW ellipse at 120 m (c), and NIW ellipse at 180 m, for the Ac at 8.65°S 78°E. 167

4.37 EDDY2_TL Energy density frequency spectra as a function of depth (a), NIW ellipse in the TL (60 m) (b), NIW ellipse at 120 m (c), and NIW ellipse at 180 m, for the CINDY station at 8°S 80.5°E. 168

4.38 EDDY2_TL Energy density frequency spectra as a function of depth (a), NIW ellipse in the TL (60 m) (b), NIW ellipse at 120 m (c), and NIW ellipse at 180 m, for the AC at 8.65°S 78°E. 169

4.39 (a) EDDY1_TL upper panel: Depth-time series of WKB scaled NIKE at 8°S 80.5°E. Lower panel: Maximum NIKE during first 8 inertial periods of integration along 80.5°E showing the extend of downward and equatorwad NIKE penetration. (b) Same for EDDY2_TL. 170

4.40 (a) EDDY1_TL upper panel: Depth-time series of WKB scaled NIKE at 8.65°S 78°E. Lower panel: Maximum NIKE during first 8 inertial periods of integration along 78°E showing the extend of downward and equatorwad NIKE penetration. (b) Same for EDDY2_TL. 171

4.41 NIKE (m^2s^{-2}) partition by mode number for the EDDY1_TL experiment at (a) a cyclone (8°S 80.5°E) and (b) at an AC (8.65°S 78°E). 172

4.42 NIKE (m^2s^{-2}) partition by mode number for the EDDY2_TL experiment at (a) a cyclone (8°S 80.5°E) and (b) at an AC (8.65°S 78°E). 173

4.43 Same as Figure 4.21, but for experiment EDDY1_TL. 174

4.44 Same as Figure 4.22, but for experiment EDDY1_TL. 175

4.45 Same as Figure 4.21, but for experiment EDDY2_TL. 176

4.46 Same as Figure 4.21, but for experiment EDDY1_TL. 177

4.47 Experiment EDDY2_WTL; Top panel: Depth-time series of WKB scaled NIKE at 8.65°S 78°E. Lower panel: Maximum NIKE during first 8 inertial periods of integration along 78°E showing the extend of downward and equatorwad NIKE penetration. 178

4.48 NIKE (m^2s^{-2}) partition by mode number for the EDDY2_WTL experiment at (a) CINDY station (8°S 80.5°E) and (b) at the Equator 179

CHAPTER 1
INTRODUCTION

1.1 Vertical mixing

The small scale (< 1 m), turbulent vertical mixing is considered a key process for a wide range of phenomena. For example, in the upper ocean vertical mixing drives entrainment processes that directly impact air-sea interactions (*Alexander and Deser* 1995; *Deser et al.* 2003), nutrient fluxes and primary productions (*Klein and Coste* 1984; *Lévy et al.* 2009). In the interior ocean, turbulence drives diapycnal mixing, a major factor maintaining meridional overturning circulations, such as the global thermohaline circulation (*Stommel* 1958; *Munk and Wunsch* 1998; *Richards et al.* 2009; *Marshall and Speer* 2012).

The physics of turbulent mixing near the ocean surface differs from that in the interior (see *Large et al.* 1994). In the near-surface boundary layer, external atmospheric forcing has a direct and large influence on the behavior of turbulence, while in the interior turbulence depends solely on local properties. An example of this non-local turbulent mixing is the night time convection induced by the surface cooling phase of the diurnal cycle of surface heating and cooling. Turbulence levels are measured by the rate of turbulent kinetic energy dissipation (ϵ), and often display a close relation to the local vertical current shear (S) via the gradient Richardson number $R_i = N^2/S^2$, where N is the buoyancy frequency, particularly in the interior where the local character of turbulence is more evident (*Polzin* 1996; *Richards et al.* 2014). A rapid increase in ϵ is observed to occur as the R_i drops below a critical value, when Kelvin-Helmholtz instabilities develop (*Richards et al.* 2014).

The turbulent kinetic energy dissipation rate typically relates to the diapycnal (vertical) mixing via an eddy diffusivity $\kappa_v = \gamma\epsilon/N^2$, where γ is an efficiency coefficient (*Osborn* 1980). Because the interior ocean is largely stably stratified, this process consumes turbulent kinetic energy. For instance, *Munk and Wunsch* (1998) estimated that an average eddy diffusivity in the interior of 10^{-4} m^{2}s^{-1}, required to support a global overturning circulation of 25-30 Sv, would consume approximately 2 TW of power. This estimate is reduced if one takes into account the Southern

Ocean upwelling regime (*Marshall and Speer* 2012) or if the spatial distribution of eddy diffusivity controlled by topographic roughness is considered (*Decloedt and Luther* 2010).

1.2 Energy Sources for diapycnal mixing

An important energy source supporting the production of small scale turbulent mixing both in the upper and interior ocean is the winds, with the other most significant source being the tides (*Munk and Wunsch* 1998). In the upper ocean, wind-induced mixing is mostly attributed to direct Ekman and inertial current vertical shear (*Sanford et al.* 1987). In the interior, wind induced mixing is achieved either by direct breaking of near-inertial internal waves or Kelvin-Helmholtz instabilities triggered by the near-inertial wave (NIW) shear (*Alford and Gregg* 2001). NIWs are considered more important to mix the interior ocean than the sub-inertial eddies generated from the wind forced large-scale circulation (*Wunsch and Ferrari* 2004).

Because of this, several studies in the previous decade (*Alford* 2001; *Watanabe and Hibiya* 2002; *Alford* 2003; *Jiang et al.* 2005; *Furuichi et al.* 2008; *Zhai et al.* 2009) have tried to estimate the contribution of wind generated near-inertial energy to the power required to mix the ocean interior. The various estimates of the wind energy input to mixed layer inertial motions indicate that there is sufficient energy to account for about half of the 2 TW power requirement. However, few of these studies (*Furuichi et al.* 2008; *Zhai et al.* 2009) address how much energy actually leaves the mixed layer as NIWs. The model results from *Furuichi et al.* (2008) suggest that only about 20% of the wind induced near-inertial energy escapes the surface boundary layer region. The few observational studies, however, tend to indicate the existence of vigorous NIW energy in the deep ocean (*Alford* 2010; *Alford et al.* 2012).

1.3 Near-Inertial Energy in the Tropics

The input of near-inertial energy by the wind has two preferential forms: impulsive or continuous broadband forcing (*Kim et al.* 2014). Furthermore, when the rotation rate of the wind approaches the local inertial frequency, there is the possibility of maximizing the input of near-inertial energy

into the mixed layer, thus resonantly forcing strong inertial oscillations therein (*Crawford and Large* 1996).

Several of the maps of wind work on inertial oscillations draw attention to elevated inputs of near-inertial energy to the mixed layer in the tropical regions, and these inputs are shown to vary seasonally quite significantly (see Figure 5 in *Furuichi et al.* 2008). In the Pacific, *Mickett et al.* (2010) estimate about 30% of the wind input of inertial kinetic energy into the mixed layer is due to Easterly Wave synoptic scale forcing, largely because of a favoring of resonant forcing episodes as Easterly Waves comprise broadband variability with times scales overlapping with the inertial period of the tropics. In the Indian Ocean, the Madden-Julian Oscillation (MJO), although an intraseasonal variability, is known for abrupt west wind bursts and therefore could supply the inertial energy during non monsoon periods, while during monsoon season, the enhanced convective activity in the area can lead to intense storms such as those discussed by *Cuypers et al.* (2013).

In the tropical regions, where inertial periods are in the order of days, tidal motions are less likely to interfere significantly with near-inertial signals, facilitating the isolation of the near-inertial band with filtering techniques. Yet data sets that capture all aspects of the generation, propagation and dissipation of NIWs are rare, in part because the intermittent nature of near-inertial motions requires a comprehensive array of field measurements or sampling of opportunity. In particular, very few studies have examined how near-inertial energy escapes the mixed layer in the tropics as downward propagating NIWs. Noted exceptions include *Alford and Gregg* (2001); *Plueddemann and Farrar* (2006); *Cuypers et al.* (2013), however, quantification of the NIW energy in relation to the input by the wind, or its dissipation was limited or lacking. Most model studies and data sets of propagating NIWs in the literature are for midlatitude regions, such that a detailed assessment of NIWs and its relationship to vertical mixing in tropical regions is still lacking.

A recent study by *Sasaki et al.* (2013) indicates significant sensitivity of air-sea interactions in the tropical Pacific to how vertical mixing is vertically distributed, i.e. if preferentially confined near the surface or spread within the thermocline. This warrants further investigation on the contribution of near-inertial motions to mixing in tropical regions.

1.4 Objectives

This work examines aspects of the generation, propagation and dissipation of wind induced near-inertial waves in tropical oceans. It does so by combining numerical models of varying complexity with analysis of direct observations of near-inertial motions. The primary objectives are to:

1. Investigate how the decay of inertial kinetic energy in the upper ocean partitions among upper ocean turbulent mixing versus radiation of near-inertial waves during several Pacific Easterly Wave forcing events.

2. Estimate wave energy fluxes and wave energy dissipation in relation to the wind input of energy to the ML from *in-situ* observations in the tropical Indian Ocean.

3. Understand the role of different mechanisms favoring the depth penetration of near-inertial energy into the Indian Ocean thermocline.

Each of these objectives is addressed in the following three chapters. The dissertation concludes with a discussion of the implications of its results for a parameterization of near-inertial wave induced mixing for climate models.

1 References

Alexander, M. A., and C. Deser (1995), A mechanism for the recurrence of wintertime midlatitude sst anomalies, *J. Phys. Oceanogr.*, *25*(1), 122–137.

Alford, M. (2003), Improved global maps and 54-year history of wind-work on ocean inertial motions, *Geophys. Res. Lett.*, *30*(8), doi:10.1029/2002GLO16614.

Alford, M. H. (2001), Internal swell generation: The spatial distribution of energy flux from the wind to mixed layer near-inertial motions, *J. Phys. Oceanogr.*, *31*, 2359–2368.

Alford, M. H. (2010), Sustained, full-water-column observations of internal waves and mixing near mendocino escarpment, *J. Phys. Oceanogr.*, *40*(12), 2643–2660.

Alford, M. H., and M. C. Gregg (2001), Near-inertial mixing: Modulation of shear, strain and microstructure at low latitude, *J. Geophys. Res.*, *106*(C8), 16,947–16,968.

Alford, M. H., M. F. Cronin, and J. M. Klymak (2012), Annual cycle and depth penetration of wind-generated near-inertial internal waves at ocean station papa in the northeast Pacific, *J. Phys. Oceanogr.*, *42*(6), 889–909.

Crawford, G., and W. Large (1996), A numerical investigation of resonant inertial response of the ocean to wind forcing, *J. Phys. Oceanogr.*, *26*(6), 873–891.

Cuypers, Y., X. Le Vaillant, P. Bouruet-Aubertot, J. Vialard, and M. J. Mcphaden (2013), Tropical storm-induced near-inertial internal waves during the Cirene experiment: Energy fluxes and impact on vertical mixing, *J. Geophys. Res.*, *118*(1), 358–380.

Decloedt, T., and D. S. Luther (2010), On a simple empirical parameterization of topography-catalyzed diapycnal mixing in the abyssal ocean, *J. Phys. Oceanogr.*, *40*(3), 487–508.

Deser, C., M. A. Alexander, and M. S. Timlin (2003), Understanding the persistence of sea surface temperature anomalies in midlatitudes, *J. Climate*, *16*(1), 57–72.

Furuichi, N., T. Hibiya, and Y. Niwa (2008), Model-predicted distribution of wind-induced internal wave energy in the worlds oceans, *J. Geophys. Res*, *113*, C09,034.

Jiang, J., Y. Lu, and W. Perrie (2005), Estimating the energy flux from the wind to ocean inertial motions: The sensitivity to surface wind fields, *Geophys. Res. Lett.*, *32*(15).

Kim, S. Y., P. M. Kosro, and A. L. Kurapov (2014), Evaluation of directly wind-coherent near-inertial surface currents off Oregon using a statistical parameterization and analytical and numerical models, *J. Geophys. Res.*, *119*(10), 6631–6654.

Klein, P., and B. Coste (1984), Effects of wind-stress variability on nutrient transport into the mixed layer, *Deep Sea Research Part A. Oceanographic Research Papers*, *31*(1), 21–37.

Large, W. G., J. C. McWilliams, and S. C. Doney (1994), Oceanic vertical mixing: a review and a model with a nonlocal boundary layer parameterization, *Rev. Geophys.*, *32*, 363–403.

Lévy, M., P. Klein, and M. Ben Jelloul (2009), New production stimulated by high-frequency winds in a turbulent mesoscale eddy field, *Geophys. Res. Lett.*, *36*(16).

Marshall, J., and K. Speer (2012), Closure of the meridional overturning circulation through southern ocean upwelling, *Nature Geosci.*, *5*(3), 171–180.

Mickett, J., Y. Serra, M. Cronin, and M. Alford (2010), Resonant forcing of mixed layer inertial motions by atmospheric easterly waves in the northeast tropical Pacific*, *J. Phys. Oceanogr.*, *40*(2), 401–416.

Munk, W., and C. Wunsch (1998), Abyssal recipes II: energetics of tidal and wind mixing, *Deep-Sea Research Part I*, *45*(12), 1977–2010.

Osborn, T. (1980), Estimates of the local rate of vertical diffusion from dissipation measurements, *J. Phys. Oceanogr.*, *10*(1), 83–89.

Plueddemann, A., and J. Farrar (2006), Observations and models of the energy flux from the wind to mixed-layer inertial currents, *Deep Sea Research Part II: Topical Studies in Oceanography*, *53*(1-2), 5–30.

Polzin, K. (1996), Statistics of the richardson number: Mixing models and finestructure, *J. Phys. Oceanogr.*, *26*(8), 1409–1425.

Richards, K., S. Xie, and T. Miyama (2009), Vertical mixing in the ocean and its impact on the coupled ocean-atmosphere system in the eastern tropical Pacific*, *J. Climate*, *22*(13), 3703–3719.

Richards, K. J., A. Natarov, E. Firing, Y. Kashino, S. M. Soares, M. Ishizu, G. S. Carter, J. H. Lee, and K. I. Chang (2014), Shear generated turbulence in the equatorial Pacific produced by small vertical scale flow features, *J. Geophys. Res., (submitted).*

Sanford, T. B., P. G. Black, J. R. Haustein, J. W. Feeney, G. Z. Forristall, and J. F. Price (1987), Ocean response to a hurricane. part i: Observations, *J. Phys. Oceanogr.*, *17*(11), 2065–2083.

Sasaki, W., K. J. Richards, and J.-J. Luo (2013), Impact of vertical mixing induced by small vertical scale structures above and within the equatorial thermocline on the tropical Pacific in a cgcm, *Clim. Dynam.*, *41*(2), 443–453.

Stommel, H. (1958), The abyssal circulation, *Deep-Sea Res.*, *5*, 80–82.

Watanabe, M., and T. Hibiya (2002), Global estimates of the wind-induced energy flux to inertial motions in the surface mixed layer, *Geophys. Res. Lett.*, *29*(8), 80–1.

Wunsch, C., and R. Ferrari (2004), Vertical mixing, energy, and the general circulation of the oceans, *Annu. Rev. Fluid Mech.*, *36*, 281–314.

Zhai, X., R. Greatbatch, C. Eden, and T. Hibiya (2009), On the loss of wind-induced near-inertial energy to turbulent mixing in the upper ocean, *J. Phys. Oceanogr.*, *39*(11), 3040–3045.

CHAPTER 2
RADIATION OF INERTIAL KINETIC ENERGY AS NEAR INERTIAL WAVES FORCED BY TROPICAL PACIFIC EASTERLY WAVES

2.1 Introduction

The wind generated near-inertial wave (NIW) field, also known as internal swell (*Alford* 2001), may be a significant source of energy fueling the turbulent diapycnal mixing in the ocean interior, which in turn is believed to balance the strength of the meridional overturning circulation (*Munk and Wunsch* 1998). The majority of wind energy input to inertial motions occurs under the mid-latitude storm tracks (*Alford* 2003; *Watanabe and Hibiya* 2002; *Furuichi et al.* 2008), where *D'Asaro* (1985) showed that a few intense forcing events account for over half of the annual integrated input of inertial kinetic energy (IKE) to the mixed layer (ML). These events were associated with the passage of small scale, fast moving storms and fronts where predominant anticyclonic rotation of the wind occurred as the system moved overhead, which can lead to resonant forcing conditions when the winds are in phase with the inertial currents (*D'Asaro* 1985; *Crawford and Large* 1996).

Recently, significant IKE input from the wind to the ML is shown to occur on the northeastern tropical Pacific ocean during June to November associated with the passage of synoptic atmospheric disturbances known as Easterly Waves (EW, Figure 1a) (*Mickett et al.* 2010). EW are ubiquitous low level convectively coupled waves with periods of 2 to 7 days propagating westward along the Inter Tropical Convergence Zone (ITCZ) over the Atlantic and Pacific oceans (*Serra et al.* 2008). Clockwise rotation of the wind tends to occur on the right side of the EW track, favoring the occurrence of resonant forcing (Figure 1b), and thus strong inertial currents in the ML. *Mickett et al.* (2010) suggest that this EW driven resonant forcing may contribute 30% of the total IKE flux from the winds to the ML in the tropical Pacific and Atlantic oceans.

Once excited, the upper ocean IKE is thought to be dissipated by three main mechanisms: NIW radiation (*D'Asaro et al.* 1995), turbulent dissipation (*Crawford and Large* 1996) and wind stress opposing the surface inertial currents (*Pollard and Millard Jr* 1970). *Alford* (2001, 2003)

and *Watanabe and Hibiya* (2002) used slab models to estimate and map the flux of KE from winds to the ML and infer its contribution to the energy demanded by interior dyapicnal mixing. These models balance the wind flux of IKE to a given H deep ML with a single linear sink term, requiring prescription of an appropriate, albeit ad-hoc decay rate. Thus, they implicitly assume that all IKE inputed eventually resides in the form of NIWs. *Plueddemann and Farrar* (2006) demonstrated that such slab models lack a short timescale, turbulent-like form of IKE dissipation, resulting in overestimates in the wind IKE flux to the ocean. This imbalance was particularly acute under resonant forcing conditions, emphasizing the need to model separately the turbulent dissipation and NIW radiation dissipation processes to arrive at realistic estimates of IKE partition.

A debate about which process dominates the near-surface IKE decay, and hence its contribution to interior mixing still remains. Recent global and regional model results suggest that most of the IKE from the wind is dissipated in the upper ocean by turbulent dissipation (*Furuichi et al.* 2008; *Zhai et al.* 2009). In contrast, *Park et al.* (2009) found good agreement of a linear NIW disperion model with IKE decay timescales derived from drifter data, implying NIW radiation as the dominant form of energy loss.

In this paper we empirically estimate how IKE loss partitions between these two processes by looking at the integrated kinetic energy budget of several simulated EW forcing events, in an attempt to assess their importance to NIW generation. EW anomalous winds display successive periods of clockwise rotation lasting over a day (Figure 1b), thus making EW forcing closer to an ideal resonant system. The simulated forcing events indicate that NIW radiation is at least equally important as turbulent dissipation for the wind inputed IKE loss, leading to high vertical wave energy fluxes at the base of the ML.

2.2 Methods

2.2.1 Data

The data is composed of quality controlled temperature, salinity, currents and surface meteorology (winds, air temperature, humidity, shortwave and longwave radiation) measurements from two

National Oceanic and Atmosphere Administration (NOAA) Tropical Atmosphere Ocean/Eastern Pacific Investigation of Climate Processes (TAO/EPIC) buoys located at 8° and 12°N along 95°W. Temperature and salinity recorded at 10 min intervals and available at 1, 5, 10, 20, 40, 60, 80, 100, 140, 200, 300 m (Salinity at 1, 5, 10, 20, 40, 80, 120 m) are used as initial conditions for numerical simulations. Current data available at 20 min intervals is obtained from a single point acoustic current meter (ACM) moored at 10 m depth, and the inertial currents are isolated by bandpassing at frequencies $0.6f$ and $2\pi/32h$ with a third-order Butterworth filter. The meteorological data is used primarily to force the model with surface heat and momentum fluxes, using the COARE 3.0 bulk algorithm (*Fairall et al.* 2003). Buoy wind data is also combined with twice daily outgoing longwave radiation (OLR) data and the inertial currents to find EW forcing events in the time series. The inertial currents are also used to tune the one-dimensional turbulence model. Although the TAO/EPIC dataset is remarkably long, wind and current data overlap was the limiting factor in this study, with the usable dataset only covering the boreal summer/fall periods of 2002 at 8°N and of 2003 at 12°N. The 10°N, 95°W buoy had no quality wind measurements concomitant with currents but its wind data is used to make the composite EW structure shown in Figure 1b.

2.2.2 Finding easterly wave forcing events

This study investigates eight EW wind forcing events, four occurring at 8°N and four at 12°N. The events are located in the time series based on observed near-surface inertial currents, wind rotation rate and OLR anomalies. First, deep convection events associated with EW passage are flagged by negative anomalies in the bandpassed (in wavenumber and frequency domain) OLR data, following the method described in *Serra et al.* (2008). Second, wind rotation rate is computed from TAO/EPIC winds using a moving average with window size equal to the local inertial period. Clockwise rotation within ±50% of the local inertial rate occurring in the vicinity of deep convection events are also flagged. Finally, these two factors are aligned with ML IKE local maxima to determine when the forcing events occurred and their approximate duration. Note that one or more EW deep convection events may be associated with an IKE maximum. Figure 2a, b shows the EW events, which are grouped and labeled according to the calendar month they occurred

mostly in: Jun/02, Jul/02, Oct/02 and Nov/02 at 8°N and Jun/03, Jul/03, Sep/03, Oct/03 at 12°N. The forcing events vary in intensity and in the importance of rotation to the flux of energy from the winds to the currents.

2.2.3 Numerical modeling

The numerical model used is the one-dimensional General Ocean Turbulence Model (GOTM), a multiple turbulence parameterization platform. In this study we added a simple linear damping term of the form $-r\vec{u}$ to the model's momentum equations to account for the energy dissipation by NIW radiation, following *Plueddemann and Farrar* (2006). We then utilize the four turbulent dissipation schemes available, KPP (*Large et al.* 1994), K-omega (*Umlauf et al.* 2003), K-epsilon (*Burchard* 2001) and GLS (*Umlauf and Burchard* 2003) to simulate the upper ocean response to each EW forcing event and study their energy budget. Such one-dimensional models have been used before to study the response of the upper ocean to resonant forcing (*Crawford and Large* 1996), in particular, the KPP scheme has been demonstrated to represent well the dynamics when compared to LES runs (*Skyllingstad et al.* 2000) and field data (*Large and Crawford* 1995).

The events are modeled using high resolution ($\Delta z = 0.25m$), short duration (15-30 days) simulations of the upper 250m to capture the rise and fall of IKE as seen in the observed time series (Figure 2a, b), thus avoiding the need to reinitialize model runs when solutions diverge from observations. Model run start and end times are set for periods where the IKE is at a minimum before and after the target IKE maximum (green lines in Figure 2a, b). The initialization date is varied by ±1 day, yielding 12 simulations for each event. To obtain more accurate initial kinetic energy and wind work, the simulations are initialized with the observed currents uniformly spread over a 10 m ML. For each simulation the value of the damping coefficient r is tuned so that the model inertial current variance matches the observed inertial current variance to within ±10%. Separating the near-inertial and residual frequencies and forming the kinetic energy equation, we can compute the IKE budget for each simulation as

$$\Delta IKE = \int \Pi_w dt + \int \Pi_m dt + \int \Pi_r dt + NL, \tag{2.1}$$

where Π_w is the flux of IKE from the winds to the ocean, Π_m is the IKE dissipation by turbulence, Π_r is the dissipation by NIW radiation and NL represent the three interaction terms with residual frequencies. The same filtering technique of section 2.1 is applied to separate near-inertial and residual frequencies.

2.3 Results and discussion

2.3.1 IKE decay timescales

First we evaluate the NIW decay timescales (r^{-1}) values used in tuning the one-dimensional model. The cyan bars in Figure 2c show average, minima and maxima of r^{-1} for each EW forcing event, computed by averaging over the four different mixing parameterizations and the three initialization dates. It is evident that r^{-1} varies considerably between forcing events and even among the different parameterizations and initialization dates as shown by the error bars. The typical decay timescale found with GOTM is of ≈ 7.5 days, substantially longer than the 5.1 days used by *Plueddemann and Farrar* (2006) for this region, while the maximum r^{-1} was five times this average.

To give some confidence in such a range of values, we compare the GOTM empirical r^{-1} with the linear e-folding decay timescale of *Park et al.* (2009). Their timescale relies on an initial wavelength of the NIW as well as the local ML depth (H_{ML}) and the maximum buoyancy frequency squared (N_o^2) below the mixed layer, which in their model is assumed constant with depth. In this study, values for H_{ML} are obtained from model potential density profiles using a surface density difference criterion of $0.03 kgm^{-3}$ and and then averaged over the length of the simulation after the diurnal cycle is removed. N_o^2 values are also calculated from model potential density averaged over the length of the simulation. As in *Park et al.* (2009), our best guess for the NIW initial wavelength is the climatological wind meridional decorrelation scale value of 180 km for the region.

The magenta bars on Figure 2c represent event averaged, minima and maxima of the Park scale obtained from the GOTM H_{ML} and N_o^2. The GOTM empirical r^{-1} are in general in good agreement with the Park scale. Noted exceptions occur for Jun/02 and Nov/02. The former displays very little IKE input by the wind with several simulations producing an estimate of zero NIW damping

(r =0). The latter, although has a large input of energy, displays net dissonance characteristics and is discussed below.

2.3.2 Kinetic energy budget

Figure 3a summarizes the results of the momentum budget of the GOTM simulations, showing the typical fraction of the integrated IKE input by the wind accounted by each term in equation 2.1. Roughly, for every unit IKE generated by the wind work on inertial currents, another 0.15 is added via nonlinear transfer from other frequencies. Turbulent dissipation ($\int \Pi_m$) removes about 0.65 and NIW radiation 0.50. The large variation of the Π_m and NL terms (denoted by the over-bars) are evidence that turbulent dissipation largely acts to dissipate the IKE coming from other frequencies, and in fact the turbulent dissipation terms in the total KE budget are responsible for removing over 80% of the wind input of KE. Because the model is integrated from a low initial IKE to a low final IKE state, the ΔIKE term is very small, typically 1-5% of $\int \Pi_m$. The residual or computation error of the momentum budget is smaller, but of the order of the ΔIKE term, and thus no more than 3% of $\int \Pi_m$.

As with the decay timescale, the NIW radiation fraction showed significant variation among events, ranging from 0% to a maximum of 87% occurring in one simulation of the Oct/03 event. High NIW radiation fractions are found for the Jun/03, Sep/03, Jul/02 events, where the average contribution of NIW radiation to the model IKE loss is of about 60%. For the other four events the average is ≈35%, closer but still above the estimate by *Furuichi et al.* (2008). The zero NIW radiation estimates were found for cases where the wind IKE input was very low, such as Jun/02 and Oct/02.

As expected, the more energetic internal swell events are associated with the fastest decay rates. However the decay rate is a poor predictor of NIW radiation due to large scatter. In contrast, there is a robust linear relation between each simulation's averaged wind input of IKE ($\bar{\Pi}_w$) and its average NIW radiation flux ($\bar{\Pi}_r$) (Figure 3b). The slope of the linear fit is ≈0.6, a value only slightly above the average fraction cited above. A similar pattern between Π_w and total dissipation ($\Pi_m + \Pi_r$) was observed by *Plueddemann and Farrar* (2006). Nonetheless, we believe we have

provided the first explicit evidence of an empirical relation between the amount of wind forcing and the energy carried by generated internal swells.

Significant deviations from the 60% loss due to NIW radiation are the Oct/03 event (80% slope) which was highly stratified (several simulations with N_o^2 in excess of $8 \times 10^{-3} s^{-2}$) thus reducing the turbulent dissipation efficiency and increasing NIW radiation, and the Nov/02 event where net dissonance occurred (see *Mickett et al.* (2010) figure 8g). In this case, the wind forcing, although strong, at times acted to remove a portion of the IKE preventing its build-up. At the same time, the model IKE pool was being increased via an anomalously high nonlinear transfer, which however, is dissipated almost exclusively by Π_m, leading to lower than expected values of r and hence NIW radiation (Figure 2c). Therefore, we believe that the wind input of IKE and the stratification are the primary factors controlling the strength of NIW radiation.

The average wind input of IKE during the study period is in good agreement with published boreal summer seasonal averages of the eastern tropical Pacific, e.g. *Alford* (2003) and *Furuichi et al.* (2008). However, the seasonal mean EW induced NIW vertical energy flux is $\approx 1 \times 10^{-3} W m^{-2}$, a value slightly above the summer/fall seasonal means predicted for this region by *Furuichi et al.* (2008). The highest NIW flux estimated here for a strong resonant forcing event (Jul/02), with an average Π_r of $4.3 \times 10^{-3} W m^{-2}$, is four times the average indicating that few events contribute to majority of the total flux of NIW over a season. It is also an order magnitude more than was recently observed propagating below 600 m at station PAPA in the northeastern Pacific (*Alford et al.* 2012). This suggests that highly stratified tropical regions may be hot spots for internal swell generation since EW are active over the western Pacific as well as the Atlantic.

Even though the general picture of NIW fluxes by *Furuichi et al.* (2008) may be correct, these intense resonant forcing events tend to be not well resolved by the coarse wind products forcing today's OGCMs, thus application of the method employed here to other regions would aid in quantifying the global average fraction of wind forced IKE radiated away as NIWs. The strong correlation between the wind work on inertial currents and the IKE flux due to radiating NIWs could be used to predict when large internal swell events occur, aiding in field measurement campaigns and in developing vertical diffusivity parameterizations for coarser gridded climate

models. The usefulness of this relationship has two caveats: first, there has to be significant IKE input to overcome dissipation and second, no significant contributions from remote sources of IKE occur. Pre-selection of forcing events plays a key role in minimizing both of these uncertainties. Comparison of model and observed IKE indicates (Table 2.1) that remote sources were insignificant in this study. The model also show reasonable skill in simulating the inertial currents (Table 2.1).

Finally, it is likely that these EW forced internal swells travel equatorward and downward into the ocean interior and could be associated with observed mixing episodes at the equatorial thermocline, as observed for instance by *Richards et al.* (2012).

2.4 Conclusions

By finding an appropriate energy decay timescale due to NIW radiation and using an array of modern turbulent dissipation parameterizations we were able to estimate the upper ocean IKE budget for several EW wind forcing events, which under a wide range of conditions accounted for the vast majority of IKE input to the ocean in this study. The results indicate that, although turbulent dissipation is the dominant form of KE loss, accounting typically for the majority of the upper IKE loss, for most cases it acts to balance a large portion of IKE coming from nonlinear terms rather than the wind work on inertial currents itself. Therefore, we conclude that the radiation of NIW is an important loss term for the IKE input by EW in this region, radiating $\approx 50 - 60\%$ of the wind input of IKE and thus generating large amplitude internal swells.

It is possible that observed mixing episodes at the equatorial thermocline (*Richards et al.* 2012) are related to these EW forced internal swells. The findings reported here, therefore, have strong implications to the debate on the contribution of wind energy fueling mixing in and below the thermocline, suggest there are significant sources of IKE to support interior mixing outside of the midlatitude storm tracks, and point to the need to represent such mixing in climate models.

Appendix

2.A Model energy budget

To obtain equation 2.1, the model's momentum equations are separated into the near-inertial component and a residual component, i.e. $u = u_i + u_r$ and $v = v_i + v_r$, and depth and time integrated to form the following kinetic energy equation:

$$\Delta IKE + \Delta RKE + \Delta NKE = \int \Pi_{wi} dt + \int \Pi_{wr} dt + \int \Pi_{mi} dt + \int \Pi_{mr} dt + \int \Pi_{mn} dt + \int \Pi_{ri} dt + \int \Pi_{rr} dt + \int \Pi_{rn} dt. \quad (2.A.1)$$

In the above

$$\Delta IKE = \int_0^T \int_H^0 \frac{\partial}{\partial t} \left(\tfrac{1}{2} u_i^2\right) dz dt, \quad (2.A.2a)$$

$$\Delta RKE = \int_0^T \int_H^0 \frac{\partial}{\partial t} \left(\tfrac{1}{2} u_r^2\right) dz dt, \quad (2.A.2b)$$

$$\Delta NKE = \int_0^T \int_H^0 \frac{\partial}{\partial t} \left(u_i u_r\right) dz dt, \quad (2.A.2c)$$

are the rate of change of energy components integrated on time and depth, where T is the integration time and H is the model depth. The terms

$$\int \Pi_{wi} dt = \frac{1}{\rho_\circ} \int^T \tau_\circ u_i \left(z = 0\right) dt, \quad (2.A.3a)$$

$$\int \Pi_{wr} dt = \frac{1}{\rho_\circ} \int^T \tau_\circ u_r \left(z = 0\right) dt, \quad (2.A.3b)$$

represent the wind input of IKE and RKE respectively, where $\tau_\circ$ is the wind stress at the ocean surface. The turbulent dissipation terms, or eddy diffusivity terms are

$$\int \Pi_{mi} dt = -\int^T \int_H^0 \kappa_v \left(\frac{\partial u_i}{\partial z}\right)^2 dz dt, \tag{2.A.4a}$$

$$\int \Pi_{mr} dt = -\int^T \int_H^0 \kappa_v \left(\frac{\partial u_r}{\partial z}\right)^2 dz dt, \tag{2.A.4b}$$

$$\int \Pi_{mn} dt = -\int^T \int_H^0 2\kappa_v \left(\frac{\partial u_i}{\partial z}\right)\left(\frac{\partial u_r}{\partial z}\right) dz dt, \tag{2.A.4c}$$

where κ_v is the eddy diffusivity calculated by the model turbulence parameterization scheme. Finally, the terms

$$\int \Pi_{ri} dt = -\int^T \int_H^0 r u_i^2 dz dt, \tag{2.A.5a}$$

$$\int \Pi_{rr} dt = -\int^T \int_H^0 r u_r^2 dz dt, \tag{2.A.5b}$$

$$\int \Pi_{rn} dt = -\int^T \int_H^0 2 r u_i u_r dz dt, \tag{2.A.5c}$$

are the KE damping terms representing NIW radiation. Note that non-inertial energy is also damped at the same rate and constitutes another model limitation.

Equation 2.1, therefore, considers only terms related to the IKE (equations 2.A.2a, 2.A.3a, 2.A.4a, 2.A.5a) and sets $NL = \int \Pi_{mn} dt + \int \Pi_{rn} dt + \Delta NKE$, in addition to a small, roughly the size of ΔIKE, error in the budget calculation. It should be noted that the eddy diffusivity terms are the source of nonlinearity in the system. For a typical simulation, the term $\int \Pi_{mn} dt$ acts as a source of KE which offsets the dissipation of the $\int \Pi_{mi} dt$ and $\int \Pi_{mr} dt$ terms. The nonlinear terms (NL), in some sense, are an artifact of the mathematical separation used above and may have little physical meaning.

2 References

Alford, M. (2003), Improved global maps and 54-year history of wind-work on ocean inertial motions, *Geophys. Res. Lett.*, *30*(8), doi:10.1029/2002GLO16614.

Alford, M. H. (2001), Internal swell generation: The spatial distribution of energy flux from the wind to mixed layer near-inertial motions, *J. Phys. Oceanogr.*, *31*, 2359–2368.

Alford, M. H., M. F. Cronin, and J. M. Klymak (2012), Annual cycle and depth penetration of wind-generated near-inertial internal waves at ocean station papa in the northeast Pacific, *J. Phys. Oceanogr.*, *42*(6), 889–909.

Burchard, H. (2001), Simulating the wave-enhanced layer under breaking surface waves with two-equation turbulence models, *J. Phys. Oceanogr.*, *31*(11), 3133–3145.

Crawford, G., and W. Large (1996), A numerical investigation of resonant inertial response of the ocean to wind forcing, *J. Phys. Oceanogr.*, *26*(6), 873–891.

D'Asaro, E. (1985), The energy flux from the wind to near-inertial motions in the surface mixed layer, *J. Phys. Oceanogr.*, *15*(8), 1043–1059.

D'Asaro, E. A., C. C. Eriksen, M. D. Levine, P. Niiler, C. A. Paulson, and P. V. Meurs (1995), Upper-ocean inertial currents forced by a strong storm. part i: Data and comparisons with linear theory, *J. Phys. Oceanogr.*, *25*, 2909–2936.

Fairall, C., E. Bradley, J. Hare, A. Grachev, and J. Edson (2003), Bulk parameterization of air-sea fluxes: Updates and verification for the coare algorithm, *J. Climate*, *16*(4), 571–591.

Furuichi, N., T. Hibiya, and Y. Niwa (2008), Model-predicted distribution of wind-induced internal wave energy in the worlds oceans, *J. Geophys. Res*, *113*, C09,034.

Large, W., and G. Crawford (1995), Observations and simulations of upper-ocean response to wind events during the Ocean Storms experiment, *J. Phys. Oceanogr.*, *25*(11), 2831–2852.

Large, W. G., J. C. McWilliams, and S. C. Doney (1994), Oceanic vertical mixing: a review and a model with a nonlocal boundary layer parameterization, *Rev. Geophys.*, *32*, 363–403.

Mickett, J., Y. Serra, M. Cronin, and M. Alford (2010), Resonant forcing of mixed layer inertial motions by atmospheric easterly waves in the northeast tropical Pacific*, *J. Phys. Oceanogr.*, *40*(2), 401–416.

Munk, W., and C. Wunsch (1998), Abyssal recipes II: energetics of tidal and wind mixing, *Deep-Sea Research Part I*, *45*(12), 1977–2010.

Park, J., K. Kim, and R. Schmitt (2009), Global distribution of the decay timescale of mixed layer inertial motions observed by satellite-tracked drifters, *J. Geophys. Res.*, *114*(C11).

Plueddemann, A., and J. Farrar (2006), Observations and models of the energy flux from the wind to mixed-layer inertial currents, *Deep Sea Research Part II: Topical Studies in Oceanography*, *53*(1-2), 5–30.

Pollard, R., and R. Millard Jr (1970), Comparison between observed and simulated wind-generated inertial oscillations, in *Deep Sea Research and Oceanographic Abstracts*, vol. 17, pp. 813–816, Elsevier.

Richards, K., Y. Kashino, A. Natarov, and E. Firing (2012), Mixing in the western equatorial Pacific and its modulation by enso, *Geophys. Res. Lett.*, *39*(2), L02,604.

Serra, Y. L., G. Kiladis, and M. F. Cronin (2008), Horizontal and vertical structure of easterly waves in the Pacific ITCZ, *J. Atmos. Sci.*, *65*, 1266–1284.

Skyllingstad, E., W. Smyth, and G. Crawford (2000), Resonant wind-driven mixing in the ocean boundary layer, *J. Phys. Oceanogr.*, *30*(8), 1866–1890.

Umlauf, L., and H. Burchard (2003), A generic length-scale equation for geophysical turbulence models, *Journal of Marine Research*, *61*(2), 235–265.

Umlauf, L., H. Burchard, and K. Hutter (2003), Extending the k-[omega] turbulence model towards oceanic applications, *Ocean Modelling*, *5*(3), 195–218.

Watanabe, M., and T. Hibiya (2002), Global estimates of the wind-induced energy flux to inertial motions in the surface mixed layer, *Geophys. Res. Lett.*, *29*(8), 80–1.

Zhai, X., R. Greatbatch, C. Eden, and T. Hibiya (2009), On the loss of wind-induced near-inertial energy to turbulent mixing in the upper ocean, *J. Phys. Oceanogr.*, *39*(11), 3040–3045.

Table 2.1: Comparison between model and observed depth and time integrated IKE, wind IKE input in a 10m thick layer and model inertial velocity component skill for each EW forcing event. Skill estimated by Root Mean Square Differences between model and observations normalized by the observed range of velocities, with lower fractions indicating better skill. Integrated quantities shown as model to observed fractions. Observed IKE and wind input were estimated assuming a 10m thick layer with constant velocity. All fractions shown as mean and standard deviation of event simulations.

Quantity	Jun/02	Jul/02	Oct/02	Nov/02	Jun/03	Jul/03	Sep/03	Oct/03
$\int IKE$	-10 ± 24 %	23 ± 8 %	50 ± 18 %	5 ± 3 %	16 ± 14 %	6 ± 4 %	7 ± 8 %	27 ± 10 %
$\int \Pi_w$	-7 ± 58 %	12 ± 11 %	34 ± 48 %	-9 ± 10 %	70 ± 28 %	62 ± 12 %	-6 ± 12 %	-13 ± 11 %
$RMS\ u_i$	33 ± 1 %	13 ± 1 %	15 ± 0.4 %	19 ± 3 %	29 ± 4 %	15 ± 2 %	19 ± 2 %	16 ± 2 %
$RMS\ v_i$	33 ± 1 %	15 ± 2 %	18 ± 1 %	13 ± 3 %	22 ± 3 %	15 ± 2 %	17 ± 2 %	17 ± 2 %

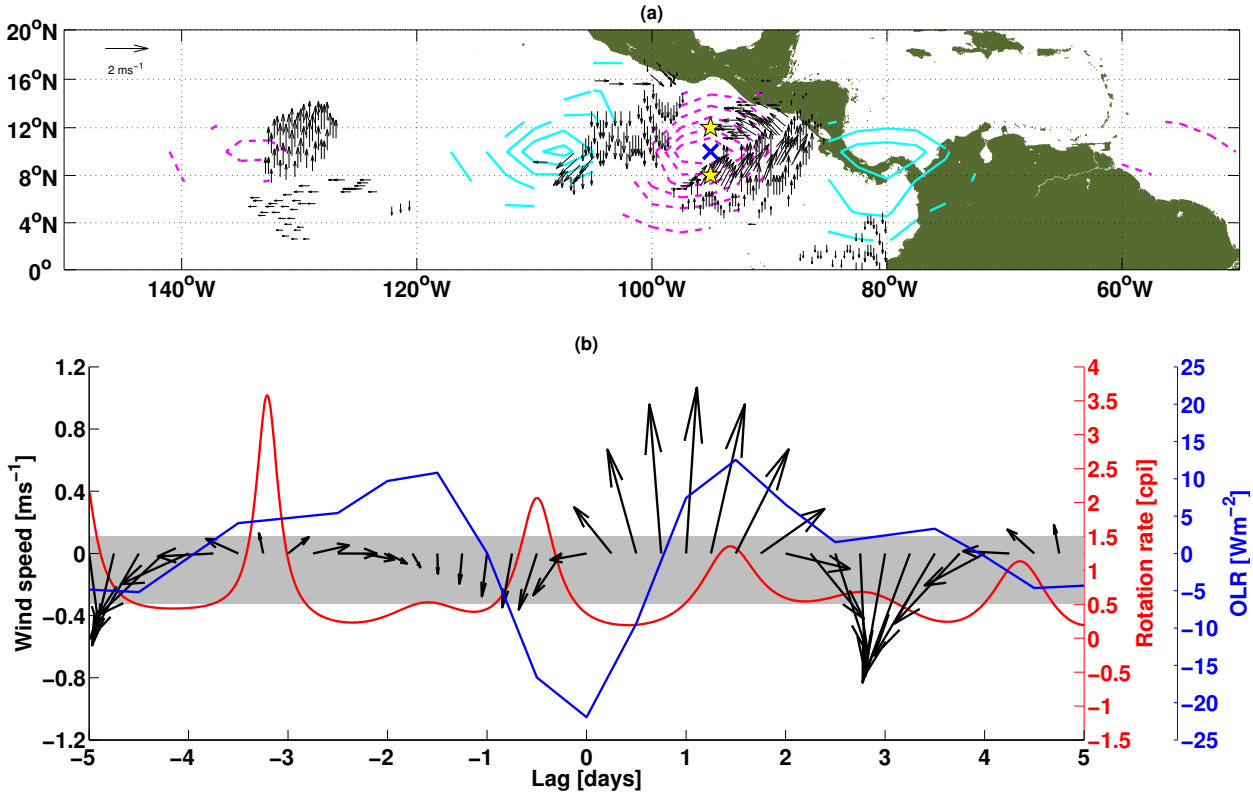

Figure 2.1: (a) Map of the study area with yellow stars marking the locations of the TAO/EPIC buoys at 12° and 8°N, 95°W used in this investigation and the composite structure of an EW at lag zero obtained by linear regression onto EW Outgoing Longwave Radiation (OLR) anomalies at 10°N, 95°W for June-November 2000-2003 periods (blue X). Arrows represent regressed Cross-Calibrated Multi-Platform (CCMP) ocean surface winds, while magenta dashed contours represent negative OLR anomalies and cyan contours represent positive OLR anomalies at 5 Wm^{-2} intervals from -30 to 30 Wm^{-2}. The OLR anomaly threshold that defines EW deep convection events is $18Wm^{-2}$. (b) Time series of lagged EW wind anomalies obtained from the 10°N, 95°W buoy in black arrows. The red curve shows the rotation rate of the wind anomalies scaled by the local inertial period and the grey filled area denotes the rate interval where winds are near resonant, while the blue line shows the EW OLR anomalies.

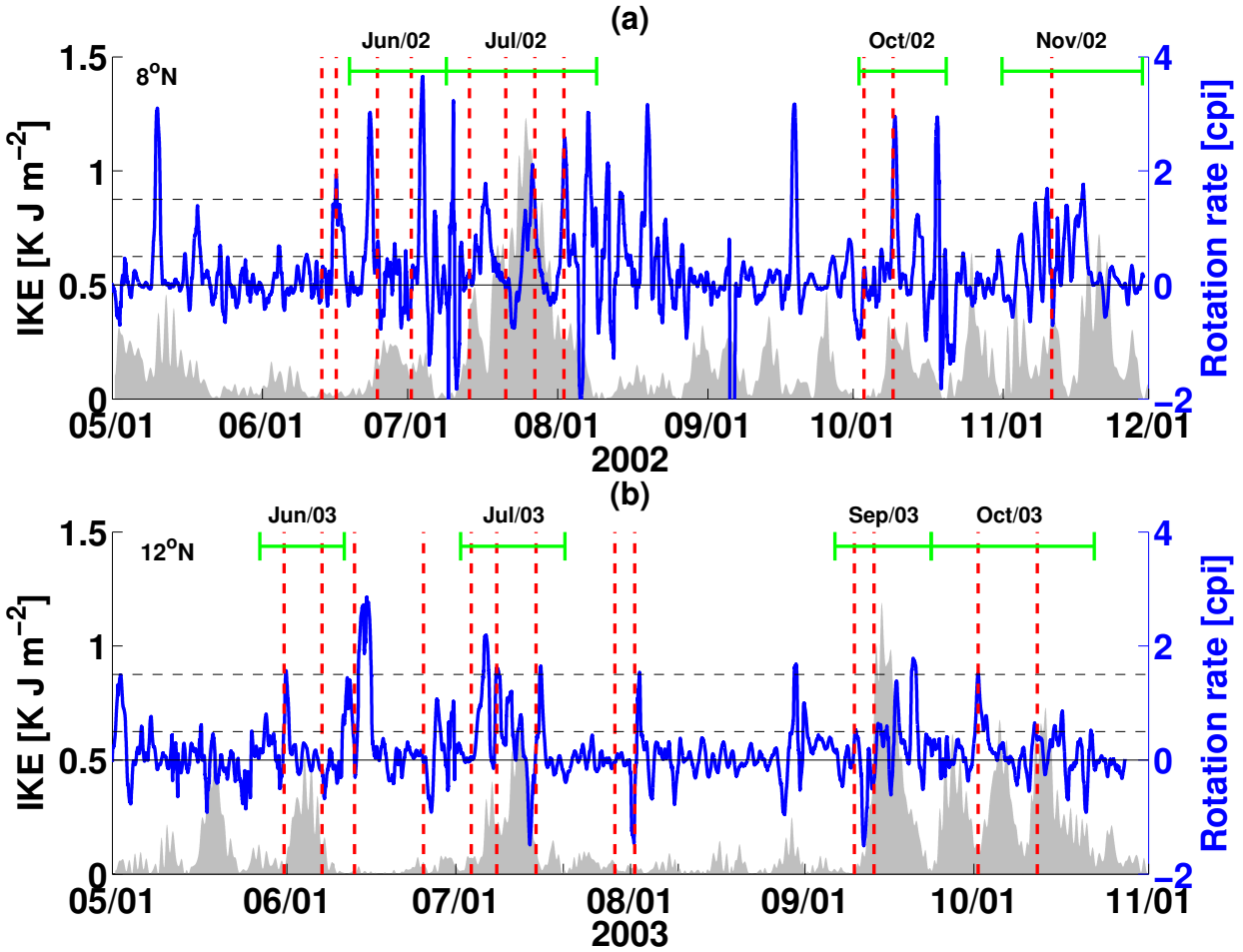

Figure 2.2: Time series of IKE at 10 m depth from moored current meters (grey filled) and wind rotation rate scaled by the local inertial period(blue line) overlain with EW deep convection events (red dashed line) used to define EW forcing events: (a) 8°N, 95°W buoy for June-November 2002 period; (b) 12°N, 95°W for June-November 2003 period. The dashed black lines indicate the rotation rate interval where resonant forcing is likely to occur and the green lines the model start/end dates. (c) Average value overlain with maximum and minimum of the decay timescale r^{-1} used to tune GOTM simulations of each EW forcing event (cyan bars). Average overlain with minima and maxima Park decay timescale for each EW event using ML depths and N^2 maxima below the ML from the GOTM simulations (magenta bars).

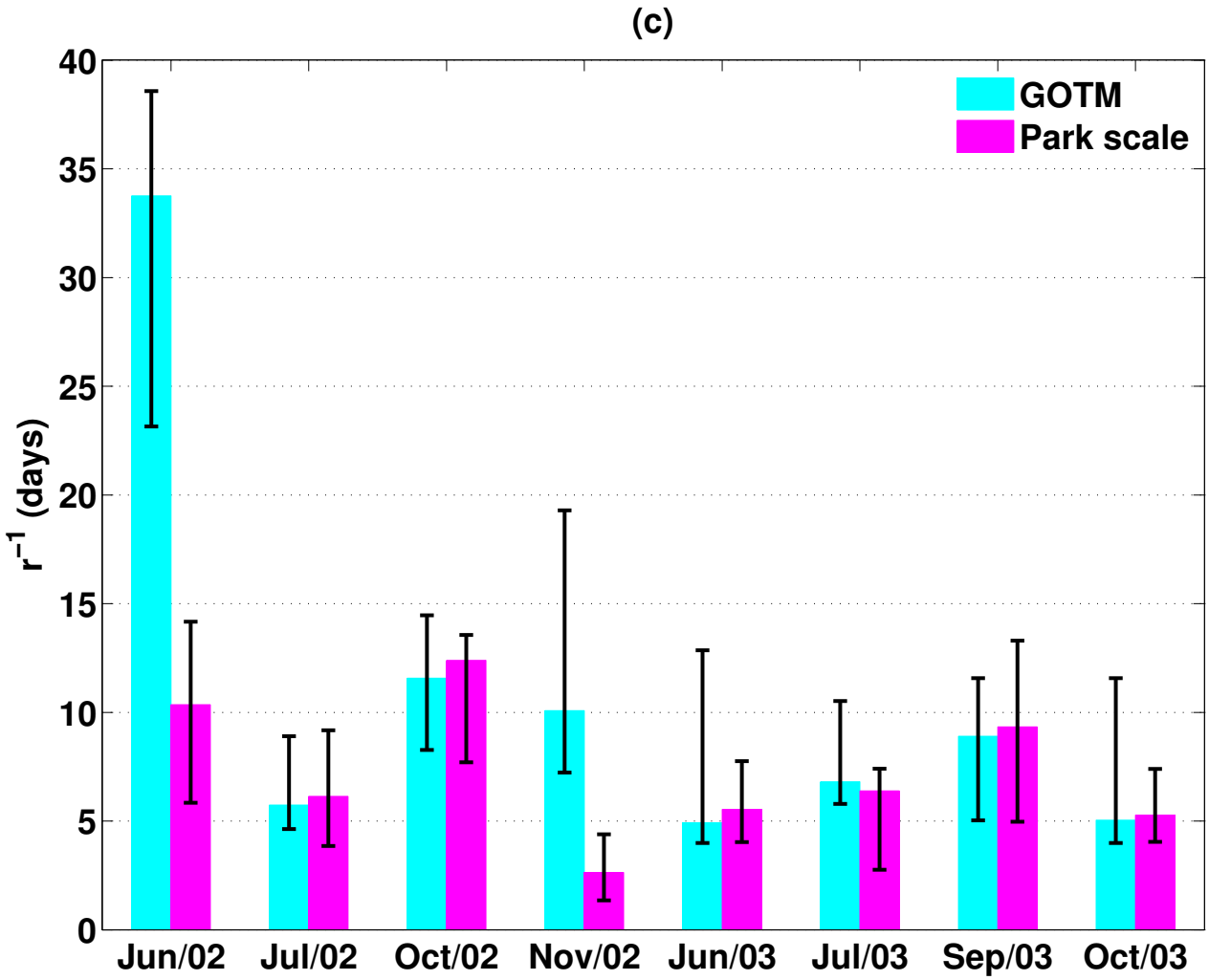

Figure 2.3: Average value overlain with maximum and minimum of the decay timescale r^{-1} used to tune GOTM simulations of each EW forcing event (cyan bars). Average overlain with minima and maxima Park decay timescale for each EW event using ML depths and N^2 maxima below the ML from the GOTM simulations (magenta bars)

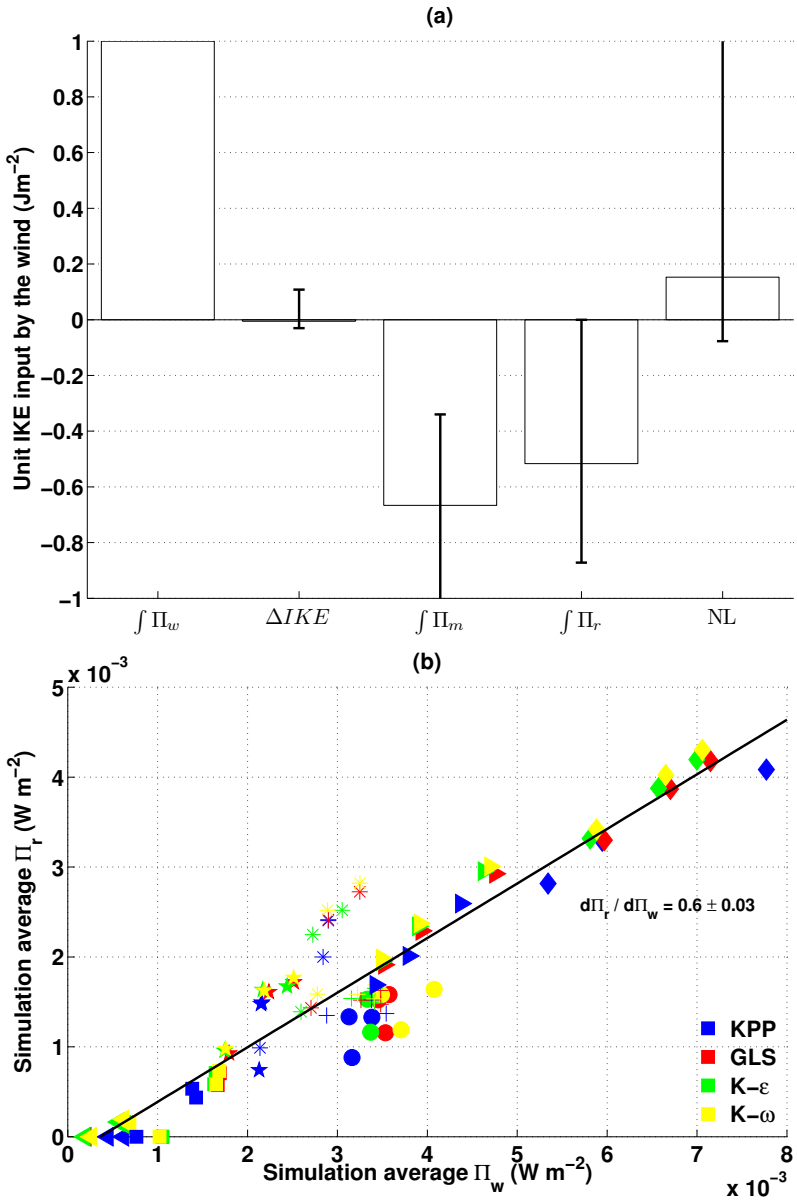

Figure 2.4: (a) Median IKE for each term in equation 3.6.1 normalized by its wind input of IKE, over-bars denote the minima and maxima found across all simulations. (b) Scatter plot of GOTM simulation average NIW vertical energy flux ($\bar{\Pi}_r$) to the simulation averaged wind input of IKE ($\bar{\Pi}_w$). The black line is the linear fit with slope given by $d\Pi_{NIW}/d\Pi_w$. Symbols denote individual simulations as: $\triangleleft$ Jun/02; $\Diamond$ Jul/02; $\square$ Oct/02; $\bigcirc$ Nov/02; $\star$ Jun/03; $+$ Jul/03; $\triangleright$ Sep/03; $*$ Oct/03. Colors denote the parameterization scheme.

CHAPTER 3
NEAR INERTIAL WAVES DURING CINDY 2011: ENERGY FLUXES AND DISSIPATION

3.1 Introduction

Internal swells are groups or packets of near-inertial internal waves (NIW) generated by mixed layer (ML) inertial oscillations that propagate downward into the ocean interior (*Alford* 2001). Inertial oscillations are an integral part of the oceanic response to wind forcing and contain a large fraction of the work done by the wind on the surface ML currents (*Pollard and Millard Jr* 1970; *D'Asaro* 1985). The decay of inertial oscillations is a complex process that involves, for example, the radiation of NIWs and shear driven turbulent mixing at the base of the oceanic ML (*D'Asaro* 1989; *Plueddemann and Farrar* 2006; *Soares and Richards* 2013). Therefore, near-inertial energy is believed to supply a significant fraction of energy supporting the vertical mixing in the ocean, which is an important mechanism for heat and tracer exchange between water masses (*Munk and Wunsch* 1998). Depending on the preferential decay path the wind induced inertial kinetic energy (IKE) takes, its ultimate dissipation will occur either locally via turbulent mixing near the base of the surface ML or remotely in the thermocline or deep ocean The sensitivity of climate to where and when this IKE fueled mixing occurs is only now beginning to be explored (*Jochum et al.* 2013).

Because the NIW are not well resolved by typical ocean general circulation models (OGCM), their contribution needs to be parameterized. Successfully parameterizing NIW induced mixing will thus rely on a comprehensive understanding of the sources, pathways and sinks of IKE.

Although the sources of ML IKE are relatively well mapped, their magnitudes are poorly constrained (*Watanabe and Hibiya* 2002; *Alford* 2003; *Jiang et al.* 2005), and it is still unclear what fraction of the wind work on inertial currents is emitted as internal swells into the ocean interior versus the local dissipation through turbulence at the base of the ML. Some numerical modeling studies with global and regional OGCMs suggest that in midlatitudes at most 20% of the wind input of IKE to ML propagates into the ocean interior below the surface boundary layer (*Furuichi et al.* 2008; *Zhai et al.* 2009). In contrast, *Soares and Richards* (2013) show that in the tropical eastern

Pacific large fractions of IKE input by the wind during intermittent resonant forcing episodes can escape the boundary layer, penetrating the ocean interior. Characterized by their strong upper ocean stratification, tropical regions may be hotspots for NIW activity. Other studies, such as *Alford et al.* (2012) and *Cuypers et al.* (2013) (hereafter, C13) also provide observational support for the hypothesis that a significant fraction of IKE must radiate downward into the thermocline.

Even less understood is when, where and how much of the radiated fraction of the IKE gets dissipated and induces diapycnal mixing. *Hebert and Moum* (1994) and *Alford and Gregg* (2001) (hereafter HM94 and AG01), find significant dissipation rates associated with NIW vertical energy fluxes, yet they did not have wind work measurements required for a quantification in relation to a definite source. Therefore, more observations of near-inertial energy fluxes and dissipation rates are particularly needed for development, implementation and validation of parameterizations. The paucity of such observations hinders all stages of parameterization developments.

Data collected during the DYNAMO/CINDY2011 field campaign (hereafter referred as CINDY) in the tropical Indian Ocean provide a rare opportunity to derive estimates of energy fluxes and wave energy dissipation from direct, *in situ* observations and relate them to the local wind input. The goal of the CINDY project was to study air-sea interactions at intraseasonal timescales, particularly the developing stages of atmospheric convective disturbances such as the Madden Julian Oscillation (MJO) (*Yoneyama et al.* 2013). During the beginning of the first leg of the CINDY observations, a convective disturbance propagated over the R/V *Mirai* (Figure 3.1a,b), triggering inertial oscillations in the ML and subsequent NIW radiation in the thermocline. Additionally, another NIW packet is observed at depth in associated with elevated dissipation rates.

This paper analyzes the mixed layer inertial oscillations and subsequent internal swell evolution as observed during the CINDY leg one field campaign. The primary goal is to estimate the fraction of wind induced inertial energy fluxed downwards by the radiating internal waves. A second goal is to speculate about their long term propagation and final dissipation. Results of the various analyses indicate that about 40% of the wind input of IKE to ML is radiated downwards into the thermocline and that significant loss of NIW energy occurs within the seasonal thermocline.

First we describe the observed and numerical datasets used in this study (Section 2), followed

by a description of the atmospheric forcing episode (Section 3) that triggered the ML inertial oscillations and of the background oceanic conditions relevant to the dynamics of near-inertial motions (Section 4). In Section 5 we analyze the ML inertial response and estimate the flux of IKE from the winds to the oceanic mixed layer. Section 6 describes the methods and results of the NIW packet analysis, as well as of ray tracing and energy budget calculations. Section 7 contains the discussion and concluding remarks.

3.2 Data and Model output

Data used in this study consists of *in situ*, remote and numerical model output datasets of ocean and meteorological variables. The *in situ* observations allow a detailed examination of vertical and temporal aspects, while remote satellite data permits investigation of the horizontal structure of atmospheric and oceanic conditions that occurred during the *in situ* collection. Model data aids in connecting the remote and *in situ* observations.

The *in situ* data consists of several types of measurements made aboard the R/V *Mirai* during the CINDY cruise as part of an international MJO investigation field campaign, see *Yoneyama et al.* (2013) for details. The CINDY cruise was realized in two legs, involving a 24 and 28 days survey of meteorological and oceanographic conditions at a single station at 8°S 80.5°E (Figure 3.1). In this chapter, focus is on the data from leg one (September 28th to October 26th 2011).

Lowered acoustic Doppler current profiler (LADCP) and conductivity temperature depth (CTD) casts down to 500 m were conducted approximately every 3hrs. In between LADCP-CTD casts, one to three Micro-Structure Profiler (MSP) casts down to typically 350m were also performed in order to measure the turbulent kinetic energy dissipation rate (ϵ). The 600 kHz LADCP data was binned into $\approx 2m$ depth bins, while the post-processed CTD data was binned in 1db ($\approx$1m) bins. The R/V *Mirai* was also equiped with a hull mounted 75kHz *Ocean Surveyor* acoustic Doppler current profiler (SADCP), which was post-processed for quality yielding a vertical resolution of 16 m, range down to 700 m and a temporal resolution of 5 minutes. Following Alford and Gregg 2001, we produced 30min bin averages of SADCP data to reduce noise. These observations are presented on Figures 3.2a,c, 3.3a−−d and 3.4. From the CTD potential density (ρ) data we compute a ML

depth as the depth where ρ exceeds its surface value (taken as the upper 5m average ρ) by 0.125 kgm^{-3}. This ML estimate seems to correspond well with both the base of the deepest mixing layers seen in the ϵ data (Figure 3.4a) and with the top of the high stratified layer in the upper thermocline that inhibits surface forcing, implying this definition is appropriate for our study. Winds were measured at 6 seconds interval by the anemometer array on the foremast of the R/V *Mirai* (24m height), then post-processed to 10min averages and converted to a $10m$ height wind estimate. Winds were further averaged to 30min bins to reduce noise and the COARE algorithm version 3.0 (*Fairall et al.* 2003) was used to compute stresses relative to the surface currents (taken as the upper most SADCP current bin).

Oceanographic remote data consists of upper-ocean absolute geostrophic currents from the Archiving, Validation and Interpretation of Satellite Oceanographic data (AVISO) delayed time product available on a 1/4° grid and weekly interval. The altimeter products were produced by Ssalto/Duacs and distributed by Aviso and CNES (http://www.aviso.altimetry.fr/duacs/). We also use the Ocean Surface Oceanographic Current Analysis-Real Time (OSCAR) pentad product available on a 1/3° grid, which contains both wind driven Ekman currents and geostrophic currents (*Bonjean and Lagerloef* 2002). These data are used in Section 3 to construct spatial maps of the background ocean conditions in the area and to assist in evaluating model skill.

Remote meteorological dataset products are satellite derived outgoing longwave radiation (OLR) and 10 m winds from the Cross-Calibrated Multi-Platform Ocean Surface Wind Vector Analyses (CCMP). CCMP is a blended analysis product between several satellite data sources and European Centre of Medium-Range Weather Forecasts (ECMWF) ERA-I reanalysis (*Atlas et al.* 2011). These data are used to describe the atmospheric forcing prior and during the CINDY cruise.

Finally, output from the MERCATOR OCEAN global analysis (graciously provided by Mercator Océan of France, http://www.mercator-ocean.fr) is used to provide three-dimenstional maps of stratification and currents of the study area. MERCATOR is based on OPA (Océan PArallélisé), a z-coordinate primitive equation model that assimilates satellite sea surface temperature (SST) and sea surface height anomalies (SSH) along with available *in situ* temperature and salinity from ship-borne sensors, drifters, moorings and CTD and expendable bathythermograph (XBT)

casts. Atmospheric forcing for this version of MERCATOR-OPA is from daily averaged ECMWF operational forecasts. Output is available as daily averages at a 1/12° horizontal resolution grid and a total of 50 vertical levels, of which 29 are in the upper 300m, yielding vertical resolutions varying from 1m near the surface, to 20-50m below 100m and to 400m near the bottom. Model u, v and N^2 fields are also show in bottom panels of Figures 3.2 and 3.3. The model output is used to evaluate vorticity estimates derived from the NIW packet analysis and as background conditions for the three dimensional ray tracing experiments.

3.3 Atmospheric Forcing

A large convection area, marked by the low values of OLR in Figure 3.1a, is seen west of the CINDY station on September 27th accompanied by a large area of weak winds east of its center and over the CINDY station location (Figure 3.1c). Just prior to the station sampling period and during its earlier stages, this convective activity was driven by both the developing dry phase of an MJO event as well as eastward propagating convective coupled Kelvin waves (*Gottschalck et al.* 2013). After the 27th of September, the convection area west of the R/V *Mirai*'s position appears to break apart and subside slightly as it spread eastward, contributing to the maintenance of the weak wind conditions during the first day and half of the sampling period (Figure 3.5a). Between October 1st and 2nd, a center of deep convection (large negative OLR anomalies) quickly develops just northwest to the CINDY station (Figure 3.1) triggering an onset of SE Trade winds over the area (Figure 3.1d). As this deep convection center moves northeast on the next two days, the Trade winds relax once again. During the following week (October 4-11), convective variability in the area seems to be related to the Trade wind pulses measured by the ship's anemometer (Figure 3.5a).

After October 11th, typical SE Trade winds resume for about 10 days (Figure 3.5a). Around the 20th, convection due to the developing wet phase of the MJO brings about another relaxation of the winds in the area. Detailed discussions about the meteorological conditions during all of the DYNAMO/CINDY2011 campaign can be found in *Yoneyama et al.* (2013); *Gottschalck et al.* (2013); *Shinoda et al.* (2013); *Seiki et al.* (2013).

3.4 Background Upper Ocean Conditions

Here we describe the evolution of background oceanic conditions prior and during leg I of CINDY, particularly circulation and stratification (measured by the Buoyancy frequency squared, N^2) of the upper 500m. Some of this has already been presented and discussed in *Seiki et al.* (2013) and *Shinoda et al.* (2013). We define "background" as the variability with timescales longer than about 4 local inertial periods (IP, of $\approx$ 3.6 days). We rely both on the *in situ* observations and model output. In terms of circulation, we are primarily interested in vorticity (ζ) and mean currents, secondarily on lateral strain rates (normal and shear strain rates, S_N and S_S respectively) and divergence (δ) since the former properties impact the dynamics of near-inertial motions.

In the beginning of the sampling period, we observe a $\approx$ 40m deep ML over a sharp strongly stratified layer at the top of the thermocline (Figure 3.2) known as the transition layer (TL, *Dohan and Davis* (2011)). Throughout the leg one record, the ML and TL exhibit a deepening trend. As the TL deepens, its stratification weakens while the stratification within the thermocline strengthens. These changes coincide with the arrival of a positive SSH anomaly signal (*Seiki et al.* 2013). The variability in stratification is mostly captured by the model (Figure 3.2f), particularly the deepening trend of both the ML and TL, although the TL in the model is substantially broader and weaker than observed.

According to *Seiki et al.* (2013), during most of leg I, the R/V *Mirai* was located on the front side of the northern half of a Rossby wave gyre (see also Figure 3.8), resulting in southwest mean surface currents as observed *in situ* (Figure 3.6b) and by OSCAR and AVISO (and to a lesser extend MERCATOR). The background currents veer W-NW with depth and are directed W-SW in the TL and ML (Figure 3.6a). During leg I there are only small changes between currents in the first half and the latter half of the sampling record, particularly on the SADCP measurements, supporting the use of time mean currents (Figure 3.3). Unlike the observations, MERCATOR has stronger meridional currents than zonal currents, resulting in more southward surface currents and northwestward currents in the thermocline. By comparing the depth-time series of u and v from the ADCP observations with MERCATOR output (Figure 3.3) we see that high frequency current variability is not resolved by the model, but the slow varying pattern is somewhat represented at

most depths.

Time series of ζ, δ, S_N and S_S at the station location are shown in Figure 3.7. Anticyclonic vorticity develops in the near surface over the first week of sampling at the station location (Figure 3.7a), consistent with the Rossby gyre pattern (Figure 3.8a-f) and the deepening of the ML. In contrast, divergence is very weak, consistent with a quasi-geostrophic background flow field, while the dominant vorticity and strain rates are consistent with the existence of a vigorous mesoscale eddying field as depicted in the maps of Figure 3.8. The relative contribution of each term is consistent among all products depicted in Figure 3.7, although MERCATOR output shows increased short timescale variability (expected due to daily averaging only) and perhaps the timings of signal arrivals may be slightly off in the model. However the model can provide information of the flow field beneath the surface layer. Vorticity from depth levels beneath 100m and 200m (the lighter grey lines in Figure 3.7a) suggest a two-layered system during the sampling period, with predominant anticyclonic vorticity near the surface and cyclonic vorticity beneath 100m or so.

Note the vorticity in the layers appears to change sign in the model around Oct 10th (solid lines in Figure 3.7a). It seems reasonable to construct a scenario where neutral or perhaps weak anticyclonic vorticity dominated the surface ML at the CINDY station while relatively stronger AC vorticity dominated the TL and thermocline prior and during the first few days of the sampling period. The translation of the Rossby wave over the station within the first week of sampling steadily deepens the ML and TL (with the latter weakening while increasing the stratification of the thermocline), thus inducing the surface vorticity to rotate anticyclonically, with this pattern dominating from the surface down to about 100-150m, where cyclonic vorticity dominates. Comparing the model with AVISO and OSCAR vorticity maps in Figure 3.8 shows the occurrence of more filaments and smaller eddies associated with the main Rossby wave feature, these shorter scale features produce the localized high frequency vorticity and strain variability seen in Figure 3.7.

3.5 Mixed layer inertial oscillations

The onset of SE Trade winds is visible in the shipboard time series shown in Figure 3.5a. During the first 10 days of October the winds pulsated on and off, generating inertial oscillations in the

ML, as seen in the demodulated current time-series (Figure 3.5b). This wind variability translated to a positive wind work on ML inertial currents for the first two inertial periods (Figure 3.5c), when the ML IKE reaches its peak on Oct 6th. Afterwards, when inertial currents and wind pulses go out of phase, the wind work becomes negative and the ML IKE quickly decreases.

The spectrum of ML currents shows a peak at 0.92 $f_\circ$ (Figure 3.9a), albeit at low statistical confidence. A dispersion relation for ML motions indicate that inertial oscillations in the absence of strong background divergence and strain rates should have a frequency ($\omega_\circ$) equal to f_{eff}, the effective inertial frequency (*Chavanne et al.* 2012). This sub-inertial peak frequency suggests anticyclonic background relative vorticity dominated the first three inertial periods of the sampling, in agreement with both the MERCATOR and AVISO/OSCAR vorticity shown in Figure 3.7a.

Figure 3.9b shows the near-inertial current ellipses, obtained via complex demodulation (see Appendix for details) of SADCP currents at the peak frequency reported above. The ellipses are tilted SW-NE, roughly the same orientation of the wind disturbance front (see Figure 3.1), with a major to minor axis ratio r_2 of 1.38 to 1.47. The u and v polarization relations (the eccentricity of inertial current ellipses) can be used to provide an estimate of the background horizontal shear along the direction of the orientation of the current ellipses (see Appendix for further details), assuming that ML inertial oscillations have $\omega_i = \omega_\circ$, i.e. are not Doppler shifted, a reasonable approximation as long as the ML inertial oscillations have large horizontal scales. The calculation yields a shear of the cross propagation component in the direction of wave propagation, $V^r_{x^r}$, of -0.36$f_\circ$, thus resulting in anticyclonic background vorticity if background is either in solid body rotation, parallel shear flow or if $U^r_{y^r} > V^r_{x^r}$. If indeed $f_{\text{eff}} = \omega_\circ = .92 f_\circ$, $U^r_{y^r} = -0.32 f_\circ$, implying that assumptions of solid body rotation or parallel shear flow are likely invalid.

The amount of IKE in the ML is significantly less than reported by C13 following an Indian Ocean tropical storm, but is on par with typical inertial oscillations reported by *Soares and Richards* (2013) in the eastern tropical Pacific. With inertial currents root mean square (RMS) speeds near 0.2 ms^{-1}, the IKE in the ML during CINDY is clearly well above background levels (Figure 3.5b). This is obvious as maximum wind IKE inputs estimated during CINDY barely reach 20 mWm^{-2}, while peak IKE input observed by *Cuypers et al.* (2013) are 50% higher as a consequence of higher

wind stress magnitudes.

The wind work on the ML inertial oscillations or the flux of IKE from the winds is on average $\approx$4.1 mWm^{-2} up to the time of the IKE peak in the ML (Figure 3.5c). Averaged over the period to when the IKE returns to background levels, about three inertial periods since record start, the flux is much lower at 1.4-1.1 mWm^{-2}, in part due to the wind forcing as pointed out above. These averaged fluxes are similar to the weaker, non resonant, easterly wave forcing events described in *Soares and Richards* (2013). However, relatively energetic NIW packets or groups are observed in the following days propagating downwards in the thermocline, as clearly shown in Figure 3.10 by the slanted phase lines of meridional current upward-phase (downward propagating energy) filtered current anomalies. These are the telltale signs of near-inertial internal waves, which signature is even observed in the raw LADCP/SADCP currents shown in Figure 3.3, following the time of the peak of ML IKE.

3.6 Near inertial Waves

In this section, using the methods detailed below, the characteristics of the NIW packets are examined with the ultimate goal of deriving wave kinetic energy flux estimates. The packets are clearly seen in the band-passed near-inertial kinetic energy (KE) depth time-series plots (Figure 3.11). Three main packets are identified, termed from top down as WPI, WPII and WPIII and centered at 65-70m, 110-120m and 200-220m respectively (Figure 3.11b).

Re-scaling the near-inertial currents with the Wentzel-Kramers-Brillouin (WKB) scale allows removing the wave energy dependency on $N(z)$ (resulting energy "correction" factor is $N_\circ/N(z)$) (*Sanford* 1991; *Alford et al.* 2012). The reference $N_\circ$ used for scaling is the average N beneath the TL, roughly between 80-500m. Because of the rapid variation of N in the TL, depth bins inside the TL are stretched/shrunk assuming the TL N is constant. When plotted in WKB stretched depth (*Sanford* 1991), WPI and WPII appear as part of the wake following the ML forcing event. As for WPIII, its elevated energy density and the timing of its energy peak suggest that another source of near-inertial KE must be present, or that different dynamics are occurring. Because elevated turbulent kinetic energy dissipation rates were measured at the same time and depth of

WPIII (the magenta box in Figure 3.4a) we calculate a diagnostic energy balance to estimate how much near-inertial KE was lost in this event. This diagnostic is also used to estimate the relative contribution of the horizontal and vertical wave energy flux divergence, wave advection by the background currents and dissipation along its possible propagation path, which are compared with a three-dimensional ray tracing exercise.

3.6.1 Wave packet analysis methods

The observed near-inertial signals are assumed to be plane waves with close neighboring frequencies and wavenumbers propagating in a slowly varying background field (i.e. the WKB approximation), superposing to form a packet or group, thus dominated by relatively narrow peaks.

Under the assumption that the background geostrophic flow is in solid body rotation and that it's divergence and strain rates are negligible, this theoretical framework allows combining direct estimates of wave frequency, propagation direction, vertical wavenumber and energetics to derive an estimation of the effective inertial frequency (f_{eff}) felt by the wave packet and, with further information on the background geostrophic currents, of the wave's intrinsic frequency ω_i (*Alford and Gregg* 2001).

The intrinsic frequency of a NIW packet, written as

$$\omega_i = \omega_\circ - |k_H|\,|\mathbf{U}|\cos(\phi - \Theta), \tag{3.6.1}$$

is simply defined as the frequency of a wave following the background motion. The Eulerian frequency, $\omega_\circ$, observed at a fixed location is the intrinsic frequency ω_i plus the Doppler shift by the mean currents. The intrinsic frequency is an important parameter for waves propagating in an inhomogeneous medium (*Kunze* 1985, see) and is necessary to estimate the energy flux of a NIW. In the above equation, ϕ is the direction of wave propagation and Θ is the direction of the background current.

The ratio of the wave's average kinetic energy (KE) to potential energy (PE) is proportional to the ratio of ω_i to f_{eff}, that is $r = \frac{\omega_i}{f_{\text{eff}}}$. Similarly, the major to minor axis ratio of a near-inertial current ellipse is also proportional to ω_i/f_{eff} (see the Appendix 3.A). As in AG01, one can combine

a simplified dispersion relation for internal waves propagating in a geostrophic sheared environment given by

$$\omega_i^2 = f_{\text{eff}}^2 + N^2 \frac{k_H^2}{m_\circ^2}, \tag{3.6.2}$$

where N is the background buoyancy frequency, k_H the horizontal wavenumber and $m_\circ$ the vertical wavenumber, with (3.6.1) and $r = \frac{\omega_i}{f_{\text{eff}}}$ and obtain

$$f_{\text{eff}} = \frac{\omega_o}{r + \frac{m_\circ |\mathbf{U}|}{N} \cos(\phi - \Theta)\sqrt{r^2 - 1}}. \tag{3.6.3}$$

We then use the CINDY I measurements and three methods to provide estimates for the parameters ω_o, ϕ, r and $m_\circ$ to calculate f_{eff} via equation 3.6.3. The first method is based on the Fourier transform (FFT) rotary spectrum and coherency spectrum as in AG01, the second method uses the Wavelet transform (WLT) (as in C13) and the third is described in HM94. Each of these three methods pinpoints a peak or dominant Eulerian frequency $\omega_\circ$ and infers a wave propagation direction ϕ. The peak frequency is then used to complex-demodulate the current and density time series to obtain estimates for r and $m_\circ$. How each of these parameters are estimated is detailed below.

The remaining wave properties, ω_i and k_H, are obtained using (3.6.2). For these calculations we use as background flow the cruise time mean and linear trend in the current and stratification observations. Our main interest is the vertical wave energy flux $F_z \approx c_{gz} KE^i$, where KE^i is the band-passed NIW kinetic energy and $c_{gz} = \frac{\omega_i^2 - f_{\text{eff}}^2}{m\omega_i}$. Since we focus on the downward energy (upward phase) propagation only, the first step prior to any of the analyzes above, is to use a two-dimensional (in time and depth) Fourier transform filter on the u, v and ρ fields filter to isolate the signals with upward phase propagation (u_{up}, v_{up} and ρ_{up} respectively) as shown in the top panels of Figure 3.10 for v. Because the SADCP and LADCP currents are in excellent agreement below the ML, the analysis is carried out using LADCP currents only since these are measured at the same time as CTD data and have higher vertical resolution. WLT and FFT spectra computed for SADCP currents (not shown) are in agreement with those computed for LADCP currents. Using the SADCP currents in various analysis performed in this study give similar results.

Estimation of $\omega_\circ$ and ϕ

The data analysis begins with the determination of the NIW packet's dominant frequency. We seek to estimate an appropriate Eulerian peak frequency $\omega_\circ$ in the near-inertial band for the u_{up} and v_{up} fields. The near-inertial band is defined here as the variability in the 2 to 6 days period, or roughly $0.6f_\circ$ to $1.5f_\circ$, where $f_\circ$ is the local inertial frequency at 8°S.

One of the methods to determine $\omega_\circ$ uses the FFT rotary power spectral density (*Gonella* 1972) of upward phase propagating horizontal current anomalies ($u_{up} + iv_{up}$). A spectrum is computed at every depth level for the entire sampling period (about 24.5 days long), yielding a frequency resolution of approximately $15\% f_\circ$ and a peak uncertainty of $8\% f_\circ$. No windowing is applied to the input time series to avoid distortions in the current amplitudes measured at the beginning of the time series, but padding the ends of the time series with zeros is done to improve peak localization. To reduce uncertainties in the estimation of $\omega_\circ$, the spectra are smoothed in the vertical using 10m bin averages. Accuracy of this method relies on the signal of interest being dominant throughout the observed record. The rotary spectrum of upward phase current anomalies is shown in Figure 3.12a.

Another estimate of $\omega_\circ$ is obtained from the continuous WLT spectrum (*Torrence and Compo* 1998). The WLT is most suited to study intermittent signals in a time series, and can unravel the frequency content at a specific point in time. The standard Morlet mother wavelet is chosen for this study and the WLT is applied at every level (*Cuypers et al.* 2013). As is typically done in geophysical applications of the WLT, signals are deemed significant if they are above a model red noise spectrum and are also located in time away from the influence of edge effects (*Torrence and Compo* 1998; *Grinsted et al.* 2004). Fortunately, our near-inertial signals are outside the cone of influence of edge effects (not shown). Figure 3.13a shows the currents variance in wavelet scales corresponding to the 2-6 day frequency band. The WLT peak frequency within this band is shown in Figures 3.13b and Figure 3.13c for the u_{up} and v_{up} components respectively.

A third estimate of $\omega_\circ$ is derived using the HM94 method, which uses complex demodulation to obtain near-inertial u_{up} and v_{up} at a given frequency. This frequency is varied in increments of $0.02f_\circ$ and $\omega_\circ$ is chosen as the frequency that minimizes the RMS error between demodulated

currents and observed currents, as well as maximizes the variance within the near-inertial band. Note that the demodulation of HM94 does not involve low-pass filtering of the complex amplitudes (see Appendix 3.B). Instead, RMS errors and hence the complex amplitude and phase are calculated only for the time interval of interest. Thus unlike the FFT technique, the HM94 method is able to target only the time period where a given near-inertial signals is more robust, further reducing the influence of other "uninteresting" signals. The time interval used at a given depth are those where significant and elevated near-inertial variance is observed (e.g as estimated with the WLT, Figure 3.13a). The HM94 estimated $\omega_\circ$ vertical profile is shown in Figure 3.15a.

Subsequently we attempt to determine a propagation direction ϕ for the waves with peak frequency $\omega_\circ$. There are two complimentary ways to infer this direction from single point depth-time series data. One is to use the phase relation between u_{up} and ρ_{up} that we refer to as ϕ_1 (AG01). The other, of a qualitative nature, is to use the tilt of the near-inertial current ellipses (HM94) which tends to align with the direction of wave propagation (ϕ_2). While ϕ_2 is only obtained via complex demodulation or from the rotary spectrum, ϕ_1 can be determined in a variety of ways. According to AG01 and C13, the lead/lag phase between upward phase density (ρ_{up}) and zonal velocity anomalies (u_{up}) in the coherence spectrum yields the propagation direction (ϕ_1) in degrees true, when in the southern hemisphere (see Appendix 3.A). Therefore, to estimate ϕ_1 we compute the FFT and WLT coherence spectrum u_{up} and ρ_{up} at every depth level. It is worth pointing out that ϕ_2 gives a more robust estimate of the axis of wave propagation than ϕ_1, as long as the background cross propagation gradients are weak (see Appendix 3.A).

Figure 3.12b,c,d and Figure 3.14 show the directional spectra of the upward phase propagating zonal velocity anomalies, narrowing our analysis to the 2-6 day band variability, using a FFT-based and a WLT-based coherence spectrum respectively. Note that the ϕ_1 estimates from FFT and WLT coherence are usually consistent. Also the phase relations between ρ_{up}, u_{up} and v_{up} are self consistent (not shown), as is expected from the polarization relations (Appendix 3.A).

Estimation of r

Once the dominant frequency $\omega_\circ$ is known, the value of r is backed out from the observations by two approaches: (i) taking the ratio of KE to PE of a NIW (AG01), and (ii) taking the ratio of the major to minor axis of a near-inertial ellipse with peak frequency $\omega_\circ$, after it has been rotated along the propagation axis (e.g by ϕ_2 see HM94), essentially measuring the NIW ellipse eccentricity.

In the former approach, $r_1 = \sqrt{(R+1)/(R-1)}$, where $R = \frac{\overline{KE}}{\overline{PE}}$, and $\overline{KE\,(t,z)}$ and $\overline{PE\,(t,z)}$ are obtained from the amplitude of complex demodulated u_{up}, v_{up} and ρ_{up} at $\omega_\circ$. The overbars denote averaging or smoothing over a wave period (see Appendix 3.A), calculated here using a running Blackman window with width $2\pi/\omega_\circ$. Three estimates of r_1 are presented. In two of these estimates, the typical demodulation technique is used with either the FFT peak frequency $\omega_\circ\,(z)$, which produces $r_1(z)$, or the WLT peak frequency $\omega_\circ\,(t,z)$, which produces $r_1(t,z)$. The third estimate uses the HM94 complex demodulation technique and its associated $\omega_\circ$, hence also producing a $r_1(z)$.

In the ellipse eccentricity approach, $r_2(z)$ can be estimated using either the HM94 complex demodulation technique or from the rotary spectrum (*Gonella* 1972). Note that estimating r_1 and r_2 via HM94 demodulation requires averaging or integrating over a time interval where the direction of wave propagation and frequency is fairly constant. Observed NIW ellipses at select depths are shown in Figure 3.16. Various estimates of r_1 and r_2 are shown in Figure 3.17, and only values where $\omega_\circ$ is significant are retained.

As noted by *Polzin et al.* (2003), energy ratio estimates are compromised by aliasing from other waves and near-inertial vortical motions, as well as by the background horizontal shears themselves (from polarization relations discussed in the Appendix 3.A). These introduce unmeasurable uncertainties in our estimates. Likewise, near-inertial ellipse eccentricities estimates are also compromised, since in order to calculate r_2 it is required to rotate near-inertial currents by ϕ_2, but as discussed and demonstrated in Appendix 3.A, observed estimates of ϕ_2 may also be contaminated by the background shears. Therefore, r_2 estimates are most reliable (more than r_1) for WPI which shows a narrower directional spectrum (Figures 3.14a and 3.16a). The accuracy of $\overline{PE}$ estimates for WPI may also suffer from the proximity to the base of the ML, where near-inertial

ρ_{up} anomalies may be contaminated by mixing due to the ML inertial oscillations.

Estimation of $m_\circ$

The vertical wavenumber for the calculations is obtained using the method of C13. Rotary upward phase propagating currents $u_{up}+iv_{up}$ are first complex demodulated at a dominant frequency $\omega_\circ$ to provide complex amplitude and phase vertical profiles at every time point. In both types of complex demodulation used in this study (traditional and HM94), $\omega_\circ$ is varied at short increments within the band $0.5f_\circ$-$1.5f_\circ$. Linear fits to vertical phase segments are performed to estimate $m_\circ$ and fits are calculated in WKB stretched coordinates. Following C13, these segments are identified from the complex amplitude vertical profiles using spline knots. The knots capture the local maxima and minima in the amplitude profile, with the to-be-fitted segments lying between two knots. At any given time, a minimum in amplitude is usually associated with a break in the vertical phase profile, thus delimiting a wave packet space (*Cuypers et al.* 2013). Examples for this procedure are given in Figure 3.15b-d for the HM94 demodulation technique using the $\omega_\circ$ values expected for WPI, WPII and WPIII respectively.

Only estimates of $m_\circ$ associated with peak frequencies $\omega_\circ$ that have passed a hypothesis test whose null hypothesis is that the fit slope ($m_\circ$) is zero at a 95% confidence level are retained. Three estimates for $m_\circ$ are calculated: When using the traditional demodulation technique, both WLT and FFT $\omega_\circ$ are used, resulting in a $m_\circ(z)$ and a $m_\circ(t,z)$, respectively. When using the HM94 demodulation technique, time and depth intervals where near-inertial signals are not significant are masked out, resulting in amplitude and phase vertical profiles that "follow" WPI, WPII and WPIII energy (e.g. Figure 3.15b-d), hence also yielding a $m_\circ(z)$ profile. The resultant dominant $m_\circ$ are shown in Figure 3.18 for various methods. Note the relatively narrow error bars in $m_\circ$ are simply given by the 95% confidence interval of the fits, however some uncertainty in $m_\circ$ is inherited from the determination of $\omega_\circ$, which is not formally propagated.

For comparison, the vertical wavenumber spectrum in non-stretched coordinates is shown in Figure 3.18c. The HM94 method outlined above is also applied in non WKB stretched coordinates and shown in Figure 3.18a. Both non-streched methods produce similar results, e.g. higher vertical

wavenumbers associated with WPII and WPIII are found in normal depth coordinates than in WKB stretched coordinates, particularly so for WPII. For the WPI period (the blue curve in Figure 3.18c) the spectral energy peak occurs at a wavenumber of ≈ 0.045 rad m^{-2} in good agreement with the non-stretched HM94 estimate between 50-65m (Figure 3.18a). The difference between stretched and non-stretched wavenumbers highlights the vertical refraction that NIW undergo when propagating in a variable $N(z)$. WKB stretching of depth coordinates allows differentiating two wave packets by their vertical wavenumber. Note the non-streched depth $m_\circ$ and WKB $m_\circ$ are self consistent by a factor of $N(z)/N_\circ$. Consequently so are all sub-derived estimates k_H and F_z.

3.6.2 Results

Prior to detailing the results of the NIW packet analysis, it is worthwhile to examine the behavior of thermocline currents observed after the initiation of the wind forcing episode on Oct 2nd. From Figure 3.10 one can see that the current anomalies with upward phase propagation dominate over the anomalies with downward phase propagation. No significant upward energy (downward phase) propagation is observed in association with the wave packets labeled in Figure 3.11b. The near-inertial band explains 60% the of variance of the upward phase currents that occur in response to the wind pulses. Two distinct stages of this response can be delimited, prior to and after Oct 13th. In both stages, a series of phase breaks can be noted in the upper panels of Figure 3.10, indicating the existence of distinct wave groups (*Cuypers et al.* 2013). Groups with low vertical wavenumbers appear to dominate the 1st stage of the response while relatively higher vertical wavenumbers dominated the 2nd stage. The wave packet labeled WPI is associated with this first stage, while WPII and WPIII appear to be related to the second stage. During the 1st stage, we also note near-inertial motions extending down to about 250m, although these are clearly less energetic than the signal in the TL associated with WPI.

Figures 3.12a and 3.15a show that observed Eulerian frequencies increase with depth down to about 150m, from sub-inertial values near the base of the ML to about 12-30% super-inertial. This same behavior is observed in the WLT peak frequencies shown in Figures 3.13b,c. However, the WLT clearly highlights that the sub-inertial frequencies dominate earlier in the record, e.g. after

the ML forcing episode, while the frequency increase with depth occurs at progressively later times. Therefore, WPI is constituted by waves with sub-inertial frequencies occurring between ≈50-90m, while WPII is associated with the increasing super-inertial waves between ≈100-140m. A shift back to sub-inertial and inertial dominant frequencies occurs below 150m in all methods (Figures 3.12a, 3.13b,c and 3.15a). The WLT analysis shows that this shift occurs at approximately the same times as the high frequencies are observed above 150m. Note that, in accordance, packets WPII and WPIII in Figure 3.11b share part of this time interval. Below 150m, peak frequencies again appear to increase with depth, albeit at a slightly faster rate (e.g Figure 3.15a). Furthermore, the time versus depth plots of WLT peak frequency (Figures 3.13b,c) suggest that, at any given depth level between 150-250m, significant changes in dominant frequency also occur over the time scale of the near-inertial oscillations (≈2 inertial periods -IP-), with $\omega_\circ$ decreasing from $\approx 1.07 f_\circ$ to $\approx 0.98 f_\circ$. This is the region referred to as WPIII, despite the apparent lack of homogeneity in wave properties.

According to the directional spectra computed using the FFT and WLT coherence spectrum (Figures 3.12b-d and 3.14 respectively), the low frequency NIW signals above 150m appear to be propagating towards N-NE (20-40° true). Dominant wave propagation direction ϕ_1 veers northward then north-northwestward as the peak frequency of the NIW increases with depth. Between 170 and 250m, the directional spectra suggest dominant propagation towards NW-N, although significant E-SE propagation is also found particularly in the WLT analysis (Figure 3.14c). The E-SE ward waves usually dominate the 170-200m depth range, while the northwestward waves dominate below 200m. The directional spectrum of both the FFT and WLT additionally indicates that the E-SE propagating waves have sub-inertial and inertial frequencies, and that the super-inertial waves propagate NW ward. This is seen more easily in the FFT (Figure 3.12d) because in the WLT these lower frequencies largely did not appear coherent or deemed significant at the 95% level. It is noted here that the overlap of these two signals could likely induce considerable uncertainties in the ϕ_1 and ϕ_2 estimates for WPIII.

Near-inertial ellipses are plotted in Figure 3.16 at select depths for the time intervals where near-inertial variance is significant, which coincide with the labeled packets (i.e. times where variance

is deemed insignificant are masked out). The blue curves trace near-inertial ellipses obtained from demodulated current anomalies with upward phase propagation, while the black and red lines show the near-inertial ellipses predicted by the HM94 and FFT methods, respectively. The ϕ_1 estimates (green dashed lines in Figure 3.16) are in reasonable agreement with the orientation angle of near-inertial ellipses (ϕ_2). The ϕ_2 estimated with both the HM94 (Figure 3.15a, red line) and the FFT (Figure 3.16a) methods agree quite well with ϕ_1 for WPI. Agreement is rather poor for WPII and WPIII, but blue curves in Figure 3.16b,c indicate that for WPII and WPIII, near-inertial currents do not trace a consistent ellipse over time. Instead, it appears that the ellipse tilt changes within the observation period. Since these two methods are based on time averages, significant mismatch is produced between time varying ellipses and mean ellipses, c.f. the large variability of ϕ_2 over small depth differences around WPII and WPIII shown in Figure 3.15a. Nonetheless, the general ellipse orientation associated with WPIII (blue curve in Figure 3.16c) largely support the notion of wave propagation along a NW-SE axis (green dashed line in Figure 3.16c).

The dynamics of NIWs are essentially controlled by r, the ratio of intrinsic frequency to effective inertial frequency, i.e. how much above the lower limit of f_{eff} a wave frequency is. The various methods used here suggest that this ratio decreases with depth and time, along the propagation path of the NIW packets (Figure 3.17). Elongated near-inertial ellipses (Figure 3.16a) and lower ratios of wave $\overline{KE}$ to $\overline{PE}$ (from Figure 3.17b) support the high values of r (above 1.4, c.f. quoted values in Figure 3.16) found in the TL, thus implying very super-inertial intrinsic frequencies (relative to the background f_{eff}) for WPI. Again, it is worth pointing out that estimates derived from energy ratios (r_1) vary substantially over the WPI period (Figure 3.17b), and are possibly impacted by the exchanges of PE between the TL and the ML, whilst the two estimates of r_2 are quite robust (Figure 3.17a). As already discussed, this robustness is afforded by the ellipses being tilted consistently.

In contrast, r estimates based either on eccentricity or energy ratios are in good agreement for WPII (Figure 3.17), despite predicted ellipse tilts not agreeing very well with the propagation direction from the coherence spectrum ϕ_1 (Figure 3.16b). Calculations indicate a substantial reduction in r associated with WPII, implying NIW with super-inertial intrinsic frequencies $\approx$10%

above f_{eff}. This reduction in r can be at least partially explained by the Doppler shift as will be discussed below. Increases in r below about 135 m occur concomitantly with increases in $\omega_\circ$, suggesting that perhaps the Doppler shift effect is no longer relevant, i.e. $\omega_i \to \omega_\circ$, requiring waves to propagate towards SSW or NNE. However the confidence level at these depths is much lower than between 90-120 m.

Waves in WPIII appear to behave more inertially than in WPII (Figure 3.17b). Indeed one of the methods utilized suggests a minimum r value near unity (HM94, Figure 3.17a), thus implying no wave propagation. Beneath ≈150m, however, energy ratio and ellipse eccentricity estimates of r start to diverge. While energy ratios computed using the HM94 technique and WLT suggest a significant reduction in r_1 for WPIII in relation to WPII, ellipse eccentricities obtained either with the FFT or HM94 methods, as well as energy ratios calculated using the FFT peak frequency (instead of the WLT), produce similar r_2 values between WPIII and WPII (Figure 3.17a), i.e. super-inertial like. The near-inertial ellipses drawn by demodulated currents (Figure 3.16c, blue curve) seem to corroborate a wave with super-inertial intrinsic frequency and propagation axis oriented NW-SE. A close inspection of Figure 3.17b indicates that high r_1 occur mostly above 200m, and perhaps slightly after the r_1 minimum, and are associated with the ESE sub-inertial signal (not shown), suggesting that these waves have relatively super-inertial intrinsic frequency.

Estimates for the vertical wavenumber $m_\circ$ are compiled in Figure 3.18. As was noted in the beginning of this section, NIWs observed prior to Oct 13th typically display low wavenumbers, roughly in the range 0.02 - 0.04 rad m^{-1} or 300-150m wavelength, while NIWs observed after Oct 13th display higher wavenumbers, in the range 0.04 - 0.07 rad m^{-1} (e.g. Figure 3.18b). Note these values are in WKB stretched meters. For comparison, Figure 3.18a shows vertical wavenumbers estimated with the HM94 method in WKB stretched meters, as well as in non-stretched depth as one would typically observe (black dashed line). This reveals the refraction pattern of the NIWs induced by $N(z)$: In normal depth, WPII and WPIII have similar vertical scales, however this occurs because of because of elevated stratification (Figure 3.2e) in WPII relative to WPIII. The TL stratification causes the same effect in WPI waves. WKB scaling therefore allows a clearer separation of wave packets, indicating a decrease in vertical scale from WPI to WPIII. These

changes in WKB $m_\circ$ are likely driven by the background flow, see discussion below. Furthermore, Figure 3.18b suggests that $m_\circ$ tends to increase with both depth and time for waves within WPII and WPIII. As an independent check of the method used here, we plot two vertical wavenumber spectra for upward-phase currents in Figure 3.18c, calculated and averaged for the first (blue curve) and second stages (green curve), showing peaks at $0.024 rad m^{-1}$, $0.047 rad m^{-1}$ and $0.08 rad m^{-1}$, in good agreement with the non-streched HM94 method.

We now apply the various wave property estimates in equation (3.6.3) to calculate f_{eff} and later ω_i using the definition for r. As already mentioned, the remaining wave properties are then calculated via equation (3.6.2). We discard wave properties estimated outside the depth and time (for WLT) limits specified for each wave packet, where low signal to noise ratios are observed. Assuming wave properties do not vary significantly within a couple of wave periods and within the depth range of a packet, weighted averages of wave properties are computed for WPI, WPII and WPIII using weights given by the near-inertial variance (c.f. Figure 3.13a). The most likely values of wave properties for each wave packet are reported in Table 3.1 alongside their likely range. Most likely value determination is based on the distribution function of a wave property considering all estimates obtained from the different methods and is usually represented by the median, while the likely range displays the minima and maxima found within the wave packet depth interval. The choice to report these minima and maxima as the likely range for properties stems from the fact that variations in property are often larger along the vertical than between methods, probably reflecting the influence of different signals within a wave group or packet, as well as the changing background influence on them, although notwithstanding that there is at least a 8% uncertainty in $\omega_\circ$ (half the spectral resolution) that should have been propagated through the various estimates. Comparing most likely values for the different methods allows identification of biases or other systematic errors inherent in some of these methods, such that outlier estimates are not considered in Table 3.1, see the Appendix for a brief discussion of some possible sources of error. The implications of the results shown in Table 3.1 will be discussed next.

3.6.3 Observed NIW patterns

Based on the results summarized in Table 3.1, we construct the following picture:

WPI: This wave packet is the most energetic during the first stage of the response. Waves are observed with sub-inertial frequencies of about $0.93f_\circ$ and to propagate toward NNE. Ellipse and energy ratios indicate very super-inertial intrinsic frequencies of $\approx 1.46f_\circ$. This is consistent with NIWs propagating against the background geostrophic currents, which are towards WSW, and within a region of anticyclonic vorticity, as suggested by the low value of f_{eff} in Table 3.1. Waves also appear to have shorter vertical scales ($\approx 80m$) in relation to the weaker near-inertial signals observed further down in the water column caused by refraction in the strong stratification of the TL. After WKB correction, waves display lower vertical wavenumbers - longer vertical scales of about $215m$ - in much closer agreement with the remaining signals below the TL. Notwithstanding large contamination by background shear in the estimates of r_1 and r_2 or deviations of the circulation from a state of solid body rotation, the horizontal wavelength is about $100km$. The super-inertial character of WPI implies downward group speeds above 30 stretched meters per day (much reduced in normal depth), yielding a wave average vertical KE flux of $\approx 0.6Wm^{-2}$, with maximum flux at least as high as $1.7Wm^{-2}$ considering peak energy.

WPII: This wave packet appears in the second stage of the ocean's response, indicating the occurrence of energetic NIW over three inertial periods after the ML IKE peak. Incoming waves mostly propagate toward NNW and higher, super-inertial, frequencies are observed to arrive as the near-inertial energy deepens (e.g. Figure 3.12). Waves are entering a region of slightly weaker background stratification in relation to WPI, and where background currents veer W-NW, such that the waves are now propagating with the background flow. Estimated WKB stretched vertical wavenumbers show a decrease in vertical scale relative to WPII driven by changes in the background flow rather than stratification, while the negative doppler shift reduces the intrinsic frequency, as evidenced by the low r_1 and r_2 values. The r values are consistently around 1.12 until at least $125m$ (Figure 3.17), because

the background current vertical shear is weak. This r value can only be maintained by a positive $f_{\text{eff}}/f_\circ$ gradient. Note that when $\omega_\circ$ and r increase below 130m, waves appear to propagate more westward which increases the doppler shift effect, leading to a reduction in the f_{eff} gradient. These are however low confidence/energy signals. In agreement with NIWs of reduced intrinsic frequency, estimated horizontal wavelengths are longer for waves in WPII at $\approx 140km$, and have slower downward group velocities and weaker energy fluxes.

WPIII: This wave packet is highly energetic despite being located well below the main thermocline, with WKB energy levels well above expected (Figure 3.11c), in part because waves arrive sooner than would be predicted from a typical internal swell pattern following a storm forcing episode (as in *Qi et al.* (1995)), questioning, therefore, whether this wave group is indeed part of the response to the forcing event early in the time series. In spite of the larger uncertainties in the analysis conducted for this packet, a bimodal distribution of wave properties (except vertical wavenumber) suggests the presence of two distinct internal swells with high vertical wavenumber within the 70 m extension where this wave packet is observed. A swell with sub-inertial to inertial $\omega_\circ$ and S-ESE propagation dominates signals above 200 m, albeit at lower significance levels, while below 200 m the dominant swell has inertial to super-inertial frequencies and NW-NNWward propagation. The low frequency waves appear to have high intrinsic frequency relative to the local effective inertial frequency, while the high frequency waves appear to behave inertially with a low ratio of intrinsic frequency to local effective inertial frequency (low r, Figure 3.17). In contrast, the WKB stretched vertical wavenumber $m_\circ$ associated with both these waves is further reduced relative to WPII and WPI, implying that background vorticity and/or flow gradients offset the effects of the weakening stratification. The Doppler shift raises ω_i above $\omega_\circ$ and lowers ω_i below $\omega_\circ$ for the sub-inertial swell and the super-inertial swell, respectively (Table 3.1). Since the background currents remain WNW ward it is unlikely that Doppler shift gradients alone explain all observed refraction. Therefore, the combined evidence suggests that waves are propagating into high $f_{\text{eff}}/f_\circ$ relative to WPII, specifically in what more likely is now an environment with cyclonic vorticity (Table 3.1). Although based on rather circumstantial

evidence, the analysis suggests a scenario where the northward super-inertial NIWs are approaching a turning point, resulting in inertial like intrinsic frequency, long horizontal scales, near zero vertical group speeds and energy flux (*Kunze* 1985), as determined by the analysis. In this scenario, the sub-inertial southward signal could be explained by waves that have been reflected from a turning point located somewhere downstream and therefore have reduced horizontal scales and enhanced group speed and flux. As will be discussed later, this may be the most likely of the possible explanations to the elevated energy levels associated with this wave packet.

Uncertainty in most wave property estimates tend be narrower for WPI because all methods used consistently point to dominant sub-inertial frequency and waves appear to propagate in the same direction throughout the WPI period and depth interval. In WPI, the main source of uncertainty lies in the large differences between r_1 and r_2 estimates. Such large differences between r_1 and r_2 are not observed for WPII. Therefore, due to the possible contamination of near-inertial PE from ML entrainment and de-trainment driven by boundary layer processes, the r_2 are deemed more reliable for WPI. For WPII, uncertainties in wave property estimates are derived from the difficulty in establishing a dominant signal because of the fast changes of peak frequency with depth. In contrast, the larger uncertainties in the various estimates for WPIII stem from difficulty in establishing reliable direction estimates.

The time series collected during DYNAMO-CINDY is about seven inertial periods (IP) long, and NIW packets are present only for a small fraction of time (typically 2-3 IPs), often overlapping as seems to be the case with WPIII. This makes determining a peak frequency very challenging due to frequency resolution issues, as well as determining a dominant propagation direction due to the intermittency of the NIW signal. For instance, the FFT spectrum has better peak localization confidence but does not handle the intermittent signals well, while although the WLT can account for the intermittency, it produces less reliable frequency peaks, and the RMS minimizing demodulation method (HM94) although potentially allowing fine frequency resolution, also tends to produce wide peaks and appears sensitive to high frequency noise. It is noteworthy that in spite of these limitations, sensitivity experiments do show that r and $m_\circ$ estimates display little sensitivity

to the particular choice of peak frequency as long as the $\omega_\circ$ used for demodulation are within two or three $\Delta\omega_\circ$, the typical FFT frequency resolution. This sensitivity is slightly higher for the HM94 demodulation technique than for the traditional demodulation. Finally, significantly coherent frequencies between variables are harder to identify for intermittent broadband processes, making ϕ_1 the most sensitive wave parameter. Therefore, combining these various methods improves confidence in interpreting their results and in the identification of what is perhaps spurious signals picked up by the HM94 and WLT techniques.

The scenario described above suggests that NIWs are propagating downwards into an increasingly cyclonic environment, i.e. where $f_{\text{eff}}/f_\circ$ increases with depth (Table 3.1). An independent check for these f_{eff} estimates can be made by comparisons to AVISO, OSCAR and MERCATOR f_{eff} (*Cuypers et al.* 2013). The blue curves in Figure 3.19 show MERCATOR cruise period averaged f_{eff} depth profiles at the CINDY station and at several locations within a 1° radius. The model relative vorticity switches from anticyclonic to cyclonic between 100 and 250m, in qualitative agreement with the pattern proposed by the wave packet analysis. The magnitudes of model f_{eff} however are significantly lower than estimated from observations, particularly those associated with WPI, as are both AVISO and OSCAR, regardless of the averaging timescale used to compute model and product f_{eff}. This vorticity reversal is also observed in instantaneous model outputs (solid lines in Figure 3.7). The frequency of ML inertial oscillations is often equal to f_{eff} (*Chavanne et al.* 2012), and therefore it is reasonable to expect that the f_{eff} of WPI should be fairly close to the observed ML inertial oscillation frequency of $\approx 0.9 f_\circ$ (Figure 3.9a). The bias towards higher $|f_{\text{eff}}|$ in the analysis performed here may imply that the background circulation may not be in solid body rotation (see the Appendix 3.A). In fact if a background parallel shear flow is assumed instead, the WPI f_{eff} would be reduced to $0.87 f_\circ$, a value in closer agreement with both model output and ML inertial oscillation frequency. This bias may have a significant impact in second order estimates like k_H and c_{gz}, whereby the lower bounds of these estimates are more likely to be true, in particular the vertical kinetic energy flux.

Within the context of the plane wave (WKB) approximation, the CINDY observations constitute the arrivals of internal swells generated further "upstream" (or up-trajectory) and at perhaps

earlier times (*Qi et al.* 1995). If propagating in a time invariant background flow, the Eulerian frequency $\omega_\circ$ is constant, i.e. conserved, making it reasonable to expect that the measured $\omega_\circ$ at CINDY is the $\omega_\circ$ waves were generated at. In this framework, WPI could then be interpreted as composed of fast propagating NIWs generated at a nearby point in the immediate vicinity of the CINDY station, soon after the forcing event, while WPII would be composed of NIWs still forced by the same event somewhere southwards of the R/V *Mirai* location (likely near 9°S), but that have travelled a larger distance, undergoing refraction and advection. This would explain why $\omega_\circ$ increases and ϕ_1 veers NNW. Depending on how homogeneous the forcing and background conditions were, it is possible to interpret these point observations as representative of what occurs along a wave ray path. This notion will be examined and discussed further with the aid of ray tracing and when the energetics of the NIW are analyzed.

WPIII however defies such simple interpretation, not only because of difficulties in pin pointing a dominant frequency and direction (its properties appear to vary rapidly both in time and in the vertical), but because it arrives earlier than expected from a simple ray trajectory starting at the base of the ML in the beginning of the cruise and passing through WPI and WPII. Therefore, it is unlikely that WPIII is part of the same ray tube (see Appendix 3.C for definition) connecting WPI and WPII, and a possible explanation is discussed below. With energy density levels well above expected from just WKB refraction and with $\omega_i \rightarrow f_{\text{eff}}$ (waves approaching the inertial limit), it is possible that WPIII is approaching a critical layer (*Kunze* 1985; *Wurtele et al.* 1996). Another hypothesis to explain the elevated energy density and lack of coherence in the signal is that the observations show a *caustic*, that is when two rays cross each other, implying an interference pattern between two groups of waves next to a region with no waves (*Lighthill* 1978). The former hypothesis is investigated in the next two sections.

The unlabeled energy (Figure 3.11a,b) and anomalies (Figure 3.10a,b) observed before Oct 13th at depths greater than about 90m extending down to 250m, are also likely part of the first stage of the near-inertial response to the Trade wind bursts, as they appear concomitant or shortly after (about an IP from the ML IKE peak) the forming of WPI. These signals are too close to background levels to be significant in the WLT analysis, but close inspection shows waves with

similar propagation direction towards NNE and slightly super-inertial Eulerian frequencies (e.g. $\omega_\circ \approx 1.0 - 1.07 f_\circ$), suggesting that the thermocline can indeed respond to inertial pump in hundreds of meters below the ML. Similarly to WPI, the WKB vertical wavenumber estimated for these disturbances is in the low range, except perhaps the groups below 200m whose $m_\circ$ is slightly higher.

In the plane wave framework, the existence of anticyclonic vorticity and opposing background currents allows for fast downward propagation. To illustrate this point, ray trajectories from simple extrapolation of the c_{gz} estimates made in the previous section are shown in Figure 3.11c (white dashed lines), thus assuming no changes in direction of background currents. The ray trajectory for WPI implies that the weaker NIW packets could also be part of the wake, but belonging to a ray tube originating in the immediate vicinity of the R/V *Mirai* station, that initially descends quickly because within a region of relatively strong anticyclonic vorticity and opposing geostrophic currents, eventually slowing due to NWward shifting background currents and cyclonic veering vorticity. The initially lower levels of energy density could be due to the dispersion of the NIW. Refraction and approach to the critical level could raise the energy further, as observed in WPIII.

The backwards extrapolated ray for the second packet suggests it could have indeed been generated by this same forcing event albeit it should have its origin considerably upstream of the CINDY station, since the ray hits the base of the ML around the start of the time series. To estimate a credible ray path though will require taking into account the variable background flow and stratification, done via ray tracing in the next section.

Nonetheless, the following questions remain open and are kept in mind during the rest of this chapter: (i) Are the estimated changes between WPI and WPII representative of what occurs along a single ray trajectory? Where is the source of WPII and how close it's wavenumber at its origin matches those of WPI? (ii) Is WPIII really inertial? Can we estimate it's source and a plausible ray trajectory? (iii) If not a critical layer, what other hypothesis can explain the elevated energy density of WPIII?

3.6.4 Ray tracing

Three-dimentional (3D) ray tracing is used to estimate possible sources for, and fate of the observed near-inertial signals. More specifically, it is investigated whether WPII can be traced back to a nearby southeast location, within a time matching the wind forcing, as well as whether it is reasonable to assume that wavenumber variations along a ray are represented by the observed differences between WPI and WPII. Finally, it is also evaluated whether rays encounter critical layers or turning points.

The ray equations and algorithm are based on the work of *Kunze* (1985) and detailed in Appendix 3.C. Rays are traced backward and forward in a time invariant background stratification and circulation taken from MERCATOR output averaged between Oct 1-25, roughly the time the NIW were observed in the dataset, to represent the quasi-geostrophic flow. Initial ray conditions for position and wavenumber (k, ℓ and m) for WPI, WPII and WPIII are extracted from Table 3.1. For example, three values for vertical and horizontal wavnumbers, spanning the range of likely values, are used as initial conditions, while several propagation directions are chosen depending on the packet. Four rays are initiated at three different starting depths set in accordance to the depth span of each observed wave packet (e.g. WPII has rays seeded at 110, 120 and 130m). Initially, the four rays form a regular tetrahedron. The four rays are then traced together, and changes in the tetrahedron volume provide an estimate of energy density changes due to ray divergence (see Appendix 3.C). Note that vertical wavenumbers are adjusted from WKB values to unstretched depth coordinates using the model $N(z)$ profiles (Figure 3.19b) for dynamical consistency. Of the approximately hundred ray tubes started at a given location, only a subset of the ray tubes that have an r value consistent with those derived from the observations is shown.

First, a backwards experiment for WPII is reported. Several ray tubes were seeded at the location of the CINDY station (8°S 80.5°E) and back traced for 25 days or until rays reach the base of the ML, taken as 40m deep everywhere. The time and depth evolution of a subset of these rays is shown in Figure 3.19a by solid lines. Most rays reach the base of the ML in 5-10 days (Figure 3.19a) somewhere southeast of CINDY (Figure 3.21). Various wave properties and the background f_{eff} are shown in Figure 3.20. The wave characteristics are in good agreement with what would be

expected from observed WPI properties, i.e. the high ω_i/f_{eff} and higher horizontal wavenumbers than initialized with (this can also be observed in Figure 3.23). However, the hindcasted initial wave direction is westward rather then the observed NNE. This is discussed further below in comparison to forward traced WPI rays. The hindcasted vertical wavenumber (Figure 3.20b) decreases (as is observed in WKB coordinates only) but this is explained by the back propagation into a relatively less stratified upper thermocline in the southeast (see dashed red line in Figure 3.19b). The very low values of m near the ML base occur because of wave propagation into the zone of decreasing stratification (e.g. above the N maximum), as waves approach this N maximum, ray convergence leads to an increase in energy density (reduced volume, third column of Figure 3.23), when waves propagate past the N maximum m decreases and volume increase again.

WPIII rays were also back traced for 25 days. A larger number of rays was seeded at the CINDY station in this experiment, spanning both SE and NNW signals characteristics, and are also shown in Figure 3.19a and Figure 3.22. Rays with southeast propagation and super-inertial intrinsic frequencies though, did not yield numerical stable results and are not shown. Nonetheless, only a few of the rays propagate above 150m, even rays with relatively high ω_i/f_{eff} do not propagate more than 20m upward. From Figure 3.22 it can be seen that all rays propagate backwards towards the east. When WPIII rays are forward traced (dashed lines in Figure 3.19a), wave depth penetration is limited for the initially inertial like groups, while super-inertial groups can display significant depth penetration. This occurs because WPIII was initialized within a cyclonic vorticity layer with mean currents directed towards NW (various f_{eff} profiles in Figure 3.19b and the streamlines shown in Figure 3.22) which effectively traps rays within it, e.g. waves that would be approaching from the top refract away from this layer because of the increase in f_{eff} and negative Doppler shift.

These results are in agreement with an experiment where WPII waves are forward traced starting from the CINDY station. The forward ray trajectories (dashed lines in Figure 3.19a) show that ray depth penetration plateaus. Rays tend to become more inertial like (Figure 3.20a) and the vertical wavenumber increases (Figure 3.20b), thereby greatly reducing the vertical group speed. Reductions in ray tube volume (Figure 3.21a) indicate that ray convergence is occurring, implying an increase in wave energy. These characteristics are usually associated with a critical layer (e.g.

Lighthill (1978), *Wurtele et al.* (1996)). The energetics near this possible critical layer is explored in the next section. It is worth pointing out again that the critical layer is also brought about by the propagation into a WNW jet, suggesting that Doppler shifting, not only the vertical gradient of f_{eff}, plays a key role in setting up this process. This is also discussed further below considering a forward tracing WPI experiment. Although propagation is reduced to a halt, waves are still advected towards the NW and thus may resume propagation downwards if conditions become favorable again.

A question remains whether it is reasonable to assume the observations of WPI and WPII represent conditions along the same ray tube triggered by the Trade winds. WPII rays traced backwards however, did not produce waves with NNE propagation near the ML base as hypothesized. The question is re-evaluated using an experiment where rays with NNE propagation and wavenumbers similar to WPI are forward traced from several initial locations south of the CINDY station. These rays are traced for 25 days and their trajectories are shown in Figure 3.23. Most ray tubes starting in the south and southwest vicinity of CINDY do veer NNW as they propagate downwards. Several of these NNW veering rays also undergo a reduction in ω_i (middle column Figure 3.23) and an increase in vertical wavenumber (not shown), often associated with decreases in ray tube volume (increase in energy density) and ray depth penetration, similar characteristics of the critical layer approach described above. Although this behavior is in qualitative agreement with WPII rays, it is clear that this occurs farther north of the CINDY station than expected, i.e. the rays veer NW and approach critical layers at least half a degree north of the station, missing the station and, at least, implying a different timing of arrival for WPII than observed. This cautions about the ability to interpret the observations of WPI and WPII as belonging to the same ray. Note that several backward WPII rays reach the surface a slightly sooner than the peak of the forcing, suggesting that the high horizontal wavenumbers quoted in Table 3.1 are an overestimate resulting from the solid body rotation assumption. A number of reasons can be put forward to explain this discrepancy, one is the use of this particular time frozen background flow field. Experiments with different timescales of averaging the flow field indicate significant sensitivity of ray trajectory to the mean flow, although the qualitative conclusions are similar. Additionally, the sensitivity to initial

wavnumber conditions is at least as large as those of the mean flow.

In contrast, the rays seeded a degree directly south of the station show fast depth penetration (Figure 3.23), approaching the CINDY station with a NNE heading, where they turn towards the southeast. As they turn the intrinsic frequency reduces, however the vertical wavelength is not strongly reduced, such that critical layer behavior is not characterized. These rays are initially seeded in a region with near surface cyclonic vorticity, thereby the depth penetration in the early stages is driven by the Doppler shift. Therefore, the WPI experiments also support the notion that Doppler shift is an essential component of NIW propagation, since the initial very super-inertial characteristics of the rays leading to fast depth penetration is largely an effect of the opposing currents. The Doppler shift effect is also important in setting up most of the noted critical layers: as the mean flow veers NW from SW, i.e. V_z is negative, m increases much faster than it would by just $\partial f_{\text{eff}}/\partial z$. This path is similar to the one hypothesized to lead to the WPIII, although important details are different (e.g. the rays turn away from CINDY without encountering critical layers), these results support the plausibility of a quick downward path for CINDY NIW energy.

The following two questions remain open and are kept in mind during the rest of this manuscript: (i) A source for WPIII could not be safely determined, but rays traced support the notion that WPIII waves are really approaching an inertial frequency limit, to what degree ray trajectories and refraction patterns are induced by the initial conditions, and thus subject to possible errors in the analysis of the observations? This is an important feature of NIWs approaching a critical layer. (ii) If not a critical layer, what other hypothesis could explain the elevated energy density of WPIII?

This exercise has taken the WKB approximation beyond its limits of formal validity and should be viewed with caution. Nonetheless, the results of 3D ray tracing obtained here are considered qualitatively consistent with the scenario proposed in the previous section, at least supporting the plausibility that the observed NIW packets were generated by the Trade wind bursts at the beginning of the sampling period, though belonging to different ray tubes, thus reaching the fixed point station by different paths. Some of the useful insights provided are: (i) WPI and WPII are indeed very likely triggered by the same forcing event and backward ray tracing of WPII supports the hypothesis that it was generated to the southeast of CINDY within a degree away. However

the results neither support or disprove the interpretation of WPI and WPII as representations of a refracting ray. (*ii*) Results from backward and forward tracing experiments for WPII and WPIII, along with some the WPI predicted rays, show a reduction in ω_i and an increase in m resulting from NIW propagating into the model background flow, suggesting a critical layer is a plausible explanation for the observational behavior of the waves. (*iii*) A prominent role of Doppler shift effects in the NIW dynamics investigated here (some rays do penetrate in cyclonic environments because of it for example), such that the critical layer discussed here is essentially different than the one of *Kunze et al.* (1995) because WPIII NIWs are not trapped within a well defined feature, rather it is essentially produced by the changes in direction of larger scale jets.

A potential source for WPIII could not be determined by backward tracing. Although southeast ward waves in WPIII did not yield stable results, which could otherwise imply that such directions were a mere analysis error, several rays seeded directly south of CINDY turn towards the southeast (though not involving a critical layer). Therefore, no further evidence for the existence of a fast downward route for NIW energy was obtained. Large discrepancies are expected due to the simplifications inherent in this approach, such as the use of time averaged background fields, as well as the use of a numerical model flow field, e.g. it is possible that the model cyclonic layer is shallower than in reality. Despite these shortcomings, it is considered for simplicity that WPIII was generated by the same forcing event, but has likely followed a different ray trajectory than WPI and WPII. It should be stressed again that the goal was a qualitative check on the plausibility of the scenarios discussed above.

3.6.5 Wave Energy budget

The mechanisms responsible for the observed NIW energy patterns are investigated by estimating terms in the kinetic energy balance for NIW in an inhomogeneous background. Focus is on the changes occurring between WPI and WPII and changes occurring within WPIII. The goal though, is not to provide a closed energy budget, but rather, as in HM94 to try and diagnose the relative importance of the terms.

From the conservation of wave action, an equation for the energy density for NIW (E^i) in a

background flow, $\mathbf{U}$, can be written as:

$$\frac{\partial E^i}{\partial t} + \nabla_H \cdot \mathbf{F_H} + \frac{\partial F_z}{\partial z} + \mathbf{U} \cdot \nabla E^i + E^i \nabla \cdot \mathbf{U} = \epsilon + B + \frac{E^i}{\omega_i}\frac{d\omega_i}{dt} + S, \tag{3.6.4}$$

where $\frac{d}{dt} = \frac{\partial}{\partial t} + (\mathbf{c_g} + \mathbf{U}) \cdot \nabla$, ϵ is the turbulent dissipation of wave energy (the measured ϵ times ρ), B represents energy lost to mixing via buoyancy flux and S represents wave-wave and wave-turbulence interactions (*Kunze et al.* 1995). In this study, E^i is approximated by KE^i, B is taken as $\gamma\epsilon$, with $\gamma = 0.2$ being a typical coefficient for mixing efficiency (HM94). Following (*Kunze et al.* 1995, HM94;), S is set to zero. This is approximation is further discussed in relation to WPIII below. Note the term $\frac{E^i}{\omega_i}\frac{d\omega_i}{dt}$, represents wave energy exchanged with the background (*Kunze et al.* 1995; *Chavanne et al.* 2010). From Figure 3.7b, another reasonable approximation is $E^i \nabla \cdot \mathbf{U} = 0$.

Using the measured currents and the outputs of the linear wave analysis (Table 3.1), a simplified and depth integrated version of equation (3.6.4) can be calculated:

$$\frac{\partial}{\partial t}\int KE^i dz = \left(F_z^T - F_z^B\right) - \int (1.0 + \gamma)\epsilon dz + \mathbf{R}, \tag{3.6.5}$$

where F_z^T and F_z^B are the NIW energy flux at the top and bottom limits of the control volume, and $\mathbf{R}$ is a residual flux. The depth integration is performed between WPI and WPII (60-130m), for WPIII (between 175-245m, see magenta box in Figure 3.4) and between WPI and WPIII (65-245m). The terms in (3.6.5) are shown as averages over an integration period, corresponding to 14.25 days between WPI and WPII and 17.5 days between WPI and WPIII.

The LHS and the second term in the RHS of (3.6.5) are calculated directly from the measurements, where KE^i is taken from the 2-6 days bandpassed upward-phase LADCP currents, while ϵ is taken from the MSP measurements reduced by a constant dissipation rate associated with other processes (as in HM94). The value for this constant is calculated based on the mean dissipation over the time series, and reduces the measured dissipation rate by 30%. The first term on the RHS of (3.6.5) is the net flux of KE^i into the control volume and is calculated using the results in Table 3.1, which represent the average wave flux over ≈2IP that are then spread over the integration period. For example, for the WPI-WPII integration limits, F_z^T is taken as ≈ 0.30 mWm^{-2} from

spreading the estimated 0.61 mWm^{-2} in 7 days at 65m over the 14 days integration period, whilst F_z^B is taken as ≈ 0.06 mWm^{-2} from spreading the estimated 0.12 mWm^{-2} in 7 days over 14 days. The net flux into the region of WPIII is not so easy to calculate, due to the apparent lack of vertical propagation making it difficult to define boundaries for the fluxes. In this case, its assumed that for WPIII $F_z^B \to 0$ and $F_z^T = 0.24$ mWm^{-2} is given by WPI flux spread over the 17.5 days period between WPI and WPIII.

The residual flux $\mathbf{R}$ is then assumed to represent the combined effect of horizontal flux divergence, horizontal advection and energy exchange with the background:

$$\mathbf{R} = -\int (\mathbf{U} + \mathbf{c_{gH}}) \nabla_H K E^i dz - E^i \nabla \cdot \mathbf{c_{gH}} + \frac{E^i}{\omega_i} \frac{d\omega_i}{dt}. \tag{3.6.6}$$

Note that in this expression, the horizontal energy flux divergence is separated into the NIW ray convergence term and the NIW advection term. An estimate for the wave-mean flow exchange term can be derived from ω_i values in Table 3.1 as well, if assumed that changes from WPI to WPII and WPIII represent conditions along rays, a reasonable assumption for WPI-WPII based on the ray tracing experiments done in the previous section, less so for WPI-WPIII, however, this is still applied as an exercise to explore this possibility. Note, it is then implicitly assumed that the conditions measured at CINDY are the same along ray trajectories. Estimating the remaining terms, given the point wise observations available, is near impossible as they require information over at least a wavelength distance or quantifications done along a ray (i.e. Lagrangian).

The size of the different terms in equation (3.6.5) is summarized in Table 3.2. It can be seen that the net vertical energy flux is the largest term, while the time change of energy is negligible within the periods considered in the calculation, since observations show that the NIW comes and goes. No significant sensitivity of these results to changes in the integration period was found. Between WPI and WPII, the turbulent dissipation and mixing are expected to account for about 40% loss, implying a substantial positive residual flux that must be balanced out by wave propagation or other sinks. Because the intrinsic frequency in the WPI-WPII ray decreases as it propagates, energy is lost to the mean flow (*Kunze* 1985; *Chavanne et al.* 2010), however the contribution of this term is estimated to be small, of the order of 10% of the dissipation, in agreement with *Kunze*

et al. (1995). Since ray tracing suggests that rays converge onto the CINDY location, thereby implying an increase in energy density, lateral wave propagation and advection by the mean flow must account for most of the observed energy decrease in CINDY. Unfortunately, the role of ray convergence could not be quantified at this stage. This energy diagnostic, however, agrees with the ray tracing results showing continuous wave propagation beyond the sampling station.

Before discussing Table 3.2 results for WPI-WPIII, lets look at what is happening within WPIII. An even simpler version of equation (3.6.5) is calculated within the magenta box shown in Figure 3.4, basically integrating energy density, its rate of change and measured TKE dissipation between 175 and 245m from Oct 15 to Oct 22 (Figure 3.24). During the integration period, KE^i rises and falls (black curve), yielding a small net energy gain of about 1 kJm^{-2} during this period, and part of the energy loss is accounted for the local dissipation (shown in red, integrates to 0.08 kJm^{-2} in the period). The dissipation rate peaks with the energy density, and the measured dissipation removes 15-20% of the peak energy observed. Despite the relatively high dissipation rates, its is clear that a large residual is present throughout the period (e.g. blue curve minus red curve), resulting in a net energy excess $\int \mathbf{R}dt$ of ≈ 0.09 kJm^{-2} that needs to be accounted for by wave propagation or advection. Such a residual would translate to an average net wave energy flux into the box of about 0.15 mWm^{-2}.

To gauge what components of wave propagation are responsible for the energy pattern in Figure 3.24 we turn again to equation (3.6.5). As explained, vertical energy flux divergence for WPIII is more difficult to obtain. To compute the remaining terms it is therefore necessary to assume WPIII as a part of wake response to the forcing episode, belonging to a ray starting with similar properties as WPI. Further assuming the WPIII waves are at the inertial limit, the bottom flux is set to zero, while the top flux remains proportional to the flux estimated for WPI (Table 3.1), only this time spread over a longer period. The results shown on the second column of Table 3.2 indicate that (i) the vertical propagation from WPI accounts for more than enough of the energy consumed by turbulent dissipation and mixing, and (ii) there is still need for substantial (about half) lateral transport of energy via wave and mean flow advection to account for the excess energy fluxed down, yet a substantial fraction of the packet's energy is indeed lost, i.e. $\approx 20\%$ of the

packet peak energy. These conclusions are not altered if F_z^B is set to 0.04 mWm^{-2} (based on the expected value of 0.08 mWm^{-2} from Table 3.1), as the resulting net flux would be approximately 0.2 mWm^{-2} (Table 3.2).

To account for the possibility that wave fluxes are overestimated, due to the assumption of solid body rotation in the background circulation, the calculation is repeated using net flux into control volumes based on lower bounds of F_z from Table 3.1 (values in the parenthesis of Table 3.2). This obviously reduces the size of the residual, but shows that a non negligible amount of energy must be propagated or advected laterely. Also shown in parenthesis are quoted values for the average dissipation and mixing if the full measured dissipation rates were used, showing that there is ample dissipation to balance the NIW vertical flux, which would result in over a quarter of the peak energy in WPIII to have been lost in this event.

The diagnostic employed demonstrates that dissipation is an important term in the action balance throughout a NIW life cycle, from ML base to down into the thermocline, typically accounting for at least 50% of the largest estimated term: the net vertical input from wave flux. The data also indicates a single dissipation event in the thermocline may remove 15-20% of the peak NIW energy, indicating that the NIW packet was not completely dissipated. As hypothesized by *Kunze et al.* (1995), interactions of NIW with the background flow is estimated to be only about 10% of dissipation. In contrast to those authors, horizontal advection by mean flow and/or wave propagation accounts for at least 30 to 50% of the observed reduction in energy. Therefore, lateral processes may be an essential component in the dynamics of these observations, in agreement with the ray tracing results showing ray energy propagating well beyond CINDY station (Figures 3.21 and 3.23). In other words, the CINDY NIW are likely not trapped within a well defined mesoscale feature, in contrast to the observations of *Kunze et al.* (1995). If the observations described here are considered typical, given its similarity to other NIW datasets (e.g. AG01, HM94), these results suggest that a simple balance between the vertical flux divergence and local dissipation is not appropriate for untrapped waves.

The energy diagnostic described above remained consistent with the idea that the observed wave turbulent dissipation was directly induced by wave refraction from the background flow, with

critical layer like behavior the most probable scenario given the estimated wave properties. In this analysis, wave-wave interactions were neglected ($S = 0$), yet as discussed by *Kunze et al.* (1995), they can be an important mechanism to transfer NIW energy to smaller scales where dissipation is more effective. Conditions for wave-wave interactions such as random super-positioning of wave packets were not explored here, and therefore this theme should be re-visited. The details of the behavior of NIW approaching these critical layers are not fully understood. For instance, the work of *Wurtele et al.* (1996) found that inertia-gravity waves approaching such singularities can produce nonlinear reflections of higher harmonics of the incident waves, if the incident inertia-gravity wave has a fairly monochromatic spectrum. The data however, does not show any clear evidence of reflecting waves (high wavenumber, upward energy, downward phase waves).

3.7 Discussion and Concluding remarks

Near-inertial waves observed during leg one of the CINDY cruise in the tropical Indian Ocean were examined using a suite of methods based on linear plane wave dynamics. The data show three distinct wave packets radiating downwards in the thermocline after the excitation of ML inertial oscillations by a series of Trade wind pulses at the beginning of a fixed point station time series. These wind pulses are linked to the developing stages of an MJO event (*Gottschalck et al.* 2013).

It is estimated that the upper most NIW packets radiate 30-40% of the average wind input of IKE to the ML during the forcing event, a fraction substantially higher than the global average near-inertial radiation predicted by numerical models (*Furuichi et al.* 2008). This result is consistent with recent work by *Soares and Richards* (2013) suggesting elevated rates of NIW radiation in tropical regions, as well as other observational studies in midlatitudes showing significant NIW energy below the seasonal thermocline (*Alford* 2010; *Alford et al.* 2012). Also consistent with this picture, the observed thermocline near-inertial kinetic energy density is roughly one third of the ML IKE. This is energy that has escaped the surface boundary layer and is potentially available to mix the interior of the ocean.

The NIW energy in CINDY is observed to to propagate ≈200m into the thermocline. According to various analysis employed here, the observed NIWs propagate in an inhomogeneous background

circulation favoring the occurrence of a critical layer around the deepest observed NIW packet (WPIII), via a dynamical combination of Doppler shift effect and vertical vorticity gradients. Elevated turbulent kinetic energy dissipation rates were measured associated with this wave packet and the possible critical layer. About 20% of the NIW energy is estimated to be lost in this single dissipation event. Furthermore, dissipation of wave energy is found to be an important energy sink throughout the extension of thermocline propagation. Unlike previous observations within mesoscale eddies though (*Kunze et al.* 1995), the NIW energy in the CINDY observations is not trapped, and lateral fluxes are estimated to play a significant role.

Extrapolation of the NIW dissipation pattern derived from these observations would suggest that near-inertial energy is likely removed within the seasonal thermocline, over a depth range of 300-500m, effectively well away from the abyssal ocean. Assuming a mixing efficiency coefficient γ of 0.2, the vertical diffusion coefficient can be estimated as $\kappa_v = \gamma\epsilon/N^2$. The average κ_v associated with WPIII is .5-1$\times 10^{-4} m^2 s^{-1}$, with spikes of 10^{-3}. This value is just shy of the canonical value of 10^{-4} of *Munk and Wunsch* (1998) but well above those reported by *Gregg* (1987) and *Ledwell et al.* (1993), however it could be potentially more if NIW penetrate to the less stratified deep ocean. Given that the observed strong dissipation event occurred over approximately 2 IP, a decay timescale for NIW energy would then be about 40 days. Assuming all observed wave packets were generated at the beginning of the cruise, the life cycle of NIW could be $\approx$2 months. Estimating the extent of the lateral spreading of NIW energy is matter for future investigation. However, one may speculate, based on the results discussed here, that if NIW energy contributes quite efficiently (e.g. 20%) to diapycnal mixing, 5-10% (30-40% $\times$ 20%) of the wind work on ML inertial oscillations is used to mix the ocean interior for a couple of months.

Appendix

3.A NIW polarization relations

We briefly describe the linear polarization relations for NIWs used in this paper and discuss their assumptions and impacts on the accuracy of the method employed.

Starting from the linearized equations of motion shown in *Kunze* (1985), one can obtain polarization relations for u' and v' in terms of ρ' for NIW perturbations in a quasi-geostrophic mean background flow, which when rotated in the direction of wave propagation have complex amplitudes of the form:

$$\hat{u_r} = i\frac{g\omega_i}{N^2}\frac{m}{k_H}\frac{\hat{\rho}}{\rho_\circ}, \tag{3.A.1}$$

$$\hat{v_r} = \frac{g\omega_i}{N^2}\frac{m}{k_H}\frac{\hat{\rho}}{\rho_\circ}\frac{(f+V^r_{x^r})}{(\omega_i + iV^r_{y^r})}. \tag{3.A.2}$$

In (3.A.1), (3.A.2) ω_i is the intrinsic frequency, $V^r_{x^r}$ and $V^r_{y^r}$ are the gradients of the cross-propagation component of the background flow in the along propagation axis (x^r) and the cross propagation axis (y^r), respectively. To obtain equations (3.A.1) and (3.A.2), it was necessary to make the assumption that V^r_z and U^r_z are negligible, i.e no baroclinicity in the background flow. This approximation is justifiable for this study because of the weak vertical shears in the cruise mean flow, according to the criteria of *Whitt and Thomas* (2013).

The ratio of the wavelength average kinetic energy $\overline{KE}$ to the wave average potential energy $\overline{PE}$ yields:

$$\frac{\overline{KE}}{\overline{PE}} = \frac{\omega_i^2}{N^2}\frac{m^2}{k_H^2}\left[1 + \frac{(f+V^r_{x^r})^2}{\omega_i^2 + (V^r_{y^r})^2}\right]. \tag{3.A.3}$$

Equation (3.A.3) demonstrates that the gradients of the background flow cross wave propagation component are the most relevant to NIW dynamics. It also demonstrates that the energies ratio $R = \frac{\overline{KE}}{\overline{PE}}$ is not exactly proportional to ω_i/f_{eff} (as in AG01), and in fact this ratio is "contaminated" by the presence of background shears, particularly those relating to the background divergence and strain rates (namely $V^r_{y^r}$). In order to obtain the useful statement $r = \omega_i/f_{\text{eff}} = \sqrt{\frac{R+1}{R-1}}$ of AG01, two additional simplifications to equation (3.A.3) are required: (i) the background divergence and strain must be small, so that $V^r_{y^r}$ may be neglected, and (ii) the background flow must be either in solid body rotation such that $U^r_{y^r} = -V^r_{x^r}$, reducing $f^2_{\text{eff}} = (f + V^r_{x^r})^2$, or in simple parallel shear flow such that $f^2_{\text{eff}} = f(f + V^r_{x^r})$ admitting a certain amount of error. These assumptions are harder to justify. Divergence indeed appears to be small (Figure 3.7b), however several strain components are of similar magnitude as vorticity (Figure 3.7c,d). Solid body rotation or parallel shear flow are unlikely to dominate in a geostrophic turbulent scenario suggested by OSCAR/AVISO or the

model output (Figure 3.8). It is reasonable to expect that these processes increase the uncertainty in our estimates of indirect wave properties by an unknown factor. However, one hopes that a combination of different methods of estimation for these parameters lends confidence in, at least, our qualitatively picture.

The phase relations between u' and ρ' are also impacted by the presence of background shears. After rotating back to earth coordinates the u' and v', polarization relations for the above can be expressed as:

$$u' = \frac{g\omega_i}{N^2}\frac{m}{k_H}\frac{\hat{\rho}}{\rho_\circ}\left[i\cos\phi^E - \frac{f+V^r_{x^r}}{\omega_i + iV^r_{y^r}}\sin\phi^E\right]\exp(i\varphi), \tag{3.A.4}$$

$$\rho' = \hat{\rho}\exp(i\varphi). \tag{3.A.5}$$

Where $\varphi = kx+\ell y+mz-\omega_i t$ is the wave phase and ϕ^E is the horizontal direction of propagation in counter-clockwise degrees from East. In order for the lead/lag to accurately represent the wave propagation direction ϕ in degrees true, besides the approximations mentioned above, it is also required that $\omega_i \to f_{\text{eff}}$. This way, equation (3.A.4) when in the south hemisphere reduces to:

$$u' = \frac{g\omega_i}{N^2}\frac{m}{k_H}\frac{\hat{\rho}}{\rho_\circ}\exp(i\varphi+\phi), \tag{3.A.6}$$

where now a phase lead or lag in u' over ρ' is equal to the wave propagation direction in degrees true.

Finally, the u' to v' polarization relation can be written as:

$$\frac{\hat{u}}{\hat{v}} = \frac{-i\omega_i + V_y + \tan\phi^E_2\,(f-U_y)}{\tan\phi^E_2\,(-i\omega_i + U_x) - (f+V_x)}. \tag{3.A.7}$$

Note again that U_z and V_z have been dropped. Equation (3.A.7) shows that NIW currents draw an ellipse with tilt generally aligned with the propagation direction axis (ϕ^E_2) but with modifications by the background current shears. The ratio of major to minor axis, or its eccentricity, after rotating the complex amplitudes by ϕ^E_2 is:

$$\frac{\hat{u_r}}{\hat{v_r}} = \frac{-i\omega_i + V^r_{y^r}}{-(f+V^r_{x^r})}. \tag{3.A.8}$$

In (3.A.8) $\hat{u_r}$ is the along propagation axis NIW complex amplitude and $\hat{v_r}$ is the cross propagation axis NIW complex amplitude. From the above equation it is clear that the imaginary component of the ratio $r_2 = \hat{u_r}/\hat{v_r}$ is proportional to $\omega_i/(f+V_{x^r}^r)$ and the real part proportional to $V_{y^r}^r/(f+V_{x^r}^r)$. An easier ratio to measure (e.g. from the FFT rotary spectrum) would be:

$$|r_2|^2 = \frac{V_{y^r}^{r^2}}{(f+V_{x^r}^r)^2} + \frac{\omega_i^2}{(f+V_{x^r}^r)^2} \tag{3.A.9}$$

Again, it is obvious the necessary approximations $V_{y^r}^r = 0$ and of solid body rotation for $r_2 = \omega_i/f_{\text{eff}}$. Nonetheless, in order to estimate r_2, one needs to rotate the wave currents by ϕ_2, which is difficult to back out from the observed ellipse since its tilt is affected by the background shears. Effectively any estimate of r_2 is contaminated with the uncertainty in ϕ_2 determination. It will be shown in the next section that the HM94 method of demodulation allows separation of the imaginary and real parts of r_2, but has reduced accuracy when the ellipse tilt changes rapidly with time.

3.B Complex demodulations

In this study, two types of complex demodulation are used on LADCP currents and CTD potential density data to obtain the slow varying amplitude ($A(t)$) and phase ($\varphi(t)$) of a fixed frequency of interest ω. To demodulate a signal, a variable y is assumed to be composed of the signal of interest plus an additional component (y_n) representing other frequencies, e.g

$$y(t) = \frac{1}{2}A(t)\left[\exp\left(i\omega t + \varphi(t)\right) + \exp\left(-i\omega t + \varphi(t)\right)\right] + y_n(t), \tag{3.B.1}$$

and is then multiplied by $\exp(-i\omega t)$ to yield

$$Y(t) = \frac{1}{2}A(t)\left[\exp\left(i\varphi(t)\right) + \exp\left(-i\left(2\omega t + \varphi(t)\right)\right)\right] + y_n(t)\exp(-i\omega t). \tag{3.B.2}$$

The first method of demodulation and most common practice uses a low-pass filter to obtain

$A(t))$ and $\varphi(t)$ of the signal of interest. Low passing $Y(t)$ reduces (3.B.2) to

$$Y(t) = \frac{1}{2} A(t) \exp(i\varphi(t)), \tag{3.B.3}$$

where now $A(t) = 2|Y(t)|$ and $\varphi(t) = \arctan[\Im\{Y(t)\}/\Re\{Y(t)\}]$. Here we use a triangular window with width $4\pi/\omega - 1$, which with $\omega \approx f_\circ$ gives a retained bandwidth at half-power of roughly 5 to 13 days.

The second method of demodulation is described in HM94. The amplitude and phase are calculated by averaging over a certain time interval $\Delta T = T_2 - T_1$ of the measured record, which is set for every depth level by the significant near-inertial variance detected by the WLT (Figure 3.13a).

$$\frac{1}{\Delta T} \int_{T_1}^{T_2} A(t) \exp(i\varphi(t)) = \langle A \rangle = \frac{1}{\Delta T} \int_{T_1}^{T_2} y \exp(-i\omega t) \tag{3.B.4}$$

The method implicitly assumes y_n averages to zeros in these intervals. The amplitude, phase and ellipse tilt angle information are contained in $\langle A \rangle$. The advantage of this technique is the ability to directly estimate the complex amplitudes $\hat{u}$ and $\hat{v}$, however variability of NIW ellipse within the averaging period may cause distortions.

3.C 3D Ray tracing technique

According to *Lighthill* (1978) the basic ray tracing equations for wave position ($\mathbf{r}$) and wavevector ($\mathbf{k}$), under the WKB approximation and in time invariant background are given by:

$$\frac{d\mathbf{r}}{dt} = (c_g) + \mathbf{U}, \tag{3.C.1}$$

$$\frac{d\mathbf{k}}{dt} = -\nabla\omega_i - \mathbf{k} \cdot \nabla\mathbf{U}. \tag{3.C.2}$$

In this study, $c_g = \partial\omega_i/\partial\mathbf{k}$ and ω_i is given by the real component of the gravity wave solutions of the cubic dispersion relation shown in equation (A1) in the Appendix of *Kunze* (1985). Note that because the background flow is taken as time invariant, the Eulerian frequency ($\omega_\circ$) is conserved

and constant along a ray, i.e $d\omega_\circ/dt = 0$.

Numerical integration of equations (3.C.1) and (3.C.2) was done using a fourth-order Runge-Kutta finite difference scheme. The background conditions are obtained from time averaged fields from an OGCM output and interpolated at the ray position at every time step. Calculations for a given ray are terminated if $\omega_\circ$ departs from its initial value by more than 10%, indicating a significant violation of the WKB approximation. Following *Chavanne et al.* (2010), the method of *Edwards and Staquet* (2005) is used here to estimate wave action changes due to convergence or divergence of rays. The wave action along a ray is calculated by tracking the volume of an initially regular tetrahedron with 10m long sides formed by four rays located at its vertices (*Chavanne et al.* 2010). The integration time step is chosen as to yield stable results, given the magnitude and sharpness of the background gradients. Solutions were not overly sensitive to variations in the side length of the tetrahedron, yielding qualitatively similar results in terms of general final placement of ray tubes.

3 References

Alford, M. (2003), Improved global maps and 54-year history of wind-work on ocean inertial motions, *Geophys. Res. Lett.*, *30*(8), doi:10.1029/2002GLO16614.

Alford, M. H. (2001), Internal swell generation: The spatial distribution of energy flux from the wind to mixed layer near-inertial motions, *J. Phys. Oceanogr.*, *31*, 2359–2368.

Alford, M. H. (2010), Sustained, full-water-column observations of internal waves and mixing near mendocino escarpment, *J. Phys. Oceanogr.*, *40*(12), 2643–2660.

Alford, M. H., and M. C. Gregg (2001), Near-inertial mixing: Modulation of shear, strain and microstructure at low latitude, *J. Geophys. Res.*, *106*(C8), 16,947–16,968.

Alford, M. H., M. F. Cronin, and J. M. Klymak (2012), Annual cycle and depth penetration of wind-generated near-inertial internal waves at ocean station papa in the northeast Pacific, *J. Phys. Oceanogr.*, *42*(6), 889–909.

Atlas, R., R. N. Hoffman, J. Ardizzone, S. M. Leidner, J. C. Jusem, D. K. Smith, and D. Gombos (2011), A cross-calibrated, multiplatform ocean surface wind velocity product for meteorological and oceanographic applications, *Bulletin of the American Meteorological Society*, *92*(2), 157–174.

Bonjean, F., and G. S. Lagerloef (2002), Diagnostic model and analysis of the surface currents in the tropical Pacific ocean, *J. Phys. Oceanogr.*, *32*(10), 2938–2954.

Chavanne, C., P. Flament, G. Carter, M. Merrifield, D. Luther, E. Zaron, and K. Gurgel (2010), The surface expression of semidiurnal internal tides near a strong source at Hawaii. Part I: Observations and numerical predictions*, *J. Phys. Oceanogr.*, *40*(6), 1155–1179.

Chavanne, C. P., E. Firing, and F. Ascani (2012), Inertial oscillations in geostrophic flow: is the inertial frequency shifted by $\zeta/2$ or by ζ?, *J. Phys. Oceanogr.*, *42*(5), 884–888.

Cuypers, Y., X. Le Vaillant, P. Bouruet-Aubertot, J. Vialard, and M. J. Mcphaden (2013), Tropical storm-induced near-inertial internal waves during the Cirene experiment: Energy fluxes and impact on vertical mixing, *J. Geophys. Res.*, *118*(1), 358–380.

D'Asaro, E. (1985), The energy flux from the wind to near-inertial motions in the surface mixed layer, *J. Phys. Oceanogr.*, *15*(8), 1043–1059.

D'Asaro, E. (1989), The decay of wind-forced mixed layer inertial oscillations due to the β effect, *Journal of Geophysical Research*, *94*(C2), 2045–2056.

Dohan, K., and R. E. Davis (2011), Mixing in the transition layer during two storm events, *J. Phys. Oceanogr.*, *41*(1), 42–66.

Edwards, N., and C. Staquet (2005), Focusing of an inertia–gravity wave packet by a baroclinic shear flow, *Dynamics of atmospheres and oceans*, *40*(1), 91–113.

Fairall, C., E. Bradley, J. Hare, A. Grachev, and J. Edson (2003), Bulk parameterization of air-sea fluxes: Updates and verification for the coare algorithm, *J. Climate*, *16*(4), 571–591.

Furuichi, N., T. Hibiya, and Y. Niwa (2008), Model-predicted distribution of wind-induced internal wave energy in the worlds oceans, *J. Geophys. Res*, *113*, C09,034.

Gonella, J. (1972), A rotary-component method for analysing meteorological and oceanographic vector time series, in *Deep Sea Research and Oceanographic Abstracts*, vol. 19, pp. 833–846, Elsevier.

Gottschalck, J., P. E. Roundy, C. J. Schreck III, A. Vintzileos, and C. Zhang (2013), Large-scale atmospheric and oceanic conditions during the 2011–12 DYNAMO field campaign, *Monthly Weather Review*, *141*(12), 4173–4196.

Gregg, M. (1987), Diapycnal mixing in the thermocline: A review, *J. Geophys. Res.*, *92*(C5), 5249–5286.

Grinsted, A., J. C. Moore, and S. Jevrejeva (2004), Application of the cross wavelet transform and wavelet coherence to geophysical time series, *Nonlinear processes in geophysics*, *11*(5/6), 561–566.

Hebert, D., and J. Moum (1994), Decay of a near-inertial wave, *J. Phys. Oceanogr.*, *24*(11), 2334–2351.

Jiang, J., Y. Lu, and W. Perrie (2005), Estimating the energy flux from the wind to ocean inertial motions: The sensitivity to surface wind fields, *Geophys. Res. Lett.*, *32*(15).

Jochum, M., B. P. Briegleb, G. Danabasoglu, W. G. Large, N. J. Norton, S. R. Jayne, M. H. Alford, and F. O. Bryan (2013), The impact of oceanic near-inertial waves on climate, *J. Climate*, *26*(9), 2833–2844.

Kunze, E. (1985), Near-inertial wave propagation in geostrophic shear, *J. Phys. Oceanogr.*, *15*(5), 544–565.

Kunze, E., R. W. Schmitt, and J. M. Toole (1995), The energy balance in a warm-core ring's near-inertial critical layer, *J. Phys. Oceanogr.*, *25*(5), 942–957.

Ledwell, J. R., A. J. Watson, and C. S. Law (1993), Evidence for slow mixing across the pycnocline from an open-ocean tracer-release experiment, *Nature*, *364*(6439), 701–703.

Lighthill, J. (1978), Waves in fluids.

Munk, W., and C. Wunsch (1998), Abyssal recipes II: energetics of tidal and wind mixing, *Deep-Sea Research Part I*, *45*(12), 1977–2010.

Plueddemann, A., and J. Farrar (2006), Observations and models of the energy flux from the wind to mixed-layer inertial currents, *Deep Sea Research Part II: Topical Studies in Oceanography*, *53*(1-2), 5–30.

Pollard, R., and R. Millard Jr (1970), Comparison between observed and simulated wind-generated inertial oscillations, in *Deep Sea Research and Oceanographic Abstracts*, vol. 17, pp. 813–816, Elsevier.

Polzin, K., E. Kunze, J. Toole, and R. Schmitt (2003), The partition of finescale energy into internal waves and subinertial motions, *J. Phys. Oceanogr.*, *33*(1), 234–248.

Qi, H., R. A. De Szoeke, C. A. Paulson, and C. C. Eriksen (1995), The structure of near-inertial waves during ocean storms, *J. Phys. Oceanogr.*, *25*(11), 2853–2871.

Sanford, T. B. (1991), Spatial structure of thermocline, abyssal internal waves, in *Dynamics of Oceanic Internal Gravity Waves, Proceedings of the 6thAha Hulikoa Hawaiian Winter Workshop*.

Seiki, A., M. Katsumata, T. Horii, T. Hasegawa, K. J. Richards, K. Yoneyama, and R. Shirooka (2013), Abrupt cooling associated with the oceanic rossby wave and lateral advection during cindy2011, *J. Geophys. Res.*, *118*(10), 5523–5535.

Shinoda, T., T. G. Jensen, M. Flatau, S. Chen, W. Han, and C. Wang (2013), Large-scale oceanic variability associated with the Madden-Julian oscillation during the CINDY/DYNAMO field campaign from satellite observations, *Remote Sensing*, *5*(5), 2072–2092.

Soares, S., and K. Richards (2013), Radiation of inertial kinetic energy as near-inertial waves forced by tropical Pacific easterly waves, *Geophys. Res. Lett.*, *40*(9), 1760–1765.

Torrence, C., and G. P. Compo (1998), A practical guide to wavelet analysis, *Bulletin of the American Meteorological society*, *79*(1), 61–78.

Watanabe, M., and T. Hibiya (2002), Global estimates of the wind-induced energy flux to inertial motions in the surface mixed layer, *Geophys. Res. Lett.*, *29*(8), 80–1.

Whitt, D. B., and L. N. Thomas (2013), Near-inertial waves in strongly baroclinic currents, *J. Phys. Oceanogr.*, *43*(4), 706–725.

Wurtele, M., A. Datta, and R. Sharman (1996), The propagation of gravity-inertia waves and lee waves under a critical level, *Journal of the atmospheric sciences*, *53*(11), 1505–1523.

Yoneyama, K., C. Zhang, and C. N. Long (2013), Tracking pulses of the madden-julian oscillation, *Bulletin of the American Meteorological Society*, *94*(12), 1871–1891.

Zhai, X., R. Greatbatch, C. Eden, and T. Hibiya (2009), On the loss of wind-induced near-inertial energy to turbulent mixing in the upper ocean, *J. Phys. Oceanogr.*, *39*(11), 3040–3045.

Table 3.1: Summary table of wave properties. Most likely value, followed by range.

NIW property	WPI (50-90m)	WPII (100-140m)	WPIII (175-245m)
$\omega_\circ$ ($f_\circ$)	0.93, 0.90-0.96	1.13, 1.0-1.24	0.98, 0.92-1.04 & 1.05, 0.98-1.16
ϕ_1 (° True)	25, 0-36	336, 305-36	127, 0-150 & 338, 0-300
ϕ_2 (° True)	37, 10-45	46, 4-129	16†, 0-120
r_1	1.62, 1.18-2.51	1.13, 1.07-1.33	1.08, 1.06-1.15 & 1.03, 1.0-1.14
r_2	1.47, 1.25-1.63	1.16, 1.05-1.39	1.18, 1.08-1.29 & 1.15, 1.07-1.29
λ_z^* (m)	216, 150-260	143, 120-180	102, 75-118
f_{eff} ($f_\circ$)	0.75, 0.66-0.88	0.85, 0.74-1.02	1.14, 1.06-1.39 & 0.90, 71-1.03
ω_i ($f_\circ$)	1.06, 1.0-1.3	0.94, 0.86-1.16	1.24, 1.04-1.54 & 0.96, .78-1.06
λ_H (km)	107, 69-142	138, 62-190	100, 58-140 & 480, 120-1900
c_{gz}^* ($mday^{-1}$)	33, 25-42	7, 4-13	5, 3-12 & 2.5, 0-6
c_{gH}^* (ms^{-1})	0.19, 0.13-0.28	0.07, 0.05-0.12	0.05, 0.035-0.12 & 0.04, 0-0.07
F_z (mWm^{-2})	0.61, 0.29-0.83	0.12, 0.06-0.28	.08, 0.04-0.27 & .08, 0-.20

Asterisks denote WKB stretched meters.
† Ellipse orientation do not display bimodal distribution.

Table 3.2: Energy budget terms. Units are mWm^{-2}.

	WPI - WPII 65m - 130m	WPI - WPIII 65m - 245m
$\overline{\frac{\partial}{\partial t}\int KEdz}^{*}$	-0.003	-0.007
$\overline{\int \epsilon + Bdz}$	-.10 (-0.13)	-0.12 (-0.17)
$\overline{F_z^B - F_z^T}$	0.24 (0.16)	0.20-0.24 (0.16)
R	0.14 (0.06)	0.08-0.12 (0.05)
$\overline{\frac{KE}{\omega_i}\frac{d\omega_i}{dt}}$	-0.012	-0.013

$^{*}\overline{x} = 1/T\int dt$, where T is the period between WPI and WPII or WPI and WPIII.
$\overline{\int \epsilon + Bdz}$ in parenthesis are calculated without subtraction of the constant dissipation rate, see text for details.
$\overline{F_z^B - F_z^T}$ in parenthesis are calculated from the lower bounds shown in Table 3.1.

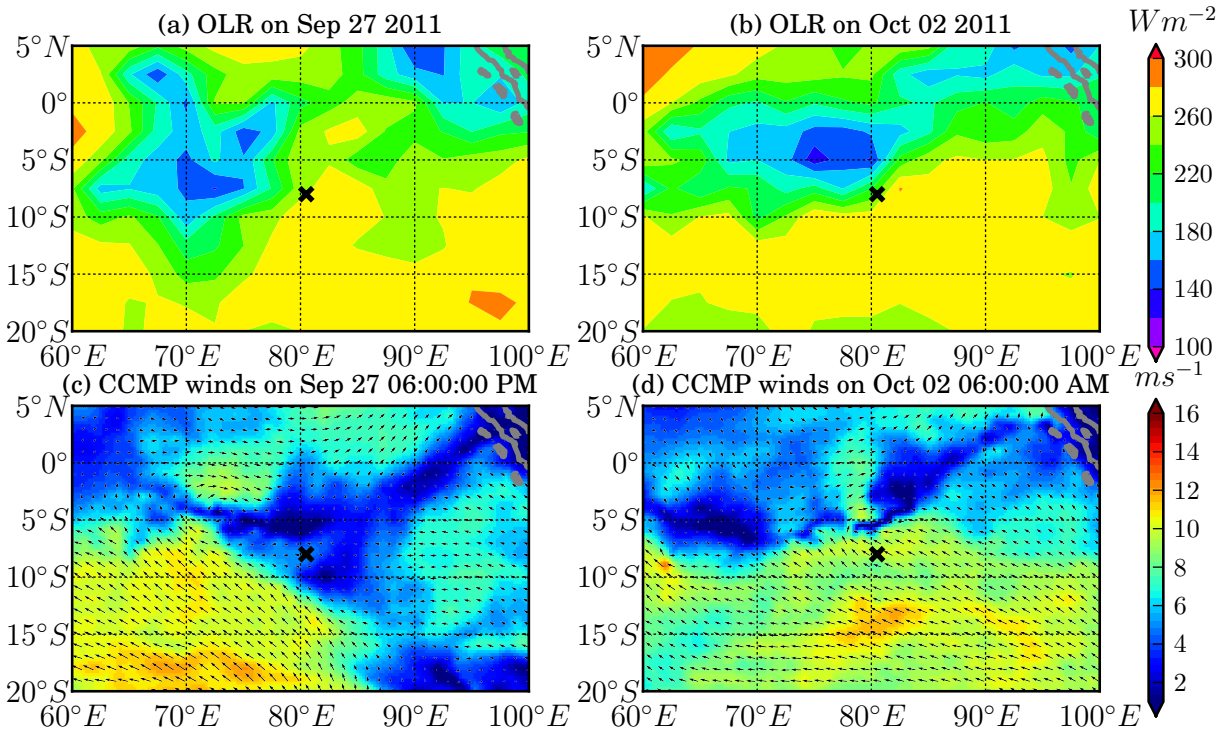

Figure 3.1: Maps of the study area with black cross marking the location of the R/V *Mirai* station at 8°S, 80.5°E. Top maps show Outgoing long wave radiation (OLR) 3 days prior to the sampling period at the station (a) and 3 days after the start of the sampling period (b). The approximate OLR threshold that defines deep convection is 180 Wm^{-2}. Bottom maps show Cross-Calibrated Multi-Platform (CCMP) ocean 10-m surface winds 3 days prior to the sampling period (c) and 3 days after the start of the sampling period (d). Arrows represent wind vectors while the shading represent wind speed magnitude.

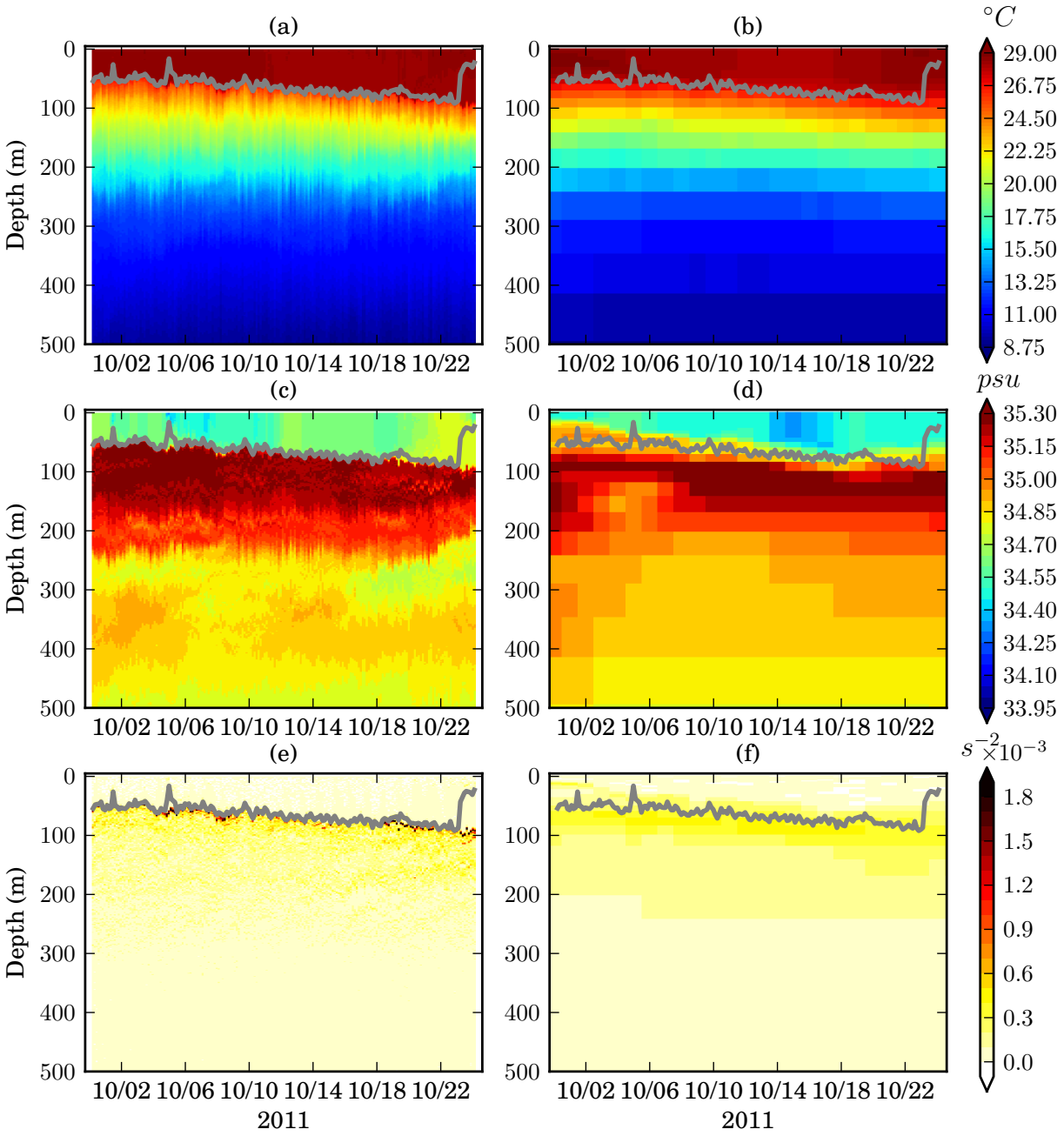

Figure 3.2: Top panels show *in situ* temperature collected during CINDY (a) and the MERCATOR model's potential temperature (b) at 8°S, 80.5°E. Middle panels show *in situ* salinity (c) and MERCATOR salinity (d). Bottom panels show the Brount-Vaisala frequency squared computed from (e) *in situ* density data and from (f) MERCATOR density output.

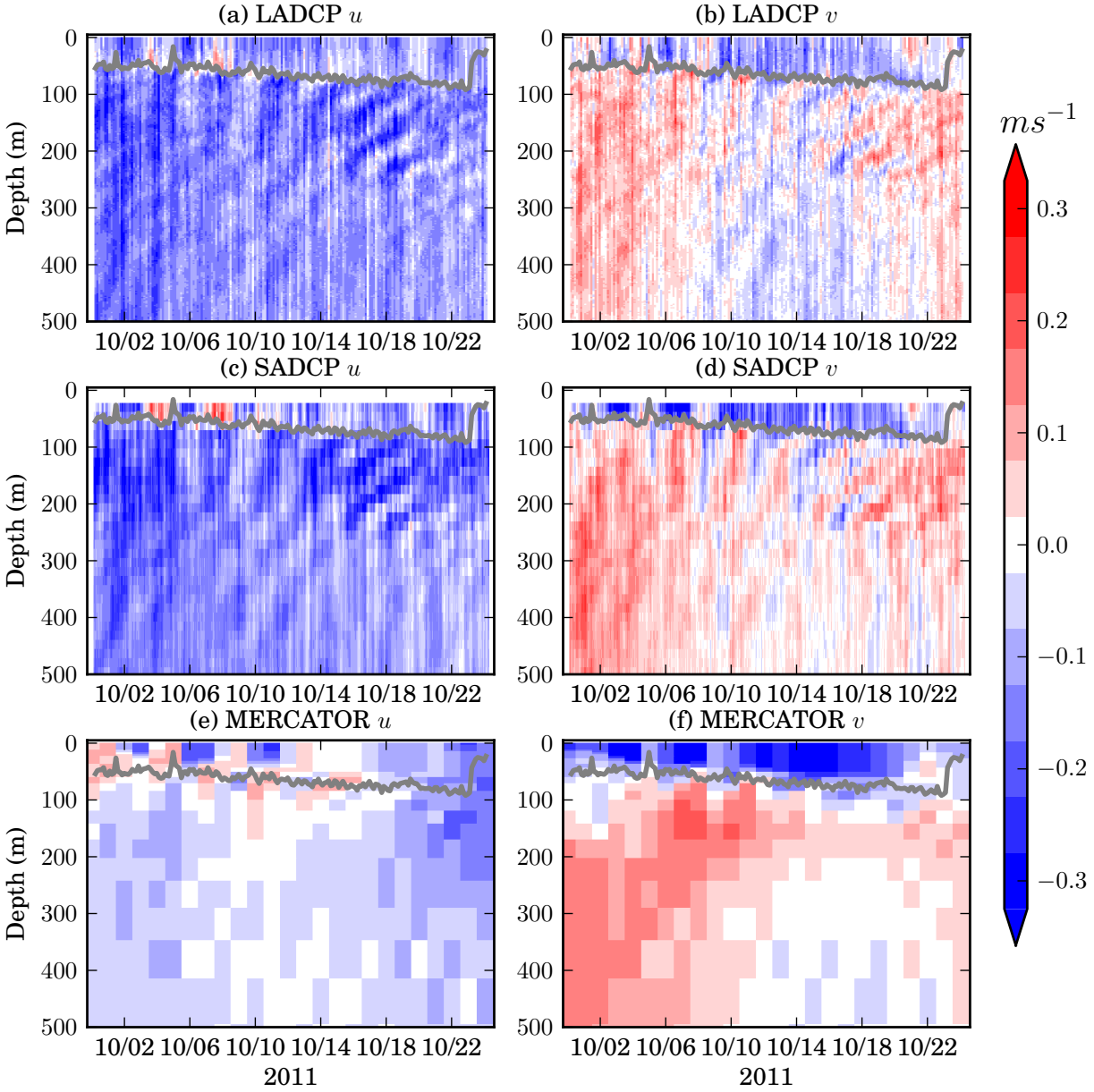

Figure 3.3: Top panels show LADCP u (a) and v (b) current components collected during CINDY at 8°S, 80.5°E. Middle panels show the SADCP u (c) and v (d) current components. Bottom panels show the u (e) and v (f) current components obtained from MERCATOR output at 8°S, 80.5°E.

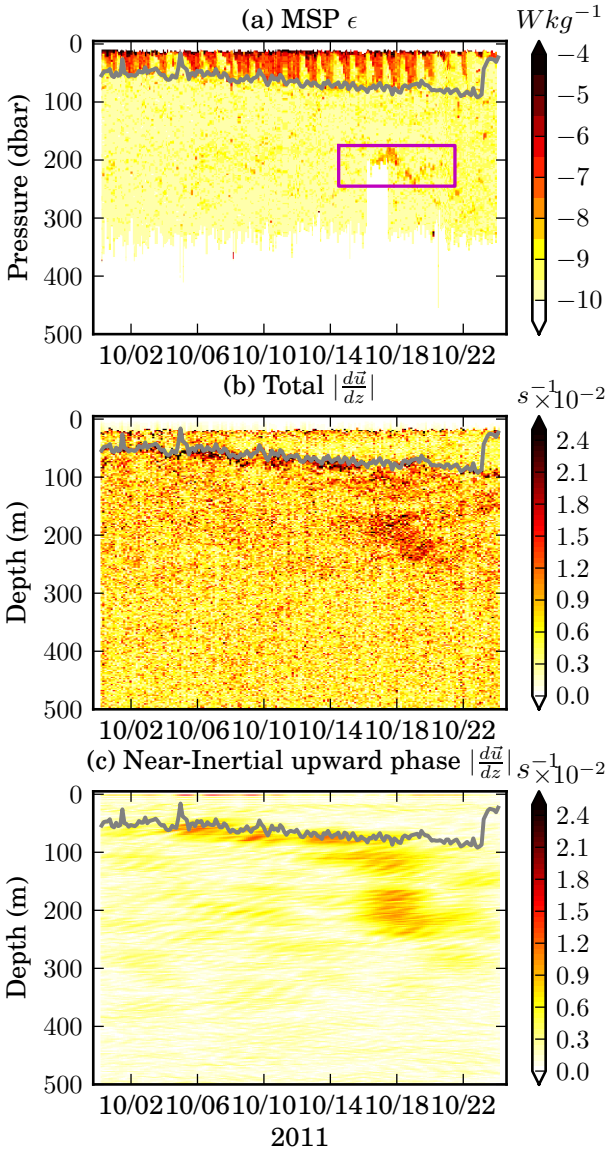

Figure 3.4: (a) Turbulent Kinetic Energy (TKE) dissipation rate (ϵ) measured from Micro-Structure Profiler casts at 8°S, 80.5°E.(b) LADCP derived current shear magnitude ($|\frac{d\vec{u}}{dz}|$) at 8°S, 80.5°E. (c) 2-6 day band-passed upward phase propagating current shear magnitude ($|\frac{d\vec{u_{NI}}}{dz}|$) derived from LADCP measurements at 8°S, 80.5°E.

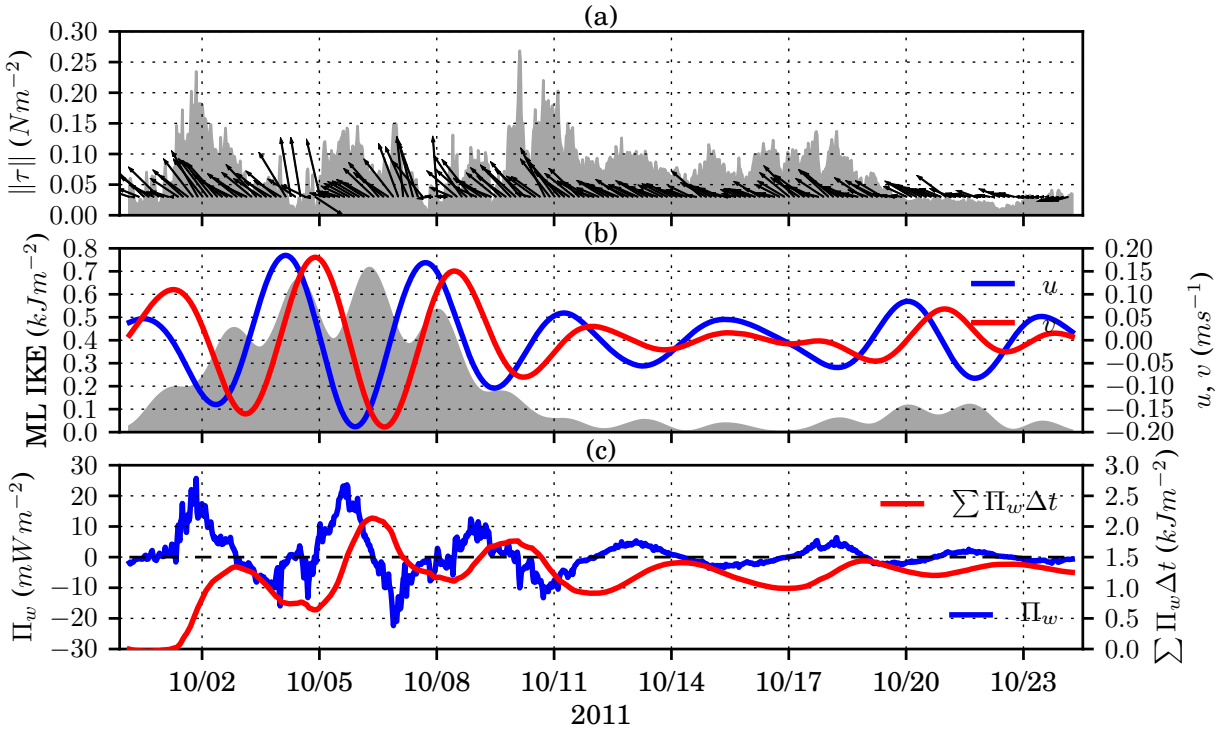

Figure 3.5: (a) Wind stress magnitude (shaded) with unit arrows indicating wind direction. (b) Inertial Kinetic Energy (IKE) in the ML (shaded) and SADCP demodulated inertial current components at 30m depth. (c) Wind work on ML inertial currents and the accumulated wind work. Time-series at 8°S, 80.5°E.

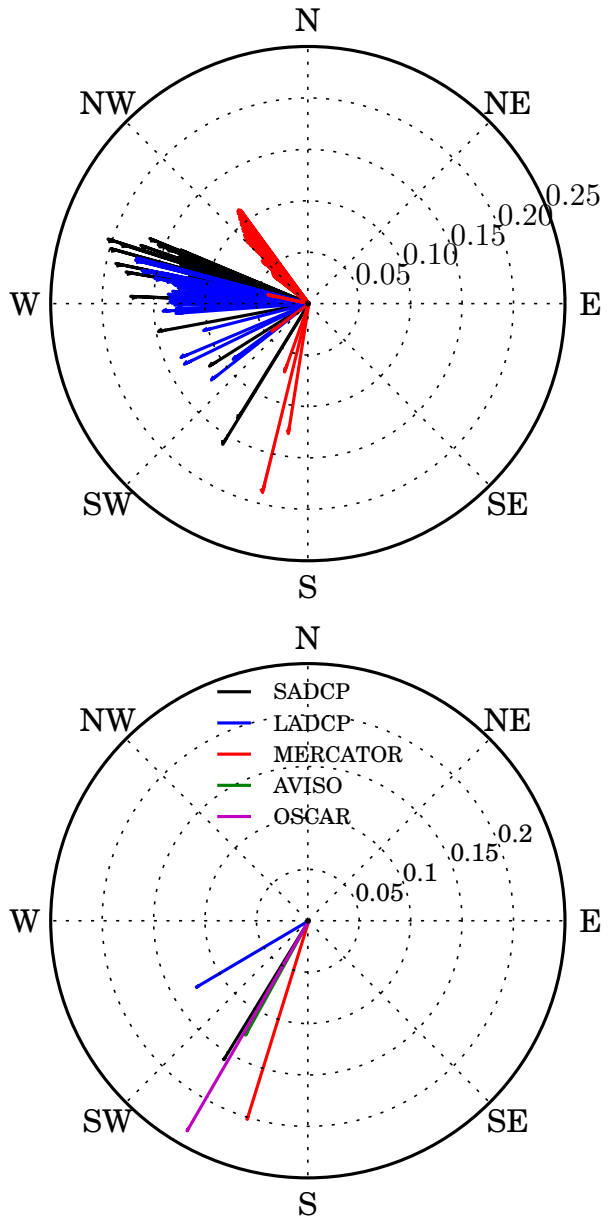

Figure 3.6: (a) Current vectors for surface down to 500m from LADCP (blue, 2 m inverval), SADCP (black, 16 m interval) and MERCATOR (red, 16 m interval) averaged for the station sampling period. (b) Near-surface current vectors averaged for the station sampling period at 8°S, 80.5°E. The LADCP and SADCP *in situ* currents (averaged over upper 45 m and at 30 m depth, respectively) are compared with MERCATOR (averaged over upper 45 m), AVISO and OSCAR products (at 15 m depth).

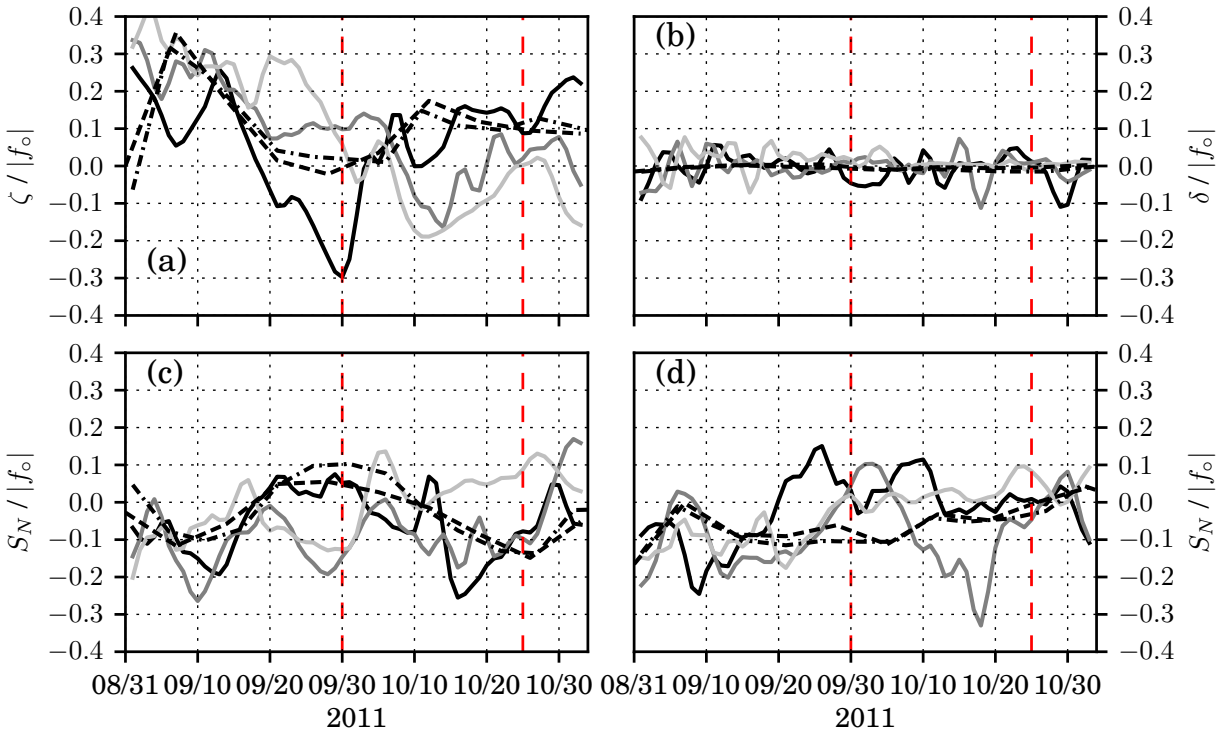

Figure 3.7: Time-series of (a) vorticity, (b) divergence, (c) normal component of the horizontal strain and (d) shear component of the horizontal strain at 8°S, 80.5°E. Dashed lines are for AVISO derived quantities, dashed dotted lines for OSCAR and solid lines represent MERCATOR at select depths (black: 15m, darker grey: 110m and light grey: 220m). Red vertical dahsed lines mark the beginning and end of the sampling period.

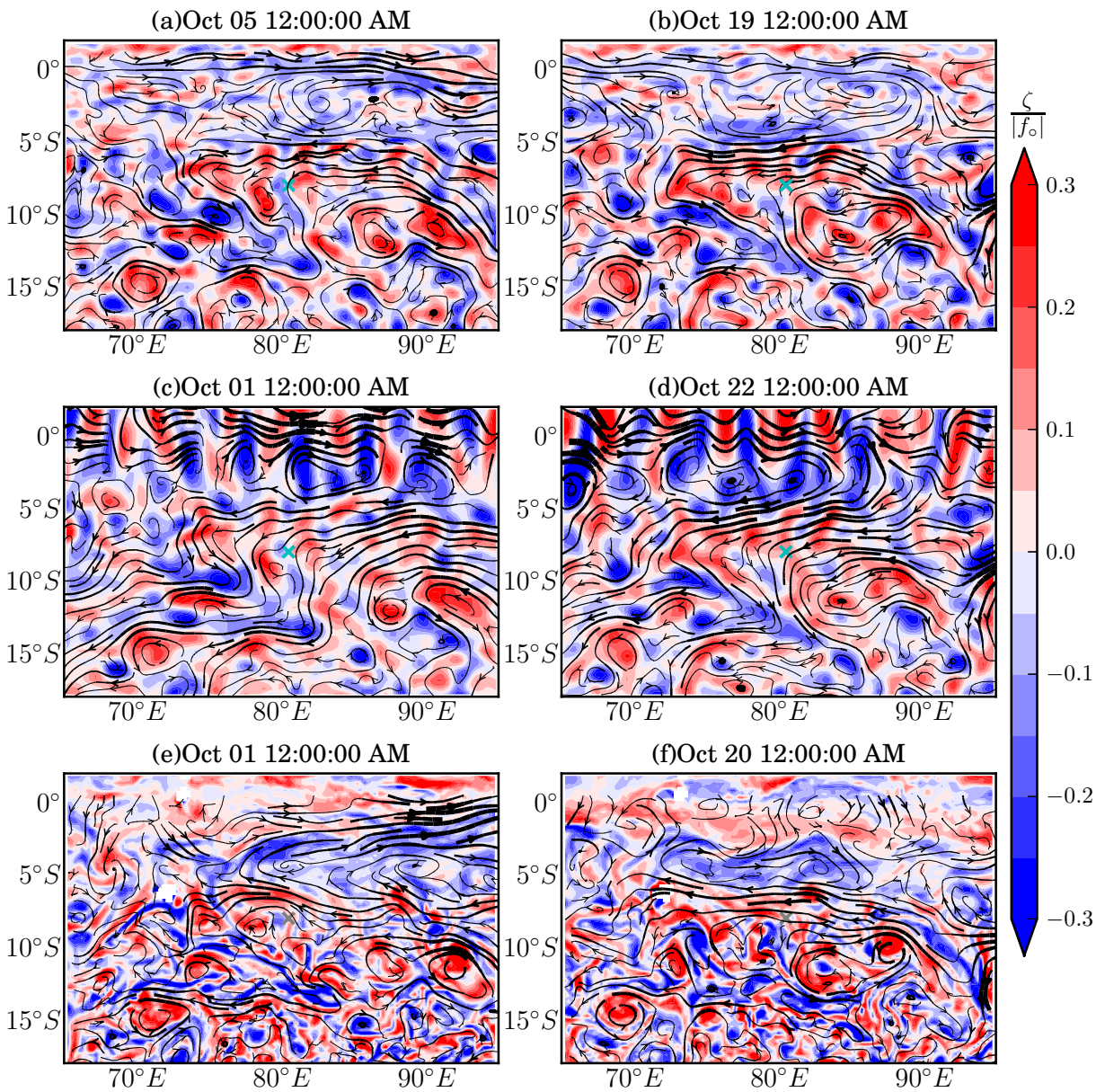

Figure 3.8: (a) Near-surface vorticity (shading) and circulation (lines) from AVISO 7 days averaged absolute geostrophic currents near the beginning of the fixed station sampling period and (b) near the end of the sampling period. (c) Same but for OSCAR 5 days averaged currents near the beginning of the fixed station sampling period and (d) at the end of the sampling period. (e) Vorticity (shading) and circulation (lines) from MERCATOR ≈90 m depth currents for the begining of the fixed station sampling period and (f) for the end of the sampling period. Crosses mark the location of the R/V *Mirai* station at 8°S, 80.5°E. Thickest lines denote flows in excess of 1 ms^{-1}.

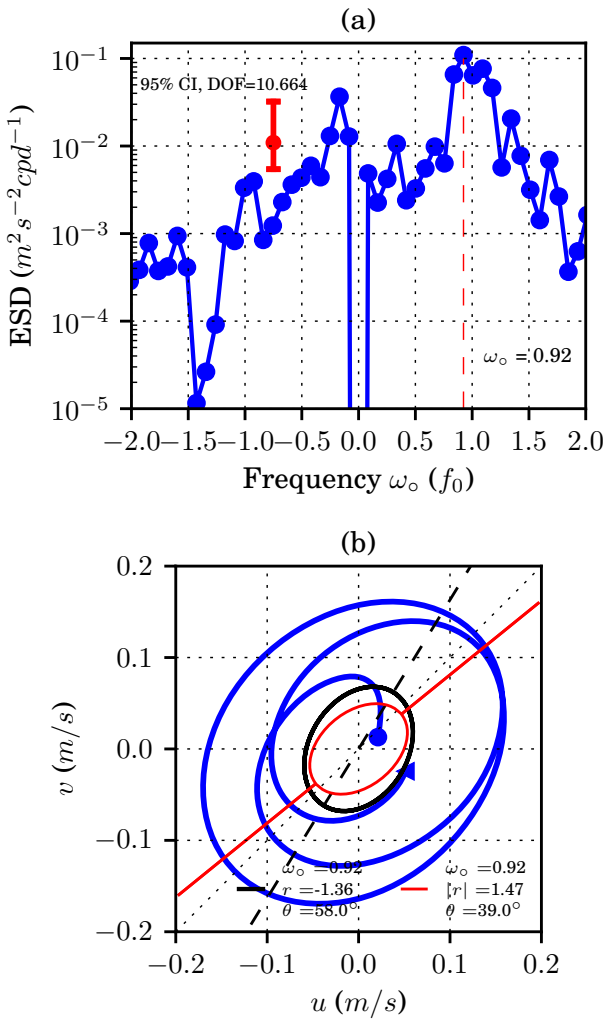

Figure 3.9: (a) Rotary spectrum for mixed layer currents from SADCP measurements. (b) Mixed layer current ellipse during the first 3 inertial periods (≈11 days) of the sampling period at 8°S, 80.5°E. Also shown are the inertial oscillation ellipses and its parameters obtained from the FFT (red) and HM94 (black, dashed line shows the major axis) methods.

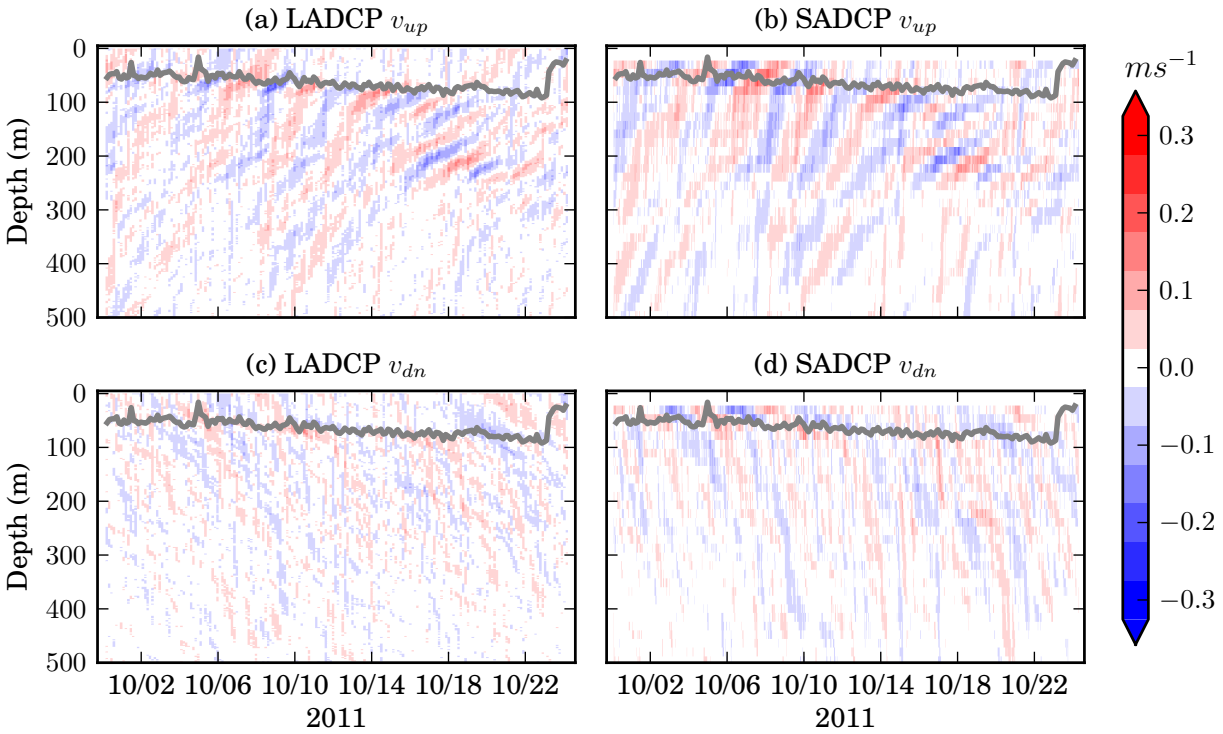

Figure 3.10: Upper panels show depth-timeseries of upward phase (downward energy) propagating meridional velocity (v_{up}) components collected during CINDY at 8°S, 80.5°E for (a) LADCP and (b) SADCP. Lower panels show depth-timeseries of downward phase (upward energy) propagating meridional velocity (v_{dn}) components collected during CINDY at 8°S, 80.5°E for (c) LADCP and (d) SADCP.

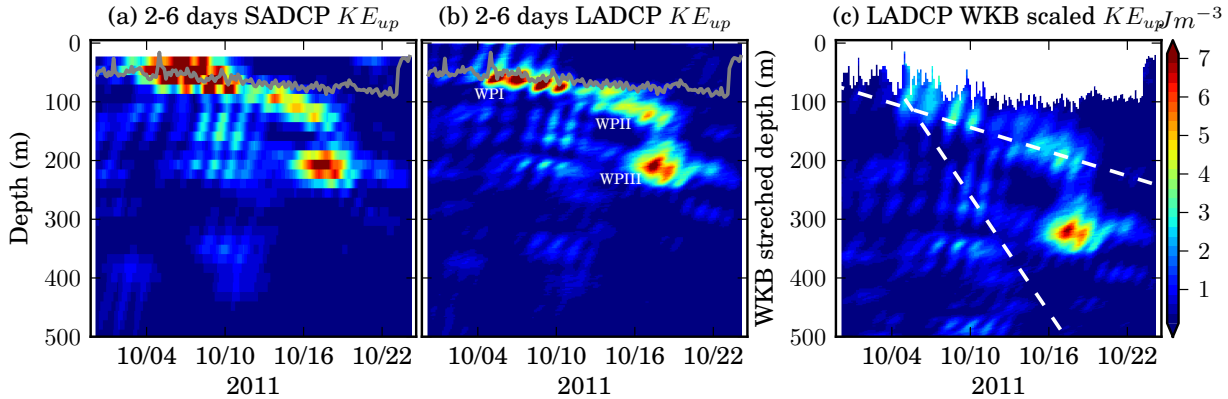

Figure 3.11: Downward radiating near-inertial kinetic energy computed from 2-6 day bandpassed current anomalies for (a) SADCP, (b) LADCP and (c) LADCP but WKB scaled and plotted over WKB stretched depth. Wave packets of interest are labeled with white text as WPI, WPII and WPIII. The white dashed lines denote ray paths, one forward ray path extrapolating WPI using the wave packet method estimated c_{gz} and a backwards ray path extrapolating the WPII estimated c_{gz}.

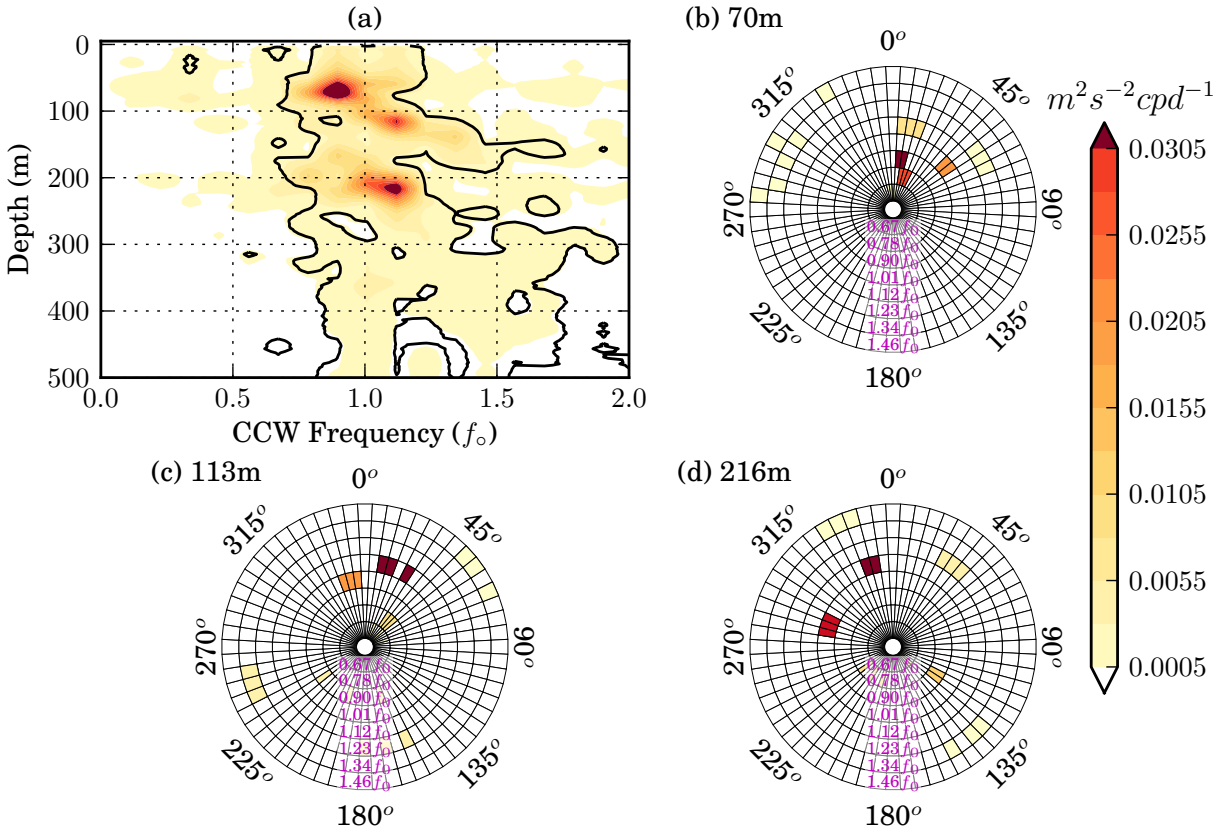

Figure 3.12: (a) Rotary frequency spectra of LADCP currents. Directional energy density spectrum of NIW band at 70m (b), 113m (c) and 216m (d). Angles denote direction waves propagate towards, with 0° being North. Bins along the radius show the frequencies in the 2-6 day band from low at the center to high at the edges. Filled bin are color-coded based on the energy density and for every frequency it is shown the high, mean and low phase and energy estimates. Only values above the coherence significant value are shown.

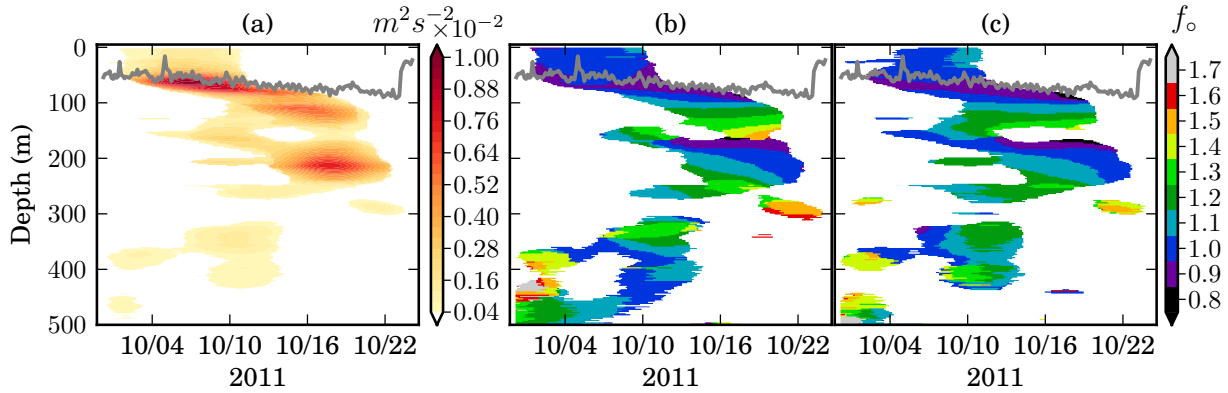

Figure 3.13: (a) Variance in the 2-6 days band from the Wavelet Transform (WLT) of LADCP currents. (b) Peak frequency of the WLT spectrum of zonal currents (u). (c) Peak frequency of the WLT spectrum of meridional currents (v). Only values above the coherence significant value are shown.

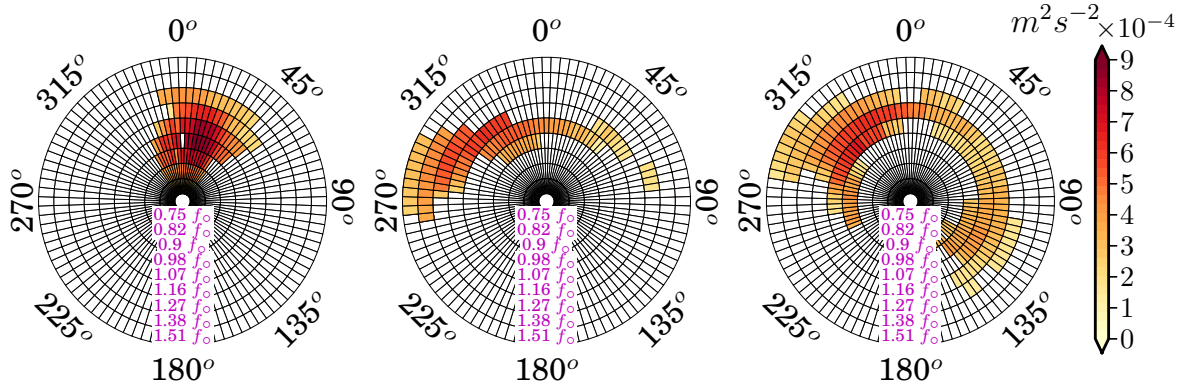

Figure 3.14: Directional spectrum of the NIW band obtained from the WTL coherence phase between u and ρ for the wave packet I (60-90m) (a), wave packet II (110-140m) (b) and wave packet III (180-240m) (c). Angles denote direction waves propagate towards, with 0° being North. Bins along the radius show the frequencies in the 2-6 day band from low at the center to high at the edges. Filled bins are color-coded based on the u energy density. Only values above the coherence significant value are shown.

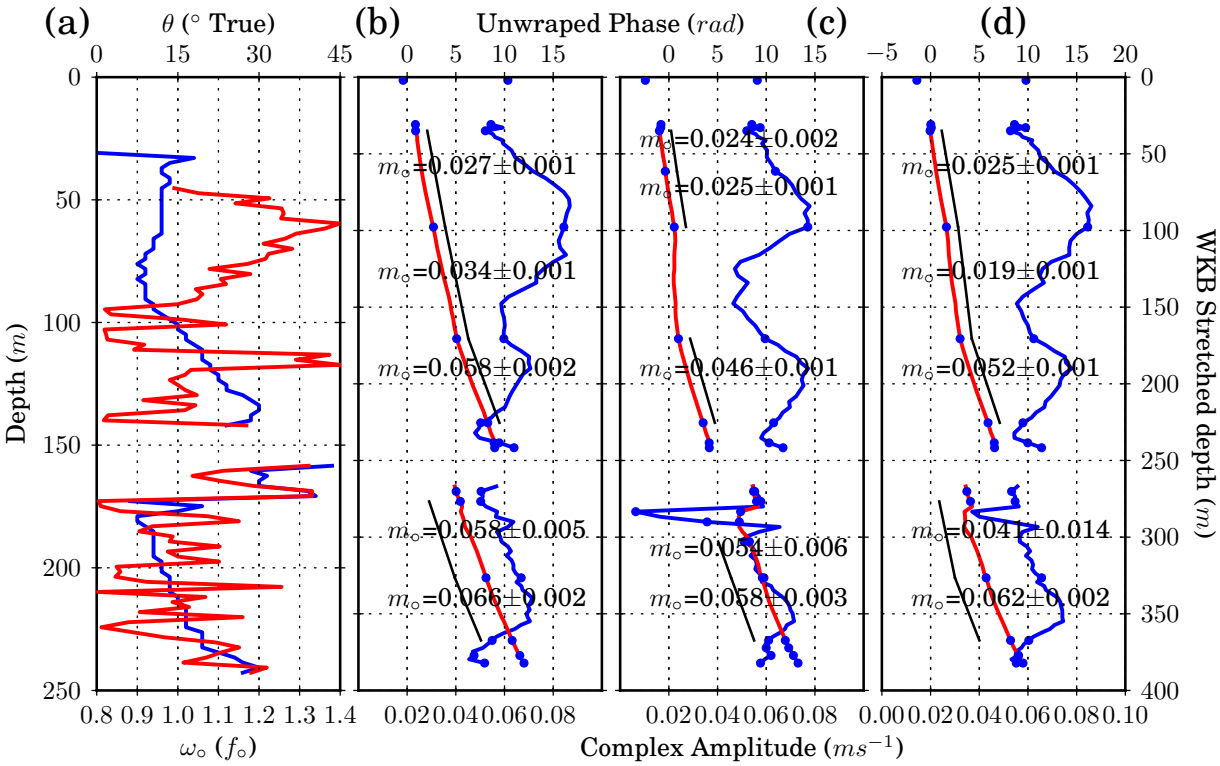

Figure 3.15: Wave properties estimated using the HM94 method. (a) Peak frequency $\omega_\circ$ (blue) and near-inertial ellipse tilt ϕ_2 (red). (b) Phase (red) and complex amplitude (blue) of demodulated rotary currents using $\omega_\circ = 0.92 f_\circ$ from WPI. (c) Same but using $\omega_\circ = 1.08 f_\circ$ from WPII. (d) Same but using $\omega_\circ = 1.0 f_\circ$ from WPIII. Also shown are linear fits to phase segments (defined by the blue dots) and it's corresponding vertical wavenumbers.

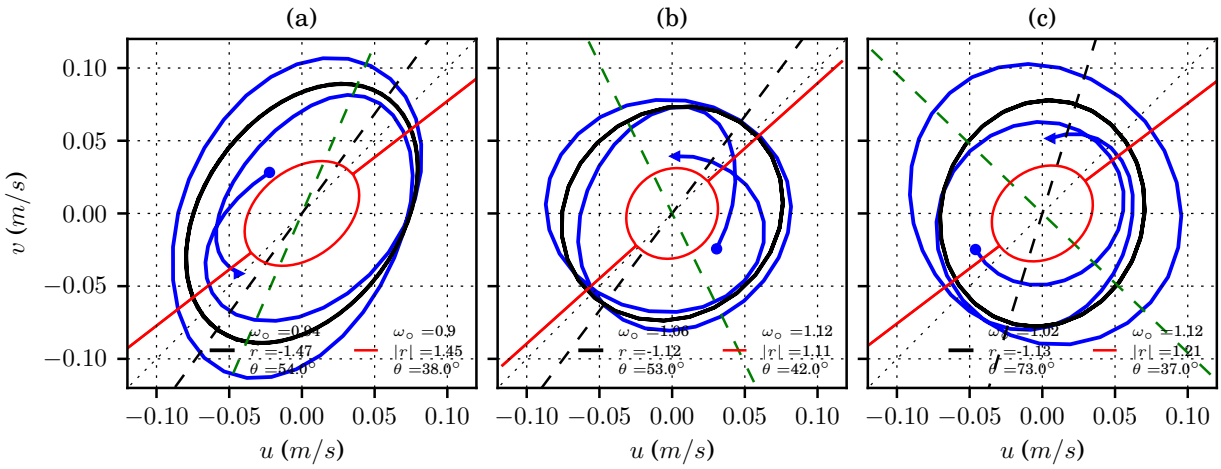

Figure 3.16: Near-Inertial ellipses computed from demodulated u_{up} and v_{up} at (a) 70 m using $\omega_\circ = 0.93 f_\circ$ (WPI), (b) at 113 m using $\omega_\circ = 1.12 f_\circ$ (WPII), (c) $\omega_\circ = 1.05 f_\circ$ at 216 m depth WPIII. Also shown are NIW ellipses obtained from FFT (red) and HM94 (black, dashed line shows the major axis) methods. Green dashed lines show ϕ_1 obtained from the coherence spectra.

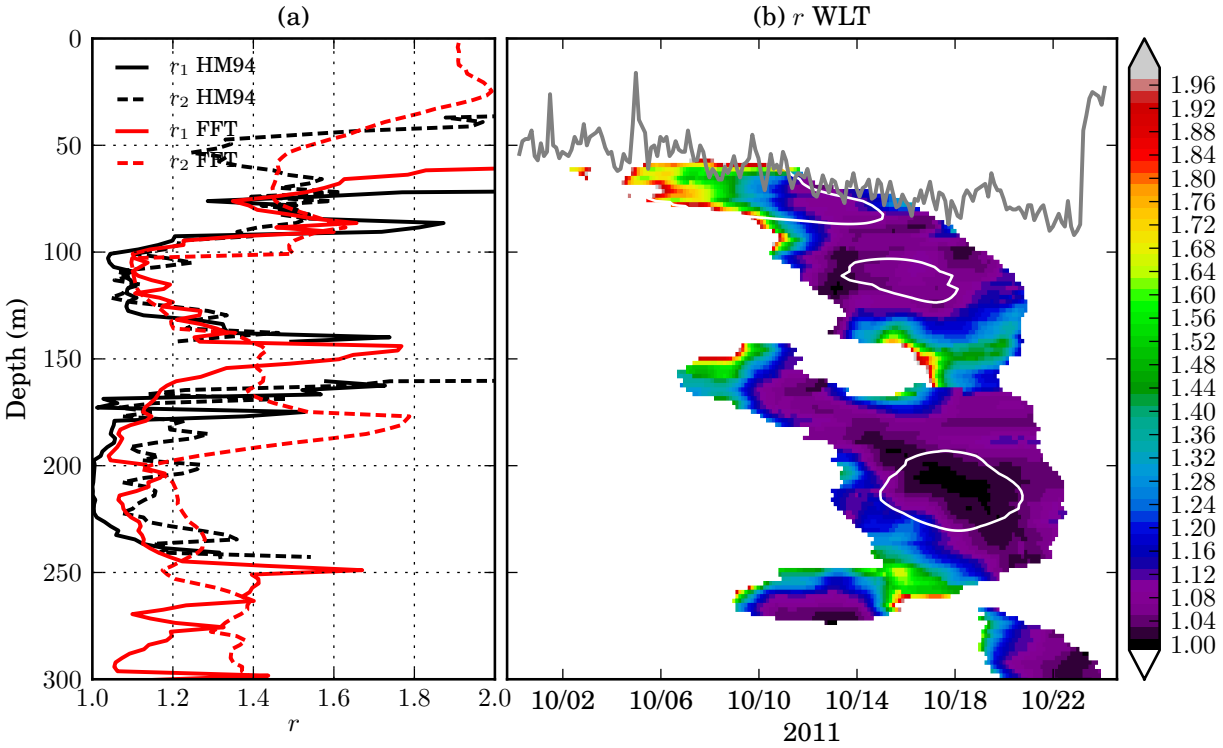

Figure 3.17: (a) Profiles for r_1 and r_2 using different methods. Note that the FFT gives an average representation of the whole timeseries for a given frequency, at a given depth, whist the HM94 method describes this average behavior within a narrower interval in the timeseries, at a given depth. (b) r_1 at every time instance and depth using its primary WLT frequency. White contours denote the regions of elevated NIW variance.

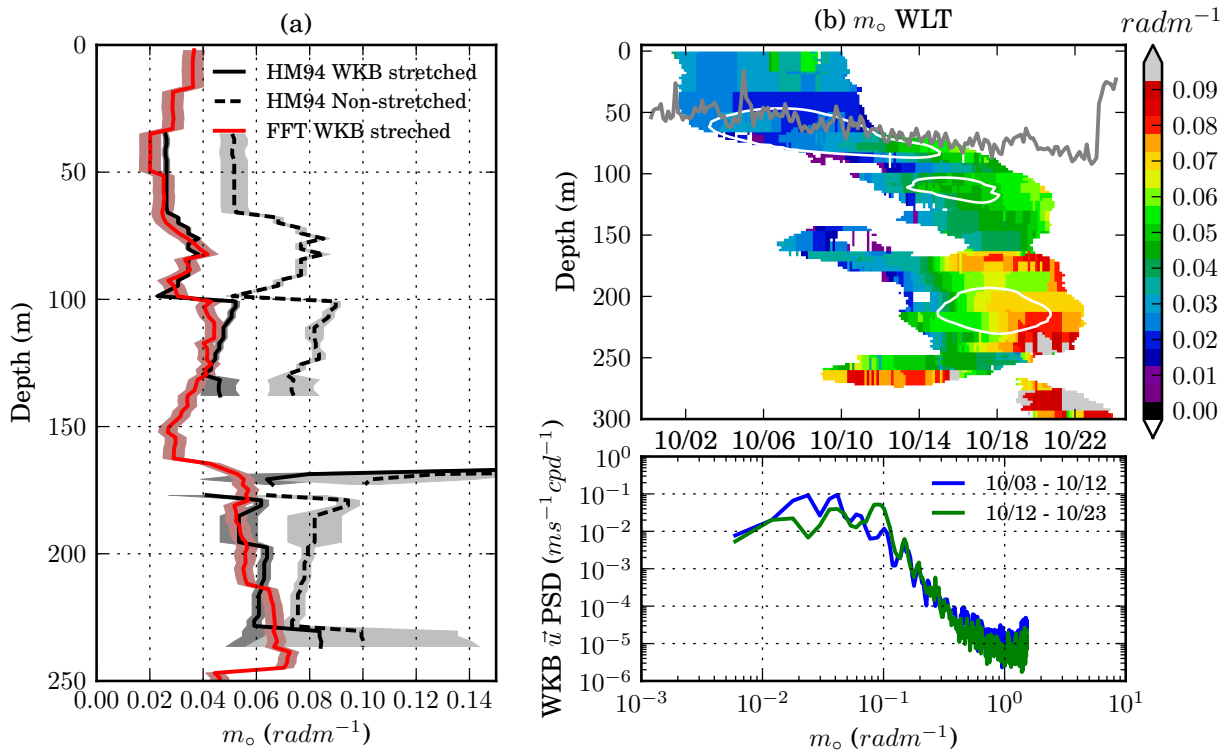

Figure 3.18: Estimates of NIW vertical wavenumber m. (a) WKB stretched m profiles using peak frequencies from the HM94 method (blue curve) and the FFT spectrum (red curve), note that these profiles follow the times where NIW energy is significant, e.g follow the ray path. (b) WKB stretched m based on demodulation with WLT peak frequencies. (c) Non stretched vertical wavenumber spectrum for wave packets I, II and III, note prominent peaks at wavelengths roughly consistent with non stretched HM94 analysis of (a) 0.27, 0.043 and 0.08-0.09.

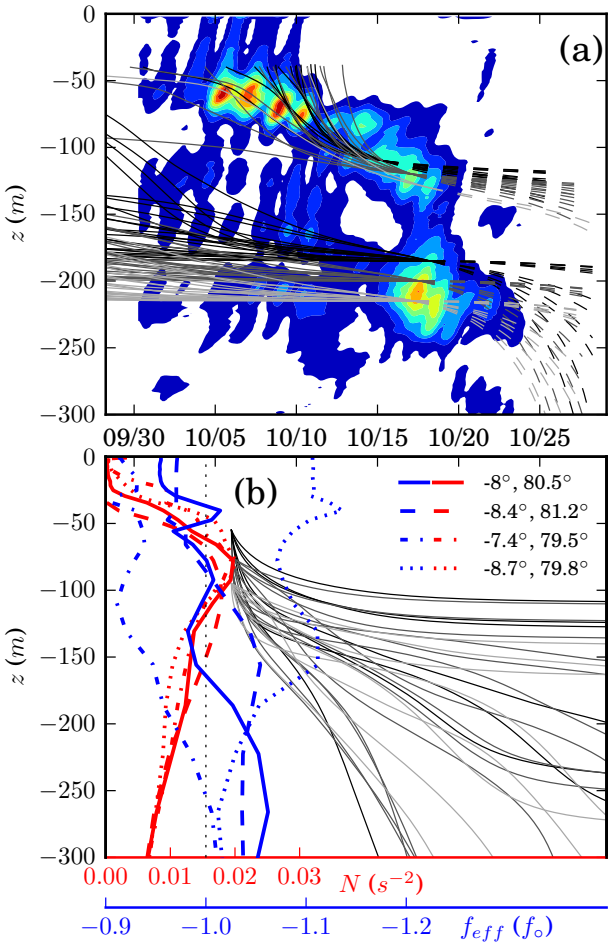

Figure 3.19: (a) Ray depths for WPII and WPIII backtracked to the base of ML (solid lines) and forward traced for 15 days (dashed lines). Each line represents a different initial wavenumber and lighter shades of gray denote rays with a deeper starting depth. For reference, the color contours show the near-inertial kinetic energy from LADCP measurements. (b) Depth of forward traced WPI rays. Also shown are MERCATOR N (red curves) and f_{eff} (blue curves) profiles at the locations marked in Figure 3.23.

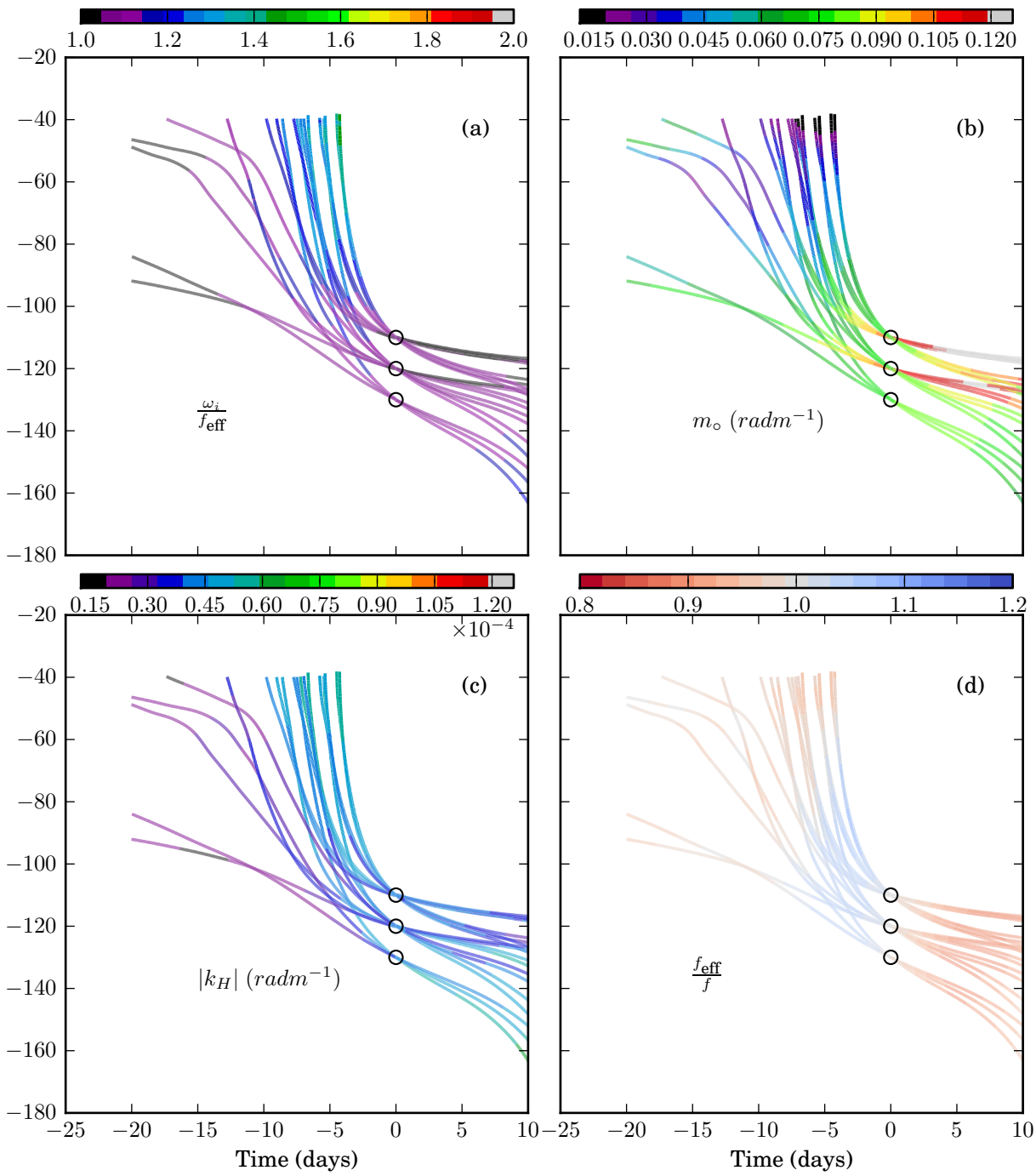

Figure 3.20: Properties for select WPII rays backwards and forwards traced from the CINDY station: (a) ω_i/f_{eff} (r), (b) vertical wavenumber $m_\circ$, (c) horizontal wavnumber $|k_H|$, (d) background f_{eff}/f. Approach to critical layer are indicated by $\omega_i/f_{\text{eff}} \to 1.0$ and $m_\circ \to \infty$. Circles denote the starting points.

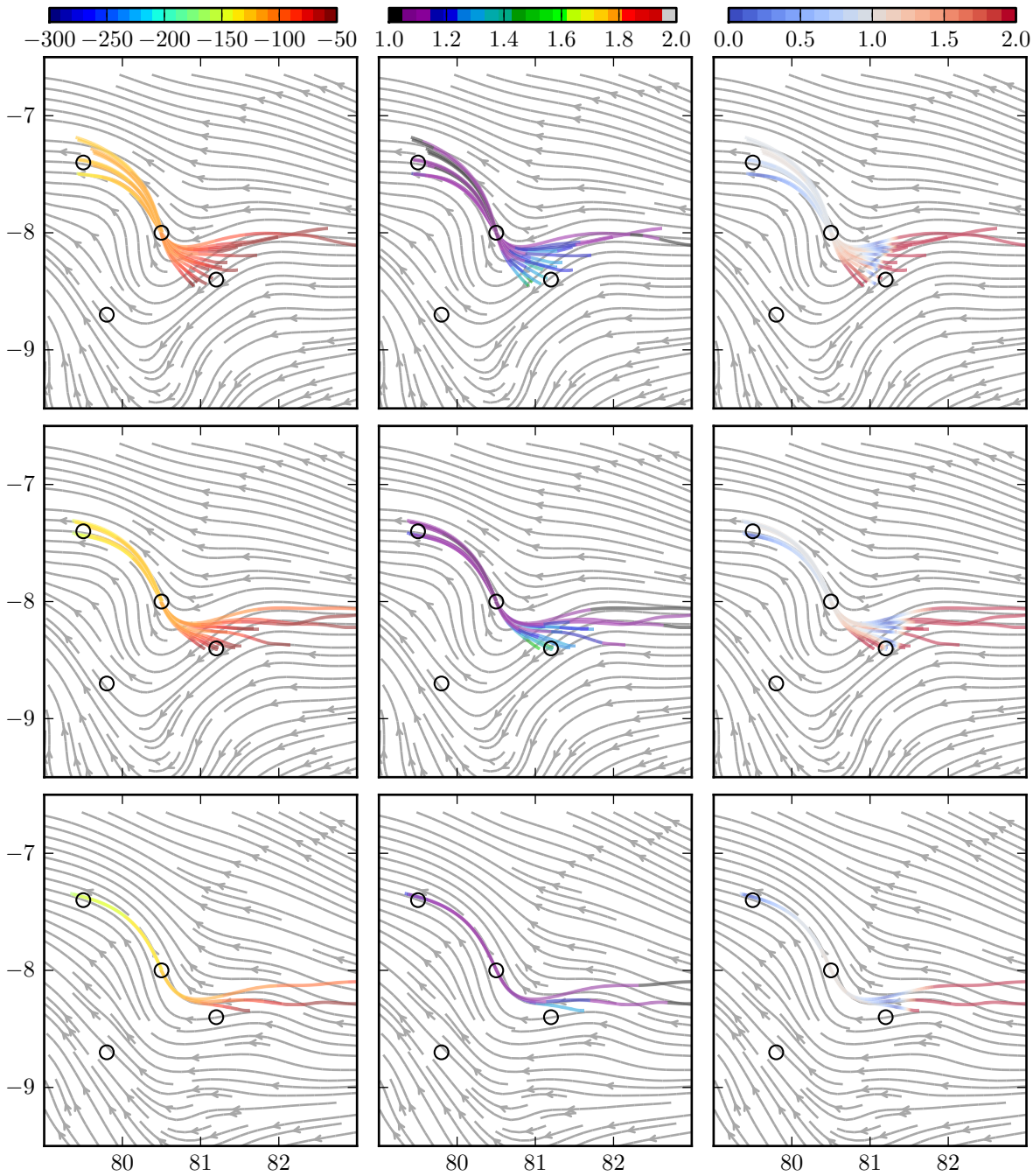

Figure 3.21: Maps for WPII rays backward and forward traced from the CINDY station starting at 110m (top row), at 120m (middle row) and 130m (bottom row). Rays are color coded by depth in meters (first column), the ratio ω_i/f_{eff} (second column) and the ray tube volume relative to its initial volume (third column). Streamlines show the background circulation at the starting depth. Black circles mark the locations where profiles of background N and f_{eff} are extracted.

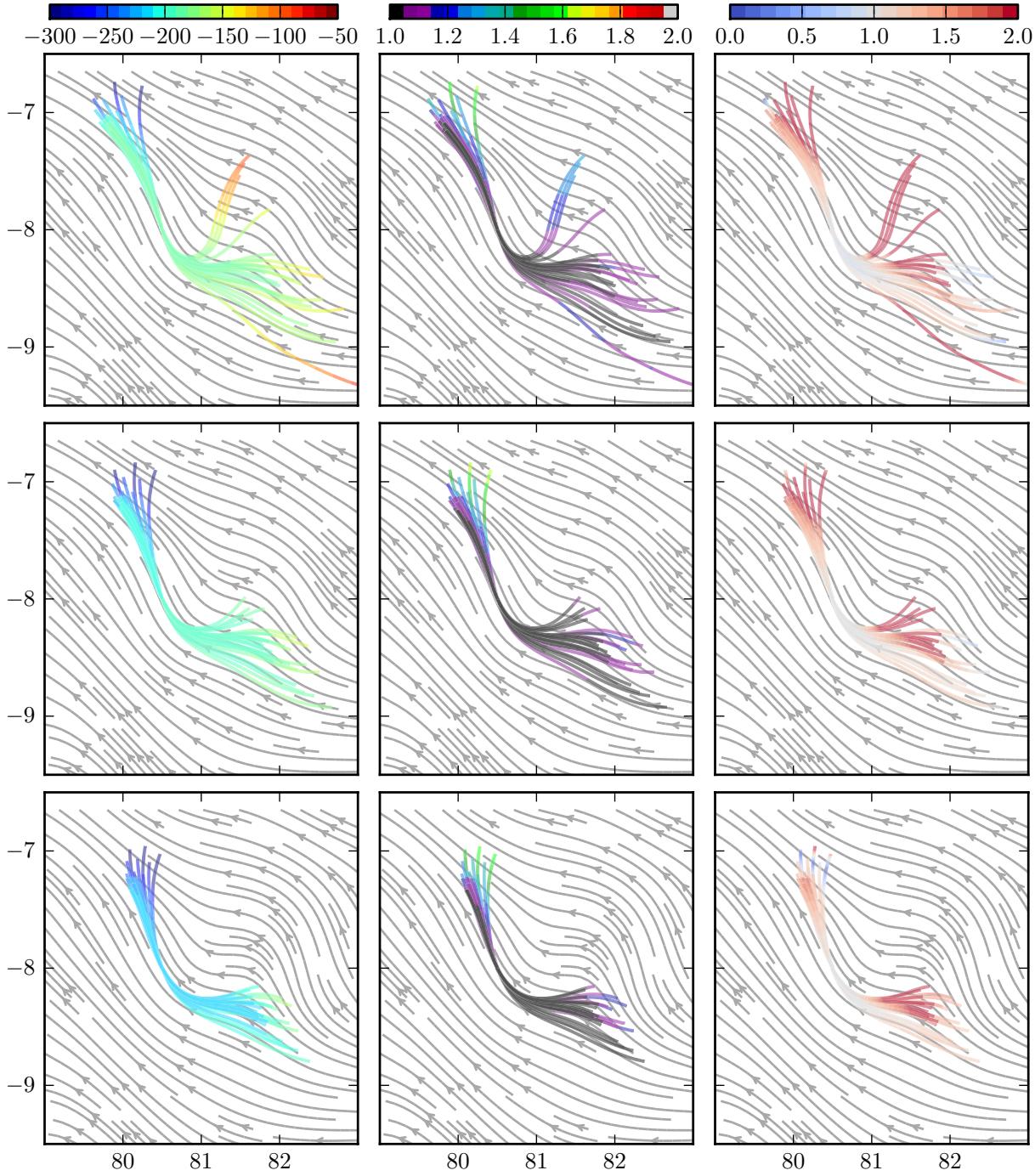

Figure 3.22: Maps for WPIII rays backward and forward traced starting at 185m (top row), at 200m (middle row) and 215m (bottom row). Rays are color coded as in Figure 3.23. Streamlines show the background circulation at the respective starting depth.

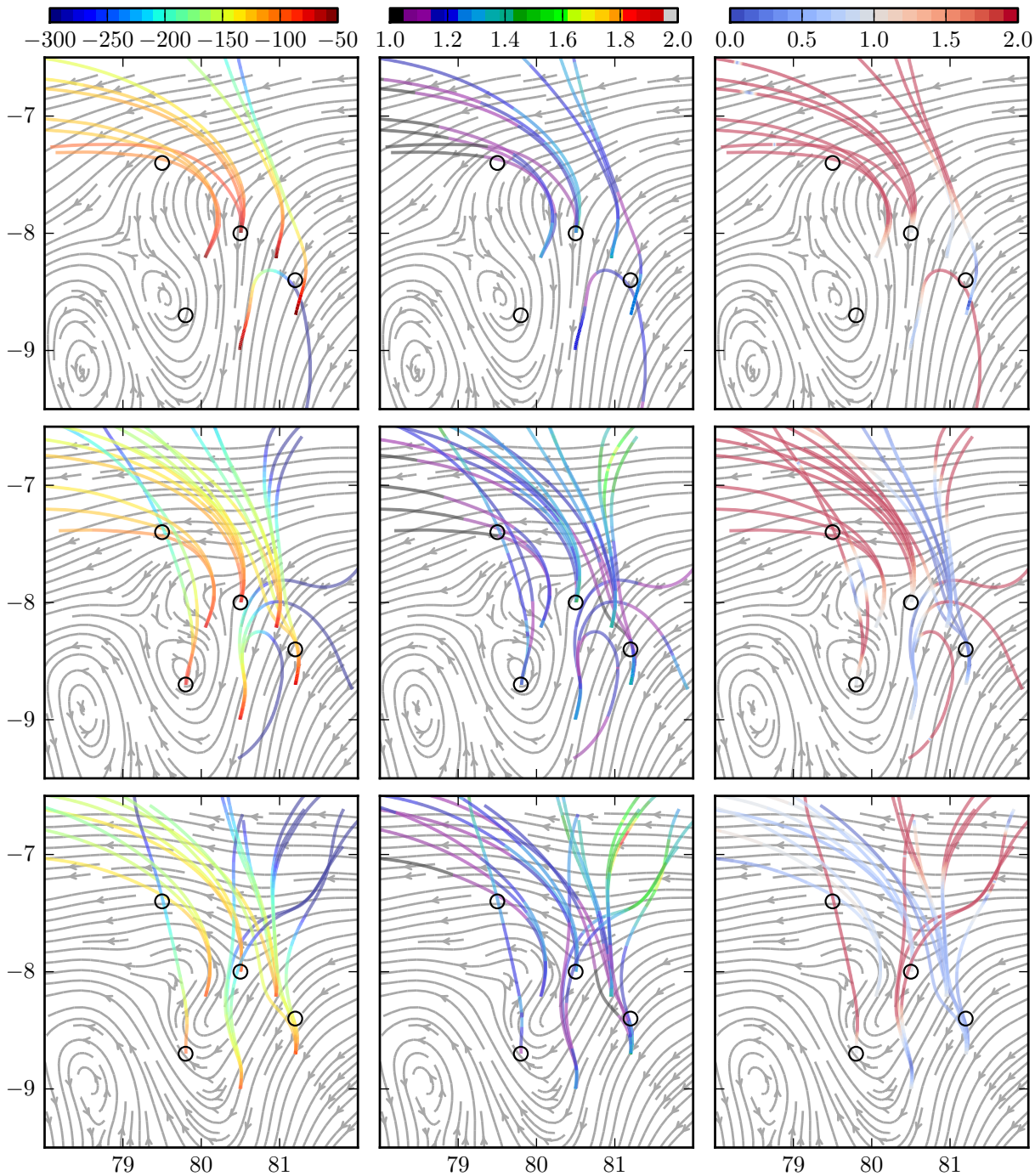

Figure 3.23: Maps for WPI rays forward traced with starting depth at 55m (top row), at 75m (middle row) and 95m (bottom row). Rays are color coded as in Figure 3.23 and streamlines show the background circulation at the respective starting depth, while black circles mark the locations where background profiles of N and f_{eff} are extracted (note the Longitudes have changed).

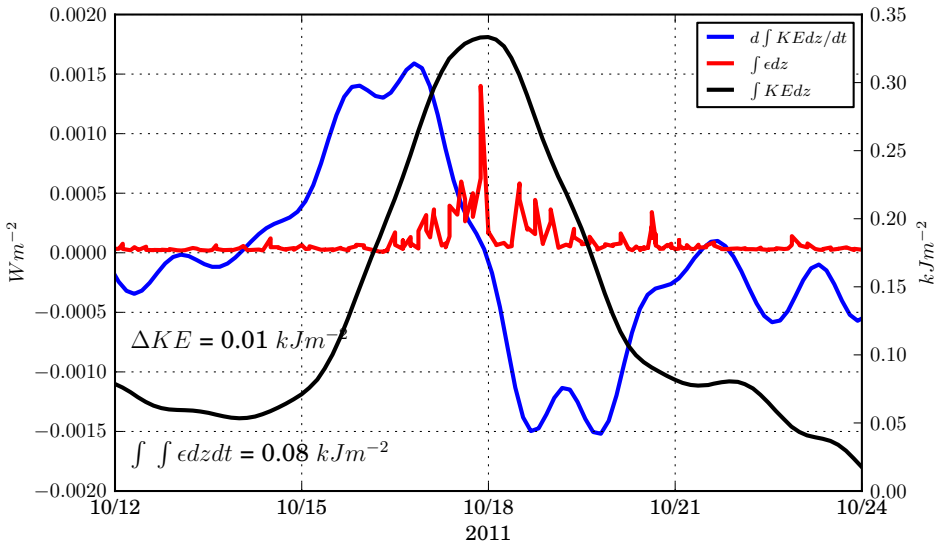

Figure 3.24: Time series of energy balance terms for WPIII, depth integrated between 170-245m. The left axis is for fluxes (local rate of change of kinetic energy and turbulent kinetic energy dissipation ϵ, blue and red line respectively), while the right axis is for kinetic energy density. Quoted values denote quantities time integrated between 10/15 and 10/22.

CHAPTER 4
IMPACTS OF BACKGROUND STRATIFICATION AND CIRCULATION ON NEAR-INERTIAL WAVE DYNAMICS

4.1 Introduction

The overarching goal of this Chapter is to diagnose the impact of the background ocean circulation, more specifically it's relative vorticity, and the ocean stratification on the generation and propagation dynamics of near-inertial waves (NIWs).

What follows is a review of the relevant literature and analysis of the CINDY2011 data set that motivated this study, followed by the statement of the specific objectives of Chapter 4 and a description of the general structure of the remaining sections.

4.1.1 Background and Motivation

The CINDY data, analyzed using the plane wave or WKB approximation in Chapter 3, showed NIWs with horizontal scales of $100--200$ km and vertical scales $\mathcal{O}(100)$ m. Similar scales have also been reported by *Alford and Gregg* (2001). The waves are present in the transition layer (TL) and thermocline (defined here as the stratified region between $75--200$ m) immediately after a series of trade-wind bursts generated mixed layer (ML) inertial oscillations, providing direct observations of the generation process of NIWs. The observations also show that NIW energy penetrates to the bottom of the thermocline, and is associated with a significant level of turbulent mixing.

Vertical normal modes have been an important analytic tool in understanding the propagation of NIWs from the surface ML to the deep ocean (*Gill* 1984; *D'Asaro et al.* 1995; *Alford and Zhao* 2007; *Danioux et al.* 2008). In this regard, it is useful to determine which vertical modes are most energetic, given that a finite number of such modes is expected to provide a sufficiently accurate representation of the near-inertial oscillations.

The lack of full-water-column current measurements prevents calculation of modal amplitudes from the CINDY observations. Instead, we examine which modes are preferentially excited by wind forcing in an ocean with a realistic stratification. This approach has been attempted in

several observational analysis (*D'Asaro et al.* 1995; *Alford and Gregg* 2001; *Cuypers et al.* 2013) with mixed success.

Application of this technique to the CINDY2011 data set does not indicate that the observed NIW vertical scales result from the dominant vertical modes. This conclusion is briefly demonstrated next.

Vertical normal modes for CINDY2011

Following *Alford and Gregg* (2001), we estimate how well vertical normal modes can explain observed features of the CINDY2011 NIW packets, particularly their vertical scale. To compute the dominant normal modes, CTD measurements of temperature and salinity in the upper ocean are merged with WOA09 climatology to provide a full depth profile of the Brünt Väisäla frequency, N^2. The resultant profiles are shown on Figures 4.1 and 4.2a, where the blue curve represents the background ocean stratification during the first half of the CINDY2011 cruise (Profile a) when the first NIW packet was generated. The eigenfunctions and the eigenvalues of the Sturm-Liuville system (defined in equations 4.3a−−4.3b) represent the modal structure $\psi_n(z)$ and the mode horizontal phase speed c_n, respectively. Expected modal amplitudes are obtained by projecting $\psi_n(z)$ onto the vertical structure function of the wind stress forcing $Z(z)$, thereby determining the fraction of wind stress forcing a given mode "feels". Details of the forcing structure are found in section 4.2, but it typically mimics a maximum stress uniformly distributed within a well-mixed surface layer that linearly decays to zero within the stratified transition layer.

Figure 4.3 shows the various parameters obtained from the modal analysis of Profile a (blue; overlain by the red curve in some panels). Focusing first on the modal vertical wavelengths, given by $c_n/\bar{N}$ (where $\bar{N} = 7.7 \times 10^{-3}\ s^{-1}$), it can be readily seen that the observed NIW range of vertical scales (denoted by the dark dashed lines) correspond to mode numbers 10 through 30 (Figure 4.3b). However, as shown in Figure 4.3c, wind forcing projects little energy onto modes higher than 5. Therefore, in contrast to *Alford and Gregg* (2001), no good correspondence in terms of vertical scales was found between such a modal decomposition and the plane wave analysis of Chapter 3.

In a variety of tests using different realistic stratification conditions and wind forcing structures,

low modes dominate. Wind forcing and ML step functions tend to project best onto lower modes, particularly mode 2 due to the presence of the sharp thermocline atop the permanent thermocline. If an N^2 profile typical of the midlatitudes is used, mode 1 tends to dominate. This property cautions that a straightforward application of such a modal decomposition may not be relevant to elucidate NIW dynamics, as it neglects the important spatial structure of the waves and of the wind forcing, focusing only on a one-dimensional representation of the ML currents. This idea is further discussed next, and is a concept used throughout this study.

Scales for Near-Inertial motions

Essentially low modes would be the ones primarily forced by large-scale winds, given typical open ocean (e.g. depths over 2000 m) conditions and absence of horizontal variations in background stratification and currents, however, higher modes are typically observed in detailed upper ocean current measurements of NIWs, e.g. *Alford and Gregg* (2001), *Jaimes and Shay* (2010), *Cuypers et al.* (2013). In that regard, note that given the modal speeds shown in Figure 4.3a, for low modes to display a near-inertial oscillation it requires very long horizontal scales, unlike what was observed during CINDY (Chapter 3), clearly illustrating the need for a mechanism to reduce these scales.

This has been extensively considered in the literature, starting with *Gill* (1984) who derived a decay timescale for ML inertial oscillations (IOs) based on their horizontal wavenumber, whereby, under typical midlatitude stratification and large-scale wind forcing, ML IOs would take months to years to radiate downwards. Later, *D'Asaro* (1989) provided evidence that the β effect is a key mechanism to quickly reduce the initial horizontal scale of the ML inertial oscillations and promote their downward propagation as NIWs. More recently, the focus changed to the impact of mesoscale eddies on the decay of ML inertial oscillations (*D'Asaro* 1995; *Van Meurs* 1998; *Balmforth and Young* 1999).

These studies mostly focused on the rate of ML IO decay, with fewer studies (*Lee and Niiler* 1998; *Danioux et al.* 2008) specifically addressing the vertical penetration of NIW energy into the thermocline and deep ocean, i.e. after leaving the ML. In particular, the numerical study by *Danioux et al.* (2008) demonstrates the impact of mesoscale features on NIWs simulated by a primitive-

equation model. The authors found that the relative vorticity ζ of a geostrophically turbulent, mesoscale eddy field promotes the depth penetration of NIW energy, as initially demonstrated by *Kunze* (1985). Furthermore, they found their results to be well described by the modal technique of *Klein and Smith* (2001), such that the mesoscale features appear to favor the production of NIW with horizontal scales smaller than the mesoscale eddy field. According to Klein's theory, at later times, the NIW amplitude resembles the Laplacian of the vorticity. A "trapping" regime dominates for the higher modes, with enhanced depth penetration of near-inertial energy within anticyclonic features, while the low modes appear more dispersive and are less affected by the background vorticity (*Danioux et al.* 2008).

Surprisingly, little attention has been paid to how the vertical scales of downward propagating NIWs are selected. In fact, both vertical scales and the depth penetration of NIWs in the context of normal modes is seldom discussed. In the studies mentioned above, the modal composition of the solutions is not explored. Based on earlier work by *D'Asaro et al.* (1995), low modes are believed to contain the bulk of the near-inertial energy input by the wind (*Alford and Zhao* 2007). A numerical study by *Furuichi et al.* (2008), using increased vertical resolution, showed a dominance of higher modes over low modes.

There is a second background feature of a realistic and eddying ocean, not discussed in the aforementioned studies. The real ocean contains lateral (horizontal) inhomogeneities in N. For example, the observed time change in background stratification during CINDY (Figures 4.1a,b) is associated, not only with local processes, but with the translation of an anti-cyclonic feature (e.g. Figure 3.7 in Chapter 3), associated with a Rossby wave (*Seiki et al.* 2013) over the station. The background $N(z)$ is characterized by a sharp and strongly stratified TL in the beginning of the time-series measurements (blue profile in Figure 4.1), as the ML deepens with time, so does the TL, and by the second half of Leg I series, the stratification in the TL is greatly reduced, while the thermocline has strengthened. By the beginning of Leg II, the stratification in the thermocline is considerably stronger (Figures 4.1a,b, red and cyan curves). Interestingly, it is during this later time that a second NIW packet is observed around 120 m.

Some of the impacts of laterally varying stratification are readily deduced from WKB theory,

for instance, wave energy scales with N (*Gill* 1982), and an inhomogeneous N field may lead to complex patterns of wave energy penetration. In terms of normal modes, the impact of the observed change in stratification, on the modal projections is shown by the red curve in Figure 4.3c. There is an increase in the role played by the higher modes (shorter vertical scales), despite otherwise similar mode speeds.

Significant mesoscale activity was present during the CINDY2011 campaign, as evidenced by the Rossby Wave described in *Seiki et al.* (2013). According to surface currents from OSCAR (see Chapter 3 Figure 3.8), this flow has a Rossby number $\mathcal{O}(10^{-1})$ and a variety of scales $\mathcal{O}(100)$ km can be detected.

One can expect that there are significant roles to be played by the wind, β effect, mesoscale eddy relative vorticity field and laterally varying stratification, in controlling both horizontal and vertical scales and hence the depth penetration of inertial kinetic energy. A systematic study evaluating the relative importance of these mechanisms is still lacking. Their impacts are difficult to untangle in complex solutions obtained from general circulation models (OGCMs), such as those attempted by *Furuichi et al.* (2008) and *Simmons and Alford* (2012), in part because normal modes are ill-defined in models with inhomogeneous stratification and topography, and a high vertical and horizontal resolution is required to resolve higher modes. Normal modes are also difficult to determine from observational data sets because of the requirement for full depth coverage of the measurements. Therefore, it is easier to conduct such an investigation using numerical or analytical models.

4.1.2 Objectives

Based on the above discussion, two background parameters, the relative vorticity $\zeta(x, y)$ field and the stratification $N(z)$ profile, likely impact the dynamics of the observed NIWs. Therefore, this study has the goal of addressing the following questions:

- How does the background stratification impact the vertical scale of NIWs and the depth penetration? Can the increase in stratification within the thermocline account for the observed downward near-inertial energy radiation?

- How does the introduction of a background relative vorticity affect the horizontal and vertical

scales of the NIWs and the depth penetration of NIW energy?

- What is the character of the NIWs when these processes combine?

The normal-mode response in the near-inertial band for several idealized cases, whether in terms of forcing or in terms of the mesoscale flow impacts, has been the subject of previous research (*Gill* 1984; *Klein and Smith* 2001), but more realistic set-ups that enable direct comparisons to observations are unreported. Therefore, to address the questions above, normal mode solutions are obtained numerically, using realistic wind forcing.

4.2 Model

In this section, we first describe the numerical model and the experimental design used to address the above questions. Then, we report several experimental results, followed by the conclusions and a discussion of the direct implications of the solutions here obtained.

4.2.1 Equations

The model utilized is a numerical implementation of the linear continuously stratified (LCS) system originally derived by *McCreary* (1981). The equations of motion for the LCS model are a version of the primitive equations that is hydrostatic and linearized about a background state of rest:

$$u_t - fv + \frac{1}{\rho_\circ} p_x = \tau^x Z(z) + (\nu u_z)_z + \nu_H \nabla^2 u, \tag{4.1a}$$

$$v_t + fu + \frac{1}{\rho_\circ} p_y = \tau^y Z(z) + (\nu v_z)_z + \nu_H \nabla^2 v, \tag{4.1b}$$

$$u_x + v_y + w_z = 0, \tag{4.1c}$$

$$\rho_t - \frac{\rho_\circ N_b^2 w}{g} = (\kappa \rho)_{zz}, \tag{4.1d}$$

$$p_z = -\rho g, \tag{4.1e}$$

where u, v and w are the zonal, meridional and vertical velocity perturbations, p and ρ are the pressure and density perturbations, f is the Coriolis parameter, g is the gravitational acceleration, $\rho_\circ$ is a reference density taken here as 1023 kgm^{-3}, $N_b(z)$ is the Brünt Väisälä frequency of a

horizontally uniform background stratification, ν and κ are the vertical eddy viscosity and diffusivity coefficients, while ν_H is the horizontal mixing constant (*McCreary et al.* 1996; *Miyama et al.* 2006). Wind stress, with zonal and meridional components τ^x and τ^y, forces the system via a body force with vertical structure $Z(z)$ (*McCreary et al.* 1996; *Miyama et al.* 2006). The forcing is described in Section 4.2.2.

The upper boundary is a flat surface at $z = 0$ and the lower boundary is at $z = -D$, where D is the depth of the ocean floor set to a constant value (*McCreary et al.* 1996; *Miyama et al.* 2006). As in *McCreary et al.* (1996) and *Miyama et al.* (2006), the coefficients ν and κ are assumed to obey $\kappa = \nu = A/N_b^2$, thereby allowing the system of equations (4.1a)−−(4.1e) to be solved using an expansion in vertical normal modes

$$w = \sum_{n=1}^{\mathrm{N}} \int_{-D}^{z} \psi_n(z')dz', \tag{4.2a}$$

$$(u, v, p, \rho) = \sum_{n=1}^{\mathrm{N}} (u_n, v_n, p_n, \rho_n)\psi_n, \tag{4.2b}$$

where N is the summation of an appropriate, finite number of modes ψ_n, which are the eigenfunctions of

$$\left(\frac{\psi_{nz}}{N_b^2}\right)_z = -\frac{1}{c_n^2}\psi_n, \tag{4.3a}$$

$$\psi_{nz}(0) = \psi_{nz}(-D) = 0. \tag{4.3b}$$

Since the barotropic mode is negligible (*Gill* 1984) for near-inertial internal waves, only baroclinic modes (n≥1) are considered. Also note that the definition for p_n now incorporates a factor $\rho_\circ$ (*McCreary et al.* 1996). In this study, N is set to 100, which resolves well all the scales believed

important. The equation for the modal amplitude coefficients u_n, v_n and p_n are then given by

$$u_{nt} - fv_n + p_{nx} = \tau^x \frac{Z_n}{\mathcal{H}_n} - \left(\frac{A}{c_n^2}\right) u_n + \nu_H \nabla^2 u_n, \tag{4.4a}$$

$$v_{nt} + fu_n + p_{ny} = \tau^y \frac{Z_n}{\mathcal{H}_n} - \left(\frac{A}{c_n^2}\right) v_n + \nu_H \nabla^2 v_n, \tag{4.4b}$$

$$u_{nx} + v_{ny} + \frac{1}{c_n^2} p_{nt} = -\left(\frac{A}{c_n^2}\right) p_n. \tag{4.4c}$$

In equations (4.4a)−−(4.4c), c_n is the modal phase speed, $Z_n = \int_{-D}^{0} Z(z)\psi_n(z)dz$ is the projection of the forcing into a given mode and $\mathcal{H}_n = \int_{-D}^{0} \psi_n^2(z)dz$ is the coupling coefficient of the forcing to a mode.

4.2.2 Grid and Forcing

The system of equations (4.4a)−−(4.4c) is solved numerically using finite differences on a staggered Arakawa C-grid (*McCreary et al.* 1996). The computational domain used (denoted by the magenta box in Figure 4.4) is a rectangular basin with horizontal resolution of 1/20° (≈5 km) and depth $D = 5000$ m everywhere.

The domain is geographically bounded, in the sense that the relative flatness of the bottom is broken, in the north by the Indian subcontinent, by the Chagos archipelago in the west and the 90°E ridge in the east. Lateral boundary conditions are taken to be no-slip to walls in the north (10°N) and south (20°S) and cyclic conditions are applied in the east (90°E) and west (70°E), as in a zonal channel. The cyclic boundary conditions are appropriate for our study of near-inertial motions because of their dominant equatorward propagation, which limits both zonal and poleward spreading. A land mask is also used in some simulations to represent Sri Lanka and Chagos shallow areas (e.g., grey contours in Figure 4.11).

The wind forcing evolution during the first two weeks of CINDY is shown in Figures 4.5 and 4.6. As previously shown in Chapter 3, the wind forcing was comprised of a series of trade-wind bursts over a large area (see Figures 3.5 and 4.5−−4.6), associated with the development of an Madden-Julian Oscillation (MJO) event (*Gottschalck et al.* 2013).

As mentioned, wind stress is introduced in the LCS model via a body force with the profile $Z(z)$. Any choice for $Z(z)$ that satisfy the constraint $\int_{-D}^{0} Z(z)dz = 1$, can be used. Our choice of $Z(z)$ is taken from *Miyama et al.* (2006),

$$Z(z) = \frac{2}{|z_1 + z_2|} \begin{cases} 1, & z > z_1 \\ \frac{z-z_2}{z_1-z_2} & z_1 \geq z > z_2 \\ 0, & z_2 \geq z, \end{cases} \tag{4.5}$$

where $z_1 = 47$ m is the depth of the ML and $z_2 = 60$ m. The choice of z_1 and z_2 are tuned to the conditions in both N^2 profiles (Figure 4.2a), they represent an efficient transmission of turbulent mixing down to the base of the ML (at $z = z_1$) and a linear decay towards the center of the transition layer (at $z = z_2$), the depth where N^2 reaches its peak.

Wind stress is calculated using $\tau = \rho_{\text{air}} C_d \left|\mathbf{U_w}\right| \mathbf{U_w}$, where ρ_{air} =1.3 kg m^{-3}, $C_d = 1.2 \times 10^{-3}$ is the drag coefficient and $\mathbf{U_w}$ is the wind velocity. Wind speed and direction are obtained from the CCMP product (Chapter 3) interpolated to the model grid. Forcing is applied throughout the model integration period at a time resolution of 6 hrs. A linear ramp is applied to the wind forcing during the first inertial period.

Some amount of horizontal viscosity ν_H (Table 4.1) is used in all integrations of the LCS model, mostly to ensure numerical stability. Since the integration time is too short for the scales to decrease sufficiently, its dynamic impact is rather small. Under the presence of strong relative vorticity, however, horizontal scales decrease much faster and horizontal viscosity becomes important to keep solutions stable. A value $\nu_H = 150$ m^{2}s^{-1} is enough to ensure the stability of those calculations within the integration period and is the value used by *Miyama et al.* (2006) scaled down to the higher grid resolution. The use of vertical viscosity is detailed in the next section.

The system of equations (4.4a)−−(4.4c) is integrated forward in time using a leap-frog scheme (*McCreary et al.* 1996). The time step Δt is set independently for each mode by the CFL criterion $0.2\Delta x/c_n$, yielding a Δt of 400 s for mode 1 to a maximum of 900 s, truncated for the high modes.

4.2.3 Experiments

To determine the individual and combined contribution of the mechanisms proposed in Section 4.1.2, a set of processes-oriented numerical experiments is conducted by adding, removing, and combining different mechanisms to a base solution. The base solution is obtained by integrating the LCS model with realistic wind forcing over a quiescent ocean, where only the β effect is active, with a stratification profile equal to the one observed during the beginning of the CINDY time series (Profile a in Figure 4.2a), and no vertical viscosity.

All experiments are obtained in the same domain and with the forcing described above. Model integration starts on September 25 and is carried out for 40 days. The focus of this study is in the near-inertial gravity waves generated in the vicinity of the CINDY station (marked by the cross in Figure 4.4) and their propagation in October 2011. The near-inertial band defined for this is study is the $2--6$ days variability, roughly corresponding to the inertial frequency in the latitudinal band from 15°S to 5°S. Throughout the text, we therefore use the term near-inertial to refer to the $2--6$ band variability. These frequencies are isolated in u and v fields outputed every 6 hrs, using a band-pass FIR filter with a Blackman window.

The set of experiments that will be discussed here is listed in Table 4.1. The process-oriented experiments are grouped according to three main properties: Experiments with the prefix VMIX have vertical viscous mixing (damping); experiments with the suffix TL and WTL refer to the ones using N^2 values from Profile a and Profile b, respectively; experiments with a quiescent background ocean are termed with QUIET, while experiments run with relative vorticity from an eddying field are termed EDDY. The base solution is named QUIET_TL, as it has zero relative vorticity ζ, zero vertical viscosity, and uses N^2 Profile a.

Experiments with suffix WTL are model integrations using N^2 Profile b (red curve in Figure 4.2). Profile b is constructed as the average of N profiles observed during the second half of Leg I through Leg II (Figure 4.1), and it represents a weakening in the stratification of the transition layer concomitant with a strengthening and broadening of the thermocline.

The LCS model allows for depth-independent (barotropic), background flow horizontal gradients to be introduced, while still admitting modal solutions. A barotropic relative vorticity (ζ) is

introduced by modifying equations (4.4a) and (4.4b) to be

$$u_{nt} + (U_y - fv_n) + p_{nx} = \tau^x \frac{Z_n}{\mathcal{H}_n} - \left(\frac{A}{c_n^2}\right) u_n + \nu_H \nabla^2 u_n, \tag{4.6a}$$

$$v_{nt} + (V_x + fu_n) + p_{ny} = \tau^y \frac{Z_n}{\mathcal{H}_n} - \left(\frac{A}{c_n^2}\right) v_n + \nu_H \nabla^2 v_n, \tag{4.6b}$$

$$\tag{4.6c}$$

where V_x is the zonal gradient of the meridional background current and U_y is the meridional gradient of the zonal background current.

The V_x and U_y gradients are obtained from the output of the OGCM MERCATOR, presented in Chapter 3. The MERCATOR velocity field is averaged for the cruise period (September 30 to October 25) and the depth-integrated barotropic component of velocity is calculated. The gradients U_y and V_x are then calculated and interpolated onto the LCS model grid. Once interpolated, the gradients are iteratively smoothed in a layer within 5° of the domain boundaries to reduce the strength of the gradients. This procedure was found necessary because the boundary areas are mostly shallow seas, with sharp and intense ζ gradients.

The sensitivity of LCS solutions to the strength of the barotropic vorticity field is examined. Relative vorticity field 1 is the one directly obtained by the procedure described above (Figure 4.7a) and thus represents the weaker ($\approx \mathcal{O}(10^{-2})$ $\mathcal{R}_\circ$, Rossby number), depth-integrated flow field. According to *Danioux et al.* (2008), the vertical modes appear to interact more with the barotropic component of the background geostrophic flow. However, upper ocean relative vorticity is considerably more intense than the depth-integrated vorticity, typically with $\mathcal{R}_\circ$ $\mathcal{O}(10^{-1})$ (e.g. Figure 3.8). To assess the impact of a stronger relative vorticity field in the upper ocean, the barotropic ζ is enhanced by a factor of 3, such that the ζ field is now typically $\mathcal{O}(10^{-1})$ $\mathcal{R}_\circ$ (see Figure 4.7b), with magnitudes comparable to the the near-surface values of MERCATOR (e.g., as shown in Figures 3.8c,d).

Finally, the impact of parameterized vertical viscosity ν is assessed in some of the LCS solutions. The coefficient ν is given in terms of the vertical diffusivity rate coefficient A, and translates into a modal inverse damping timescale in equations (4.6a)−−(4.6b). Figure 4.8 shows this damping

timescale for two values of A, one taken from *Miyama et al.* (2006) ($A = 8.84 \times 10^{-8}$ m^{2}s^{-3}), and one that obeys the observed timescale of NIW decay in the interior estimated from CINDY data ($A = 1.20 \times 10^{-8}$ m^{2}s^{-3}). It is readily seen that the *Miyama et al.* (2006) A leads to very fast decay rates. The target decay timescale, assumed to be $1/e$ fraction of the estimated NIW life cycle in Chapter 3, is approximately 25 days. The use of $A = 1.20 \times 10^{-8}$ m^{2}s^{-3} leads to an average momentum diffusivity of approximately 10^{-4} m^{2}s^{-3} in the upper thermocline using either N^2 Profile a or b, and thus is more in line with observations, while the use of Miyama's A is excessive. Note that, regardless of the choice of A, ν grows to unrealistic values in the deep ocean, where N^2 is small.

At each step, we use the CINDY observations to guide our analysis and assessment of the solutions. WKB scaling and stretching is used in the analysis, and $\bar{N}$, the reference Brunt Vaisala frequency is the same as that of Chapter 3 (see Figure 4.1b). Additional experiments with longer integration times (starting in early September and run for 90 days), as well as experiments where the wind forcing is turned off after three inertial periods, were found to support the results and conclusions presented here.

4.3 Results

In this section, we report results from our various experiments, first focusing on the quiescent ocean solutions to describe the impact of changing the model's stratification profile, and then impact of including relative vorticity is described and assessed next. Note that not all experiments shown in Table 4.1 are presented and discussed thoroughly.

4.3.1 Quiescent Ocean Solutions

The base solution

The base solution demonstrates the effects of β and the horizontal structure of the wind field on the near-inertial motions. It will be described and compared to the CINDY observations in detail, to demonstrate the ability of the LCS model to reproduce, at least qualitatively, several aspects of

the observed near-inertial response.

The model horizontal near-inertial kinetic energy density (hereafter NIKE) in the upper ocean at the location of the CINDY station (8°S 80.5°E) is shown in Figure 4.9. The ML NIKE rises and peaks at the same time as the observations, albeit at reduced levels. The weak peak is likely produced by the use of 6 hourly "block" forcing, which reduces the efficiency of the work done by the wind on the inertial currents. The decay phase of the ML NIKE initially occurs at a similar rate as observed. In this experiment, the decay is driven by both the negative wind work and the radiation of NIWs. A second bump in ML NIKE around Oct 14, absent in the observations, may result from the tendency for inertial energy in the TL to return to the ML, as noted by *Gill* (1984) in his solutions. This return likely occurs because of the absent or weak damping (no vertical viscosity and turbulent dissipation) in the LCS model. The second peak in ML NIKE towards the end of the simulation is caused by another wind-forcing event, this time located near 6°S.

The observed ML IOs are found to be fairly well represented by the quiescent base solution. As expected from quiescent background conditions, the model inertial currents oscillate very near the local inertial frequency (Figure 4.10a). Moreover, the inertial current ellipse has a tilt and eccentricity qualitatively very similar to the observations. This good agreement suggests that the observed tilt and some of its eccentricity (model eccentricity is significantly less than observed) may be a result of the direct wind forcing, rather than of the existence of a background circulation as hypothesized in Chapter 3.

The ratio of the ellipses major to minor axes of the ellipse is 1.07, less than the observed. Interestingly, the tilt of the ML IO is perpendicular to the axis of maximum wind variability, i.e. the trade wind direction, and is parallel to the estimated propagation direction of the convective anomaly that may have triggered the wind bursts (see Figures 4.5 and 4.6). Figure 4.11 indicates a large-scale pattern for the ML NIKE, which has a greater zonal than meridional extent, and that the CINDY station was not located in the region of maximum NIKE.

In the base solution, ML NIKE is lost primarily to NIW downward radiation. Consequently, similar to the observations, NIKE below the ML is dominated by perturbations with upward phase propagation (e.g., Figure 4.14). The appearance of the TL NIKE peak occurs within 3 days of the

peak in the ML, very similar to the observed behavior (green lines in Figure 4.9a). The magnitude of TL energy, however, is far larger than observed. The observations show that TL WKB-scaled energy density is around 15% of that in the ML, whereas the LCS shows similar magnitudes in both layers, in fact, the unscaled TL NIKE is much higher than of the ML. This accumulation of energy was previously noted by *Levine and Zervakis* (1995). It is worth pointing out that the level of WKB-scaled NIKE in the model TL is similar to the observed, and that the low fraction relative to the ML energy is largely due to its weaker energy levels. In the LCS framework, this may be achieved because of the increased amplitudes in $\psi_n(z)$, for the majority of modes within the TL (Figure 4.2).

Unlike the CINDY observations though, the depth penetration of NIKE in the LCS model base solution is much reduced. Figures 4.9a show that less than a third of the TL WKB scaled NIKE propagates down to 120 m, whereas the observations show vigorous energy propagation down to those depths and into the thermocline. In general, NIKE appears vertically "trapped" in the vicinity of the TL, c.f. bottom panel in Figure 4.15a which shows the maximum of NIKE over the first 30 days of the integration period for the upper ocean along 80.5°E. The TL NIKE is also horizontally confined to the generation region, c.f the various maps for TL and thermocline NIKE in Figures 4.12 and 4.13. The pattern of maximum NIKE also shows a slow equatorward propagation of energy, in agreement with the tilt in NIW phases in the y-z plane (Figure 4.16).

The snapshots in Figure 4.16 show the reduction in meridional scale with time due to the β effect (*D'Asaro* 1989), i.e. the downward and equatorward propagation of NIWs. The weak levels of NIKE below the TL suggest that the β mechanism, although efficient at flushing energy from the ML into the interior, is not sufficient to promote the range of depth penetration observed during CINDY2011. This deficiency is further discussed below.

Away from the generation region (12°S−−5°S), most of the NIKE relative maxima in bottom panel of Figure 4.15a are produced by the remote propagation of low-mode, near-inertial oscillations from the generation site, rather than locally, at least prior to the onset of the second forcing event. This property is evident, particularly at the equator, by examining a time series of NIKE partitioned by mode, as in Figure 4.17b, which shows the arrival times at the equator of each mode of near-

inertial oscillation. Furthermore, despite low modes having crossed the equator, as shown by the Hovmoeller plot in Figure 4.18, the level of NIKE in the main thermocline within these regions is insignificant.

Attention is now turned to the vertical scales within the generation region. An inspection of the model's near-inertial current anomalies with upward phase propagation (Figure 4.14c,d), taken from the CINDY station location, indicates a vertical wavelength of 240 stretched meters (sm) in the TL for the first inertial period (IP) after the ML energy peak, using the method of *Cuypers et al.* (2013), in excellent agreement with the observational estimate (c.f. WPI in Table 3.1 of Chapter 3). As seen by the increase in the slanting of the phase lines, the vertical wavelength decreases with time to about 140 sm after roughly three IPs. This decrease of NIW vertical scale is in agreement with a "trapped" wave pattern due to stratification. Within the thermocline, at the first IP after the forcing, NIW vertical scales increase abruptly relative to the TL scales (as seen by the phase lines in Figure 4.14c,d), with WKB-corrected vertical wavelengths of 300−−600 sm. A decreasing trend is noted as well, and 200−−250 sm vertical wavelengths are reached in 3−−4 IP, with the arrival of NIW packets. In the deep ocean, well below the thermocline, only a weak low mode near-inertial signal is detected and estimating its wavenumber using vertical phase differences is inaccurate due to noisy. The CINDY observations indicate that a 140-m vertical wavelength is achieved in the thermocline in about 3 IP after the forcing episode, in reasonable agreement with the LCS model.

The development of these NIW scales is well explained by the local modal composition of the solutions. Figure 4.17a shows NIKE partition by modes at 8°S, 80.5°E. Low modes, particularly mode 4, which has a wavelength of ≈200 m in the TL and 600 m below the thermocline, dominate the vertical spectrum early, with higher modes becoming increasingly more energetic in time, thereby producing the small vertical scales in the later part of the solution, as well as the downward NIW packets.

The energy-density frequency spectrum for anomalies with upward phase propagation is shown as a function of depth in Figure 4.19a. Like the observations, the LCS model spectra show an increase in peak frequency with depth. Because of the lack of relative vorticity, the model NIWs

have a super-inertial frequency of 1.06 $f_\circ$ in the TL, instead of the observed sub-inertial peak frequency (*Kunze* 1985). The increase in frequency with depth signals the arrival of groups of NIWs generated polewards of 8°S. The tilt of downward NIW ellipses (Figures 4.19b,c,d) indicates that NIWs are propagating due north in the TL, with waves veering NNW with depth as the frequency increases, in good agreement with observations. It is unclear to what degree the ratio of major to minor axis ($|r|$) estimated from the FFT spectrum is accurate, but the method consistently indicates ratios above the wave frequency. In theory NIWs have the property that the ratio $\omega/f_\circ$ is equal to $|r|$, therefore, this result is quite unexpected for free NIW propagating in a quiescent ocean, suggesting some effect of the horizontal structure of the wind forcing on the NIWs in the TL.

To understand the patterns described in the solutions obtained thus far, the global vertical modes and the horizontal spectrum are examined. Again, the idea is that the vertical scale selection arises from the horizontal scales induced in the base solution by the wind forcing and the β effect. The evolution of the zonal and meridional wavenumber spectra over the first 5 IPs after the NIKE peak in the ML (Oct 6) are shown by the colored lines in Figures 4.21 and 4.22, respectively. The zonal spectrum is red and is nearly an order magnitude weaker than the meridional spectrum, therefore, the LCS NIW u and v are oriented east-west throughout the integration period and therefore, propagate north-south. The appearance of shorter meridional scales with time is evident at all depths (Figure 4.22), as expected from NIWs propagating in a β plane (*Gill* 1984; *D'Asaro* 1989). The dominant meridional scale in the ML for the first IP is approximately 560 km, substantially shorter than what would be predicted by the β effect ($f_\circ/\beta$; shown by the magenta dotted line at ≈900 km) for an infinitely large initial oscillation, suggesting that the wind forcing horizontal structure is responsible for that particular initial scale. At a given time, the meridional scale decreases with depth (e.g. comparing Figures 4.22b,d), due to the propagation of higher frequency NIWs. On the other hand, it should be noted that the wavelengths estimated from the observations are 100−−200 km (hereafter simply referred as "observed"), and that these scales are only achieved after 5 IPs, far too slowly to represent the observations.

Figure 4.20a displays the fraction of NIKE contained in each mode integrated over the generation

region (denoted by the magenta box in Figure 4.11). This pseudo-vertical-wavenumber spectrum is quite different than that produced by projection of the wind forcing onto the vertical modes alone (red line in Figure 4.20a), with the dominant mode decreasing from 2 to 4 and larger contributions of higher modes although still essentially dominated by the lower 5 modes. It is assumed here that this deviation is a consequence of the smaller horizontal scales induced by the spatial structure of winds and the β effect, as well as by the generation of the downward-propagating NIW packets. The modal dispersion relation,

$$\omega_n^2 = f^2 + c_n^2 k_H^2, \tag{4.1}$$

implies that for k_H of around 500−−600 km, modes 4 and 5 oscillate with frequency around 1.1 $f_\circ$, as opposed to mode 2 which oscillates frequencies well above 1.5 $f_\circ$ (Table 4.2), thus matching well with the peak frequency in the TL. This topic of horizontal initial scale controlling the vertical is revisited in Section 4.4. Finally, Figure 4.20a also illustrates that no single mode alone is likely to explain the observations, e.g. as attempted by *Alford and Gregg* (2001).

In essence, the LCS model base solution is qualitatively similar to the observations in a number of aspects, including the rate of ML NIKE transfer to the interior, frequency spectra and wave direction, vertical scales in the TL. However, the NIKE is trapped in the TL during the integration period, which is at odds with the observed vigorous downward energy propagation. This confinement tendency had already been noted by *Gill* (1984) and later on by *Levine and Zervakis* (1995). Furthermore, NIW vertical scales in the thermocline are found to be somewhat longer than observed. Horizontal scales are also too large and decrease far too slowly, when compared to the 100-200 km wavelengths "observed" immediately after wave generation.

Vertical energy penetration is achieved in the LCS by de-phasing of oscillations of different modes (*Gill* 1984), hence it is limited by two main factors: First, the more energetic faster low modes, which essentially describe ML inertial oscillations leaving the region, while the remaining high modes, which are slower and de-correlate slowly, do not have as much energy. Second, all modes have a vertical structure with larger amplitudes in the TL by as much as 2 to 3 times more than in the thermocline (Figure 4.2b), as a direct consequence of the energy scaling with N.

The β effect is most effective for the low modes (*Balmforth and Young* 1999), which in the

base solution turn out to be overwhelmingly more energetic, but significant contributions from higher modes are necessary to provide energy penetration into the thermocline, within the vicinity of the generation region. It is clear that the β effect alone is insufficient to reproduce the small horizontal scales "observed" soon after the forcing, and hence promote the continuous downward energy radiation into the thermocline. The β effect is simply responsible for the equatorwards propagation of NIWs and the transfer of ML NIKE to the the TL. An additional mechanism that immediately reduces horizontal scales is necessary in order to explain the CINDY2011 observations.

Role of Stratification

The impact of N^2 Profile b on LCS solutions for a quiescent ocean (QUIET_WTL) is examined by looking at deviations from the base solution detailed in Section 4.3.1. The questions to answer are: (1) Does using Profile b promote smaller initial horizontal scales or a faster increase in horizontal wavenumbers? (2) Does using Profile b promote depth penetration of NIKE? (3) In turn, does it reduces the vertical scale of NIWs in the thermocline?

From Figures 4.3c and 4.2b one can expect the nature of the impact: Wind forcing tends to project more on higher modes on Profile b than on Profile a, and mode 1 rather than mode 2 appears to be the dominant response. Modal structure has also changed considerably and larger amplitudes are noted in the thermocline, consistent with WKB scaling. This is indeed the case, since more energy in found in higher modes for the QUIET_WTL case, relative to the base solution (e.g. 4.20b). These changes in modal amplitude and structure, are rooted in the physics though, driven in this case by the change in upper ocean stratification between Profiles a and b. For instance, the experiment QUIET_WTL produces substantially more NIKE in the ML and TL than in the base solution, as is evident by comparing Figures 4.9a and 4.9b. This increase could presumably occur because of a more efficient wind work. The ML NIKE decay appears to be slightly slower ($1--2$ days), in accordance with the increased high mode content.

Why the upper ocean has more NIKE in this case, when the wind forcing is the same? The answer may be related to higher mode characteristics of this solution and the increased importance of modes 1 and 2 (c.f. Figure 4.20b). These lowest modes have largest amplitudes in the ML (Figure

4.2b), hence increasing the energy of currents therein. According to *Gill* (1984) though, the low modes decouple much faster than the high modes and so are efficient in transferring NIKE out of the ML. As a direct consequence of the elevated high-mode contributions, NIKE is transferred to the TL slightly slower than in the base solution, wherein the vertical wavelength on Oct 10 (about 1 IP after the ML NIKE peak) is estimated at 170 sm, well within the bounds of the observational estimates for WPI in Chapter 3, but significantly smaller than the 240 sm of the base solution. Although it decreases to 100 m in about 4 IPs, at a slower rate than the base solution, the persistent smaller scales in the first IP for the QUIET_WTL experiment imply energy is more easily reflected at the base of the ML and within the TL, and so is potentially available to be returned upwards by waves with downward phase propagation, as hypothesized by *Gill* (1984).

In the thermocline, the NIW packets in QUIET_WTL (Figure 4.23) have an estimated vertical wavelength 180−−300 sm, very similar to the scales of NIW packets in the base solution. As in the base solution, the 100 sm scales "observed" in thermocline (e.g., WPIII 3.1, Chapter 3) do not occur, despite the increased wind projection onto the higher modes.

No significant alteration in the frequency spectrum and wave-propagation direction was detected (spectrum not shown). The frequency and ellipse characteristics of the ML inertial oscillations are very similar as well. Aside from the enhanced energy levels described above, the horizontal distribution of NIKE remains virtually the same as in the base solution (maps not shown), at all depths, and little to no change in spatial structure is evident in either the zonal or the meridional spectrum (also not shown)

Significant alterations on the pattern of NIKE depth penetration do occur, however. Use of N^2 Profile *b* leads to NIW energy being mostly confined between the TL and the thermocline N^2 maximum at around 95 m depth, this happens, in part, as a response to a shift to a deeper thermocline in Profile *b*. In this depth interval, there is more NIKE than in QUIET_TL (e.g. compare upper panels of Figure 4.15a,b). Proportionally, though, there is less NIKE below the TL in QUIET_WTL than in QUIET_TL and, therefore, there is a slight decrease in the depth penetration of NIKE, as shown by the WKB-scaled NIKE in the bottom panel of Figure 4.15b when compared to the bottom panel of 4.15a.

Returning to the questions asked in the beginning of the section, this experiment has found: (1) no discernible impact on the horizontal wavenumber spectrum, and the horizontal scales remain larger than "observed", (2) a small reduction in the depth penetration of NIKE, with energy now largely confined between the TL and thermocline top, (3) a reduction in the vertical wavelengths in the TL and top of the thermocline, and much like the base solution, the N^2 Profile b, does not produce NIW packets with the "observed" vertical wavelengths in the thermocline. Results (2) and (3) may be explained, in terms of the LCS model framework, by the increase in the wind forcing projection onto the higher modes (Figure 4.3c, red curve).

Role of Damping

We note in the base solution and in the Profile b solution there is excessive energy accumulation in the TL. This behavior has been previously reported by *Gill* (1984) and *Levine and Zervakis* (1995) and is quite expected from a WKB scaling point of view. In previous similar work (*Levine and Zervakis* 1995), vertical viscosity was found to favor the formation of near-inertial energy beams, facilitating the propagation of near-inertial energy into the thermocline. As shown by the CINDY2011 observations, elevated turbulent mixing and dissipation rates take place within the TL due to the strong near-inertial shear that develops therein following the vertical propagation of NIWs from the base of the ML. In the LCS model, these scales are produced by energetic high modes.

The vertical viscosity used in the LCS model (Figure 4.8) leads to preferential high mode energy damping, as confirmed in energy partition by modes shown in Figures 4.20c,d (compared to 4.20a,b). The first obvious consequence is an overall reduction in the total amount of NIKE in the system, from the ML down to the deep ocean (c.f. Figures 4.9c and 4.9d), relative to undamped solutions. A second effect can be seen in Figure 4.24c,d, where there is a noted decrease in the growth of the vertical wavenumber over time, in relation to the inviscid solution. This decrease results in a reduction of the energy trapping in the TL. Inclusion of vertical viscosity does not appear to favor the depth penetration of NIKE, rather, less NIKE penetrates into the thermocline, at least relative to the quiescent solutions. Yet, more NIKE penetrates into the thermocline relative

to the TL, suggesting that indeed some amount of viscosity is necessary to favor beam formation, as hypothesized by *Levine and Zervakis* (1995). Similar to what happened with the QUIET_WTL experiment, the alterations in the fraction of energy contained by the higher mode does not lead to any impacts that are detected on the frequency and horizontal wavenumber spectra (not shown), and the vertical scales NIW packet. Because these impacts are rather minute, our focus remains on solutions with no vertical viscosity.

4.3.2 Eddying Ocean Solutions

In this section, results from experiments that include relative vorticity are presented and discussed. To estimate the impact of relative vorticity on NIW dynamics, experiments EDDY1_TL ($\zeta \approx \mathcal{O}(10^{-2})\ \mathcal{R}_\circ$), EDDY2_TL ($\zeta \approx \mathcal{O}(10^{-1})\ \mathcal{R}_\circ$) and EDDY2_WTL are examined and compared to the base solution. Our goal is to assess whether including vorticity allows: (1) smaller initial horizontal scales and/or a faster increase in horizontal wavenumbers; (2) increased depth penetration of NIKE; (3) a reduction in the vertical scale of NIWs propagating within the thermocline.

Weak ζ vs Strong ζ

The impact of background relative vorticity in the LCS solutions can be seen in Figures 4.25−−4.30, which show NIKE contour maps overlaying the relative vorticity field used in experiments EDDY1_TL and EDDY2_WTL. High NIKE tends to concentrate in anticyclones (ACs), as previously noted by other authors (*Kunze* 1985; *Klein and Smith* 2001). This behavior is more pronounced in the TL and thermocline than in the ML (e.g. contrast Figures 4.28 and 4.29), suggesting that, in the ML, the horizontal structure of the wind forcing dominates over background relative vorticity. As the magnitude of relative vorticity increases in EDDY2_TL relative to EDDY1_TL, so does the NIKE within the ACs, prompting the appearance of more well-defined high energy density pockets within the various anticyclonic features (e.g. compare Figures 4.26 and 4.29). As indicated by the time evolution of NIKE, for instance within the TL, this trapping effect is felt even during the earliest stages of wave generation (Figures 4.26a and 4.29a), particularly if the relative vorticity is strong. These results demonstrate that a ζ field of $\mathcal{R}_\circ$ $\mathcal{O}(10^{-1})$, typically associated with upper ocean

eddies, produces a significantly more inhomogeneous horizontal distribution of NIKE than a ζ field of $\mathcal{R}_\circ$ $\mathcal{O}(10^{-2})$ which is associated with the barotropic component.

The localized effects on NIW characteristics can be quantified by examining depth-time series of near-inertial currents from two locations, within an AC (8.65°S, 78°E) and within a region of cyclonic vorticity (8°S, 80.5°E), such as those shown in Figures 4.32 and 4.31 for EDDY1_TL and Figures 4.34 and 4.33 for EDDY2_TL. There is a 15% and 40% reduction for the weak and strong ζ cases, in the energy of near-inertial signals below the ML at the CINDY station, respectively, which experiences cyclonic vorticity in these experiments. In the AC region, which in the QUIET_TL case corresponds to the ML NIKE maximum in Figure 4.11a, there is a 20% and a 50% increase for EDDY1_TL and EDDY2_TL, respectively.

The peak amplitude of ML inertial currents is virtually unaltered in the AC, while it is significantly reduced in the cyclone (CINDY station) where it also decays faster when ζ is $\mathcal{O}(10^{-1})$ $\mathcal{R}_\circ$. However, in the AC, although NIKE appears to initially decay faster (in the EDDY2_TL case), ML inertial oscillations with above background strength persist for much longer (noticeable in both EDDY1_TL and EDDY2_TL). The persistence of ML inertial oscillations occurs because of a localized increase in the contribution of the higher modes (Figures 4.41b and 4.42b). This result further illustrates that the strong, initial, ML inertial currents are essentially represented by the low modes, while the interior solutions are described by high modes, c.f. Figures 4.41 and 4.42.

In terms of the frequency spectrum, no clear impact on the NIWs dominant time scale could be detected at the CINDY station for the weak ζ case (EDDY1_TL), i.e. there is no blue shift of peak frequencies (compare Figures 4.19a and 4.35a). No effects were detected on the near-inertial ellipse orientation (Figures 4.35b,c,d) either. In the region of strong anticyclonic vorticity, although the NIW peaks remain at same frequency as the QUIET_TL, there is a noticeable spreading of energy towards lower frequencies (Figure 4.36a). When the vorticity is enhanced (EDDY2_TL), the blue and red shifts of NIW frequencies are evident (Figures 4.37a and 4.38a). In the AC, the spectral peak is clearly reddened and is dominated by a sub-inertial frequency (note $f_\circ$ is the frequency at 8°S in all plots) when compared to the base solution, whereas the opposite occurs in the cyclone. There are also marked differences in the orientation of ellipses, indicating different induced patterns

of wave propagation, relative to the base solution, c.f., Figures 4.19b,d vs 4.37b,d and Figures 4.36d, 4.38d. It should be noted that anticyclonic vorticity is observed to dominate the upper ocean during the CINDY cruise period, at least in terms of area, and therefore, the NIWs modeled at 8.65°S may be more relevant for direct comparisons to various "observed" NIW properties.

The increase in the contribution of higher modes within anticyclonic features, particularly when ζ is relatively strong, promotes a decrease in the vertical scale of the downward NIW packets in the TL. In contrast, the expulsion of high-mode, near-inertial oscillations from cyclonic features (*Klein and Smith* 2001) promotes a localized increase in the vertical scale in the surviving NIW packets within the TL. For instance, at 8°S the estimated vertical wavelength in the TL, after 1 IP, is 270 sm for EDDY1_TL and 400 sm for EDDY2_TL, as opposed to $\approx$ 250 sm for QUIET_TL. Beyond the first 2 IPs, as time increases and the NIW energy quickly decays to background levels, a rapid decrease of vertical scales is noted in these solutions relative to the quiescent case. At 8.65°S, the TL vertical wavelengths after 1 IP are 210 sm and 190 sm for EDDY1_TL and EDDY2_TL, respectively, versus $\approx$ 300 sm for QUIET_TL. In the thermocline, there are no significant differences from the base solution in the vertical wavelength of NIW packets, in either the cyclone or the AC. Within the AC at 8.65°S, however, energy at a 200 sm scale is noted in association with a wave packet 1 IP after the forcing, indicating a quicker radiation time to these depths relative to the base solution.

Attention is now turned to the depth penetration of NIKE into the thermocline. As indicated by the contours of NIKE in Figures 4.27 and 4.30, several localized high energy regions occur at thermocline levels, whereas low energy is found at these depth in the quiescent solutions. Figure 4.40 (bottom panels), clearly shows that NIKE penetrates to greater depths in beams, with two highly evident NIW beams. The focus of this discussion and comparisons is the most energetic beam originating from the TL from 9-8°S. The depth penetration of NIKE is increased in regions of anticyclonic vorticity only, while the depth penetration is reduced in cyclonic regions, as shown by contrasting Figures 4.40a,b and 4.39a,b. The downward radiation of NIWs is favored along 78°E because of stronger input of inertial energy by the wind and the presence of several ACs on this transect. In contrast, downward radiation is suppressed along 80.5°E because of the lack of

anticyclonic vorticity. Furthermore, a comparison of Figures 4.40a and 4.40b also demonstrates that as vorticity increases, so does the depth penetration of NIKE. As ζ strengthens to EDDY1_TL and then to EDDY2_TL, the NIKE density at 120−−180 m increases 2 to 6 times above the energy density in the base solution, respectively. On the other hand, it should be stressed that realistic levels of energy in the thermocline, i.e. > 8 Jm^{-3} (roughly rms velocities of 0.1 ms^{-1} at 120−−200 m), do not occur anywhere in either of these experiments.

While the local frequency content within the LCS model framework is a consequence of Kunze's shift ($\omega = f + .5\zeta$), these localized concentrations of NIKE, reductions in TL vertical scales and increased depth penetration in the AC, are produced by the high modes, see Figures 4.41b and 4.42b, for EDDY1_TL and EDDY2_TL, respectively. According to *Danioux et al.* (2008), the high modes are more susceptible to interact with ζ because of their weaker dispersivity character, a parameter directly related to the mode's Rossby radius of deformation. The theory discussed by these authors suggests that, over time, the NIKE horizontal distribution of a given mode approaches the Laplacian of ζ, truncated to retain scales larger than the distance near-inertial energy is dispersed. A close inspection of Figures 4.29 and 4.30 indicates that NIKE tends to concentrate over the anticyclonic regions where the gradient of ζ is more intense, rather than mapping directly with the contours of ζ, or its Laplacian. This property has been previously noted in drifter data by *Van Meurs* (1998).

Zonal wavenumber spectra are shown in Figures 4.43 and 4.45 for the EDDY1_TL and EDDY2_TL experiments, respectively. The horizontal scales of NIWs below the ML are readily impacted by the presence of relative vorticity. The effects are more evident in the zonal spectra than in the meridional spectra (Figures 4.44 and 4.46), where a prominent peak develops at around 300 km wavelength, in contrast to the base solution, where only large scales appear (Figure 4.22). This 300-km scale is induced as early as the time of the peak in ML NIKE, and is the dominant scale below 1000 km in either the weak-ζ or the strong-ζ case, though in the strong-ζ case the shorter scales are much more energetic. This property suggests that it is a length scale set independently from the magnitude of ζ, i.e., induced by the horizontal structure of ζ. The zonal structure of ML inertial motions do not appear to feel the impact of relative vorticity as much, or at all, presumably because they are governed by the dispersive lower modes.

Although significantly more energy is found at shorter scales, the meridional wavenumber spectra (Figures 4.44 and 4.46) do not show any prominent peaks at shorter wavelengths than found in the base solution, despite showing a subtle spreading of energy towards higher wavenumbers. The time evolution of the meridional spectrum, shown by the different colored lines in Figures 4.44 and 4.46, does not indicate any acceleration in the rate of wavenumber increase.

As proposed by *D'Asaro* (1989), one could interpret the zonal and meridional gradients of f_{eff} as the β effect, inducing a time-dependent wavenumber. The inhomogeneity of f_{eff} gradients associated with the mesoscale variability used in these experiments, could balance out over the domain, thus diminishing its global impact and providing a mechanism to explain the lack of scale reduction in the model. In this sense, the 300 km peak in the zonal spectrum is a scale associated with the high-mode NIWs preferentially trapped within a few strong ACs within the domain, while the meridional spectra is dominated by the structure of the wind forcing and the β-induced dispersion.

Nonetheless, the horizontal scales of NIWs below the ML do not approach those estimated from the observations, at least not in a suitable time frame. The plane wave method used in Chapter 3 indicates $100--200$ km wavelengths within $1--3$ IPs after the forcing. In the LCS solutions these scales appear after 4 IPs. A faster increase in wavenumber is required and possible candidates are discussed in Section 4.4.

In summary, a relative vorticity field is found to enhance the depth penetration of NIKE, and promote the reduction of vertical and horizontal scales. These impacts are localized to regions of strong AC vorticity, in accordance with previous studies (*Kunze* 1985; *Van Meurs* 1998; *Danioux et al.* 2008), and are largely associated with NIWs below the ML, which are overwhelmingly governed by the evolution of higher modes. Comparing EDDY1_TL and EDDY2_TL indicates that these results are somewhat dependent on the intensity of the vorticity fields, with more high mode energy located at sites where AC relative vorticity is stronger. Nevertheless, experiment EDDY2_TL with $\mathcal{O}(10^{-1})$ $\mathcal{R}_\circ$ did not produce the vigorous downward radiation of NIW energy observed during CINDY2011, or as the estimated decrease in vertical and horizontal scales below the TL.

Enhanced ζ and Weak TL

The CINDY observations show that the NIW energy at depth also coincides with an increase in stratification in the thermocline. The results from the QUIET_WTL experiment indicate that substantially more energy is contained in higher modes using N^2 profile b. LCS model solutions that include both $\mathcal{O}(10^{-1})$ $\mathcal{R}_\circ$ ζ with this increase in thermocline stratification are evaluated here. These conditions are believed to be the background conditions during the second half of the CINDY2011 measurements.

Results from the EDDY2_WTL experiment are found to be very similar, qualitatively, to the EDDY2_TL experiment, particularly in terms of its horizontal scales. For instance, the zonal spectrum (not shown) shows a peak at 300 km as well, albeit at much higher energy levels than in the previous case. No significant departures from previous solutions are also found in the frequency spectra at the locations discussed above.

The depth penetration of NIW energy, though, is significantly, albeit modestly increased relative to EDDY2_TL, at least for a few NIW beams (Figure 4.47 bottom panel). Again, attention is drawn to the NIW beam between $9--8^\circ$ in Figure 4.47 bottom panel. Along this beam, relatively high NIKE > 6.5 Jm^{-3} (roughly rms velocities of 0.08 ms^{-1} at $120--200$ m) is noted around 120 m or so, within less than half a degree of its origin point. NIW vertical scales in the thermocline also decrease slightly in relation to the EDDY2_TL case , but they still remain longer than the observed scale at these depths. In relation to the QUIET_WTL experiment, the TL vertical scale is also found to be substantially reduced. The increase in NIKE depth penetration and decrease in vertical scales appear to be, once more, a consequence of the local increase in high-mode energy (Figure 4.48a).

Despite not reproducing the fast reduction in horizontal scales and propagation of NIWs with 100 sm vertical wavelengths, this experiment, unlike any of its predecessors, was able to produce near-inertial currents at 120 m depth with amplitude very close to the observations. This success suggests that the combination of weak stratification in the TL and stronger stratification in thermocline with background anticyclonic vorticity could have played an important role in promoting the observed depth penetration of NIW packets during CINDY2011.

4.4 Conclusions and Discussion

Based on expansions onto vertical normal modes, we conducted a process oriented study to determine the impacts of background circulation and stratification on the dynamics of NIWs forced by large-scale winds over the tropical Indian Ocean. By solving for the response due to a finite set of such modes, NIW solutions were obtained numerically with the LCS model (*McCreary* 1981; *Miyama et al.* 2006) in a domain encompassing the central tropical Indian Ocean and forced by realistic winds. Several aspects of the observed behavior of NIWs are, at least qualitatively, reproduced by the model, including the generation of realistic ML inertial oscillations and their decay by propagation into the interior as downward NIW packets. While the ML inertial currents are well explained by the lowest modes (1−−5), which have their (Figure 4.2b) largest amplitudes in the mixed layer and transition layer, the upward-phase-propagating NIW packets (downward energy propagation) require the contribution of higher modes (6−−20), which have their largest amplitudes in the transition layer and thermocline. In an ocean bereft of mesoscale relative vorticity, taken as the baseline solution for this study, the downward NIW packets are confined to the uppermost stratified layer, the transition layer, and do not penetrate well in the thermocline, as is observed. These NIWs have initial horizontal scales of about 400 km, and vertical scales below the transition layer that are substantially longer than estimated in Chapter 3. As such, the three specific questions put forward in Section 4.1.2 and their respective answers are:

- How does the background stratification impact the vertical scale of NIWs and the depth penetration? Can the increase in stratification within the thermocline account for the observed downward near-inertial energy radiation?

  The shape of the vertical background stratification is key to select which modes are preferentially excited by the wind and where the largest wave amplitudes are found, according to WKB scaling. By itself, the increase in thermocline stratification cannot account for the observed characteristics of downward NIW radiation. Although it clearly promotes a reduction of NIW vertical scales, due to a tighter coupling of wind forcing to higher modes, these NIW packets are still largely confined to the TL and thermocline top and do not penetrate below 100 m.

- How does the introduction of a background relative vorticity affect the horizontal and vertical scales of the NIWs and the depth penetration of NIW energy?

  The addition of barotropic relative vorticity from an OGCM mesoscale eddying field favors localized increases in depth penetration of NIKE where anticyclonic vorticity is present. As a consequence, high NIKE at all levels below the ML mapped well to regions of anticyclonic vorticity. The efficiency of this trapping mechanism is proportional to the magnitude of the vorticity, such that when relative vorticity has rms values $\mathcal{O}(10^{-1})$ $\mathcal{R}_\circ$ the NIKE at depth increased six times relative to the quiescent case. The impact on the horizontal-scale evolution was less than expected, although inclusion of a mesoscale vorticity field did produce energy at significantly smaller horizontal scales than the wind field alone case, particularly in the zonal direction.

- What is the character of the NIWs when these processes combine?

  A significant enhancement of the depth penetration of NIW energy is found in relation to either process acting alone. Levels of NIKE in the thermocline very close to the observed were obtained in the vicinity of a strong anticyclone. The vertical scale of NIW packets in the thermocline was not significantly altered in relation to previous experiments and their horizontal scales remained longer than those estimated from the CINDY2011 observations.

Although the depth penetration of near-inertial wave energy was substantially increased in the experiment where a strongly stratified thermocline and weak transition layer was combined with strong mesoscale relative vorticity, none of the experiments conducted here reproduced the estimated spatial characteristics of the downward-radiating NIW packets observed during CINDY2011, neither horizontal nor vertical, despite the large number of modes solved and adequate horizontal resolution. Particularly, none of the mechanism investigated here seem to produce 100−−200 km initial wavelengths estimated from the observations using the plane-wave method (Chapter 3).

Assuming that these estimates are correct, there are several limitations of model employed here, that might account for the lack of small horizontal scales. The ray-tracing analysis used in Chapter 3 suggested that Doppler shifting by the background flow played an important role in the refraction

patterns of the observed NIWs. Because the wave packets near the surface are estimated to be propagating against the background currents, they behave more super-inertially, which favors both depth penetration of wave energy and shorter horizontal wavelengths. The impact of a Doppler shift, therefore, should be investigated in future studies, as it could be an important missing mechanism in this process. To simulate this effect, the LCS would need to include an advection term by a depth-independent background current $\mathbf{U}$.

The inefficiency of the relative vorticity may also be an artifact of the particular choice of mesoscale field used in the LCS model. Besides being depth independent (a requirement of the model dynamics), the mesoscale vorticity is a time-averaged, frozen field for a certain period of time (in this case during the cruise period), which may eliminate smaller-scale features. Future studies should investigate the sensitivity of the solutions to the use of instantaneous relative vorticity fields. For instance, a realistic, time variant field could have energetic $\mathcal{O}(1)$ $\mathcal{R}_\circ$ submesoscale features that could induce the "missing" shorter scales.

Furthermore, the CINDY2011 observations show high NIW energy propagating down to 200 m. Even the combined experiment does not reproduce this magnitude at this deep in the water column. Again, this lack may result from an inaccurate relative vorticity field and/or the lack of Doppler shifting on the simulated NIWs. It may also imply that the observed energy was generated by a previous forcing event.

As shown by these results, there are important sensitivities of the NIW energy depth penetration to the vertical distribution of stratification. Of particular interest, is the fact that the change in stratification occurs after wave generation, rather than during generation, as is done in the LCS model used here, such that there are, in reality, both horizontal and vertical refraction of the NIW packets. A specific limitation of the LCS model is that it cannot account for these lateral variations in the stratification. When also considering that the stratification of N^2 Profile b does not correspond directly to the one observed concomitant with the thermocline wave packets in the CINDY data, care must be taken in making definite assessments of the model skill in representing these waves. This limitations indicate that the major results found here should be further verified with primitive equation simulations.

Nonetheless, a robust result is that, in all cases investigated here, the vast majority of the NIKE is confined within the generation region ($12° - -8°$S) over the period studied. Although several low modes leave the generation region (e.g. Figure 4.18), they carry a small fraction of the energy that is put by the wind into the near-inertial motions, at most only about 15% of the peak mixed layer NIKE (as estimated from lower panel of Figure 4.15a), in agreement with the recent work of *Simmons and Alford* (2012). This result implies that they may contribute little to the NIKE in other regions. However, idealized results of burst forcing show that this low mode near-inertial energy collects in the turning latitude, contributing to the background near-inertial energy level therein (*Fu* 1981).

4 References

Alford, M. H., and M. C. Gregg (2001), Near-inertial mixing: Modulation of shear, strain and microstructure at low latitude, *J. Geophys. Res.*, *106*(C8), 16,947–16,968.

Alford, M. H., and Z. Zhao (2007), Global patterns of low-mode internal-wave propagation. part i: Energy and energy flux, *J. Phys. Oceanogr.*, *37*(7), 1829–1848.

Balmforth, N., and W. Young (1999), Radiative damping of near-inertial oscillations in the mixed layer, *Journal of marine research*, *57*(4), 561–584.

Cuypers, Y., X. Le Vaillant, P. Bouruet-Aubertot, J. Vialard, and M. J. Mcphaden (2013), Tropical storm-induced near-inertial internal waves during the Cirene experiment: Energy fluxes and impact on vertical mixing, *J. Geophys. Res.*, *118*(1), 358–380.

Danioux, E., P. Klein, and P. Rivière (2008), Propagation of wind energy into the deep ocean through a fully turbulent mesoscale eddy field, *J. Phys. Oceanogr.*, *38*(10), 2224–2241.

D'Asaro, E. (1989), The decay of wind-forced mixed layer inertial oscillations due to the β effect, *Journal of Geophysical Research*, *94*(C2), 2045–2056.

D'Asaro, E. A. (1995), Upper-ocean inertial currents forced by a strong storm. part iii: Interaction of inertial currents and meso-scale eddies, *J. Phys. Oceanogr.*, *25*, 2953–2958.

D'Asaro, E. A., C. C. Eriksen, M. D. Levine, P. Niiler, C. A. Paulson, and P. V. Meurs (1995), Upper-ocean inertial currents forced by a strong storm. part i: Data and comparisons with linear theory, *J. Phys. Oceanogr.*, *25*, 2909–2936.

Fu, L. (1981), The general circulation and meridional heat transport of the subtropical south atlantic determined by inverse method, *JPO*, *11*, 1171–1193.

Furuichi, N., T. Hibiya, and Y. Niwa (2008), Model-predicted distribution of wind-induced internal wave energy in the worlds oceans, *J. Geophys. Res*, *113*, C09,034.

Gill, A. E. (1982), *Atmosphere-Ocean Dynamics*, 662 pp., Academic Press, San Diego.

Gill, A. E. (1984), On the behavior of internal waves in the wake of storms, *J. Phys. Oceanogr.*, *14*, 1129–1151.

Gottschalck, J., P. E. Roundy, C. J. Schreck III, A. Vintzileos, and C. Zhang (2013), Large-scale atmospheric and oceanic conditions during the 2011–12 DYNAMO field campaign, *Monthly Weather Review*, *141*(12), 4173–4196.

Jaimes, B., and L. K. Shay (2010), Near-inertial wave wake of hurricanes katrina and rita over mesoscale oceanic eddies, *J. Phys. Oceanogr.*, *40*(6), 1320–1337.

Klein, P., and S. L. Smith (2001), Horizontal dispersion of near-inertial oscillations in a turbulent mesoscale eddy field, *Journal of marine research*, *59*(5), 697–723.

Kunze, E. (1985), Near-inertial wave propagation in geostrophic shear, *J. Phys. Oceanogr.*, *15*(5), 544–565.

Lee, D.-K., and P. P. Niiler (1998), The inertial chimney: The near-inertial energy drainage from the ocean surface to the deep layer, *Journal of Geophysical Research: Oceans (1978–2012)*, *103*(C4), 7579–7591.

Levine, M. D., and V. Zervakis (1995), Near-inertial wave propagation into the pycnocline during ocean storms: Observations and model comparison, *J. Phys. Oceanogr.*, *25*(11), 2890–2908.

McCreary, J. (1981), A linear stratified ocean model of the equatorial undercurrent, *Philosophical Transactions of the Royal Society of London. Series A, Mathematical and Physical Sciences*, *298*(1444), 603–635.

McCreary, J., W. Han, D. Shankar, and S. Shetye (1996), Dynamics of the east india coastal current: 2. numerical solutions, *J. Geophys. Res.*, *101*(C6), 13,993–14,010.

Miyama, T., J. P. McCreary Jr, D. Sengupta, and R. Senan (2006), Dynamics of biweekly oscillations in the equatorial indian ocean*, *J. Phys. Oceanogr.*, *36*(5), 827–846.

Seiki, A., M. Katsumata, T. Horii, T. Hasegawa, K. J. Richards, K. Yoneyama, and R. Shirooka (2013), Abrupt cooling associated with the oceanic rossby wave and lateral advection during cindy2011, *J. Geophys. Res.*, *118*(10), 5523–5535.

Simmons, H. L., and M. H. Alford (2012), Simulating the long-range swell of internal waves generated by ocean storms, *Oceanography-Oceanography Society*, *25*(2), 30.

Van Meurs, P. (1998), Interactions between near-inertial mixed layer currents and the mesoscale: The importance of spatial variabilities in the vorticity field*, *J. Phys. Oceanogr.*, *28*(7), 1363–1388.

Table 4.1: Table of experiments, bold denotes the experiments discussed in this manuscript.

	N Profile	ζ	ν_H (m^{2}s^{-1})	A (m^{2}s^{-3})
QUIET_TL	a	0	150.0	0
QUIET_WTL	b	0	150.0	0
EDDY1_TL	a	$\mathcal{R}_\circ$ $\mathcal{O}(10^{-2})$ Fig. 4.7(a)	150.0	0
EDDY1_WTL	b	$\mathcal{R}_\circ$ $\mathcal{O}(10^{-2})$ Fig. 4.7(a)	150.0	0
EDDY2_TL	a	$\mathcal{R}_\circ$ $\mathcal{O}(10^{-1})$ Fig. 4.7(b)	150.0	0
EDDY2_WTL	b	$\mathcal{R}_\circ$ $\mathcal{O}(10^{-1})$ Fig. 4.7(b)	150.0	0
VMIX_QUIET_TL	a	0	150.0	1.2×10^{-8}
VMIX_QUIET_WTL	b	0	150.0	1.2×10^{-8}
VMIX_EDDY2_TL	a	$\mathcal{R}_\circ$ $\mathcal{O}(10^{-1})$ Fig. 4.7(b)	150.0	1.2×10^{-8}
VMIX_EDDY2_WTL	b	$\mathcal{R}_\circ$ $\mathcal{O}(10^{-1})$ Fig. 4.7(b)	150.0	1.2×10^{-8}

Table 4.2: Mode frequency as a function of wavelength.

	100 km	200 km	300 km	420 km	560 km	890 km
Mode 2	5.54 $f_\circ$	2.90 $f_\circ$	2.08 $f_\circ$	1.64 $f_\circ$	1.40 $f_\circ$	1.17 $f_\circ$
Mode 4	2.85 $f_\circ$	1.67 $f_\circ$	1.34 $f_\circ$	1.19 $f_\circ$	1.11 $f_\circ$	1.04 $f_\circ$
Mode 5	2.38 $f_\circ$	1.47 $f_\circ$	1.23 $f_\circ$	1.13 $f_\circ$	1.07 $f_\circ$	1.03 $f_\circ$
Mode 10	1.43 $f_\circ$	1.12 $f_\circ$	1.06 $f_\circ$	1.03 $f_\circ$	1.02 $f_\circ$	1.007 $f_\circ$
Mode 20	1.12 $f_\circ$	1.03 $f_\circ$	1.01 $f_\circ$	1.007 $f_\circ$	1.004 $f_\circ$	1.002 $f_\circ$

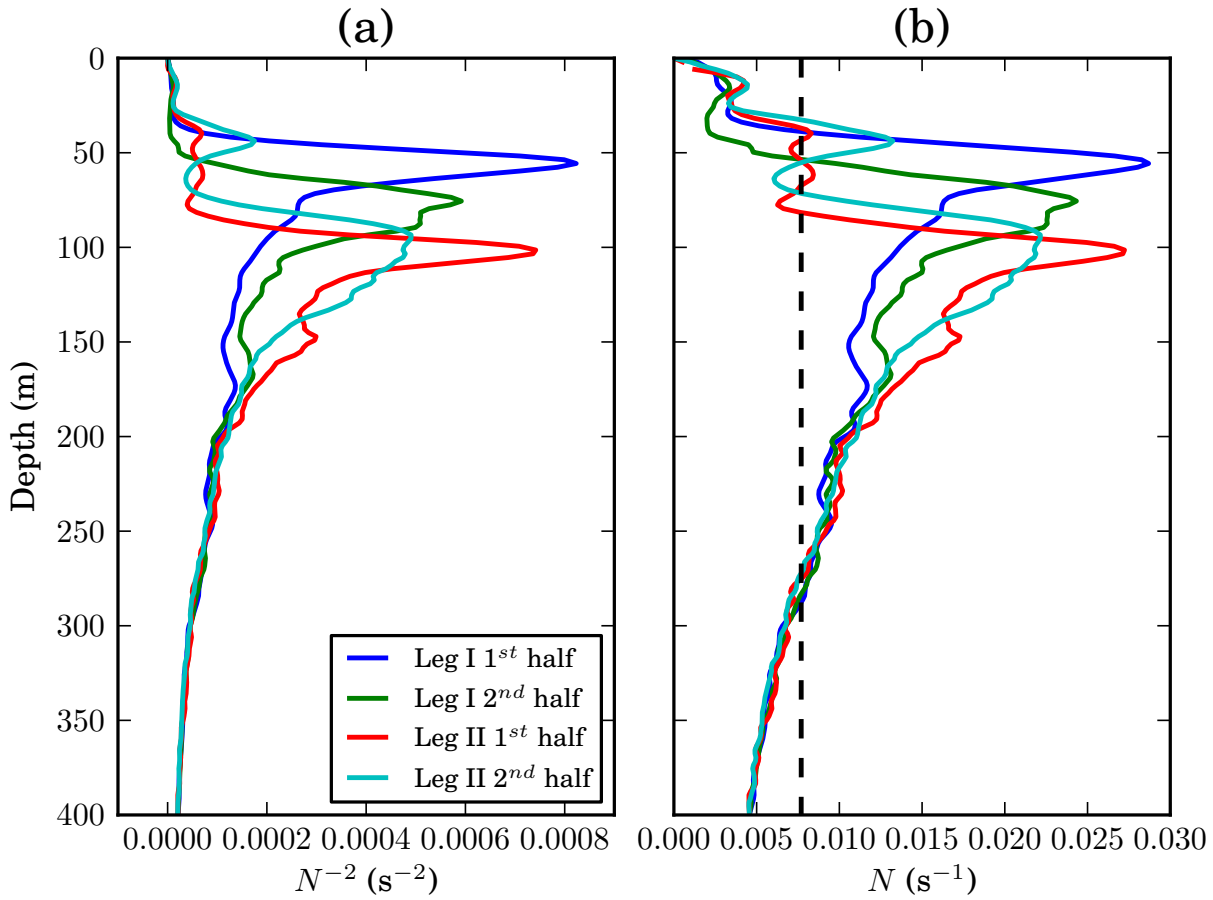

Figure 4.1: Time averaged profiles of N^2 (a) and N (b) from CINDY measurements collected at 8°S, 80.5°E. The black dashed line denotes $\bar{N}$ calculated for the thermocline between 100 and 500 m.

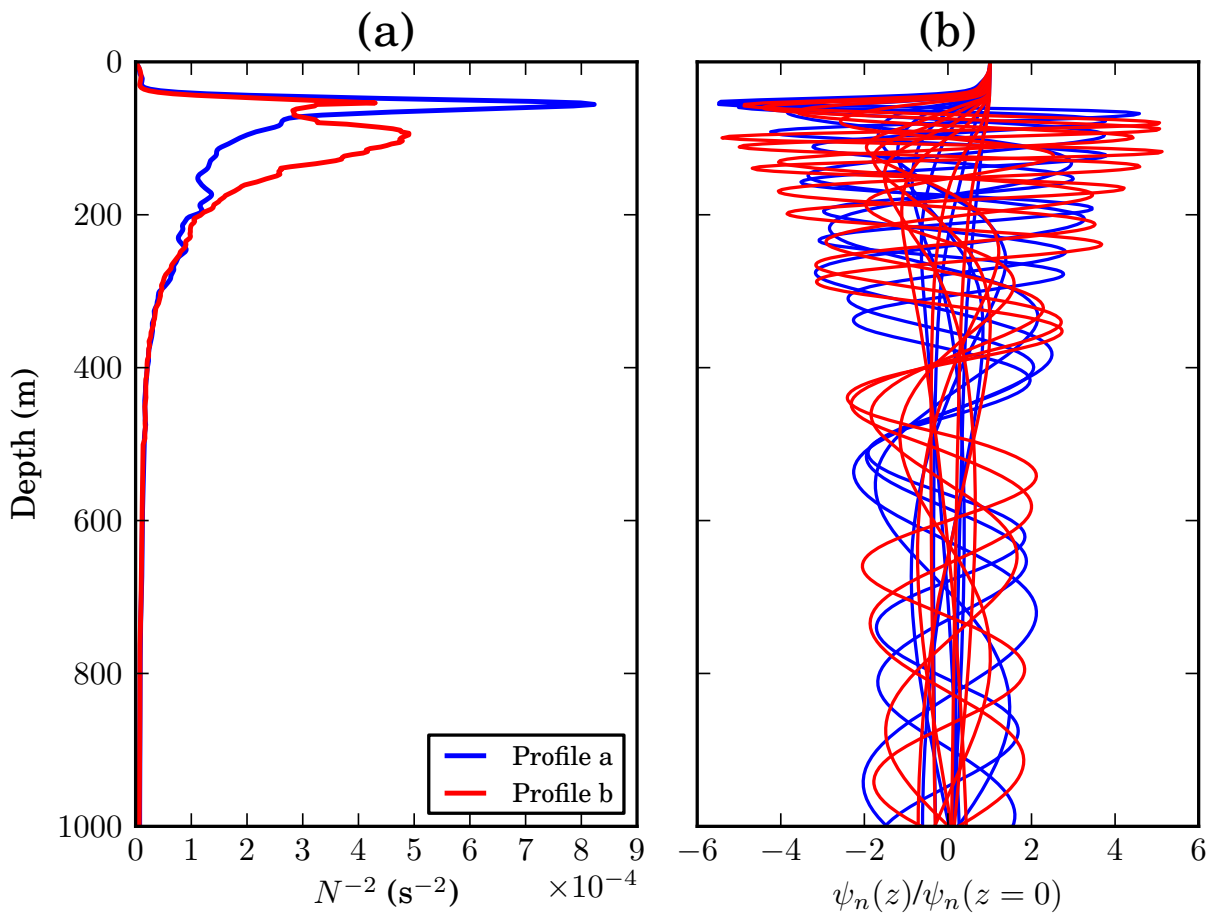

Figure 4.2: Profiles of N^2 (a) used in LCS integrations and mode structure (ψ_n) for mode numbers 1 to 5, 10, 20 and 25 structure (b).

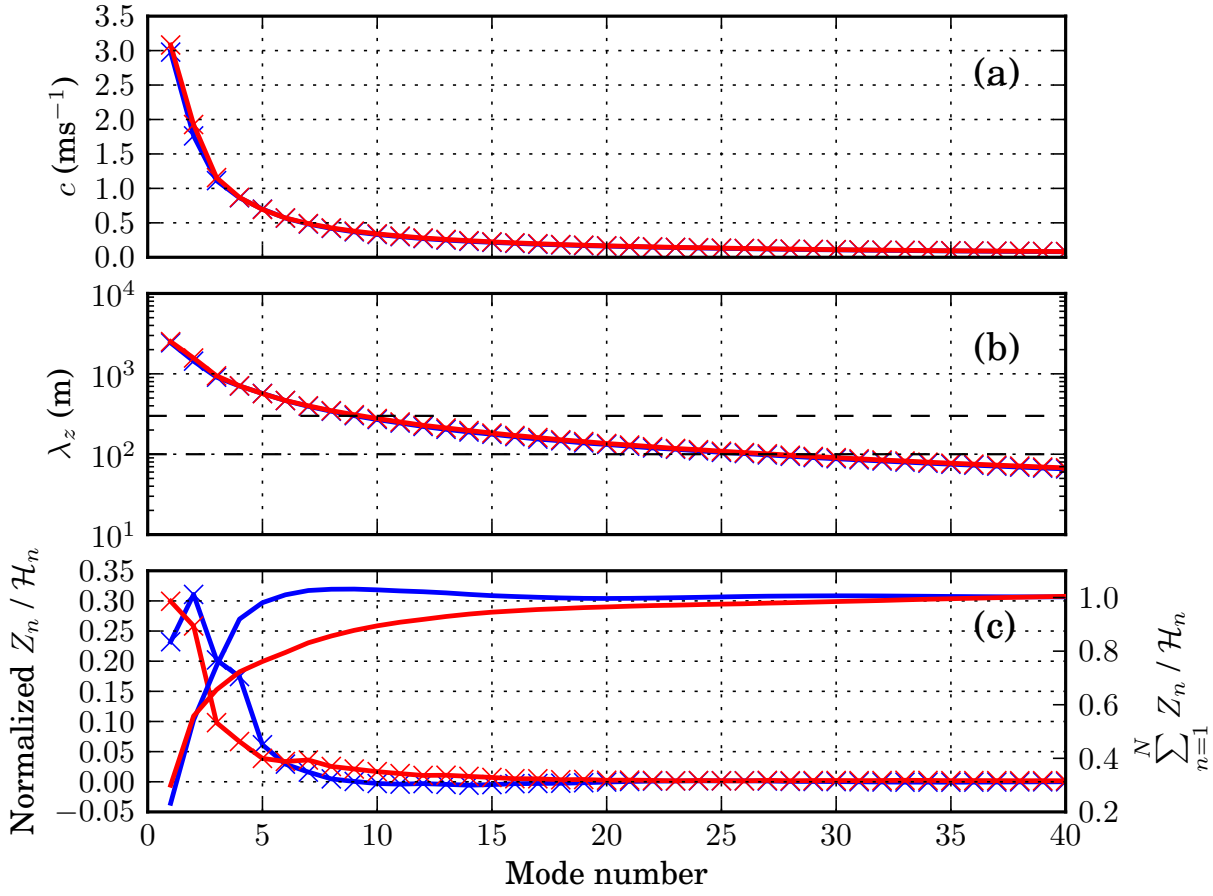

Figure 4.3: Modal decomposition parameters for the two N^2 profiles shown in Figure 4.2 (blue for Profile a and red for Profile b). (a) shows the mode phase speeds c_n. (b) shows the modal vertical wavelength (λ_z) calculated using $\bar{N}$, the black dashed lines indicate the 100−−300 m range. (c) shows the modal wind forcing amplitude, i.e. fraction of wind stress projected onto each mode, and the cumulative sum of these modal forcing amplitudes (solid lines). The lower 5 modes account for 98% and 76% of the total input for Profile a and Profile b, respectively.

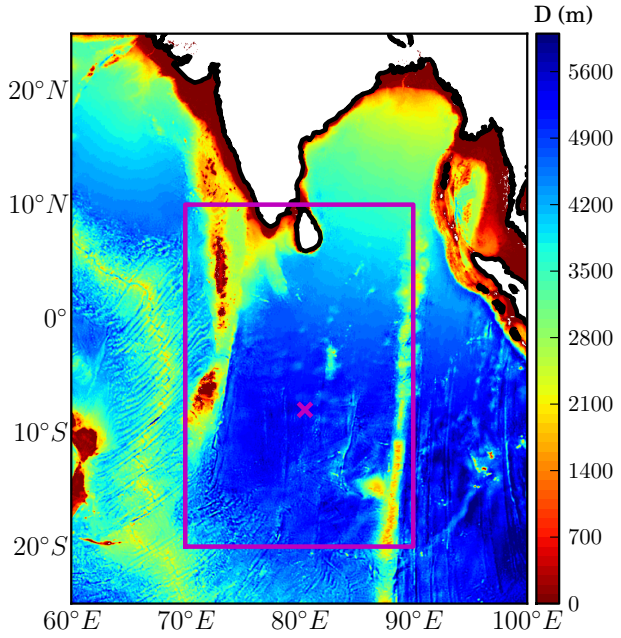

Figure 4.4: Tropical Indian Ocean bathymetry with black cross marking the location of the R/V *Mirai* station at 8°S, 80.5°E. The LCS domain is shown in the magenta box.

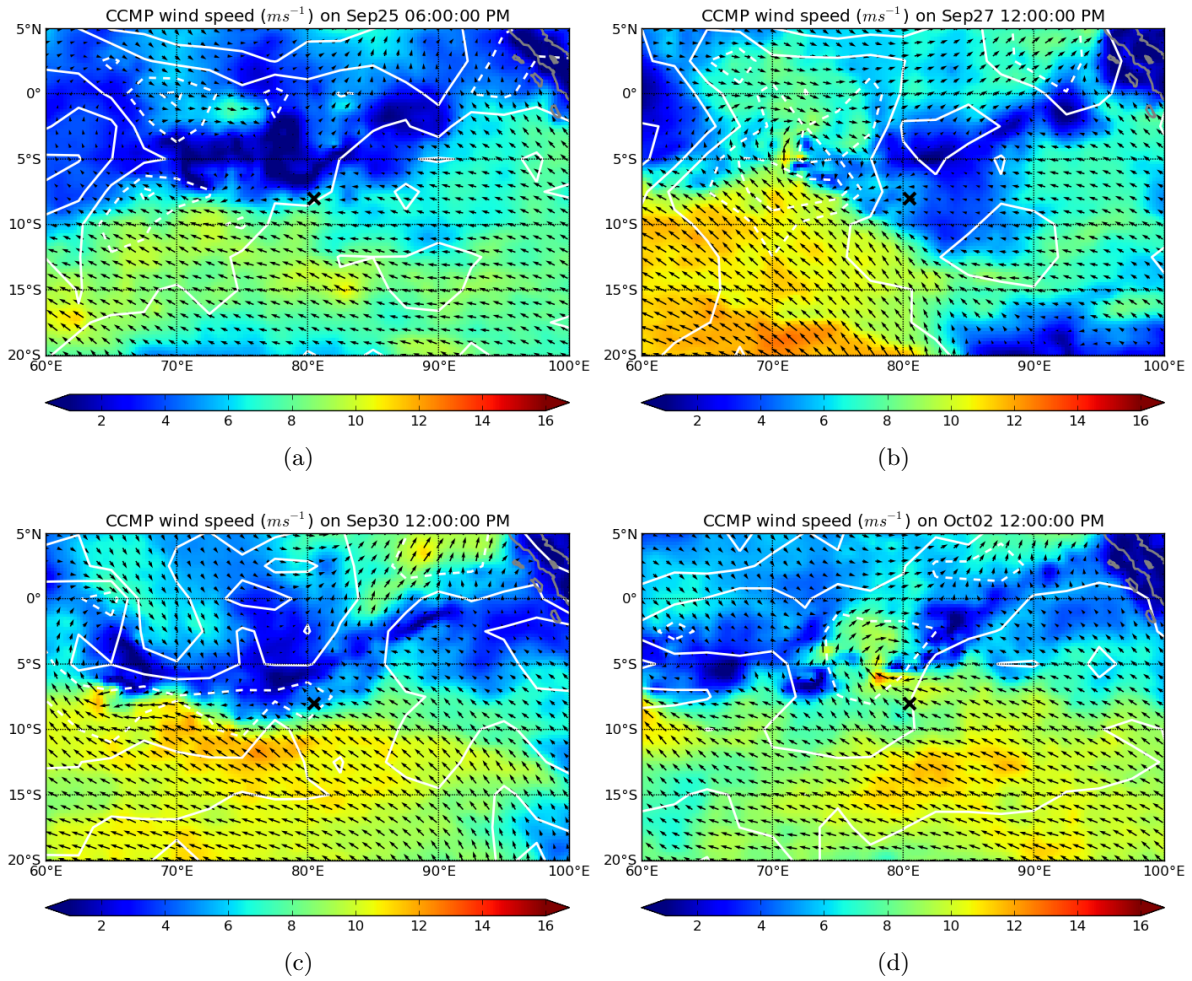

Figure 4.5: Snapshots of the wind field over part of the domain, showing the time evolution of winds during the first two weeks of the model integration period. White contours show the Outgoing Longwave Radiation (OLR) anomalies, with positive anomalies in solid and negative anomalies in dashed.

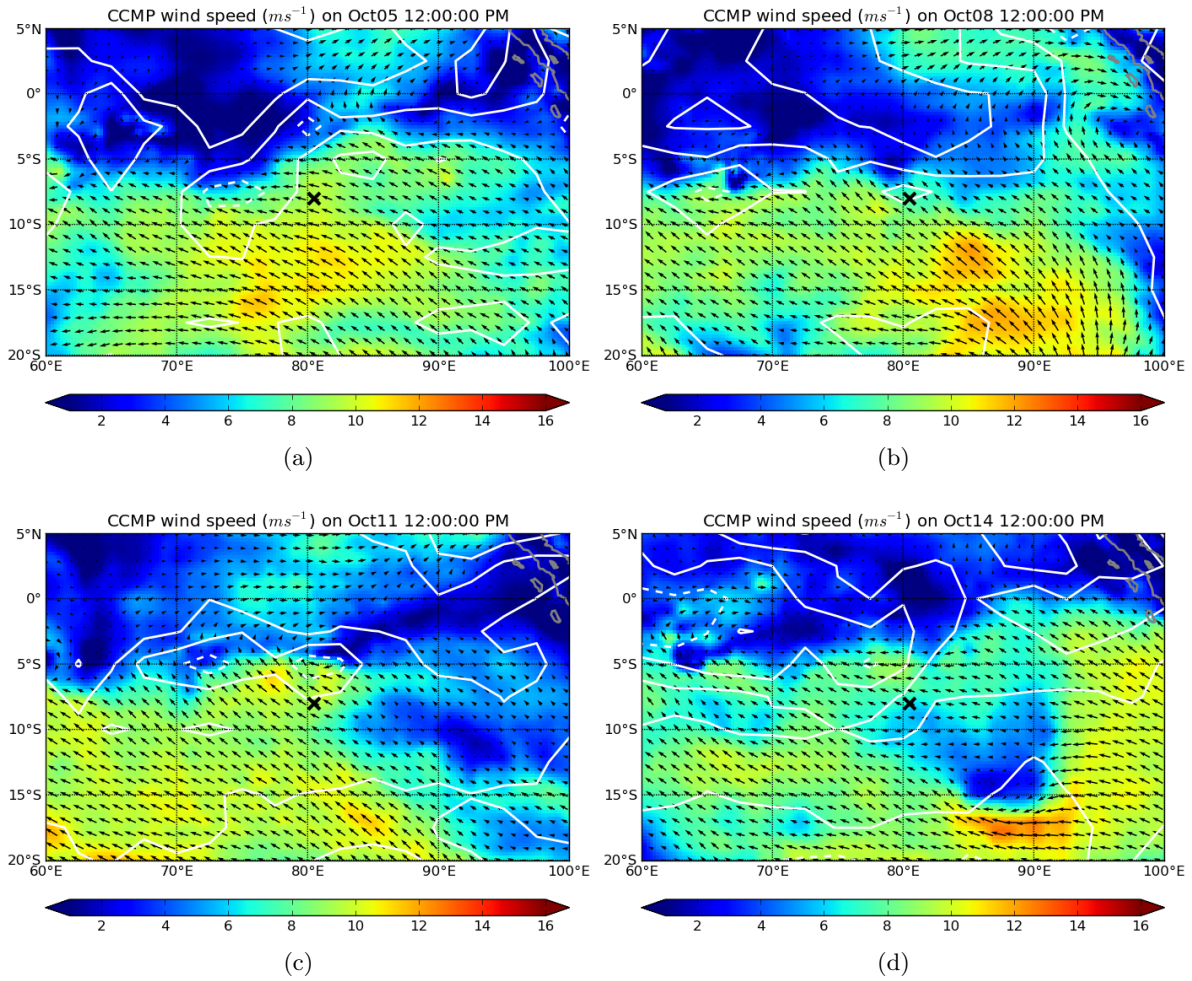

Figure 4.6: Snapshots of the wind field over part of the domain, showing the time evolution of winds during the second two week period of model integration period. White contours show the Outgoing Longwave Radiation (OLR) anomalies, with positive anomalies in solid and negative anomalies in dashed.

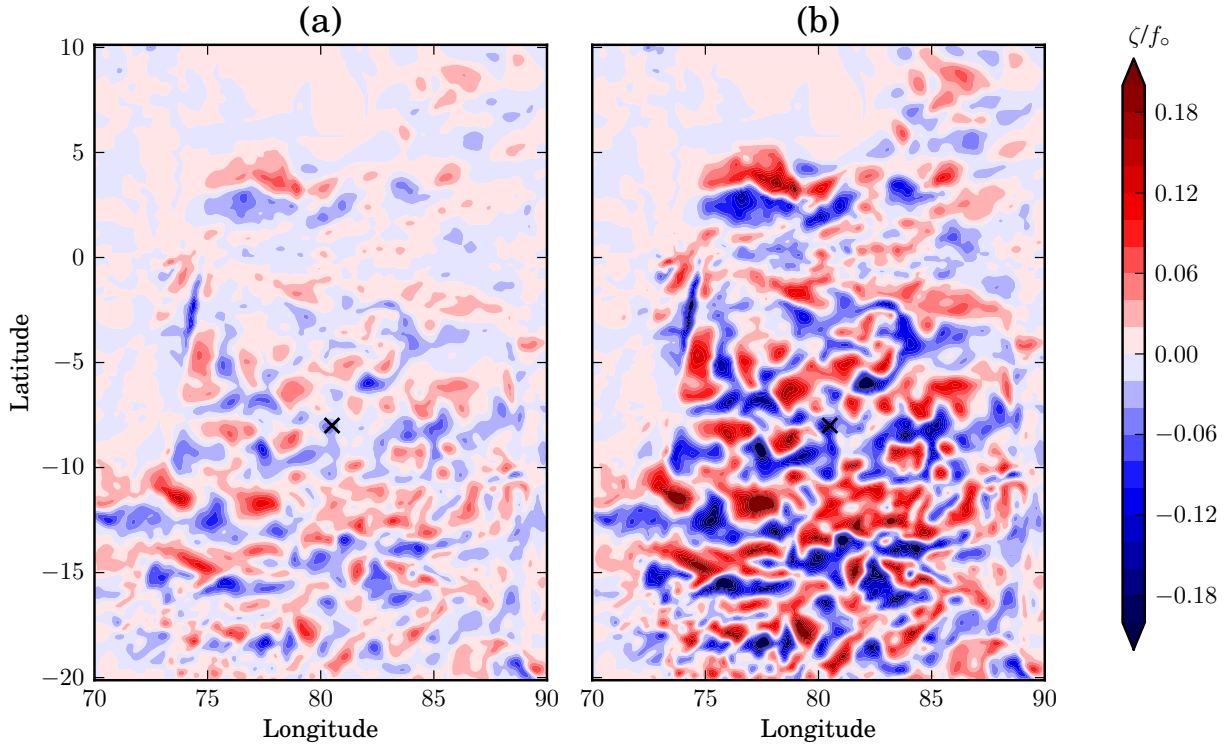

Figure 4.7: MERCATOR time averaged vorticity (ζ) normalized by the local inertial frequency at 8°S, 80.5°E (Rossby number) for model domain. The Barotropic vorticity component used in experiments EDDY1_TL and EDDY1_WTL (a), and enhanced barotropic vorticity to mimic upper ocean values used in experiments EDDY2_TL and EDDY2_WTL (b). The black cross marks the location of the R/V *Mirai* station at 8°S, 80.5°E.

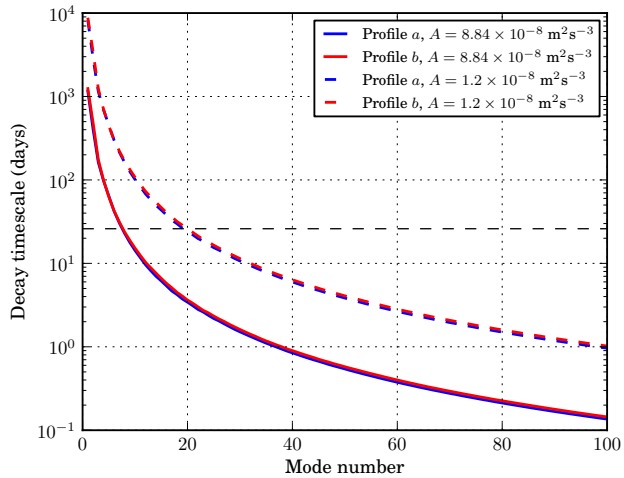

Figure 4.8: Modal damping timescale (c_n^2/A) for the profiles of N^2 used in LCS integrations. The black dashed line denotes the expected damping timescale derived from the observations.

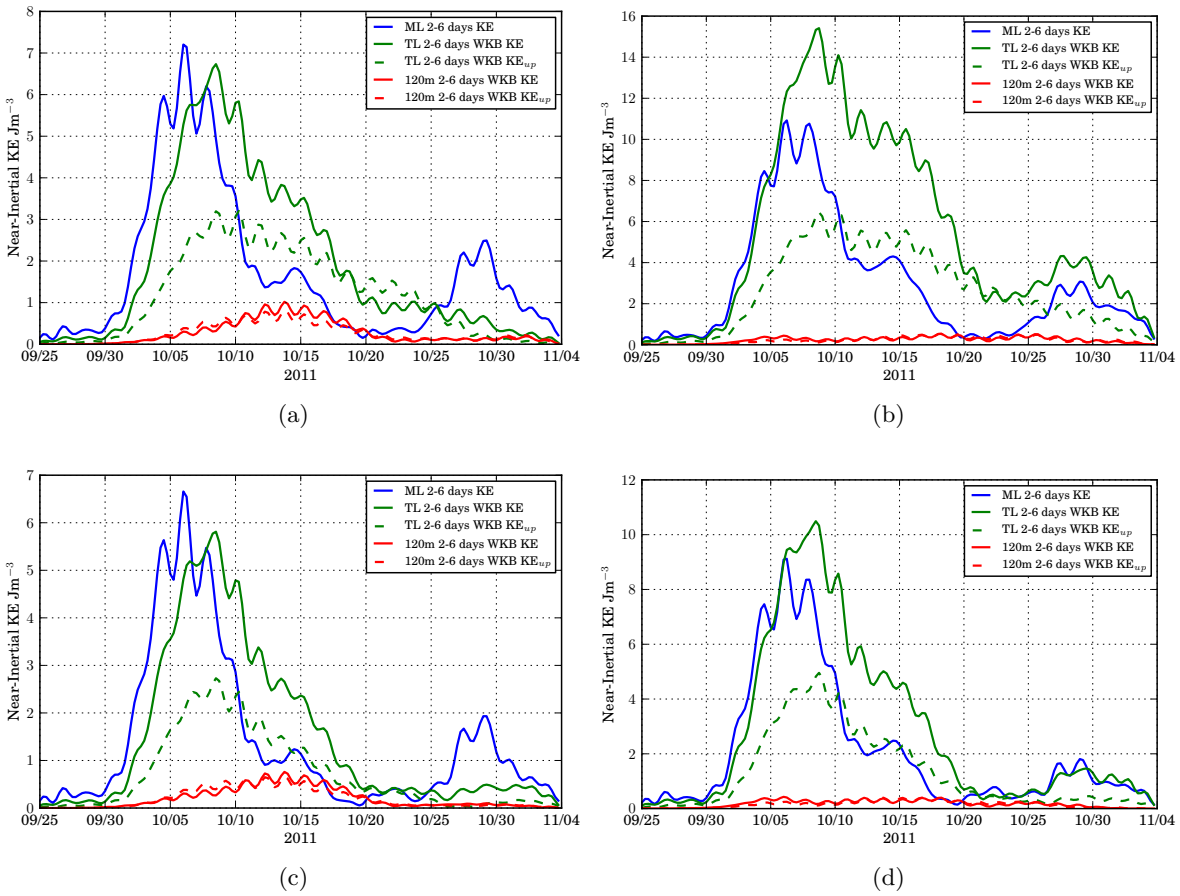

Figure 4.9: Time series of near-inertial kinetic energy (NIKE) at the CINDY station 8°S 80.5°E for the ML, TL (60 m) and 120 m (thermocline), for (a) QUIET_TL, (b) QUIET_WTL, (c) VMIX_QUIET_TL, (d) VMIX_QUIET_WTL.

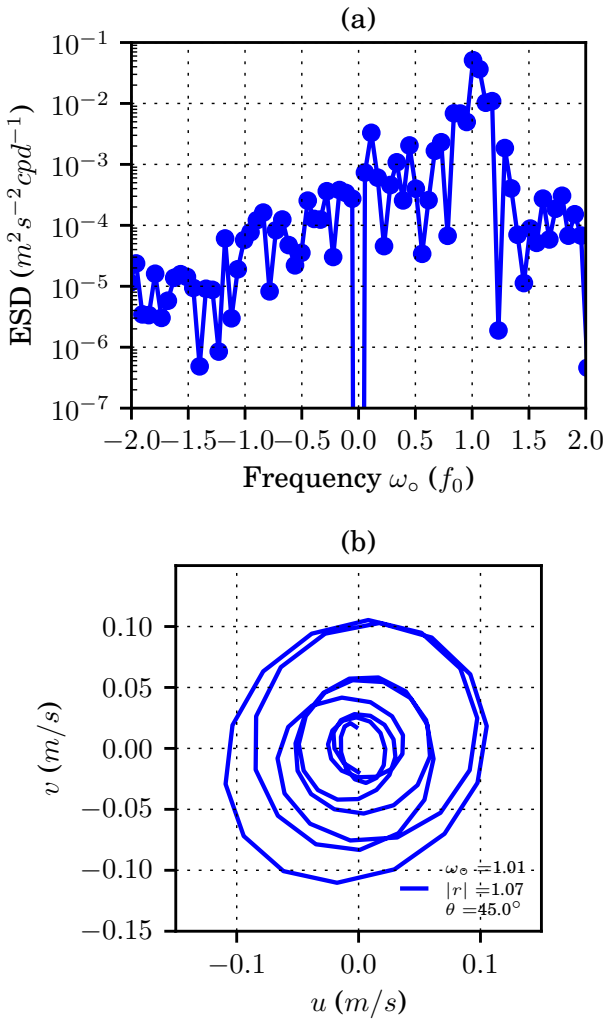

Figure 4.10: Frequency spectrum for mixed layer (ML) currents (a). Near-inertial current ellipse with parameters obtained from FFT rotary spectrum (b).

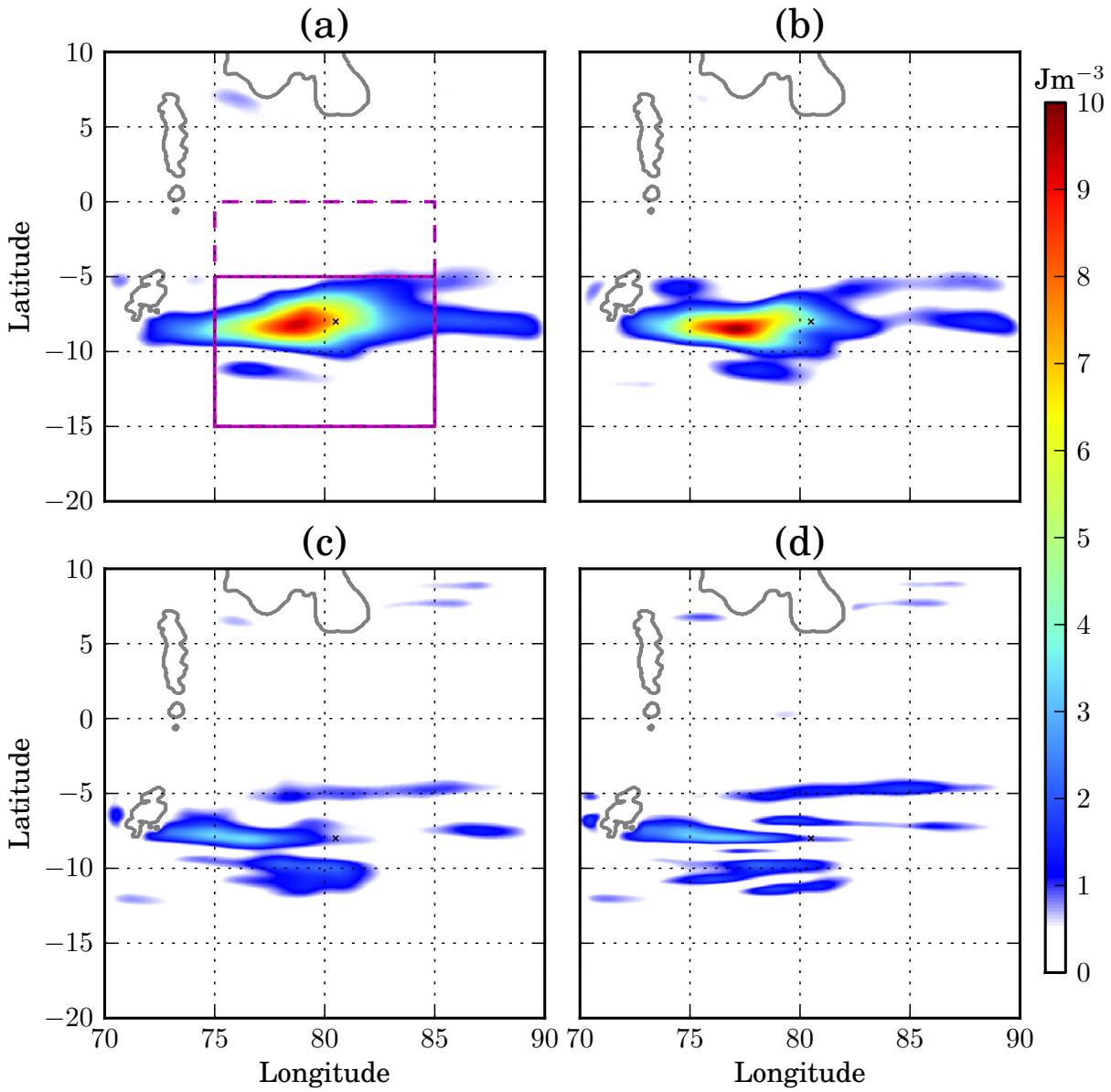

Figure 4.11: ML NIKE for Experiment QUIET_TL at (a) model day 11 ($t_\circ$, ML energy peak) (b) 1 IP after $t_\circ$ (c) 3 IP after $t_\circ$ and (d) 5 IP after $t_\circ$. The magenta box shows the region where spectrum, averages and integrations are carried out, while the dashed lines mark the extension used to calculate meridional spectra.

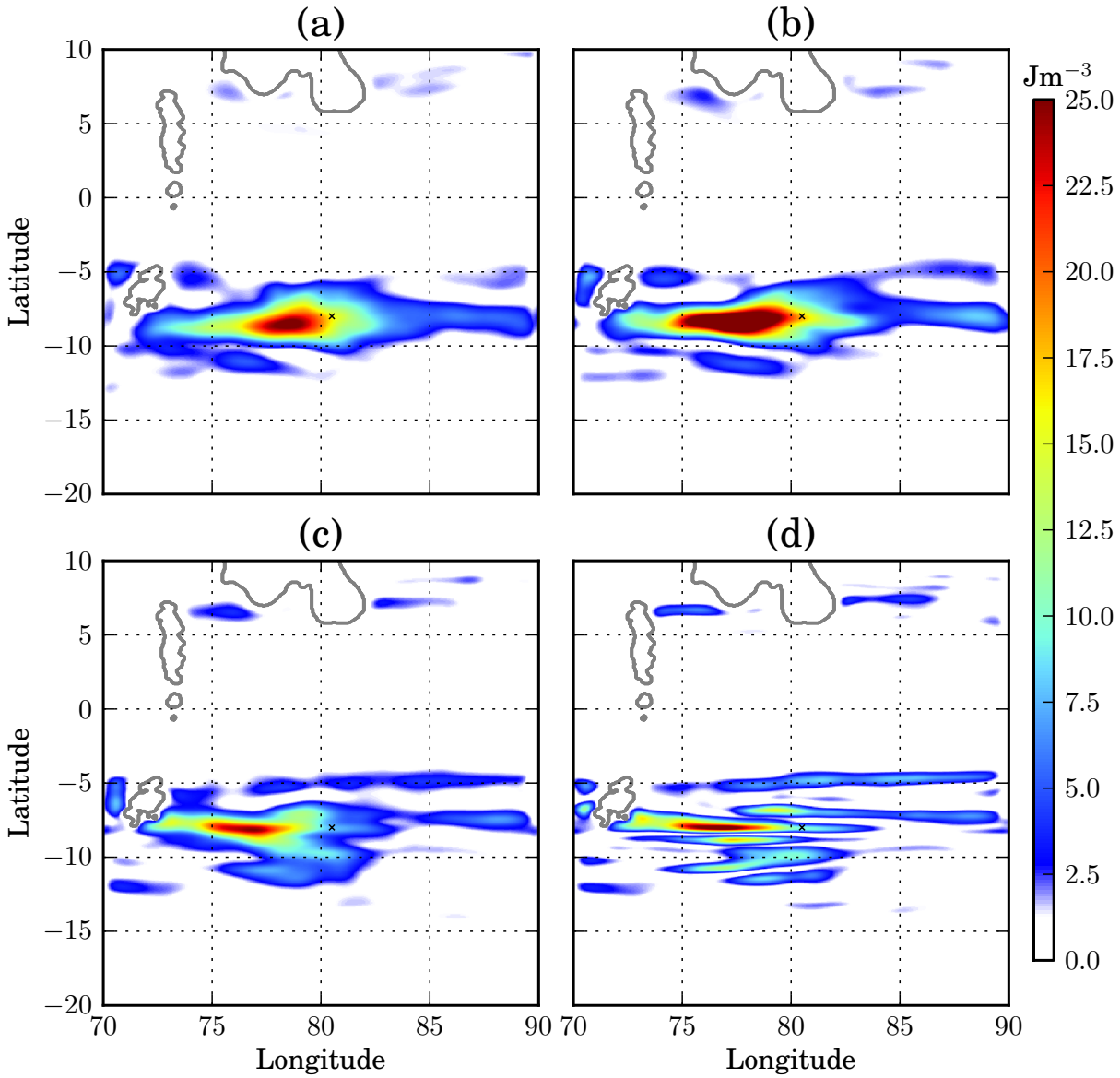

Figure 4.12: Same as Figure 4.11 but for the TL (60 m).

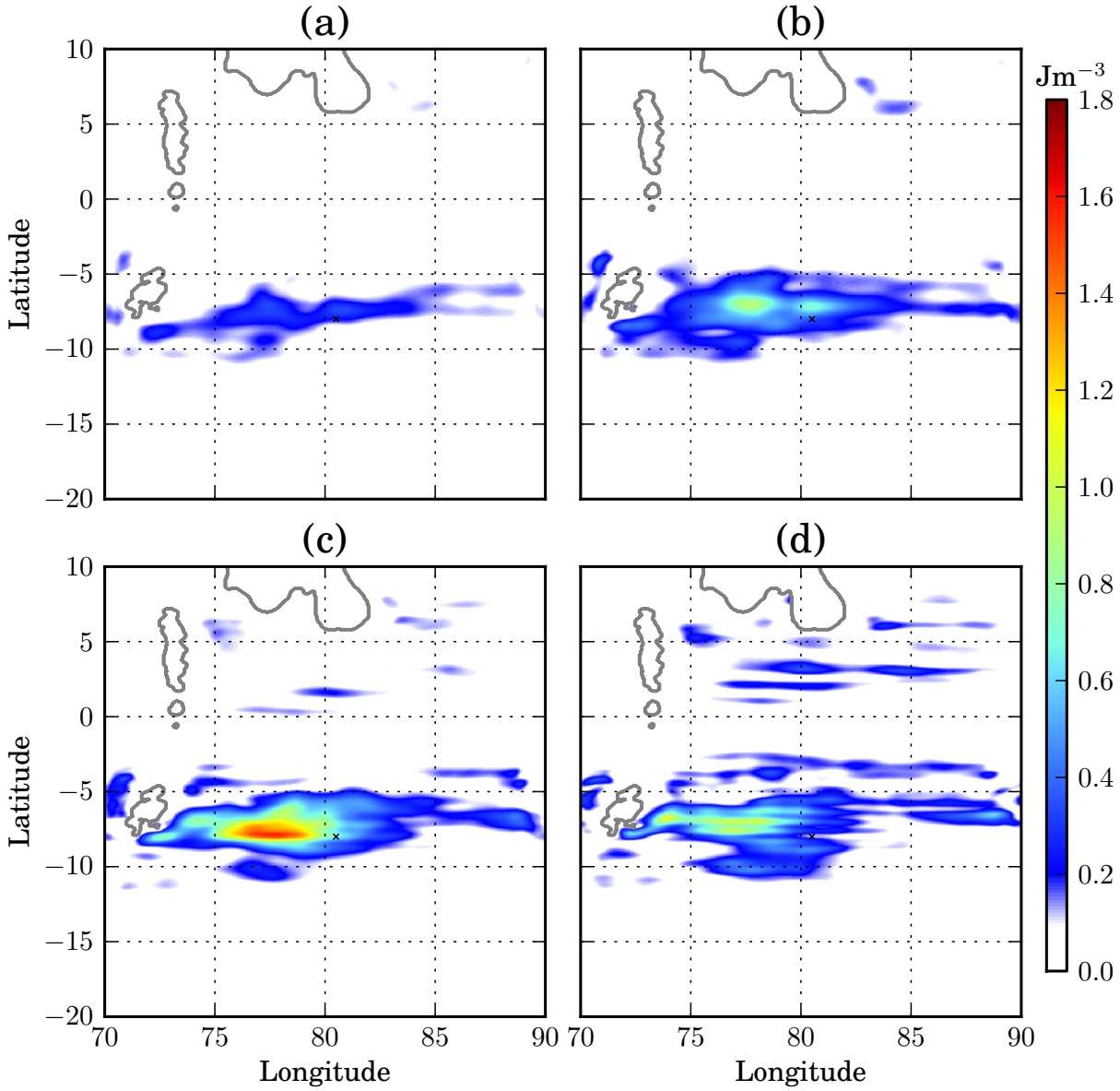

Figure 4.13: Same as Figure 4.11 but for the average thermocline near-inertial kinetic energy.

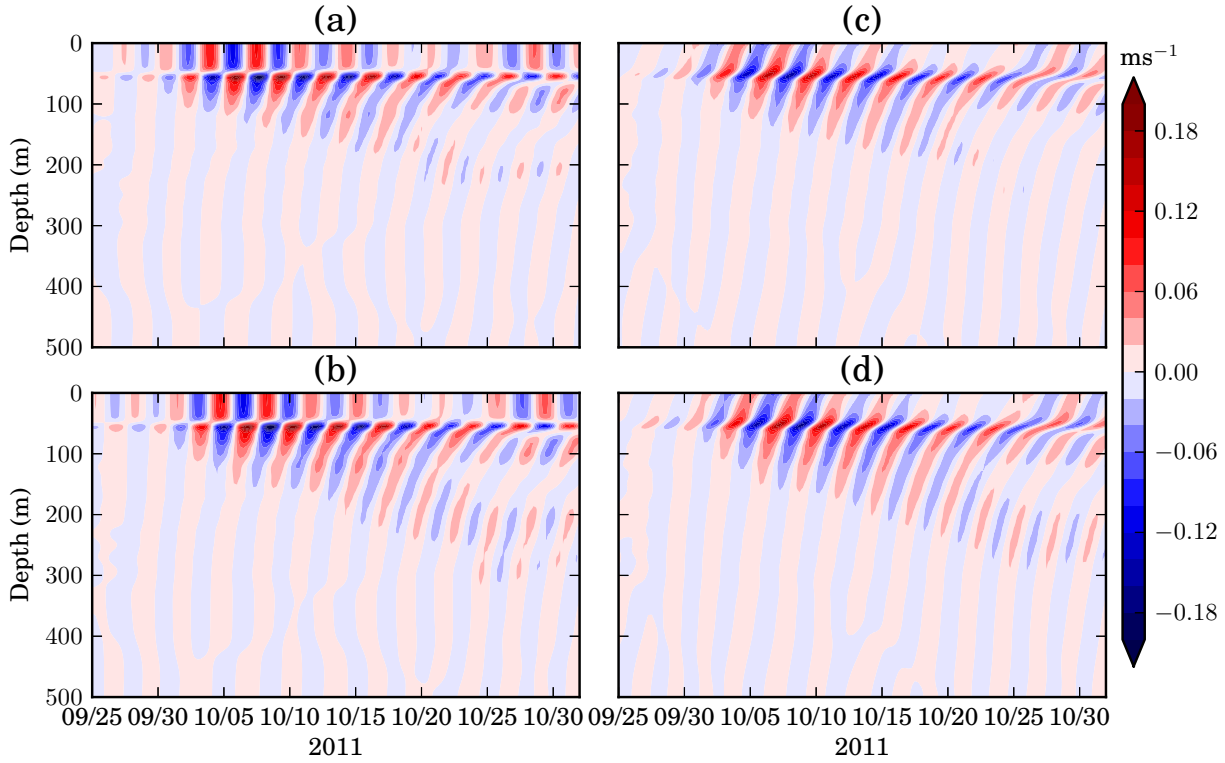

Figure 4.14: Experiment QUIET_TL depth-time series at 8°S 80.5°E of near-inertial (2-6 days band passed) zonal velocity anomalies u' (a), zonal upward phase propagating velocity anomalies u'_{up} (b), meridional velocity anomalies v' (c), meridional upward phase propagating velocity anomalies v'_{up} (d).

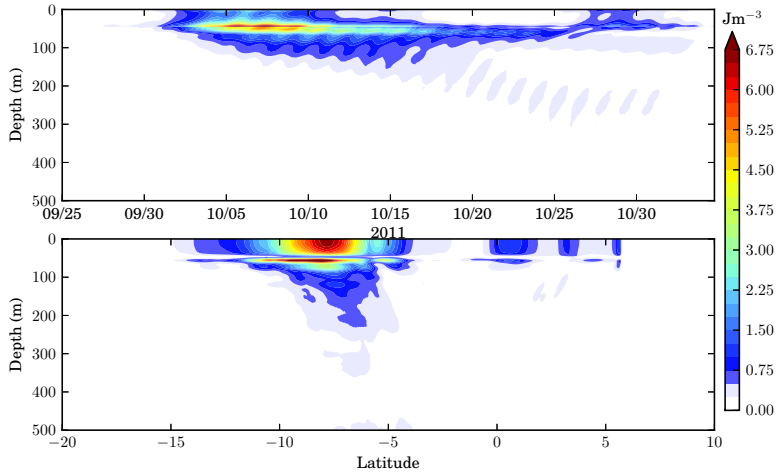

(a)

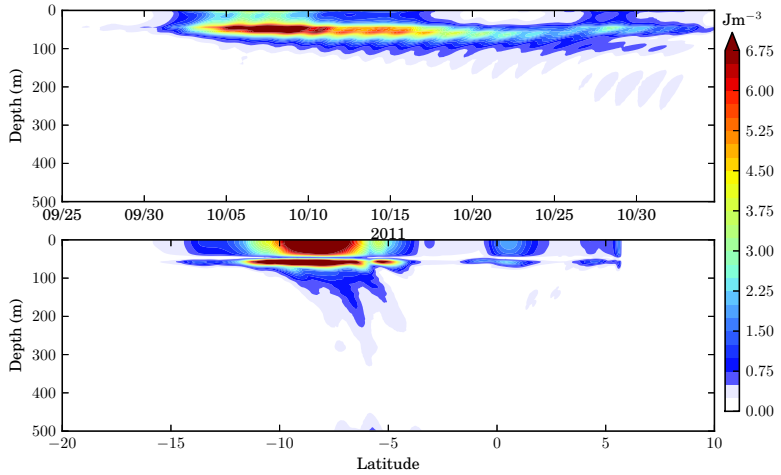

(b)

Figure 4.15: (a) For QUIET_TL; upper panel: Depth-time series of WKB scaled NIKE at 8°S 80.5°E. Lower panel: Maximum NIKE during first 8 inertial periods of integration along 80.5°E showing the extend of downward and equatorwad NIKE penetration. (b) Same but for QUIET_WTL.

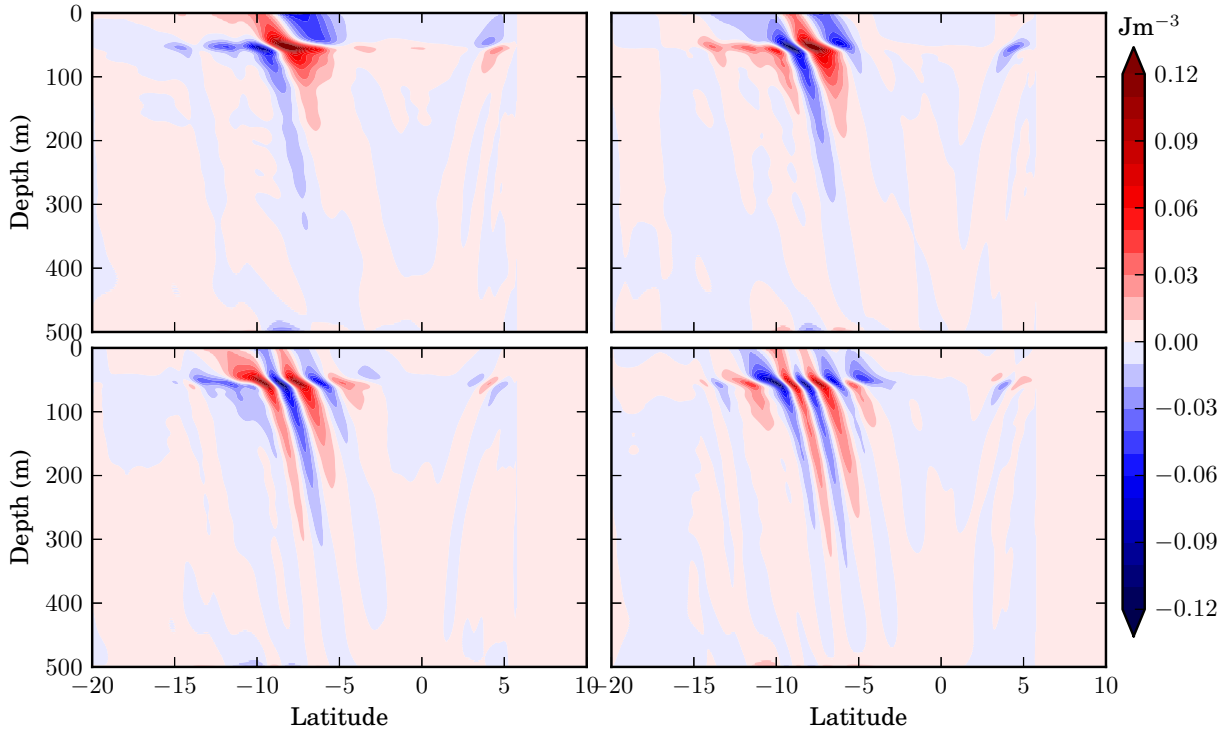

Figure 4.16: Experiment QUIET_TL depth-latitude chart of near-inertial (2-6 days band passed) u' along 80.5°E at (a) $t_\circ$ (ML energy peak), (b) 1IP after $t_\circ$, (c) 3IP after $t_\circ$, and (d) 5IP after $t_\circ$.

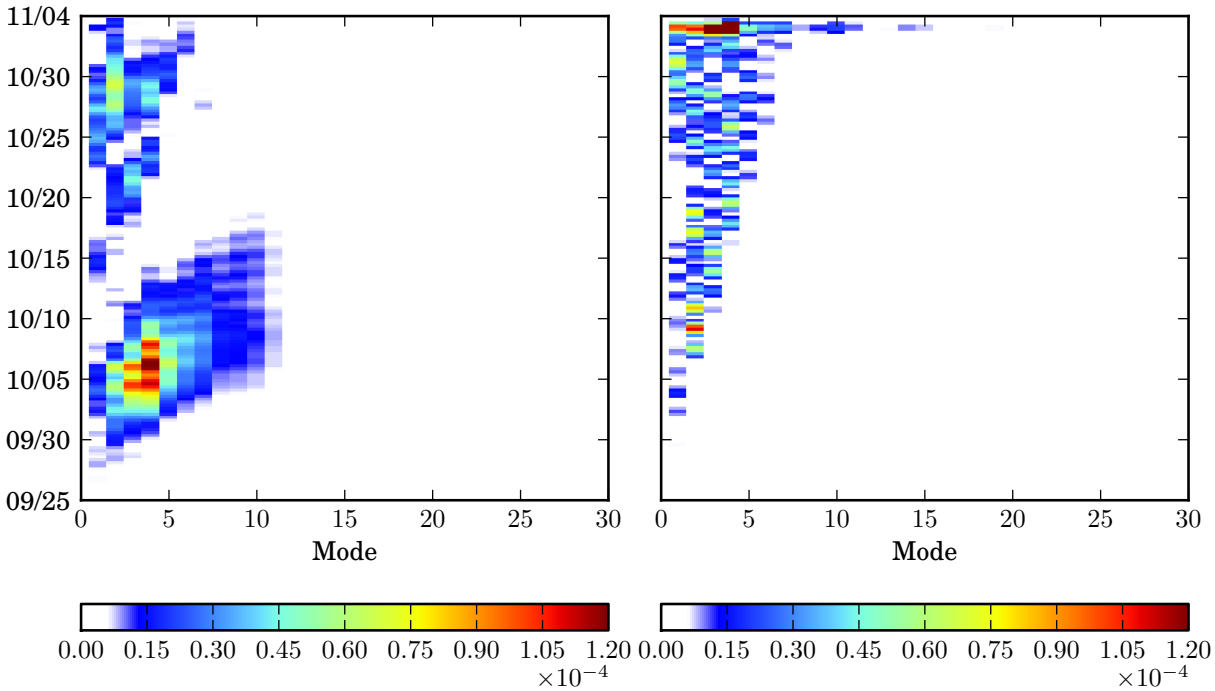

Figure 4.17: NIKE (m^2s^{-2}) partition by mode number for the QUIET_TL experiment at (a) CINDY station (8°S 80.5°E) and (b) at the Equator.

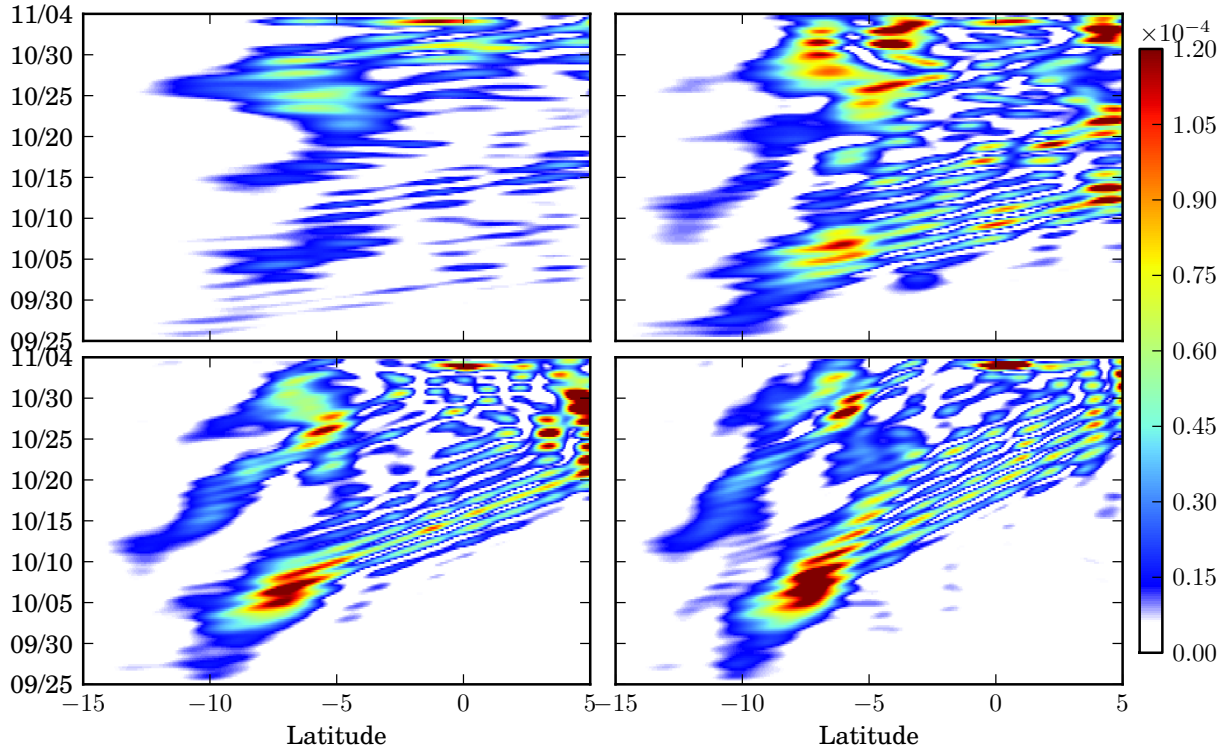

Figure 4.18: Experiment QUIET_TL time-Latitude Hovmoller plots of NIKE for (a) mode 1, (b) mode 2, (c) mode 3, and (d) mode 4, along 80.5°E.

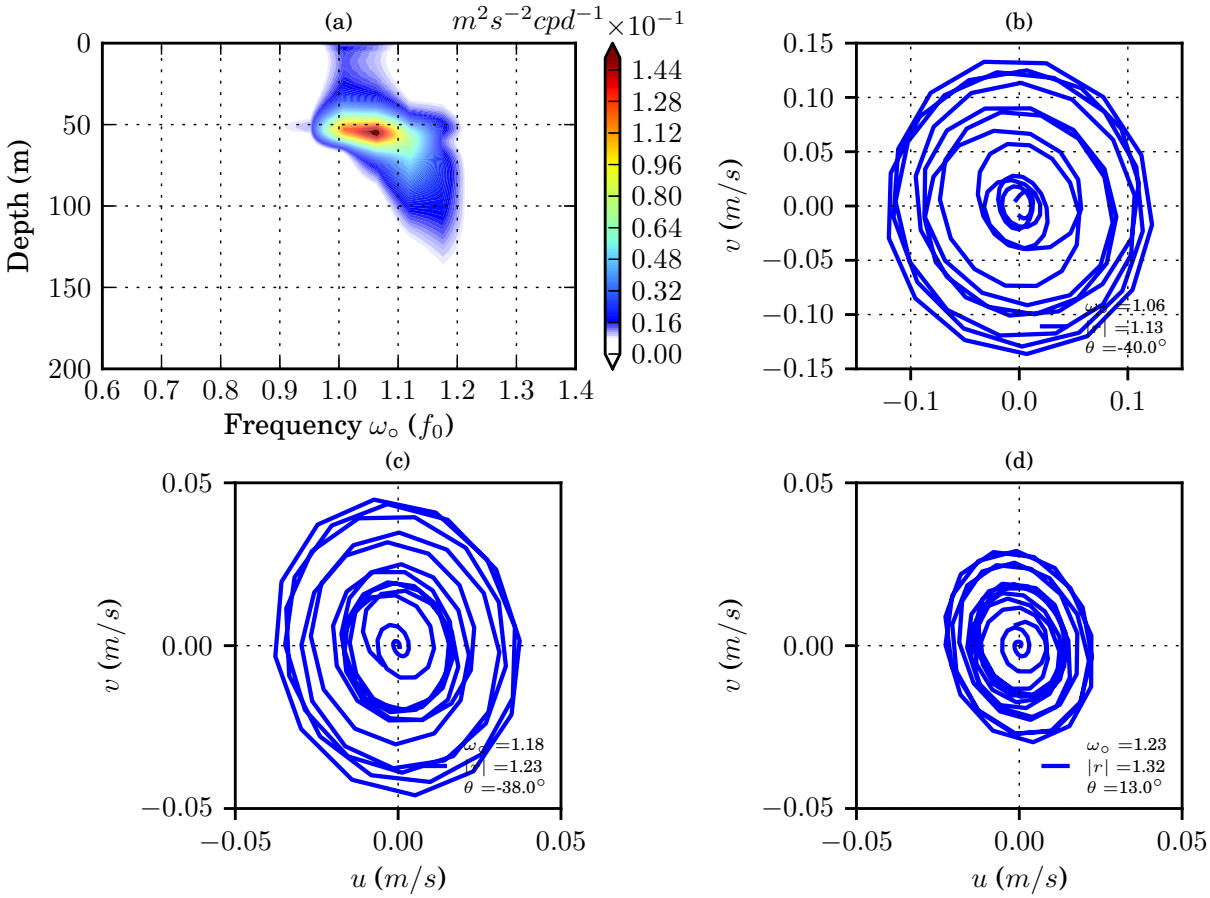

Figure 4.19: Energy density frequency spectra as a function of depth (a), NIW ellipse in the TL (60 m) with corresponding FFT parameters (b), NIW ellipse at 120 m (c), and NIW ellipse at 180 m, at the CINDY station, 8°S 80.5°E for experiment QUIET_TL.

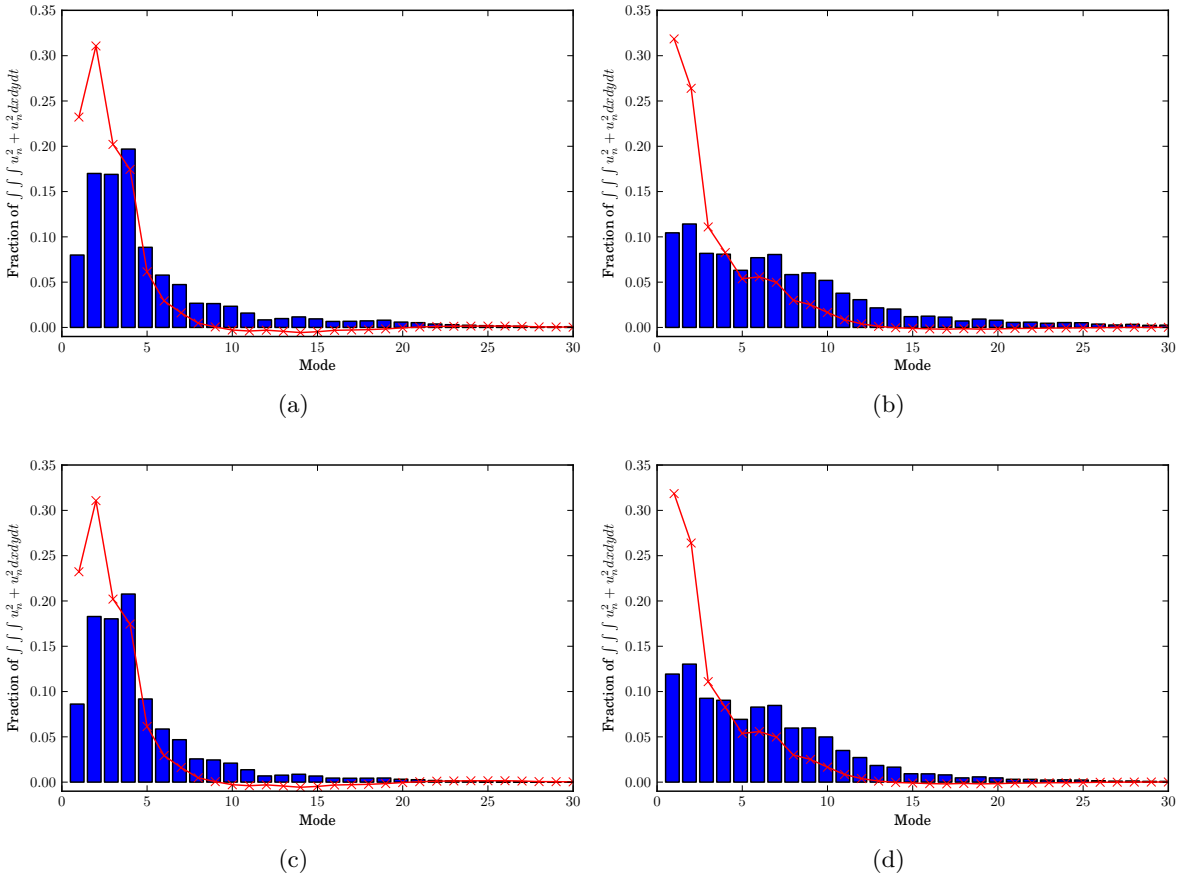

Figure 4.20: Experiment QUIET_TL time and area integrated (magenta box in Figure 4.11) NIKE partitioned by mode number. Red curve shows the 1D projection of wind forcing, as in Figure 4.3c. It should be noted that, for all quiescent ocean solution, these integrated patterns represent quite well the partition into modes at any given location.

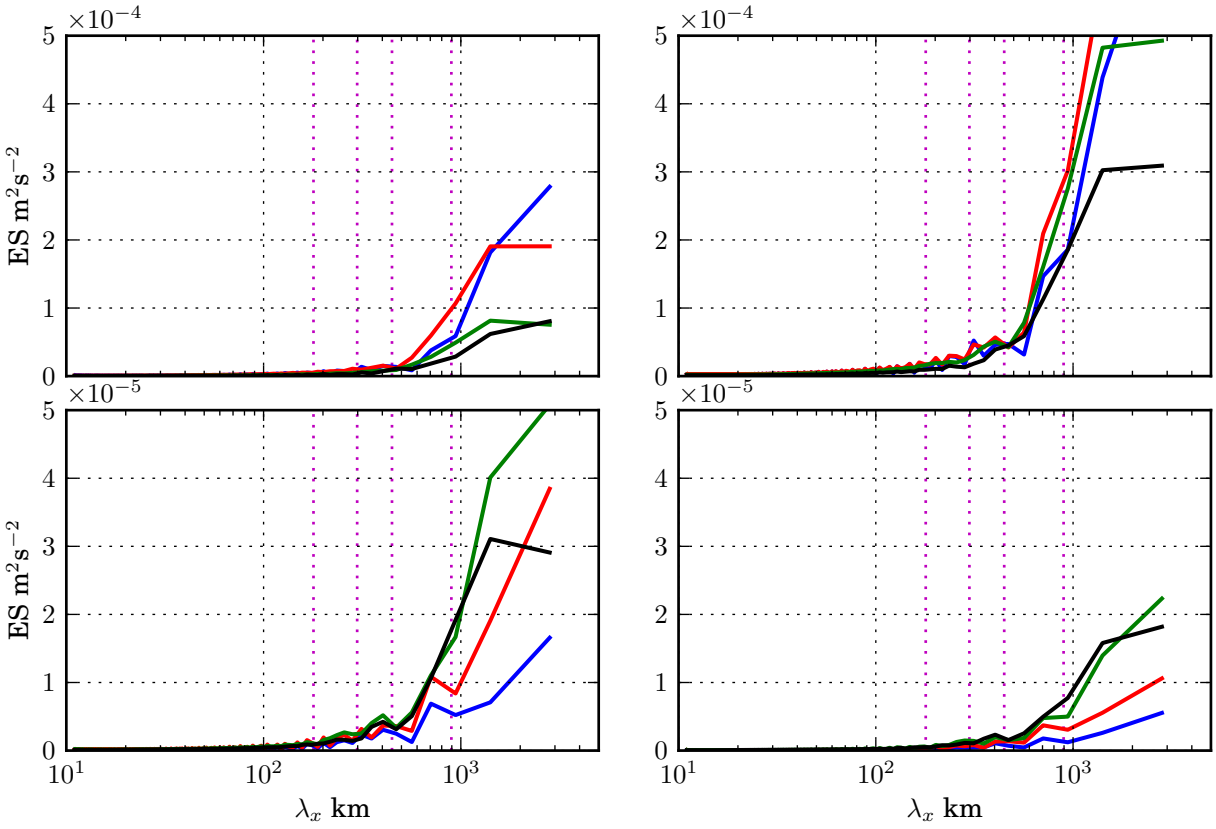

Figure 4.21: Experiment QUIET_TL variance preserving zonal spectra for (a) ML, (b) TL, (c) 120 m and (d) 180 m. Colors denote spectra calculated at times $t_\circ$ (ML energy peak) (blue), 1IP after $t_\circ$ (red), 3IP after $t_\circ$ (green) and 5IP after $t_\circ$ (black).

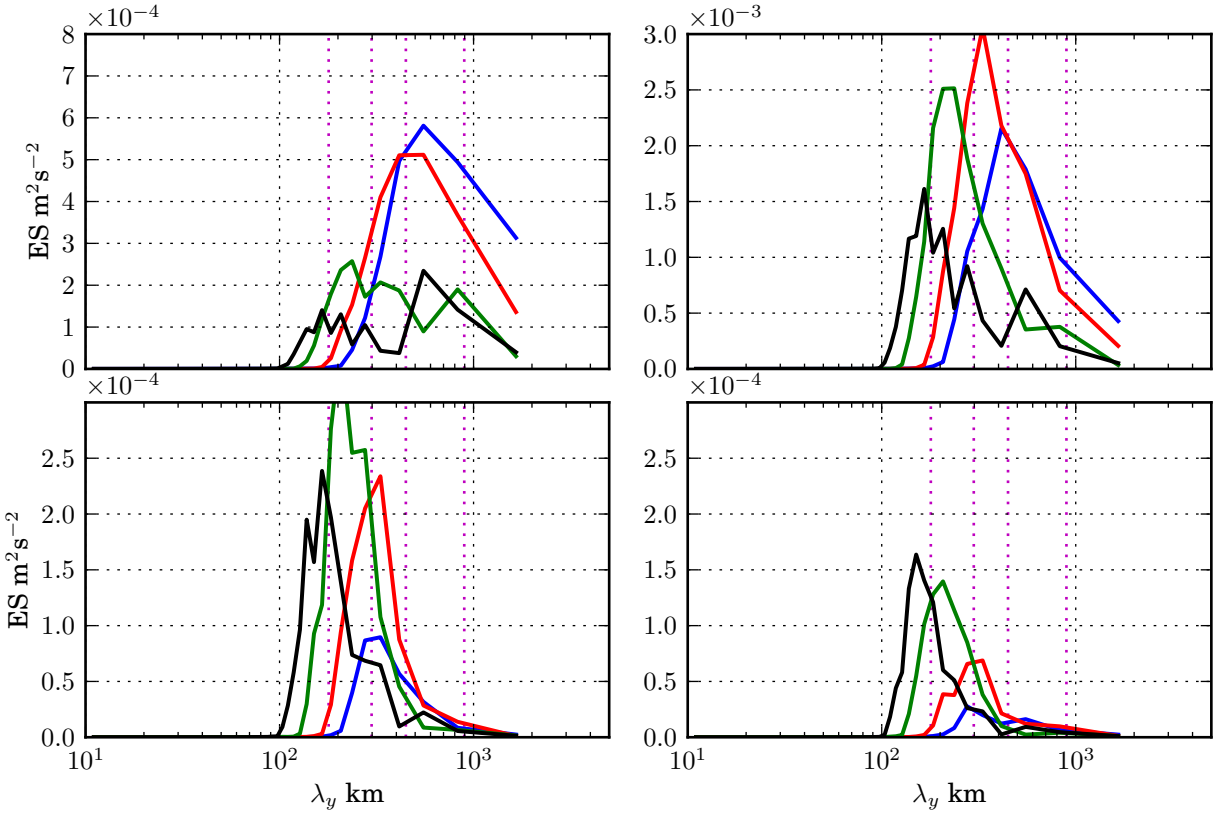

Figure 4.22: Experiment QUIET_TL variance preserving meridional spectra for (a) ML, (b) TL, (c) 120 m and (d) 180 m. Colors denote spectra calculated at times (ML energy peak ML) $t_\circ$ (blue), 1IP after $t_\circ$ (red), 3IP after $t_\circ$ (green) and 5IP after $t_\circ$ (black).

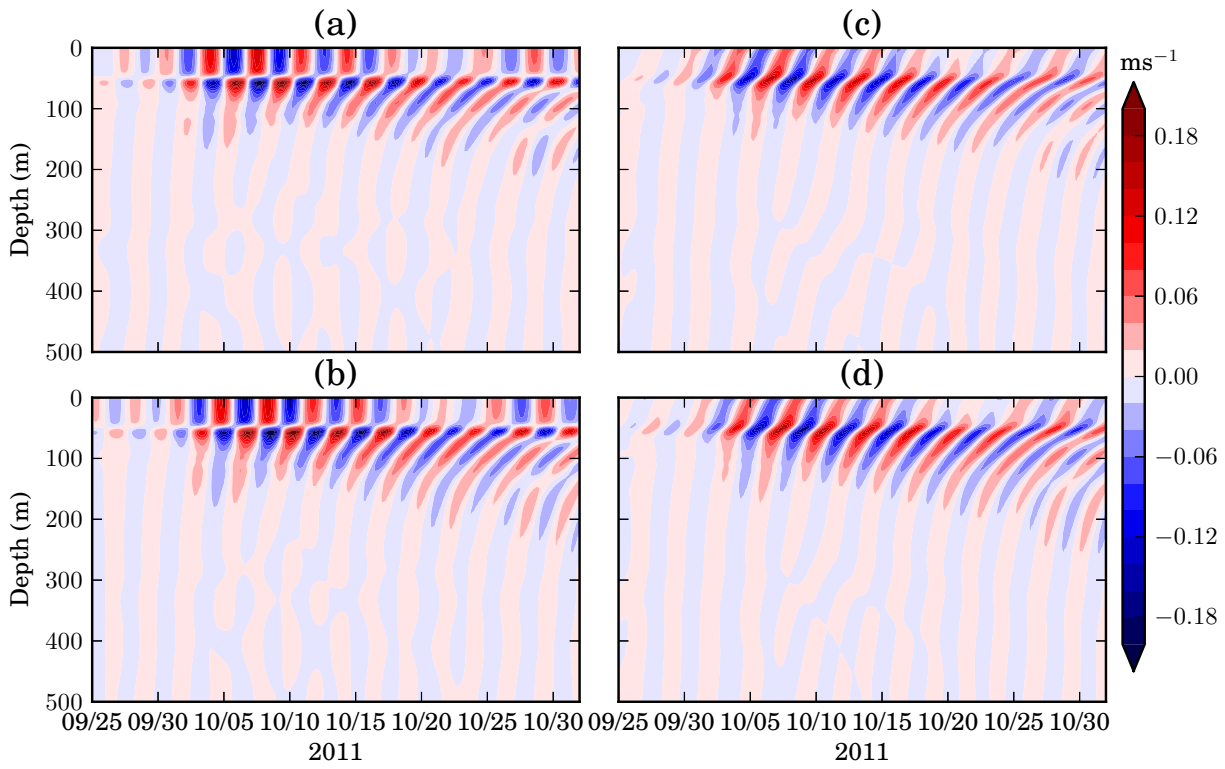

Figure 4.23: Same as Figure 4.14 but for experiment QUIET_WTL.

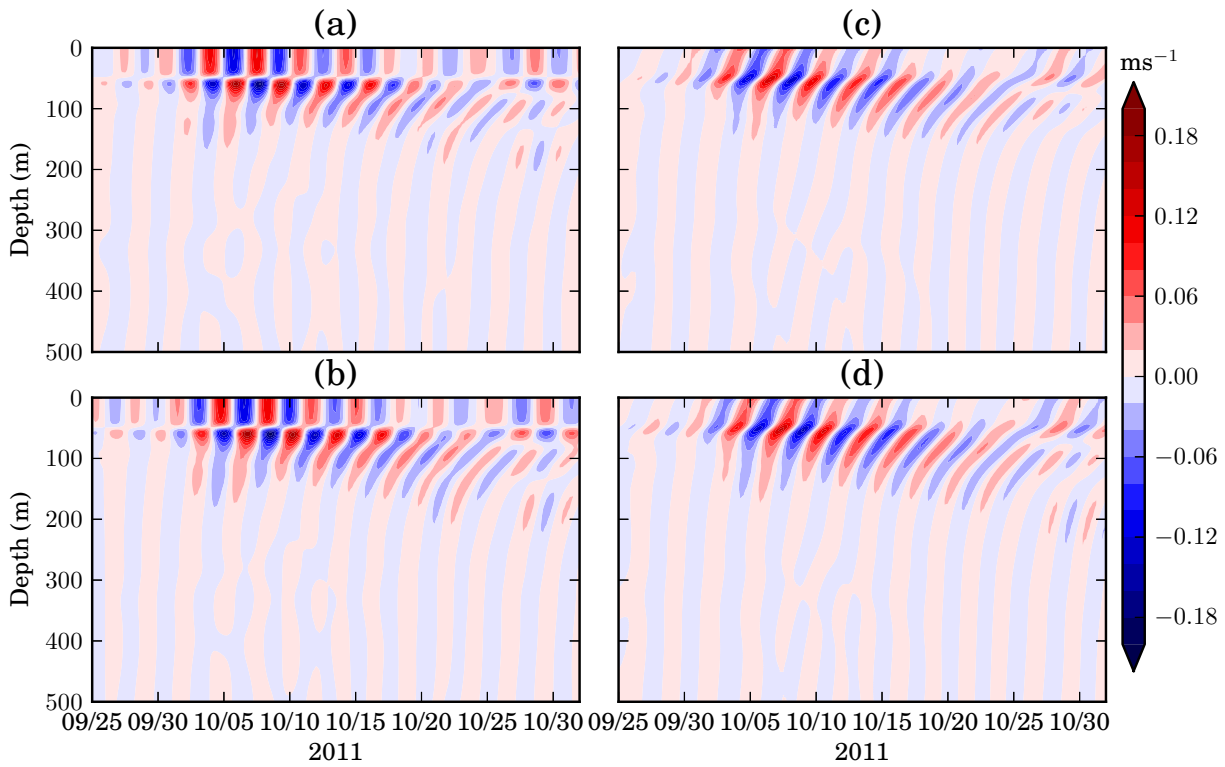

Figure 4.24: Same as Figure 4.23, but for experiment QUIET_WTL.

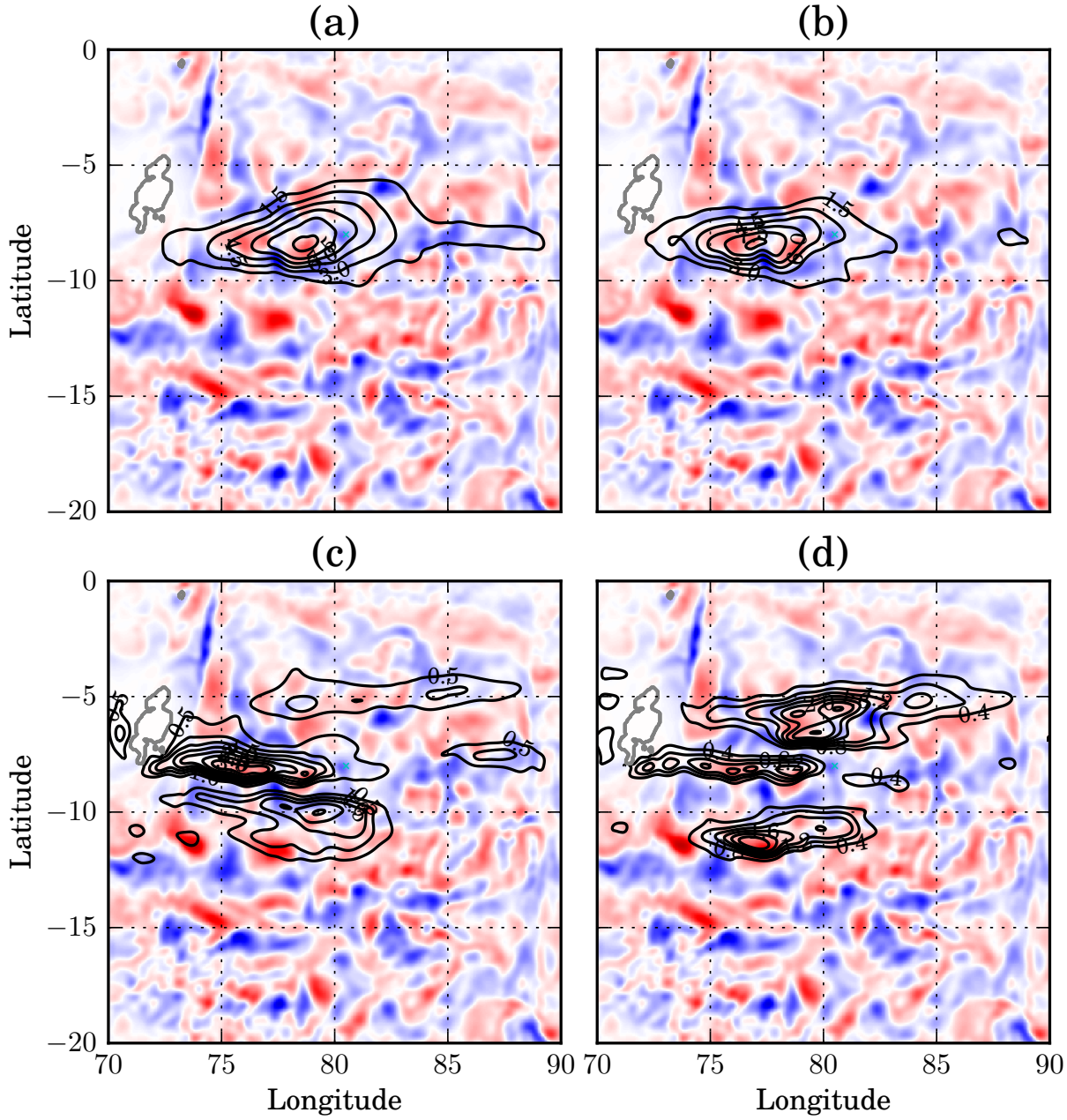

Figure 4.25: Experiment EDDY1_TL ML NIKE contours overlaying background flow ζ for (a) $t_\circ$ (b) 1 IP after $t_\circ$ (c) 3 IP after $t_\circ$ and (d) 5 IP after $t_\circ$.

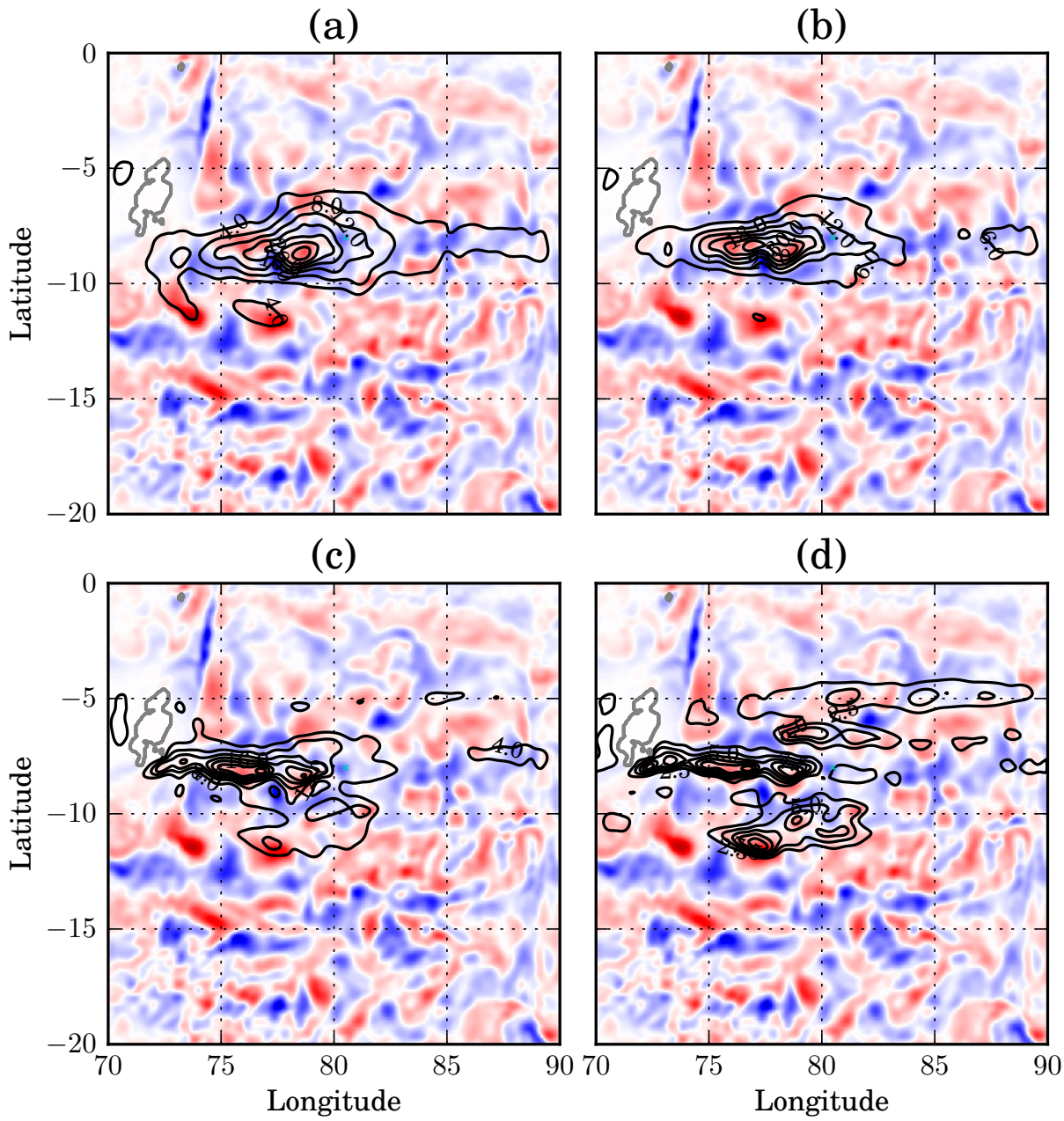

Figure 4.26: Experiment EDDY1_TL TL NIKE contours overlaying background flow ζ for (a) $t_\circ$ (b) 1 IP after $t_\circ$ (c) 3 IP after $t_\circ$ and (d) 5 IP after $t_\circ$.

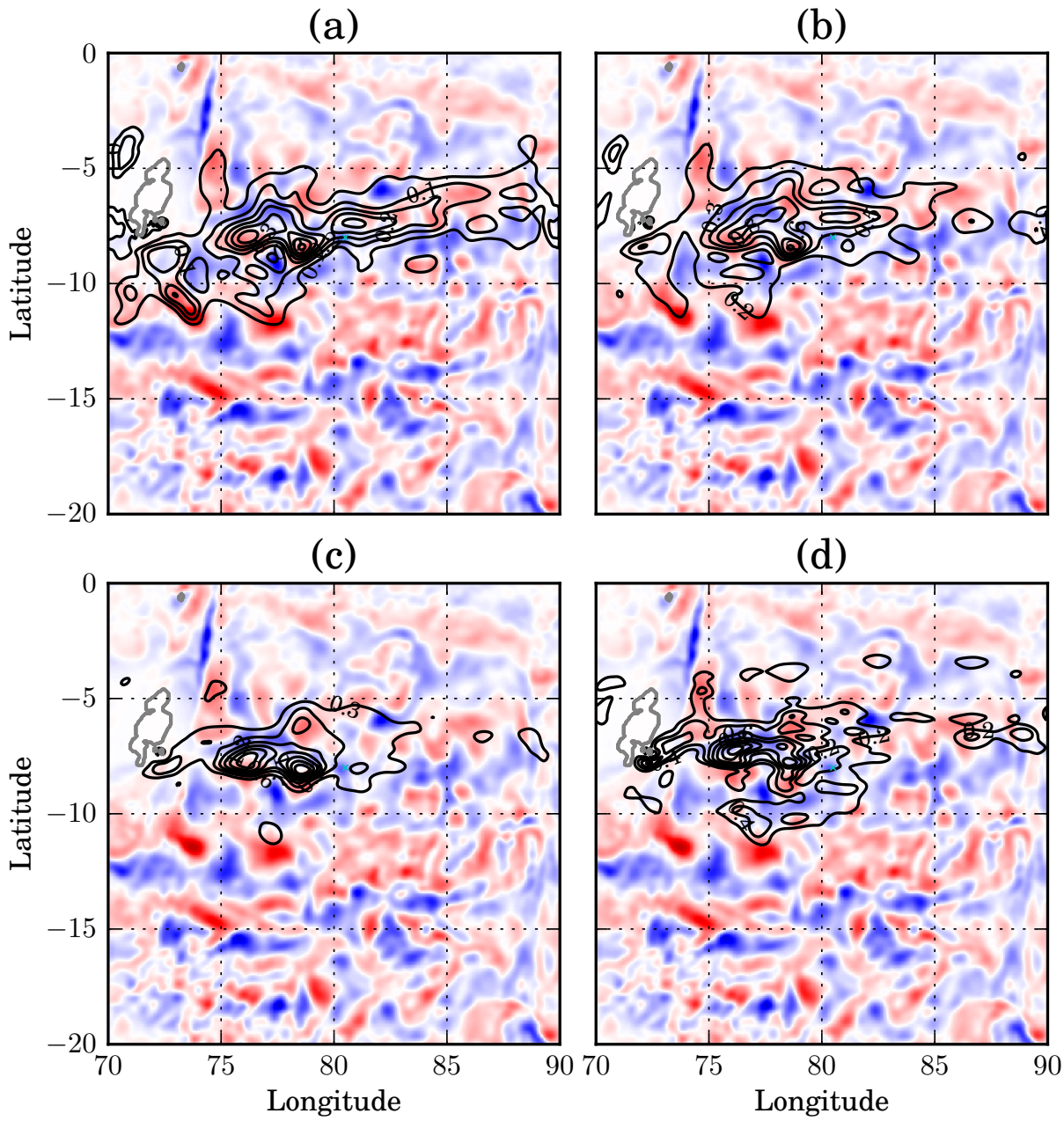

Figure 4.27: Experiment EDDY1_TL average thermocline NIKE contours overlaying background flow ζ for (a) $t_\circ$ (b) 1 IP after $t_\circ$ (c) 3 IP after $t_\circ$ and (d) 5 IP after $t_\circ$.

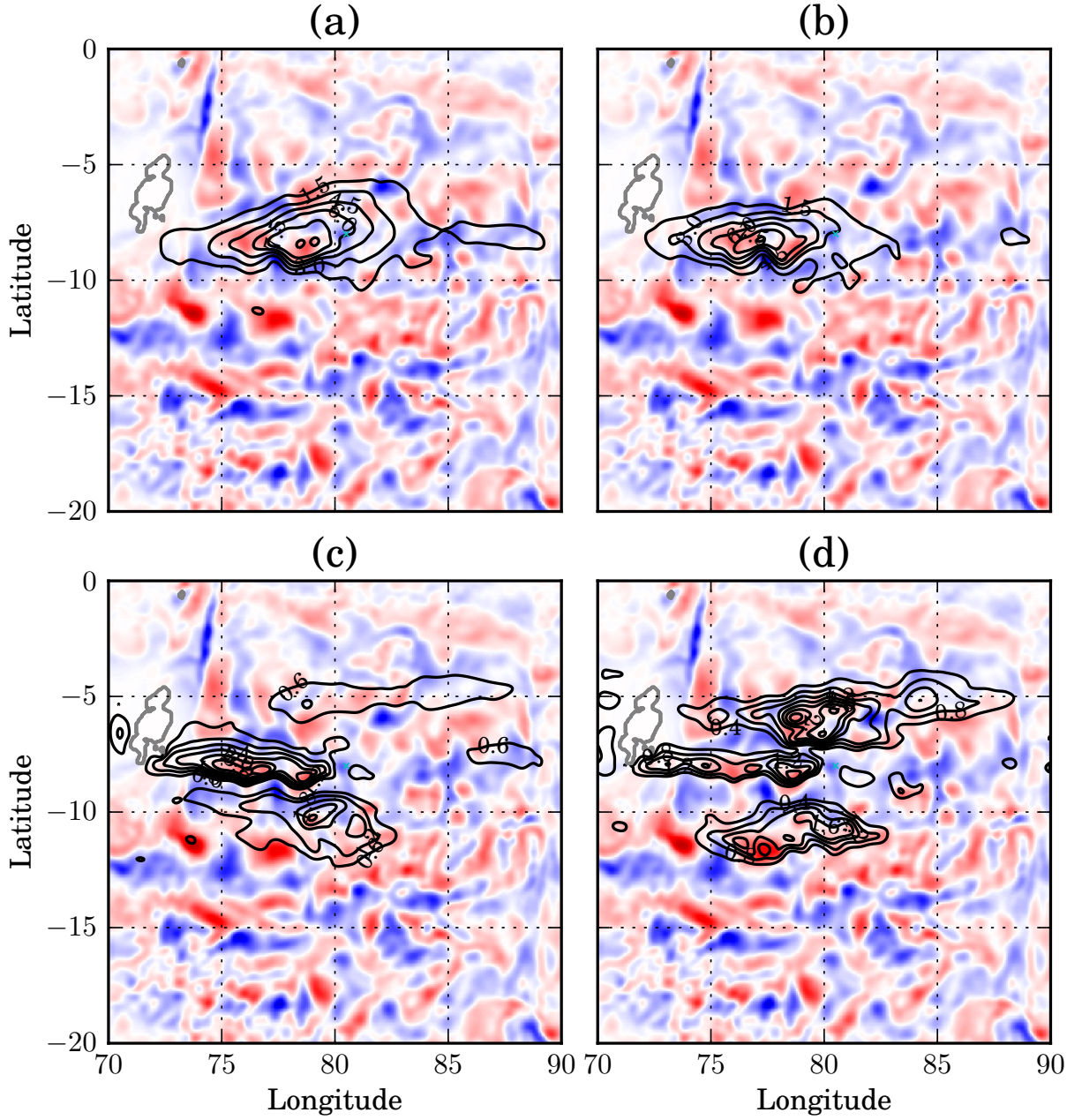

Figure 4.28: Same as Figure 4.25, but for experiment EDDY2_TL.

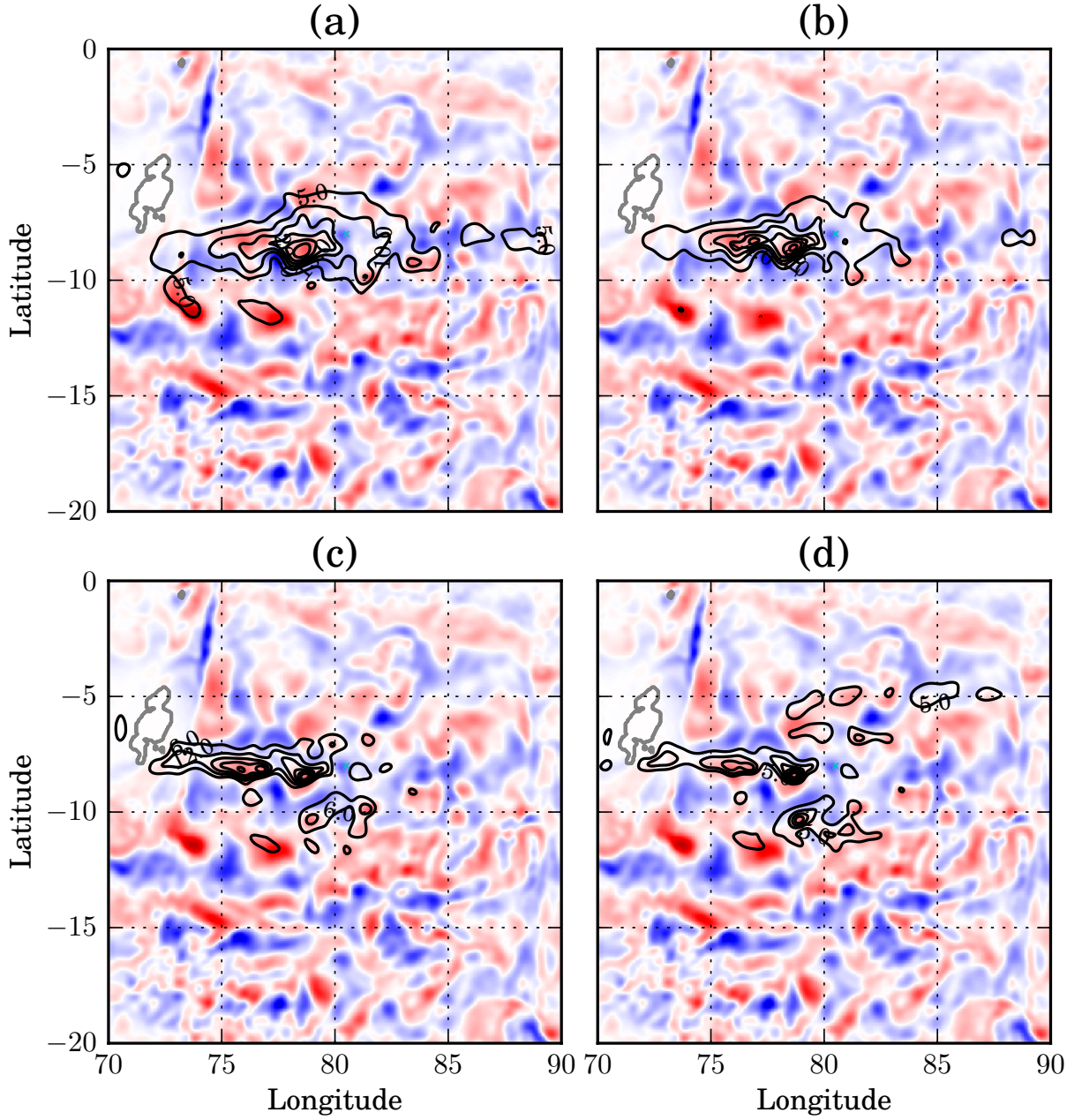

Figure 4.29: Same as Figure 4.26, but for experiment EDDY2_TL.

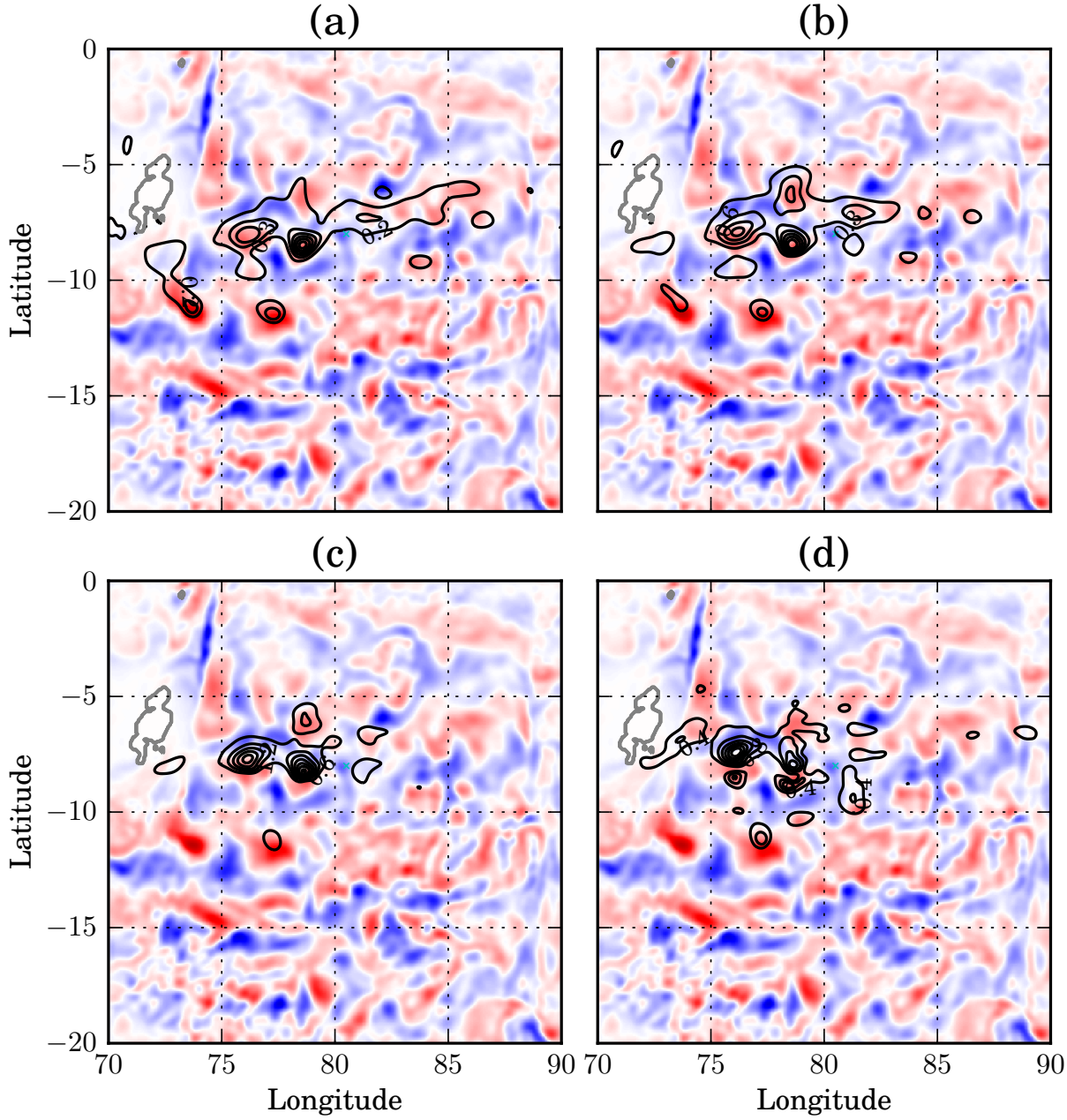

Figure 4.30: Same as Figure 4.27, but for experiment EDDY2_TL.

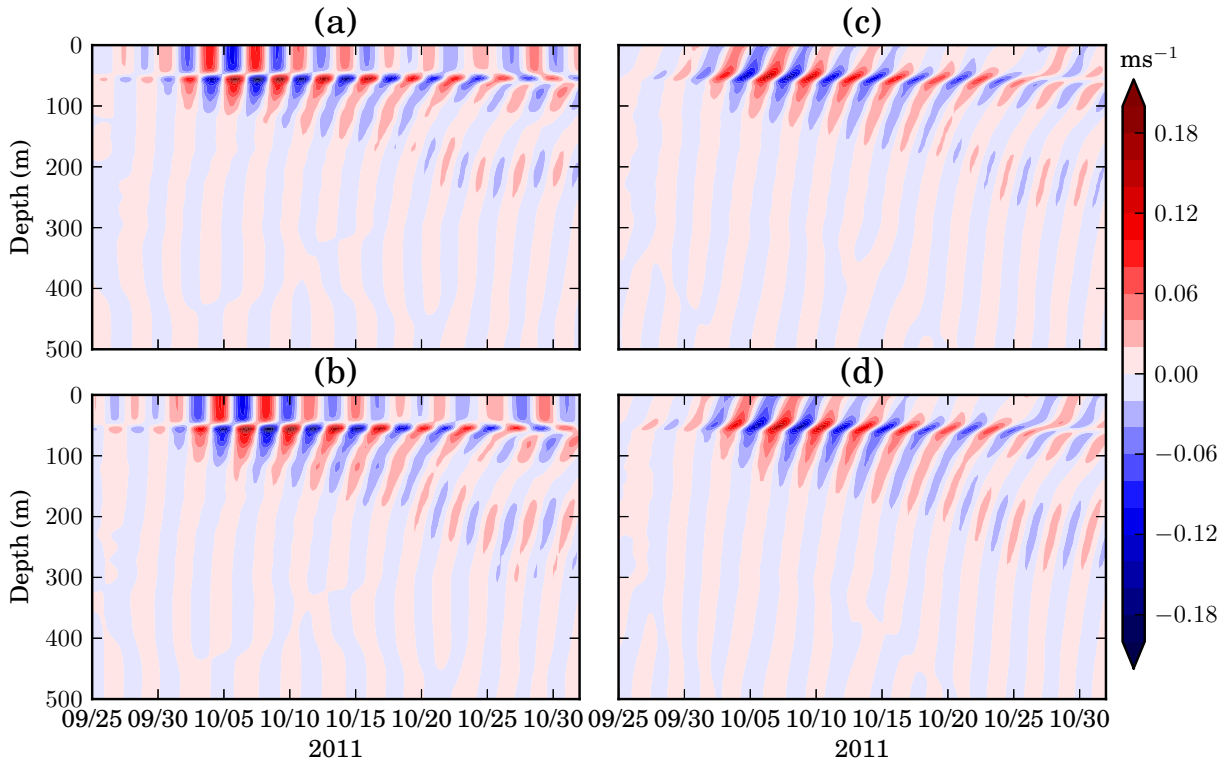

Figure 4.31: Experiment EDDY1_TL depth-time series at 8°S 80.5°E of near-inertial (2-6 days band passed) zonal velocity anomalies u' (a), zonal upward phase propagating velocity anomalies u'_{up} (b), meridional velocity anomalies v' (c), meridional upward phase propagating velocity anomalies v'_{up} (d).

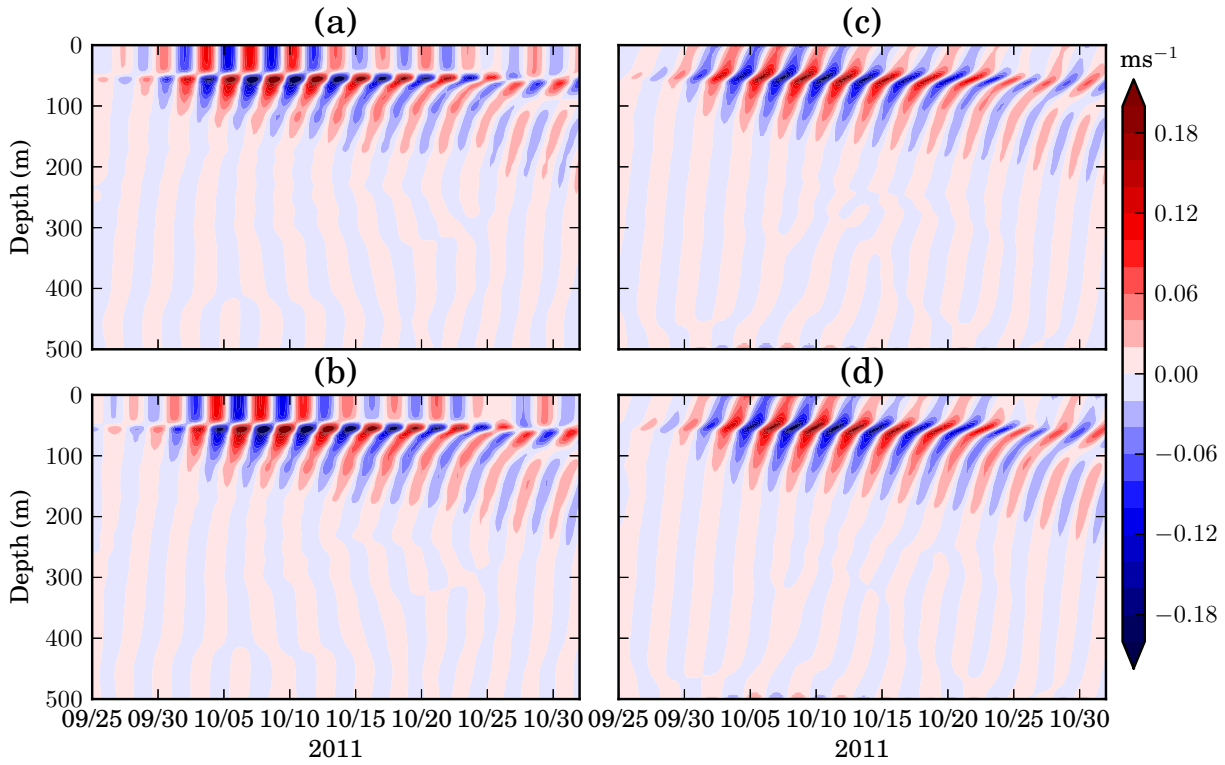

Figure 4.32: Experiment EDDY1_TL depth-time series at 8.65°S 78°E of near-inertial (2-6 days band passed) zonal velocity anomalies u' (a), zonal upward phase propagating velocity anomalies u'_{up} (b), meridional velocity anomalies v' (c), meridional upward phase propagating velocity anomalies v'_{up} (d).

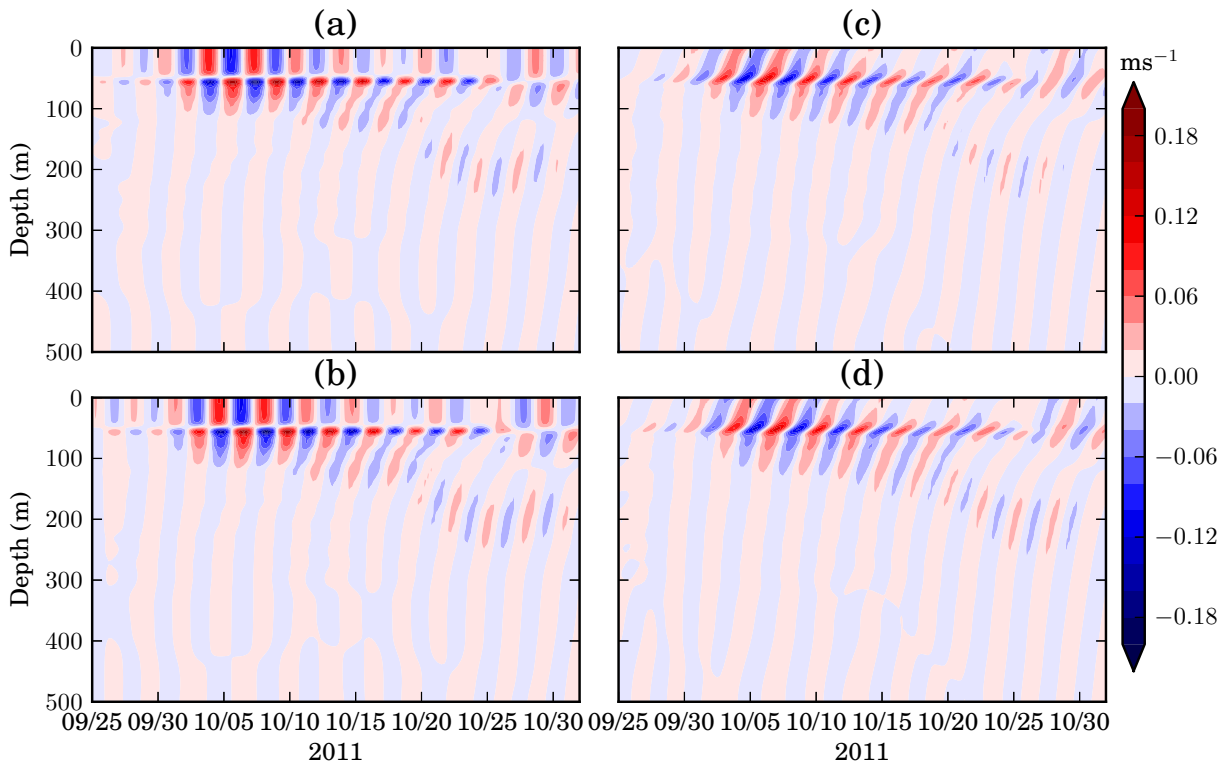

Figure 4.33: Same as Figure 4.31, but for experiment EDDY2_TL.

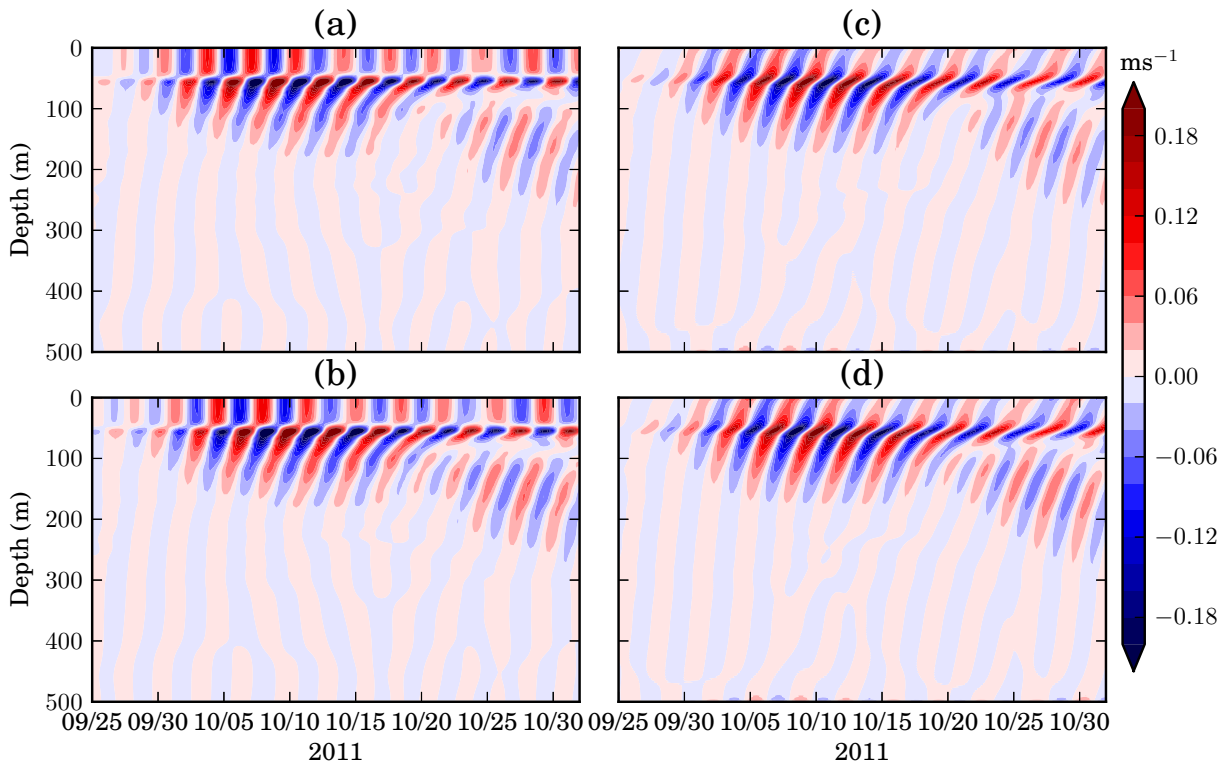

Figure 4.34: Same as Figure 4.32, but for experiment EDDY2_TL.

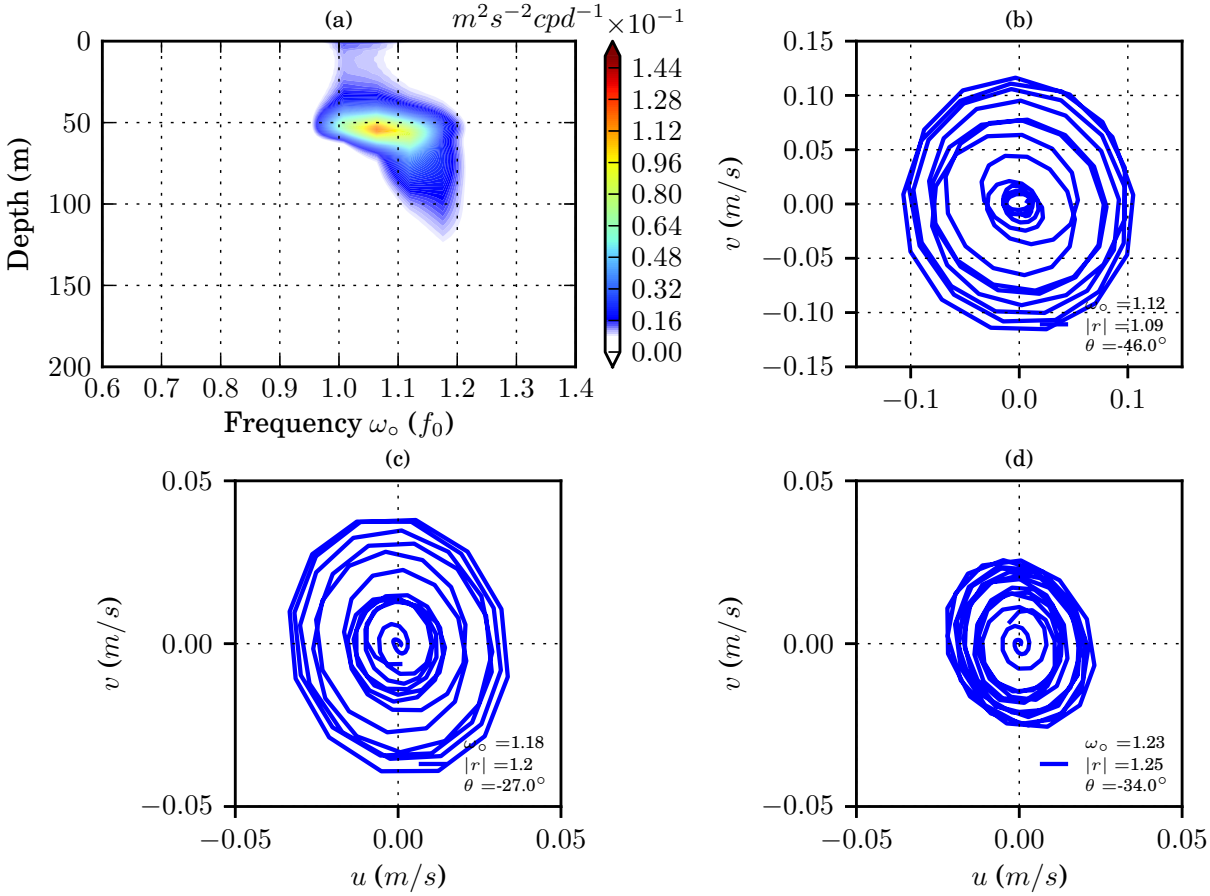

Figure 4.35: EDDY1_TL Energy density frequency spectra as a function of depth (a), NIW ellipse in the TL (60 m) (b), NIW ellipse at 120 m (c), and NIW ellipse at 180 m, for the CINDY station at 8°S 80.5°E.

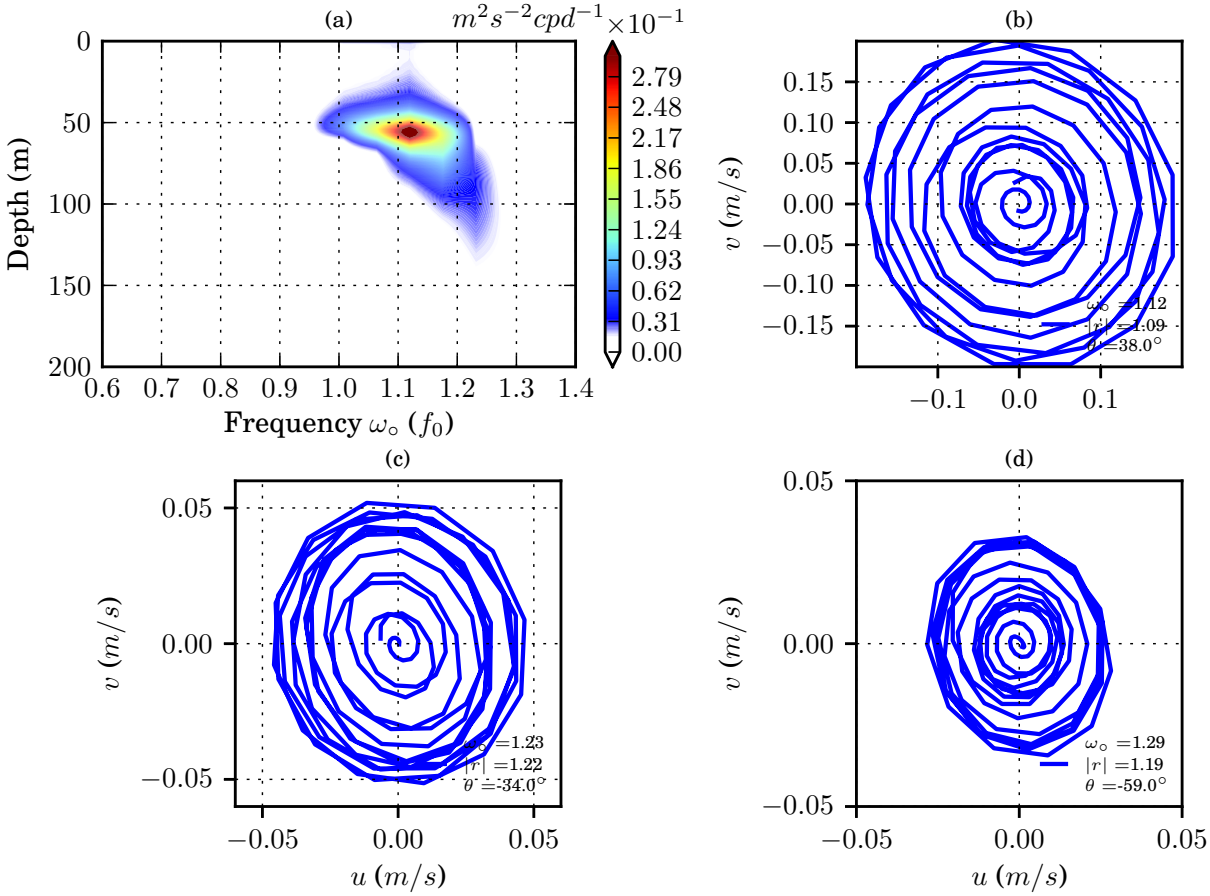

Figure 4.36: EDDY1_TL Energy density frequency spectra as a function of depth (a), NIW ellipse in the TL (60 m) (b), NIW ellipse at 120 m (c), and NIW ellipse at 180 m, for the Ac at 8.65°S 78°E.

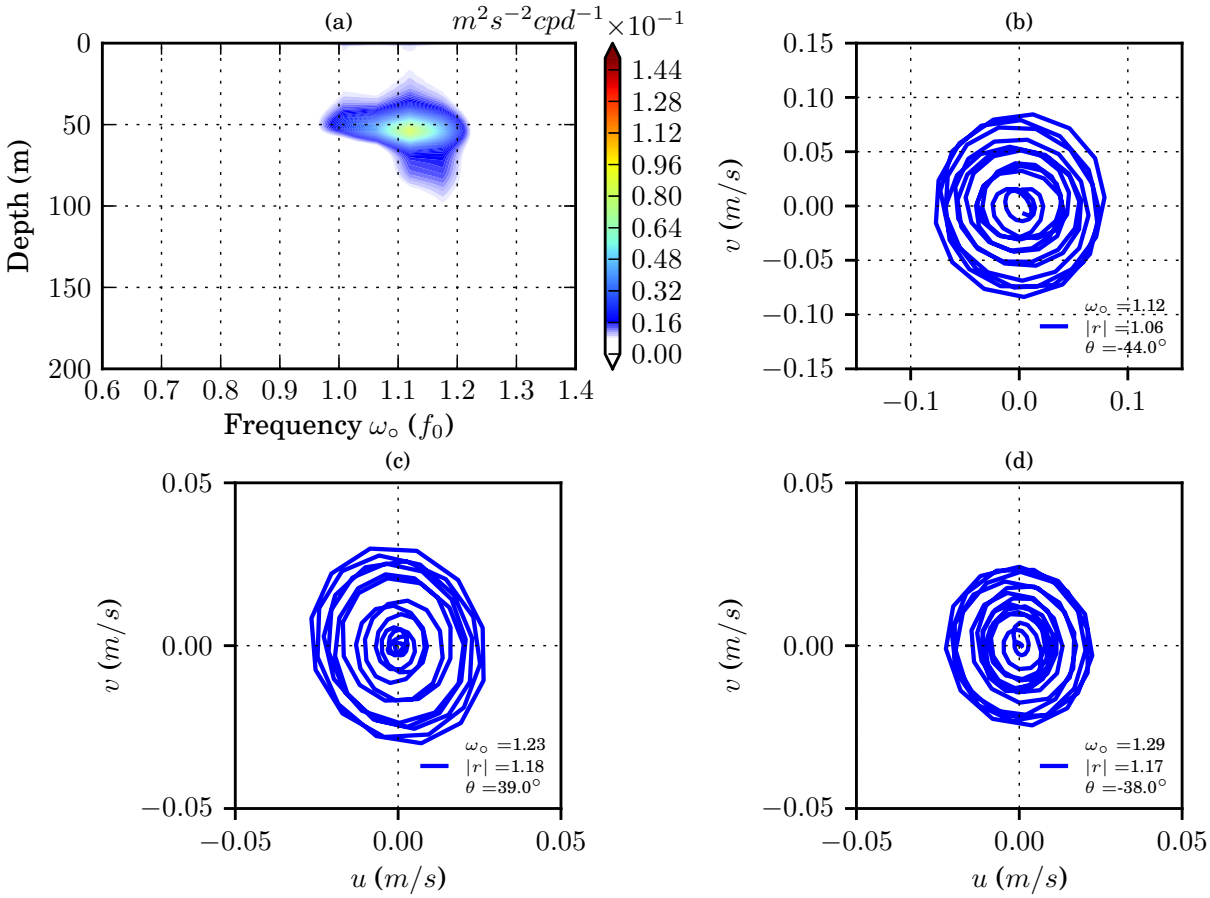

Figure 4.37: EDDY2_TL Energy density frequency spectra as a function of depth (a), NIW ellipse in the TL (60 m) (b), NIW ellipse at 120 m (c), and NIW ellipse at 180 m, for the CINDY station at 8°S 80.5°E.

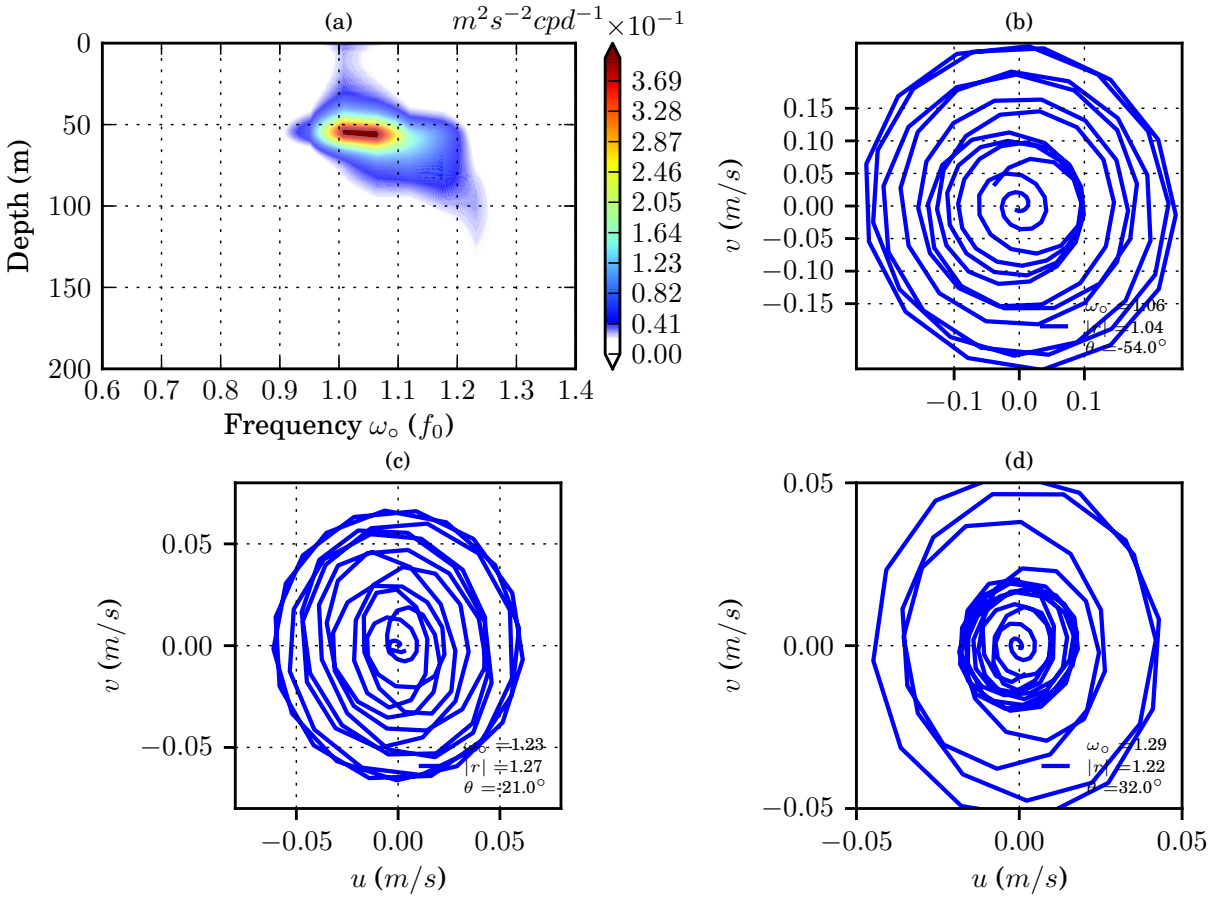

Figure 4.38: EDDY2_TL Energy density frequency spectra as a function of depth (a), NIW ellipse in the TL (60 m) (b), NIW ellipse at 120 m (c), and NIW ellipse at 180 m, for the AC at 8.65°S 78°E.

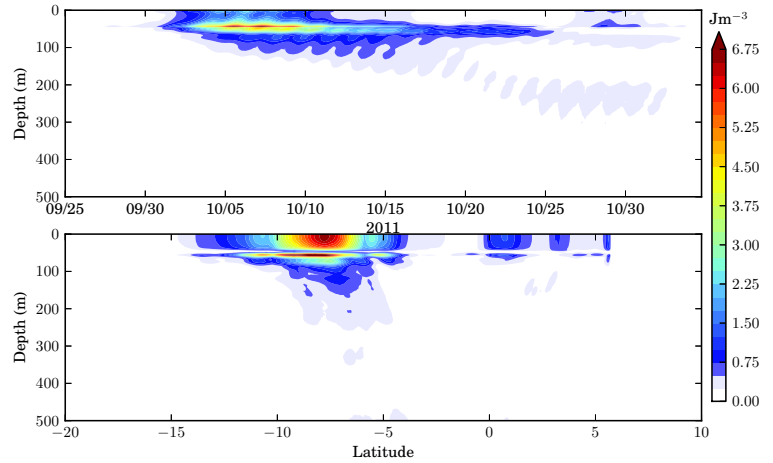

(a)

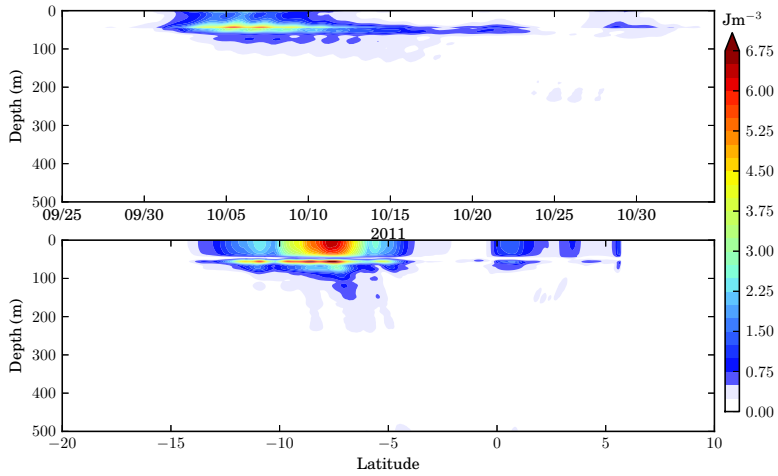

(b)

Figure 4.39: (a) EDDY1_TL upper panel: Depth-time series of WKB scaled NIKE at 8°S 80.5°E. Lower panel: Maximum NIKE during first 8 inertial periods of integration along 80.5°E showing the extend of downward and equatorwad NIKE penetration. (b) Same for EDDY2_TL.

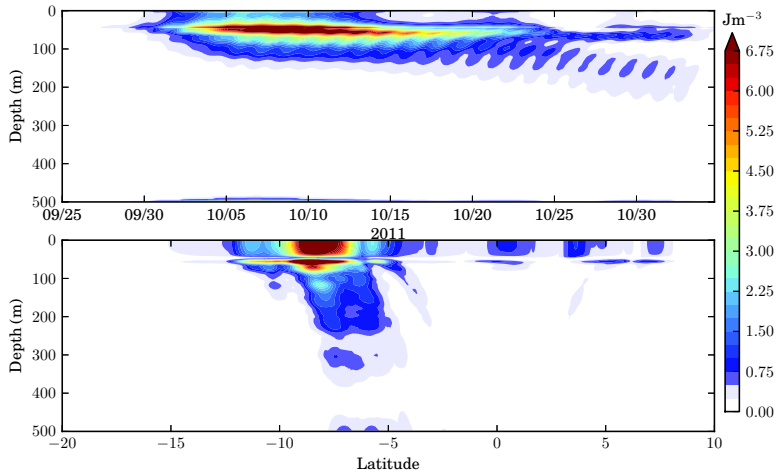

(a)

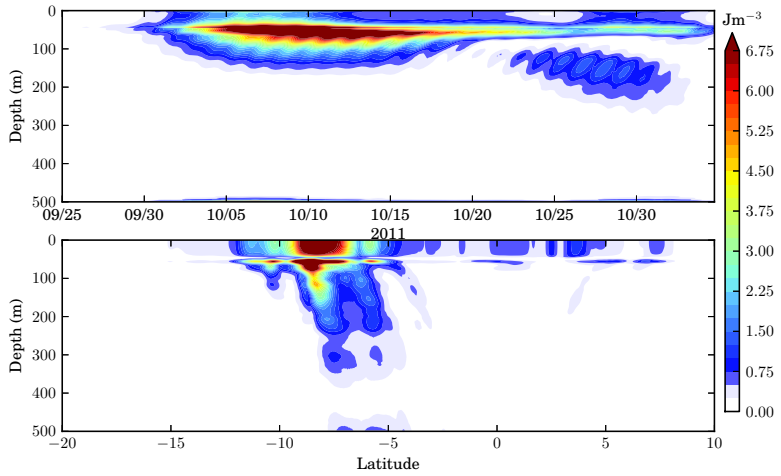

(b)

Figure 4.40: (a) EDDY1_TL upper panel: Depth-time series of WKB scaled NIKE at 8.65°S 78°E. Lower panel: Maximum NIKE during first 8 inertial periods of integration along 78°E showing the extend of downward and equatorwad NIKE penetration. (b) Same for EDDY2_TL.

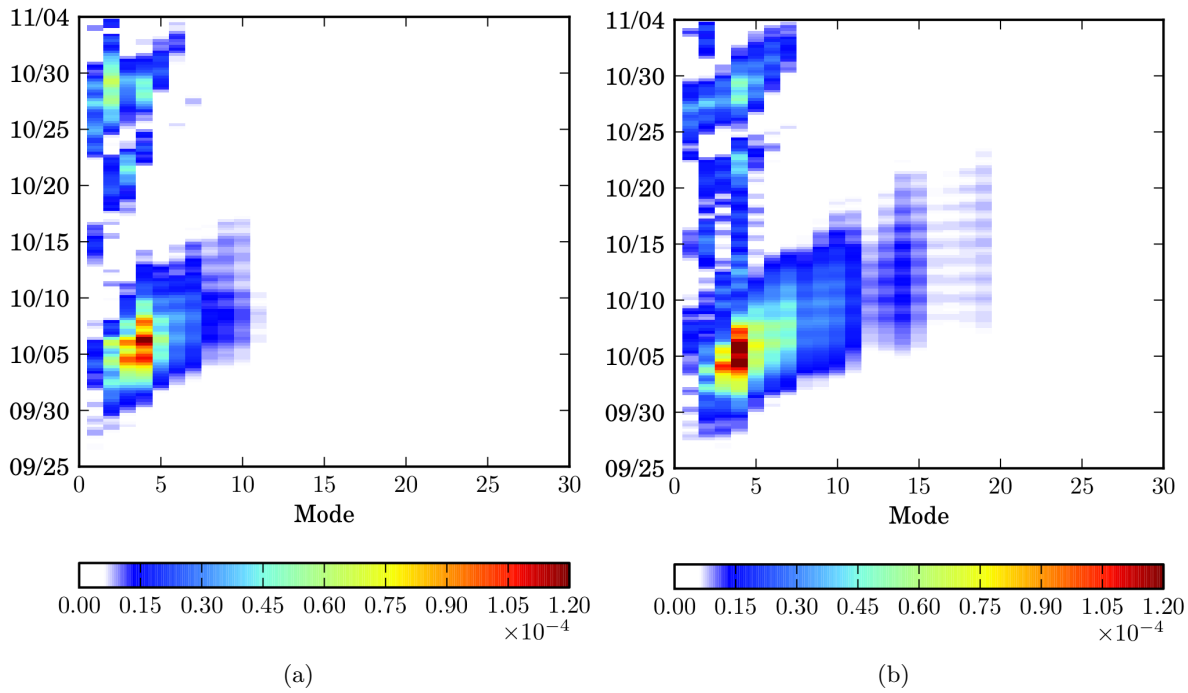

Figure 4.41: NIKE (m^2s^{-2}) partition by mode number for the EDDY1_TL experiment at (a) a cyclone (8°S 80.5°E) and (b) at an AC (8.65°S 78°E).

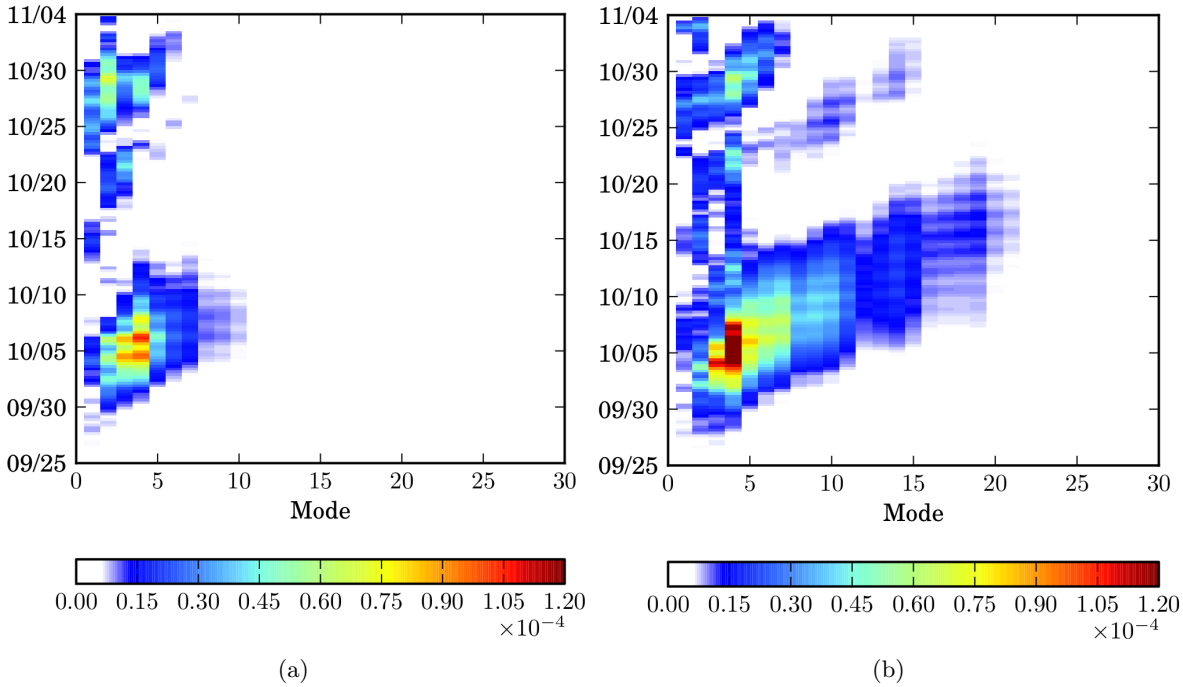

Figure 4.42: NIKE (m^2s^{-2}) partition by mode number for the EDDY2_TL experiment at (a) a cyclone (8°S 80.5°E) and (b) at an AC (8.65°S 78°E).

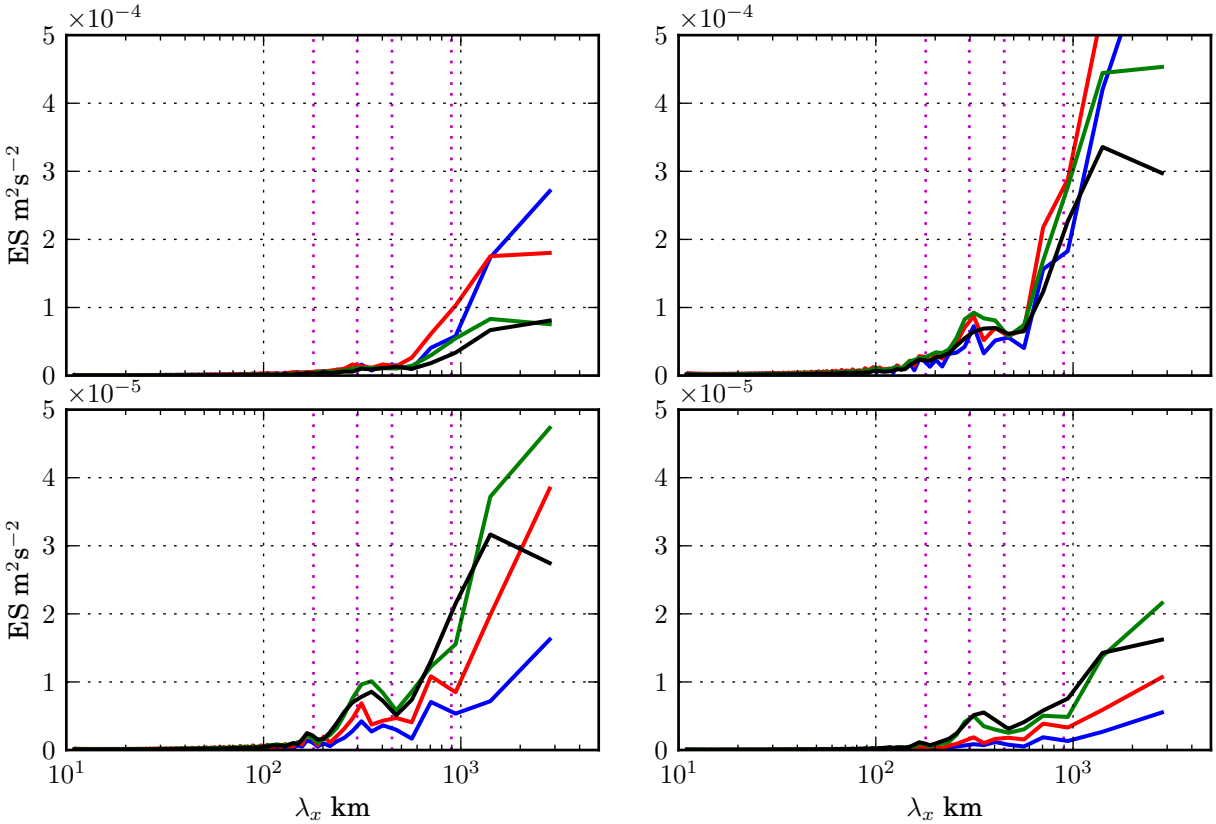

Figure 4.43: Same as Figure 4.21, but for experiment EDDY1_TL.

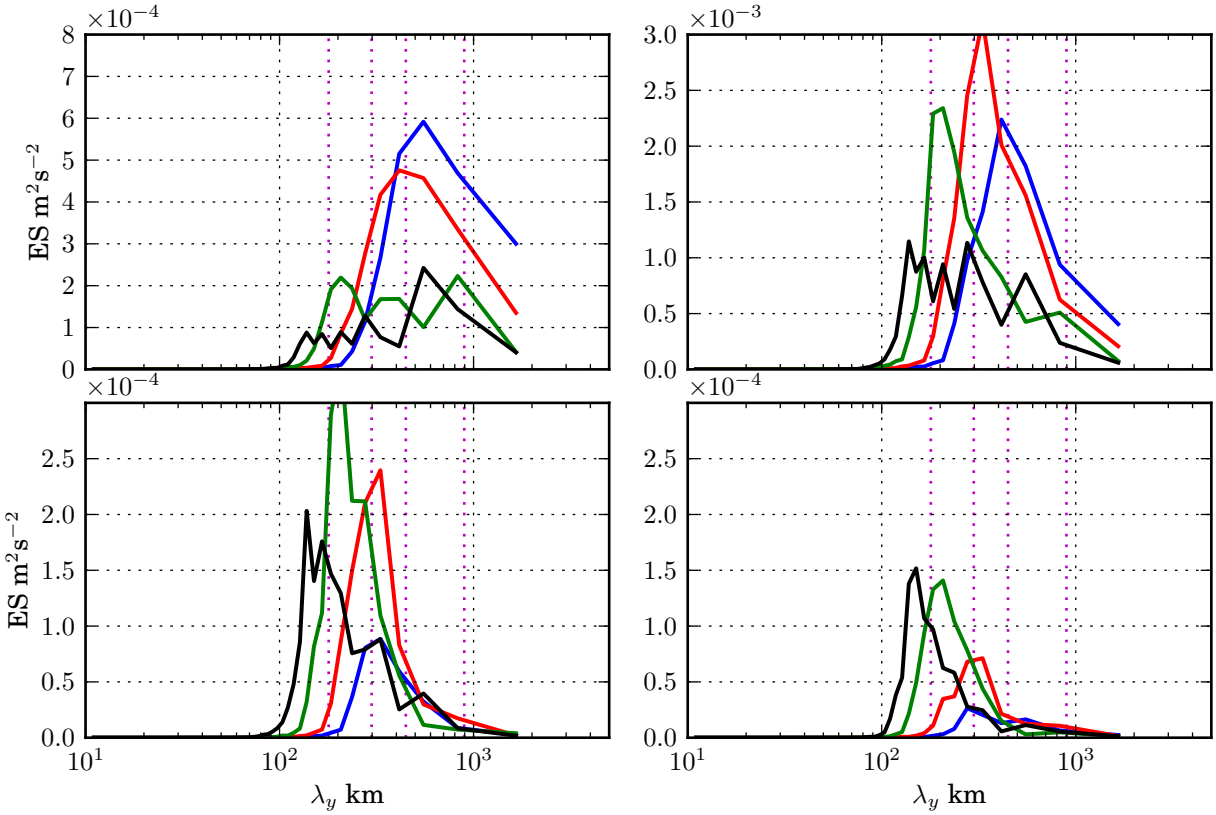

Figure 4.44: Same as Figure 4.22, but for experiment EDDY1_TL.

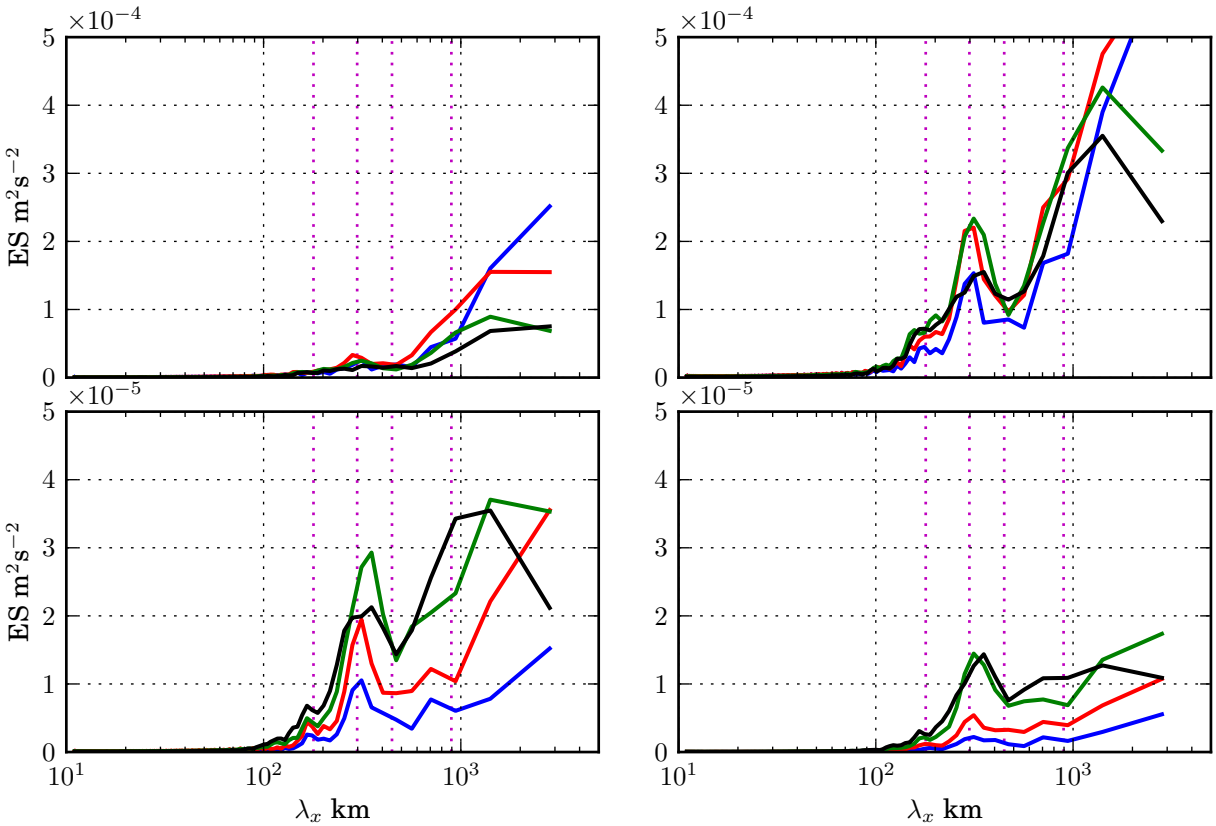

Figure 4.45: Same as Figure 4.21, but for experiment EDDY2_TL.

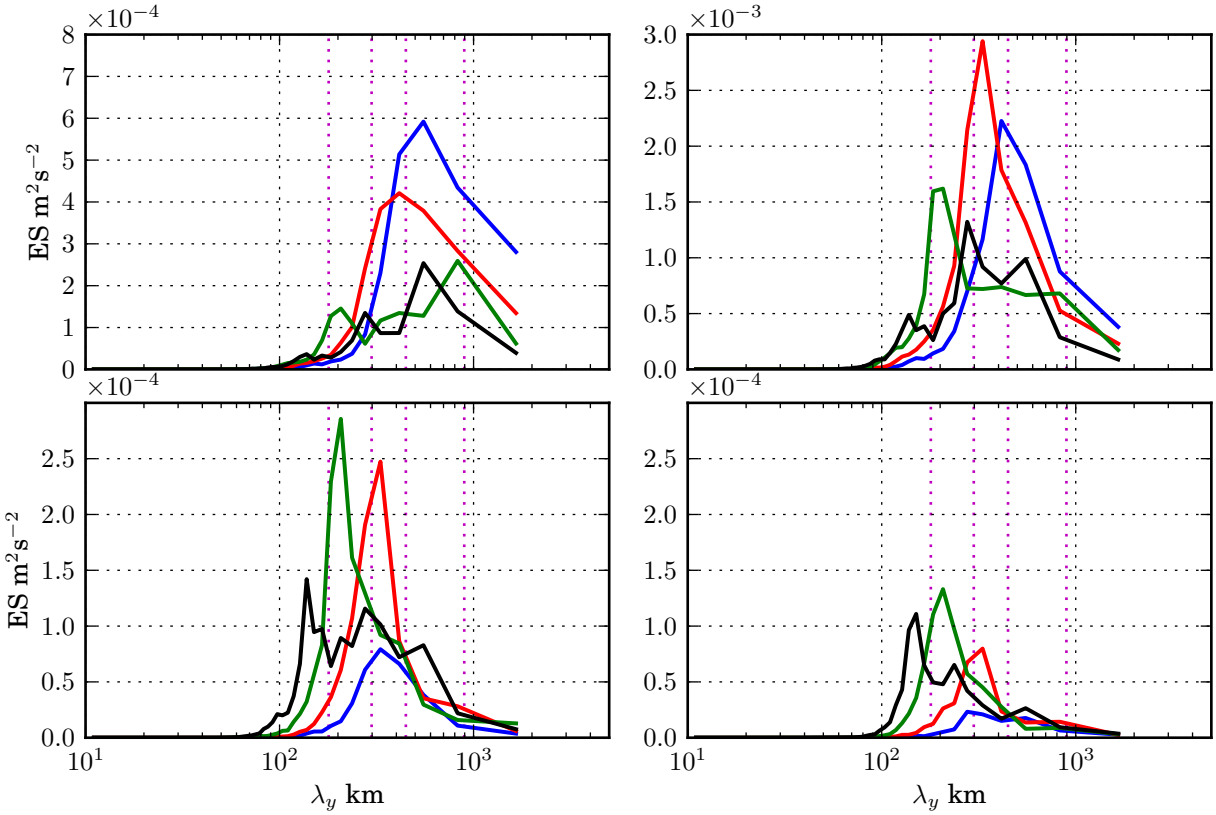

Figure 4.46: Same as Figure 4.21, but for experiment EDDY1_TL.

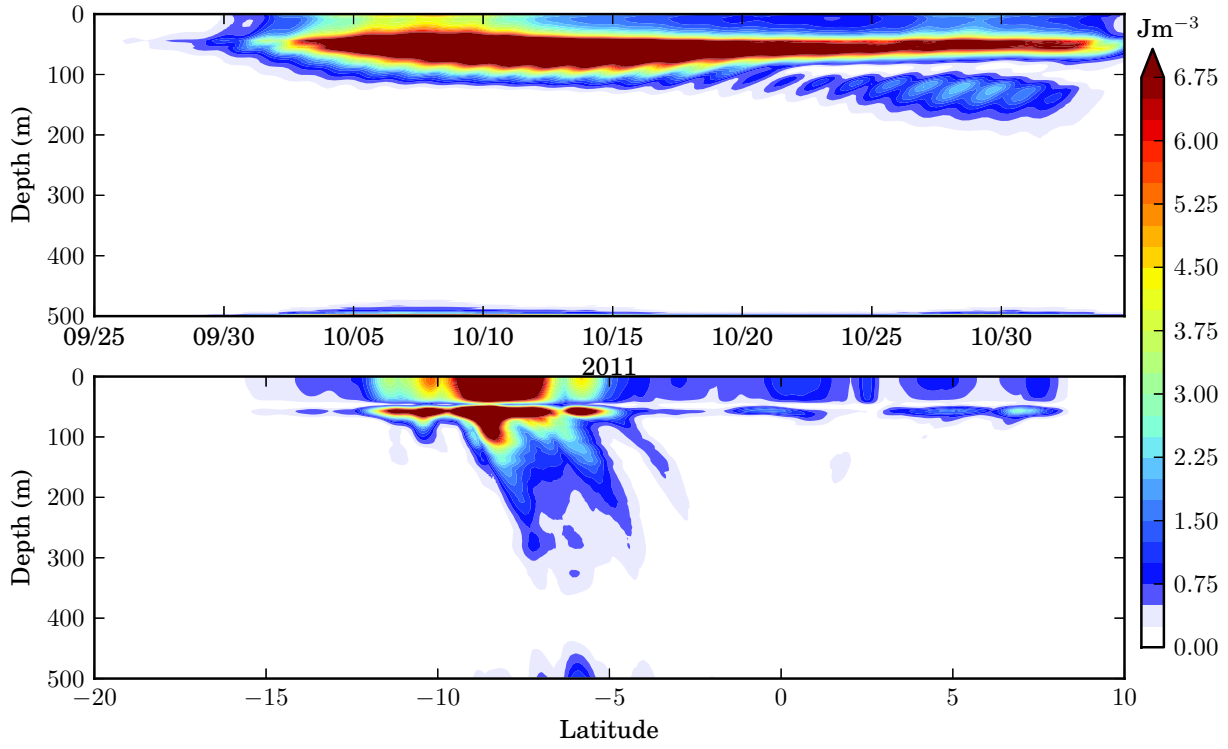

Figure 4.47: Experiment EDDY2_WTL; Top panel: Depth-time series of WKB scaled NIKE at 8.65°S 78°E. Lower panel: Maximum NIKE during first 8 inertial periods of integration along 78°E showing the extend of downward and equatorwad NIKE penetration.

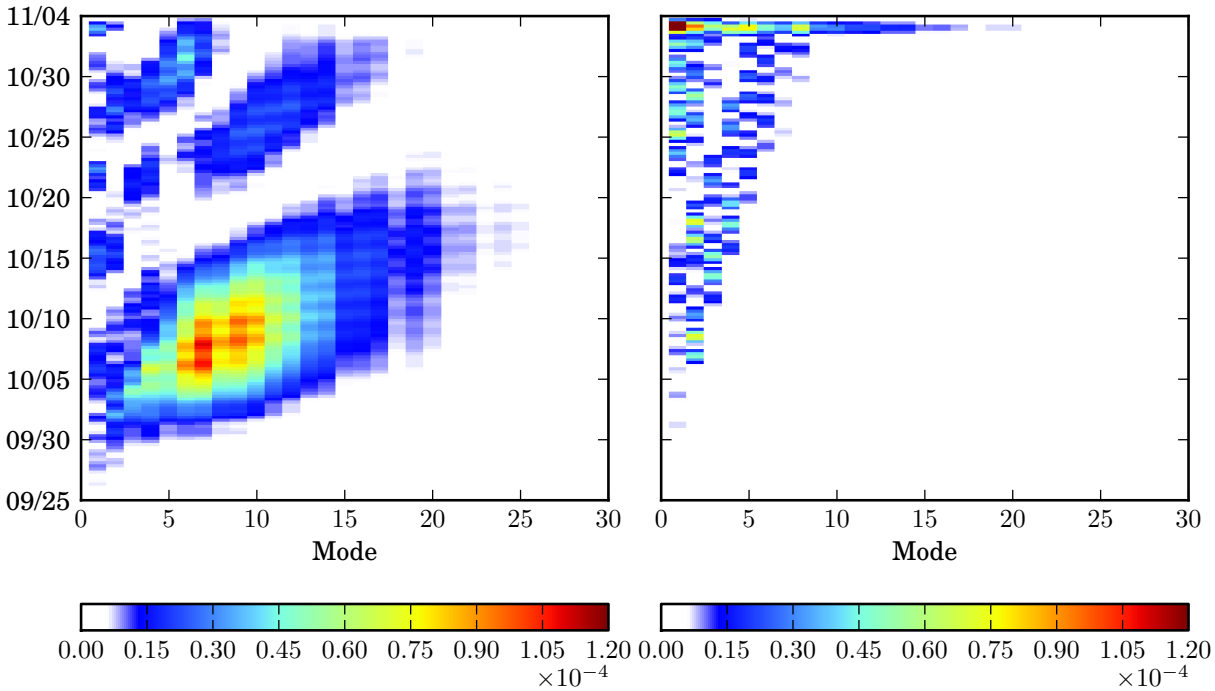

Figure 4.48: NIKE (m^2s^{-2}) partition by mode number for the EDDY2_WTL experiment at (a) CINDY station (8°S 80.5°E) and (b) at the Equator

CHAPTER 5
CONCLUDING REMARKS

5.1 Summary and Conclusions

This work set out to investigate aspects of the generation, propagation and dissipation of near-inertial waves in the tropical ocean. Model and observational data from the tropical eastern Pacific and central Indian Ocean were used to investigate different aspects of this problem. The major findings and conclusions of this study are:

1. Pacific Easterly Wave forcing is found to input relatively large amounts of inertial kinetic energy into the mixed layer in a few resonant forcing episodes.

2. The radiation of near-inertial waves is an important sink for the wind input of inertial kinetic energy by Pacific Easterly Waves, particularly for near-resonant forcing events, typically accounting for 50-60% of the mixed inertial energy decay.

3. The fraction of energy radiated is found to vary substantially between Easterly Wave forcing events, with a noted impact of the stratification at the base of the mixed layer, a region known as the Transition layer.

4. Near-inertial wave packets are observed in the thermocline following a wind forcing event early in the time series record from the CINDY2011 observations. The upper most wave packet vertical energy flux is estimated to be 30-40% of the wind input of inertial kinetic energy to the mixed layer.

5. Significant near-inertial wave energy is observed to penetrate down to 200 m.

6. A dissipation event was measured in association with the lower most NIW packet. It is estimated that approximately 20% of the wave packet's energy was removed in this event.

7. Refraction induced by the background flow accounts for several of the estimated changes in wave properties along the vertical, i.e. between the different packets, and may also have

triggered the dissipation event.

8. The inclusion of background flow relative vorticity in the LCS model plays a key role in promoting localized penetration of near-inertial energy into the thermocline, and a strong affinity of near-inertial kinetic energy to anticyclonic vorticity regions is observed in LCS model solutions.

9. The enhanced near-inertial energy in the vicinity of anticyclones appears to result from NIW trapping, as described by *Kunze* (1985), wherein high modes are much more energetic.

10. These impacts are found to be proportional to the magnitude of the relative vorticity field.

11. Contrary to expectation, no significant impact on the horizontal wavenumber spectrum of the NIWs was detected.

12. The combination of $\mathcal{O}(10^{-1})$ $\mathcal{R}_\circ$ relative vorticity with increased stratification within the thermocline favors the highest, and closest to observed, levels of near-inertial kinetic energy penetration into the thermocline. Again, this feature appears related to an increase in high vertical mode near-inertial energy.

As discussed throughout this work, the relatively high horizontal and vertical scales of NIW packets are such that explicitly resolving them in global general circulation models (GCMs) remains prohibitively expensive. In the next sections, some implications of the above results to the development of a parameterization for NIW induced mixing in GCMs are discussed, followed by a discussion of limitations in the present study and possible future work to be conducted in order to address some of these issues.

5.2 Implications to parameterization of near-inertial mixing in OGCM

Jochum et al. (2013) conducted the first climate model simulations which account for the impact of NIWs on the vertical and diapycnal mixing. The near-inertial energy induced mixing was

parameterized in the surface boundary layer as well as in the ocean interior. The author found little to no impact of NIW mixing below the boundary layer, although significant changes in model SST were detected which lead to alterations in the patterns of tropical precipitation and midlatitude wind stress through atmospheric teleconnections. Only 2% of the energy for background interior mixing was supplied by the NIWs, a result largely attributed to the coupled model's weak wind input of inertial kinetic energy. In light of the above results, the parameterization of *Jochum et al.* (2013) for the interior NIW induced mixing is examined here.

The vertical eddy diffusivity used in *Jochum et al.* (2013) reads:

$$\kappa_{\mathrm{niw}} = \frac{\gamma \epsilon F(z)}{\rho N^2}, \tag{5.1}$$

where $\gamma = 0.2$ is the mixing efficiency, ϵ is the near-inertial energy flux available for mixing below the boundary layer, $F(z)$ is its vertical structure, ρ is the density of seawater and N^2 is the buoyancy frequency. The energy flux below the boundary layer is described by

$$\epsilon = \epsilon^i \times (1 - bf) \times lf, \tag{5.2}$$

where ϵ^i is inertial energy input into the boundary layer, $bf = 0.7$ everywhere is the fraction of the near-inertial energy flux dissipated within the boundary layer, $lf = 0.5$ is the local fraction of interior near-inertial energy flux (i.e. that does not propagate horizontally away). The vertical structure of ϵ represents an exponential decay away from the bottom of the boundary layer and is given by

$$F(z) = \frac{\exp\left((z-h)/\xi\right)}{\xi\left[1 - \exp\left(-h/\xi\right)\right]}, \tag{5.3}$$

where h is the depth of the boundary layer calculated by the KPP paramerization (*Large et al.* 1994) and $\xi = 2000$ m is a decay scale.

The choice values for bf and lf are motivated by the works of *Crawford and Large* (1996) and *Furuichi et al.* (2008), respectively. Based on the results of Chapter 2 and 3, the value of bf represents somewhat of an upper bound, at least for the tropical region, the parameter bf,

therefore should perhaps, at least, vary latitudinally, decreasing towards the tropics. It should be noted that the work of *Crawford and Large* (1996) uses a midlatitude data set and does not account for the radiation of NIWs in their model energy budget, likely biasing their results towards a large role for the boundary layer turbulent dissipation. As seen in Chapter 2 though, the bf fraction exhibits dependence of how efficient the winds are at exciting surface inertial oscillations as well as on the strength of the stratification below the mixed layer. Thus, these factors, particularly the stratification, should also be taken into account, ultimately resulting in a time dependent bf.

The parameter lf represents a greater challenge. The results of Chapter 4 suggest that the vast majority (e.g. nearly 90%) of the near-inertial kinetic energy remains confined near the generation region for the following 8 inertial periods. In the analysis of the CINDY2011 observations (Chapter 3), the NIW energy has suffered significant dissipation. This is substantially more than the 50% fraction used by *Jochum et al.* (2013), attributed to the equatorward propagation of low mode NIWs (*Furuichi et al.* 2008). Furthermore, the LCS results of Chapter 4 support the notion of widespread NIW kinetic energy "trapping" by anticyclonic relative vorticity. A parameterization for lf should take into account these lateral inhomogeneities, wherein lf is increased in regions anticyclonic vorticity, assuming the GCM can adequately resolve the eddying field. The enhancement factor remains to be determined.

The choice value of 2000 m for ξ is based on average WKB scaled near-inertial energy profiles from *Alford and Whitmont* (2007). In contrast, the estimates of NIW wave dissipation from Chapter 3 suggest that the near-inertial decay may occur well within the thermocline at 8°S, and as discussed above within 30-40 days from the generation time at the surface. Again, the moored data set analyzed by the authors are for midlatitude regions and they assume low mode NIWs dominate the wavnumber spectrum. However, despite large low mode near-inertial amplitudes simulated by the LCS, most of the physical near-inertial energy is surface intensified, several inertial periods after generation, implying a slow descent towards the bottom. The appropriateness of a simple exponential decay may also need to be re-assessed.

It is reasonable to assume that increasing the parameter lf, while decreasing bf and ξ will increase the impact of NIWs mixing on thermocline ventilation, but ramifications to air-sea inter-

action patterns and deep ocean circulation are not obvious (*Sasaki et al.* 2013) and will require detailed simulations.

5.3 Future Work

The method proposed in Chapter 2 may be a promising way to quantify the partition of wind induced near-inertial energy between the radiation of NIWs and loss to turbulent dissipation at the base of the mixed layer, but requires additional validation work. Application of this methodology to the CINDY2011 data is an obvious step in the that direction. Preliminary results support the result of Chapter 3 in that about 40% of the wind input of inertial kinetic energy radiates downward from the mixed layer.

After this validation work, further use of this method in longer and more robust moored time series such as the WHOTS data set may help test some of the relationships derived in Chapter 2. Application of the method to moorings in other regions, particularly if from higher latitudes or areas of strong eddy activity, may help achieve a more comprehensive description of NIW radiation. Based on the results of Chapter 4, the GOTM simulations, in some cases, may improve by taking into account the local f_{eff} or at least a detailed study of the sensitivity of the near-inertial kinetic energy budget results to the inclusion of such. For example, a probable ramification of a significantly different f_{eff} may have impacts on the resonant frequency for wind forcing.

Some of the results of the LCS process studies should be verified by experiments using a primitive equation model, particularly the extent of the depth and equatorward penetration of near-inertial wave energy. A more thorough analysis of the relationship between near-inertial energy and the relative vorticity field should be performed next. In particular, with regards to the horizontal scales of the simulated NIWs. Additional process oriented experiments with the LCS exploring the sensitivity to different non-averaged vorticity fields should also be conducted, as well as experiments addressing the role of Doppler shift and advection by the mean flow.

5 References

Alford, M. H., and M. Whitmont (2007), Seasonal and spatial variability of near-inertial kinetic energy from historical moored velocity records, *J. Phys. Oceanogr.*, *37*(8), 2022–2037.

Crawford, G., and W. Large (1996), A numerical investigation of resonant inertial response of the ocean to wind forcing, *J. Phys. Oceanogr.*, *26*(6), 873–891.

Furuichi, N., T. Hibiya, and Y. Niwa (2008), Model-predicted distribution of wind-induced internal wave energy in the worlds oceans, *J. Geophys. Res*, *113*, C09,034.

Jochum, M., B. P. Briegleb, G. Danabasoglu, W. G. Large, N. J. Norton, S. R. Jayne, M. H. Alford, and F. O. Bryan (2013), The impact of oceanic near-inertial waves on climate, *J. Climate*, *26*(9), 2833–2844.

Kunze, E. (1985), Near-inertial wave propagation in geostrophic shear, *J. Phys. Oceanogr.*, *15*(5), 544–565.

Large, W. G., J. C. McWilliams, and S. C. Doney (1994), Oceanic vertical mixing: a review and a model with a nonlocal boundary layer parameterization, *Rev. Geophys.*, *32*, 363–403.

Sasaki, W., K. J. Richards, and J.-J. Luo (2013), Impact of vertical mixing induced by small vertical scale structures above and within the equatorial thermocline on the tropical Pacific in a cgcm, *Clim. Dynam.*, *41*(2), 443–453.